eman ta zabal zazu
Universidad del País Vasco
Euskal Herriko Unibertsitatea

UNIVERSITY OF THE BASQUE COUNTRY

DEPARTMENT OF CHEMICAL ENGINEERING

Fuel production by hydrocracking of non-olefinic plastics and vacuum gasoil blends

DOCTORAL THESIS

Juan David Trueba Fraile

Leioa, febrero, 2023

eman ta zabal zazu

Universidad del País Vasco
Euskal Herriko Unibertsitatea

UNIVERSITY OF THE BASQUE COUNTRY

DEPARTMENT OF CHEMICAL ENGINEERING

Fuel production by hydrocracking of non-olefinic plastics and vacuum gasoil blends

Author:

Juan David Trueba Fraile

Supervisors:

Prof. José M. Arandes Esteban

Dr. Alazne Gutiérrez Lorenzo

A thesis submitted in fulfilment of the requirements for the degree of Doctor in Chemical Engineering

TESI ZUZENDARIAREN BAIMENA TESIA AURKEZTEKO	AUTORIZACIÓN DEL/LA DIRECTORA/A DE TESIS PARA SU PRESENTACIÓN

Zuzendariaren izen-abizenak /Nombre y apellidos de los directores:

José M. Arandes Esteban, IFZ /NIF: **14705472-P**
Alazne Gutiérrez Lorenzo, IFZ /NIF: **45673756-B**

Tesiaren izenburua / Título de la tesis: **Fuel production by hydrocracking of non-olefinic plastics and vacuum gasoil blends**

Doktorego programa / Programa de doctorado: **Ingeniería Química**

Doktoregaiaren izen-abizenak / Nombre y apellidos del/la doctorando/a:
Juan David Trueba Fraile

Unibertsitateak horretarako jartzen duen tresnak emandako ANTZEKOTASUN TXOSTENA ikusita, baimena ematen dut goian aipatzen den tesia aurkez dadin, horretarako baldintza guztiak betetzen baititu.	Visto el INFORME DE SIMILITUD obtenido de la herramienta que a tal efecto pone a disposición la universidad, autorizo la presentación de la tesis doctoral arriba indicada, dado que reúne las condiciones necesarias para su defensa.

Tokia eta data / Lugar y fecha: Leioa, a ___ de _____ de 2023

Fdo: José M. Arandes Esteban Fdo. Alazne Gutiérrez Lorenzo
Sin. / Fdo.: Tesiaren zuzendaria / Los directores de la tesis

AUTORIZACIÓN DE LA COMISIÓN ACADÉMICA DEL PROGRAMA DE DOCTORADO

La Comisión Académica del Programa de Doctorado en **Ingeniería Química** en reunión celebrada el día ____ de _____ de 20___, ha acordado dar la conformidad a la presentación de la Tesis Doctoral titulada: **Fuel production by hydrocracking of non-olefinic plastics and vacuum gasoil blends** dirigida por el Dr. **José M. Arandes Esteban** y la Dra. **Alazne Gutiérrez Lorenzo** y presentada por Don **Juan David Trueba Fraile** adscrito o adscrita al Departamento de **Ingeniería Química**

En _____a _____de _____de 2023

EL/LA RESPONSABLE DEL PROGRAMA DE DOCTORADO

Fdo.: _____

AUTORIZACIÓN DEL DEPARTAMENTO

El Consejo del Departamento de **Ingeniería Química** en reunión celebrada el día ___ de _____ de _____ ha acordado dar la conformidad a la admisión a trámite de presentación de la Tesis Doctoral titulada: **Fuel production by hydrocracking of non-olefinic plastics and vacuum gasoil blends** dirigida por el Dr. **José M. Arandes Esteban** y la Dra. **Alazne Gutiérrez Lorenzo** y presentada por Don **Juan David Trueba Fraile** ante este Departamento.

En Leioa, a _____ de _____ de 2023

VºBº DIRECTOR/A DEL DEPARTAMENTO SECRETARIO/A DEL DEPARTAMENTO

Fdo.: **Martin Olazar Aurrecoechea** Fdo.: **Rubén López Fonseca**

ACTA DE GRADO DE DOCTOR O DOCTORA
ACTA DE DEFENSA DE TESIS DOCTORAL

DOCTORANDO/A DON/DÑA. **Juan David Trueba Fraile**
TITULO DE LA TESIS: **Fuel production by hydrocracking of non-olefinic plastics and vacuum gasoil blends**

El Tribunal designado por la Comisión de Postgrado de la UPV/EHU para calificar la Tesis Doctoral arriba indicada y reunido en el día de la fecha, una vez efectuada la defensa por el/la doctorando/a y contestadas las objeciones y/o sugerencias que se le han formulado, ha otorgado por _____ la calificación de:

unanimidad ó mayoría

SOBRESALIENTE / NOTABLE / APROBADO / NO APTO

Idioma/s de defensa (en caso de más de un idioma, especificar porcentaje defendido en cada idioma):

Castellano
Euskera
Otros Idiomas (especificar cuál/cuales y porcentaje) _____

En _____a _____de _____de 2023

EL/LA PRESIDENTE/A, EL/LA SECRETARIO/A,

Fdo.: Fdo.:
Dr/a: _____ Dr/a: _____

VOCAL 1º, VOCAL 2º, VOCAL 3º,

Fdo.: Fdo.: Fdo.:
Dr/a: _____ Dr/a: _____ Dr/a: _____

EL/LA DOCTORANDO/A,

Fdo.: **Juan David Trueba Fraile**

The greatest weapons in the conquest of knowledge are
an understanding mind and the inexorable curiosity that drives it on.

Isaac Asimov

Considerando el comienzo de esta Tesis, en primer lugar quiero agradecer al Prof. José María Arandes y a la Dra. Alazne Gutiérrez la confianza depositada en mí para realizar este viaje. Ha sido una gran oportunidad desarrollarme aquí y vuestro conocimiento y experiencia han ayudado a moldear este trabajo en numerosas ocasiones. Espero conservar lo máximo posible de lo aprendido durante este tiempo.

Al Prof. Javier Bilbao por el conocimiento, ideas y guía que confiere a cada persona que orbita cercana a él y al Prof. Andrés Aguayo por estar siempre dispuesto a echar una mano a quien necesite, lo que me incluye sin duda alguna.

De mi entorno en el laboratorio quisiera mencionar al *hydroteam*, y en especial al Dr. Roberto Palos, que no sólo ha contribuido a que esta Tesis no perdiera el enfoque, sino que ha tenido a bien no desesperar conmigo (sí que había suficiente, Rober). Mi más sincero agradecimiento por toda tu ayuda. En cuanto al resto del grupo PROCAT-VARES, me gustaría destacar el buen ambiente que generáis y que he aprovechado para evitar caer en la locura entre plásticos y azufre. Gracias a todos por estos años. En especial, querría mencionar a Sergio, un *compañero* flaneador sin igual, y Zuria, la parte *física* de ese podcast que se nos queda pendiente. Os debo el reconocimiento de haber estado ahí durante gran parte del trayecto tanto dentro como fuera del labo.

Al Dr. Pedro Castaño por darme la oportunidad de realizar mi estancia doctoral en el MuRE de KAUST (Arabia Saudí). Ha sido una experiencia increíble tanto a nivel profesional como personal. Incluyo aquí a las "motomamis", la Dra. Idoia Hita (con la que tuve la suerte de reencontrarme) y la *co-author* Naydu Zambrano, por introducirme en el mundo de la analítica y guiarme a lo largo de aquella aventura. He aprendido de vosotras más allá de las estructuras y los espectros, mi más sincero agradecimiento por cómo os portasteis conmigo.

Haciendo repaso del camino hasta aquí, siempre estaré agradecido a la casualidad de encontrarme durante la carrera al *Grupo 2*: Claudia, Borja, Álex, Irene, Edu y Óscar. Con vosotros he pasado algunos de mis mejores momentos durante estos últimos años y espero que, aunque nos desperdiguemos por el mundo, siempre

encontremos un finde para juntarnos en Anero. Héctor, como última parte de este grupo, *compañero* de piso y amigo, creo que a ti te debo el mayor de los agradecimientos. Hemos recorrido todo esto de forma paralela y siempre has tenido un rato para aguantar todo lo que supone tenerme cerca, lleno de consejos y una paciencia tremenda. Que todo lo que esté por venir sea el triunfo que te mereces. Viaje antes que destino, compañero.

A mis amigos de siempre: Manu, Iker, Laura, Naia, Andrea y Josune. Quisiera reconoceros una gran parte del mérito de que pueda encontrar cierta paz cada vez que nos juntamos, bien sea para darlo todo en alguna fiesta de pueblo o para irnos de rabas/ranas en cualquier lado. Me considero afortunado de que este grupo se haya mantenido con los años y la distancia.

Por último, a mi familia. Quiero empezar con mi *tía Inma*, quien me acogió al empezar la carrera y que confió en mi desde el principio para sacar adelante todo lo que me propusiera. He crecido inmensamente contigo y no reconocer tu contribución a ello sería inconcebible. A mis hermanas, Sara, Leire y Elsa, y en especial a Sofía, con quien he crecido de la mano. Pese a venir por detrás me has enseñado mucho más de lo que creo que nunca estaría dispuesto a admitir. Gracias. A mis padres, Marta y Jorge, por supuesto. En especial a mi madre, en quien desde pequeño he encontrado el ejemplo a seguir en términos de esfuerzo y superación y que siempre nos ha ayudado a mantenernos en el buen camino.

A Agus, quien confío en que estaría orgulloso de verme donde estoy, en gran parte gracias a él.

David Trueba

ABSTRACT

This thesis is focused on the study of the performance of a noble metals catalyst in the hydrocracking of blends of non-olefinic plastic and an intermediate refinery stream as an alternative to less efficient strategies for waste valorisation. To this end, the process has been approached from a laboratory-scale point of view with a perspective of its industrial implementation, focusing on the effect of co-feeding, the mechanisms involved, the catalytic deactivation phenomena and the kinetic study.

The catalyst used, consisting of a PtPd catalyst supported on zeolite Y, has been tested in the hydrocracking of polystyrene (PS) and vacuum gas oil (VGO) blends. The study aims to evaluate the feasibility of producing streams suitable for use as automotive fuels by understanding the hydrocracking and catalytic deactivation mechanisms involved. The operating conditions used in a batch reactor were as follows: 380-420 °C; 50-110 bar; PS content in the feed, 10 wt%; catalyst/feed ratio, 10 wt%; and time, 30-300 min. The liquid fractions have been extensively characterised by chromatographic techniques concluding that the naphtha and light cycle oil (LCO) are suitable for inclusion in the blending pools of commercial fuels. The deactivated catalyst has also been characterised in depth to check the role played by the plastic in its deactivation, playing a critical role at 380 °C. The use of temperatures above 400 °C indicates that PS incorporation into a hydrocracking reactor is effective for naphtha and LCO production without causing any operational problems. Different possibilities of catalyst regeneration have also been studied and characterised to explain the reversible and irreversible causes and to establish the best way to enhance the sustainability of the process.

The validity of the process has been tested by introducing oxygenated plastics, namely polymethylmethacrylate (PMMA) and polyethylene terephthalate (PET), which add as a new variable the presence of heteroatoms. Using the same catalyst, the reactions have been carried out in a 100 mL batch reactor under the following operating conditions: 380-440 °C; 50-110 bar; plastic content in the feed, 10 wt%; catalyst/feed ratio, 10 wt%; and time, 30-300 min. The results confirm the existence of synergy in the co-feeding, assisting the conversion of the heavier compounds and providing a high selectivity to the fractions of interest. In

addition, the influence of the presence of oxygen in the products and the effect of the nature of each plastic on the coke formation have been analysed.

Using advanced analytical techniques, the liquid products of the hydrocracking reactions of VGO and VGO mixed with oxygenated plastics have been studied for a better understanding of the mechanisms involved. Analyses of both hydrocarbons and heteroatom-containing compounds (such as nitrogen, sulphur and oxygen) have been performed using a combination of chromatographic techniques, high-resolution mass spectroscopy and magnetic resonance imaging. The combination of the results with the catalytic performance results has allowed to establish the preferential routes of the process and to identify the possible alterations due to the influence of each plastic according to its nature.

From the experimental results, different reaction networks and kinetic models have been optimised, of which an original 7-lumps model (8 lumps for the oxygenated plastic blends) has been selected for its high accuracy and fit based mainly on the effect of time and temperature. The model owes part of its originality to the introduction of individual deactivation equations related to each of the deactivation phenomena (plastic fouling, coke deposition and metal poisoning) and their contribution to the global catalyst activity.

Overall, the results highlight the potential of hydroprocessing units to contribute to a more sustainable cycle of plastics production by re-incorporating their residues into petroleum treatment cycles. The approach to the mechanisms and kinetics of the process encourages the introduction of a new way of recycling waste materials, assisting the decarbonisation of the refinery and its large-scale adaptation as a contribution to the Waste Refinery.

CONTENTS

Chapter 1

INTRODUCTION

This Chapter introduces the topic that leads to the development of this Thesis, mainly focused on the combined hydrocracking of a heavy stream of refineries and non-olefinic plastics. The background of this work is based on the actual energetic scenario and the impact of the exploitation of petroleum resources that has been carried out so far. The influence of the oil market, the distribution of the demand and utilization of these resources and the regulations on the products and the waste generated by part of the industry are here addressed. Among the potential answers for these circumstances, hydroprocessing is revealed as a versatile and already-in-use option. Thus, the fundamentals of its performance, the basis of the catalysts design and the approaches to the kinetic modelling of the hydroprocessing of complex blends are exposed to comprehend their upgrading through this process.

1.1. ENERGY SCENARIO AND WASTE PRODUCTION

The world is at a critical juncture in the energy situation, generation and distribution. As occurred in the past, the energy problem finds its origin in geopolitical drivers that lead to the rise in prices that is now bringing about some economic repercussions such as inflation. Part of this crisis repeats the importance of some tasks such as reducing oil dependence, especially the ones coming from imports. However, some additional issues must be considered to understand the current energy scenario and the multiple causes of its instability, namely COVID-19, the coal trade resurgence, the Russia/Ukraine conflict, the impact of the climate on renewable energies and the oil demand.

COVID-19 has had a great and multidimensional impact on our lives, not only in the social dimension but also in the sector of energy and industry. The full lockdown executed by most of the countries at different moments reflected a reduction of weekly consumption of energy by 25 % [1], due to the shutdown of industries, academic institutions and shopping and leisure centres. These changes, along with some observed in the usage patterns of energy-consuming resources such as transport [2], must be considered within the context of the previous pricing war (which remained through the pandemic) [3] and the oversupply that was already inducing an energetic uncertainty [4]. Globally, the general effects of this incident on the energy market and the renewable energy sector have been badly considered [5]. However, some authors have stated that there is a great opportunity for renewable energy sources since this crisis has put the focus on the investment in these sources and the promotion of their development due to their efficiency [6].

The coal trade matter is one of the main concerns regarding CO_2 emissions, as it is an industry that demands an immediate suppression of obsolete technologies and yet keeps an increasing trade density [7, 8]. In this respect, China concentrates half of the global consumption and more than 50 % of the CO_2 coal-related emissions [9]. Moreover, China as well as other countries are considering stepping back in the decarbonisation strategies due to the influence of some of the energetic issues here exposed on the power supply stability.

Related to the above, the latest international conflict between Russia and Ukraine is also strongly affecting an already fragile state. The combination of the imports cuts, the reduction of the supplies by Russia and the dependence on fossil fuels despite the transition towards renewable sources is leading to a situation in which the robustness of the energy network is tested [10, 11] and the vulnerabilities of the supply chain through cascading failures are highlighted [12].

As an alternative to the exposed dependency on fossil fuels, the transition to carbon neutrality through the implementation of renewable energy sources brings several opportunities but also remarkable challenges. In order to become competitive and gain weight in terms of contribution to co-generation schemes, renewable energy sources have to overcome the substantial subsidies for maintaining fossil fuels utilization [13], the unpredictability over the impact of renewable power plants [14] and the limitations that each of these alternative sources present [15]. Apart from that, developing countries are usually identified as the ones with higher emissions due to the rapid industrialization rate they suffer and the greater help they need to implement new technologies from an agrarian and weaker infrastructure [16].

As a global result of these factors, United Nations has reported that more than two-thirds of greenhouse emissions are related to the energy sector, and over the 75 % are related to fossil fuels. Consequently, an unusual rupture in Earth's balance (Figure 1.1) has been manifested in rises in the sea level [17], the oceans' heat gain [18], the precipitation amounts [19], CO_2 concentration in the atmosphere [20] and glacier mass loss [21]. Hence, the focus must be put once again on the exploitation of the most traded commodity in the world: crude oil.

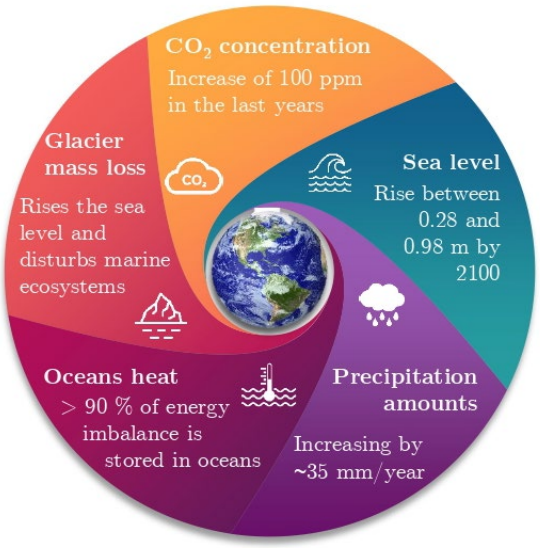

Figure 1.1. Key factors of global climate change due to greenhouse emissions.

1.1.1. Crude oil exploitation and market

Crude oil is known as the major commodity in the present-day and has been known, along with natural gas, for a few thousand years to humankind. It consists of different blends of hydrocarbons with different physical and chemical properties that depend on its origin and heaviness. As a general rule, crude oil is made by carbon (83-87 wt%), hydrogen (10-14 wt%), sulphur ($<$ 6 wt%), nitrogen ($<$ 2 wt%) and oxygen ($<$ 1.5 wt%) [22]. Apart from the major elements, there are small concentrations of heavy metals that form what are called metalloporphyrins that can affect the properties of the petroleum fluids and the posterior performance of the catalysts in the refineries [23]. It is well known that the current oil reserves are running out and even if some new are being considered for their exploitation the nature of the extracted material is heavier.

The common classification used for crude oil is the API gravity, which distinguishes between light (API $>$ 31.1), medium (22.3 $<$ API $<$ 31.1), heavy (10 $<$ API $<$ 22.3) and extra-heavy (API $<$ 10) crudes [24]. Apart from giving general information about the relative density of the crude oil compared to water, the utilization of this classification can provide some approaches to the

composition of the material being treated such as the contents of heteroatoms, asphaltenes and metals. The relevance of the character of the crude oil relies on the competitiveness of each region to being supplied with light crude oils that easily penetrate the world market at the same time that they have the infrastructure to manipulate that crude oil [25]. Besides, there is an additional classification of the crude oil attending to its total sulphur concentration, as the ones presenting lower accumulations of this element (known as sweet) will demand less quality adjustment treatments than those called bitter.

As energy price is a crucial factor for the global economy, the markers that strongly affect oil prices are the influence of supply and demand factors, the influence of the international oil market (which is inherent) and the impact of emergencies, as discussed above. Hence, the importance of crude oil in terms of exploitation, distribution and market will play a decisive role in the coming years in the international panorama.

Figure 1.2 depicts the global reserves of oil that can be certainly extracted with the actual and foreseen technologies. It can be observed that there are countries with clear control of the oil supplies (Venezuela, Saudi Arabia, Canada), as the top 14 countries account for more than 90 % of the known reserves, which implies a remarkable role of these countries on the world economy. However, as it is reflected in the Statistical Review of World Energy (2021) of BP [26], this does not imply a major production of petroleum resources, as this is just indicative of the quantity of petroleum that can be extracted in economically viable terms and therefore the refining capacity of each country must also be taken into account. Moreover, the uncertainty that surrounds the actual amount of available crude oil is also supported by the technological development that allows the extraction of heavier resources over time.

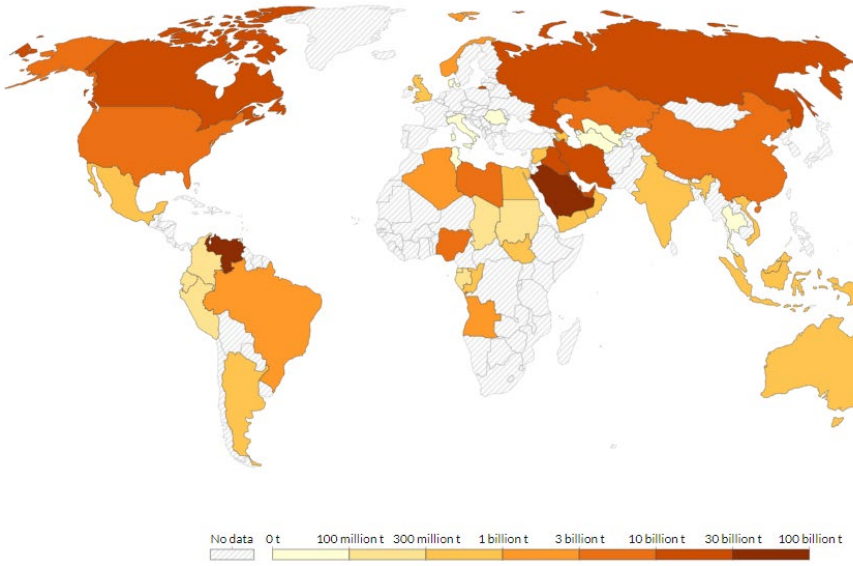

Figure 1.2. Proven oil reserves in 2020. Our world in data [27].

The increasing market for heavy oil components and the advances in recovery processes have boosted the attention to reservoirs that had been considered unfeasible so far [28]. A further consideration is the fact that each region provides a very different crude oil in terms of the above-mentioned parameters to measure the quality of the crude oil (sulphur content and API gravity) [29], even if it is increasingly poorer due to the depletion of the light and medium crude oils [30].

Furthermore hand, oil demand is a key factor for worldwide economic health, and so it has been stated that geopolitical disturbances (such as the recent pandemic and military conflicts) in this parameter are strongly reflected in the oil market and therefore in the global economy [31]. In fact, the uncertainties in this area have proved to be more negative in the countries oil-importer than those which export this commodity [32].

Oil demand has achieved a value of 96.9 million barrels per day (Mb/d) in 2021 [33] and is expected to grow by 23.6 Mb/d by 2045. A continuously increasing oil demand has been observed in the last decades as it inevitably accompanies the rapid economic growth that many regions are going through. This direct relationship between the economic capacity and the oil demand has been

remarked during the COVID-19 pandemic, as it gradually abated the oil demand due to the cessation of many oil-consuming activities, although a monthly upward quote has been observed since August 2021 [34].

When attending to the oil demand by regions, non-OECD countries hoard more than half the medium-term oil demand, exhibiting the main part of the global oil demand, led by the demand increase observed in China. The rapid growth of these economies, strictly oil importers (China accounts for almost 80 % [35]), will support oil prices in the long term. Regarding the OECD countries, the reports led to conclude that the oil demand is expected to grow at least in the period to 2024 which will be offset by a decline during the rest of the medium term. Bearing all of this in mind, the oil demand projections indicate a solid growth for the following years and the main concern is about the energetic security issues that will end in slower oil substitution.

In the long term, a gap between OECD and non-OECD countries is anticipated due to the contrary behaviours that can be foreseen: a declining trend on the first and a continuous increase in the latter. These trends for OECD regions are a consequence of the efficiency and technological development and the replacement of oil-dependent industries by alternative fuels and renewable energies, backed by a static population and the ongoing electrification in industries such as the residential and industrial sectors.

All these factors reflect the instability of a complex and dynamic market such as the one of crude oil. In order to achieve the goals marked by international consensus of decarbonisation, reduction of carbon emissions and the enhancement of biosphere resilience [36], the intensifying of the crude conversion processes seems imperative. In this context, technologies with the capacity to deeply refining heavy feeds and produce various chemical products are expanding. Moreover, the increasingly strict requirements of the products obtained in refineries underline the benefits of some of these processes such as hydroprocessing, which provides a simultaneous conversion of heavy oils and a reduction of heteroatoms in the products, which are progressively more controlled.

1.1.2. Products and wastes regulations

The light hydrocarbons obtained from the crude oil distillation and treatment present contents of sulphur, nitrogen and metals whose removal is required to accomplish the environmental regulations and the quality of the products. The absorption by the industry of heavier feeds and the stricter regulations about the emissions that are potentially hazardous for human health and the environment force the requirements to establish a balance between the satisfactory composition of the fuels for their use in engines and the limits that should be established before they harm their performance.

There are global standards development organizations such as ASTM International, the European Committee for Standardization and the International Organization for Standards. The specifications that these delegations provide for the different types of fuels include parameters such as composition, performance, volatility, combustion, contaminants and additives. However, it must be emphasized that many of them are general guidelines and they vary from region to region.

Regarding the gasoline composition, the Research octane number (RON) and the sulphur content mainly drive the performance of this fuel in engines and control catalyst deactivation, corrosion problems and environmental pollution [37]. However, there are multiple physicochemical specifications for gasoline even if they are given in ranges form according to the variety of engines and grades of fuels commercially available. In Europe, these specifications are collected in the Euro 5, Directive 2009/30/EC, whose main standards are shown in Table 1.1 [38]. It must be noted that, although outside the European Union these specifications have been laxer, in recent years several efforts have been made to adapt fuel regulations to the current environmental issues [39].

Table 1.1. Environmental specifications for market fuels to be used for gasoline vehicles (Directive 2009/30/EC).

Parameter	Unit	Limits	
		Min.	Max.
Research octane number		95	-
Motor octane number		85	-
Vapour pressure, summer period	kPa	-	60.0
Distillation:			
- percentage evaporated at 100 °C	vol.%	46.0	
- percentage evaporated at 150 °C	vol.%	75.0	
Hydrocarbon analysis:			
- olefins	vol.%	-	18.0
- aromatics	vol.%	-	35.0
- benzene	vol.%	-	1.0
Oxygen content	wt%	-	3.7
Sulphur content	mg kg^{-1}	-	10.0
Lead content	g L^{-1}	-	0.005

On the other hand, diesel engines usage is open to discussion after the chain of events related to their usage. This type of engine has been extensively used for transportation, shipment and the agricultural industry due to its high reliability and efficiency [40]. However, and even considering that they provided low carbon monoxide and unconverted hydrocarbons emissions related to the combustion characteristics [41], they are also responsible for the major contribution to the air of pollutants such as nitrogen oxides and particulate matter. For this reason, and along with the deterioration of in-cylinder combustion as well as oil depletion, both diesel engines' performance and economy are under high back pressure [42]. In this context, the regulations of diesel engines are becoming more severe and

environmental agencies are pressing for reducing the health conditions and environmental emissions related to diesel combustion. As an example, the specifications for commercial diesel covered in Directive 2009/30/EC, the same as those used for gasoline in Europe, are exposed in Table 1.2.

Table 1.2. Environmental specifications for market fuels to be used for diesel vehicles (Directive 2009/30/EC).

Parameter	Unit	Limits	
		Min.	Max.
Cetane number		51.0	-
Density at 15 °C	kg m^{-3}	-	845.0
Distillation:			
- 95 vol.% recovered at:	vol.%	-	360.0
Polycyclic aromatic hydrocarbons	wt%	-	8.0
Sulphur content	mg kg^{-1}	-	10.0
FAME content – EN 14078	vol.%	-	7.0

Aside from the guidelines imposed on the refinery products, there is a large list of wastes being generated in refineries that usually go unnoticed [43, 44]. Some of them have also an influence on human health (i.e. hydrocarbons, metals, PAHs), and are being monitored and often treated through biological methods [45]. However, there are remaining wastes that need to be handled in different ways (such as solid waste from the spent catalysts). Furthermore, the effects of some of these compounds and materials are unknown and there is scarce literature about the combined effect of hydrocarbons, chemicals and blends of refinery wastes on contaminated environments [46].

The process intensification that is now coming into vogue must be focused on the optimization of the refining processes in such a way that wastes are minimized and properly treated and on the effective recovery of the wastes whether they are produced either during the refining process or they are discarded at their end-of-

life as added-value products. In this regard, plastics reveal themselves as a potential source of transformable hydrocarbons blends as they are more valuable than crude oil and can contribute to the intensification of refining through their integration into fuel production.

1.2. PLASTICS MANAGEMENT DILEMMA

1.2.1. Plastics trade market

Plastics are organic polymeric materials that consist of very large organic molecules that, depending on the fabrication and moulding treatment that is given to them, can adopt interminable forms and properties. Among the good properties related to these materials, one could find resistance, durability, corrosion resistance and high thermal and electrical insulation [47]. Because of this, these materials have been applied in recent years to agriculture, industry, construction, packaging and even medicine [48]. As they have proved to considerably increase the living standards of society, the plastic industry has been further developed across the last century in a search of continuous upgrading of these materials, optimizing their properties and applications. Consequently, the growth of the plastics industry has been progressively increasing until it has become one of the most profitable and extended industries, including the creation of employment, a great turnover, the contribution to public finances and ranking at the top of the industrial value-added contribution.

Nowadays, with the world focusing on climate change, the plastics industry has been carefully evaluated from the beginning of the supply chain. As the production of so many different plastics comprehends a wide spectrum of raw materials, processes and final additives, there is a lack of research that encompasses all parts of the supply chain [49]. The production of virgin plastics has a prominent impact on petroleum exploitation, as more than half of the light olefins demand, e.g. ethylene and propylene, that mainly come from the catalytic processing of natural gas and crude oil (or their products) [50, 51] is aimed at plastics manufacturing [52]. In fact, 15 % of the CO_2 emissions are related to primary chemical production, of which 27 % is attributed to high-value chemicals and most of these are used for plastics production [53]. Hence, the dramatic scale-up of the plastics production industry must be rigorously broken down.

Global plastics production reached 368 million tons in 2019 [54], excluding PET fibres, PA fibres and polyacrylic fibres, representing an increase of 2.4 % in

comparison with the previous year. This output is directly related to the regions of higher oil imports, as Asia accounts for 51 % (China provides 31 % of the total), the United States, Canada and Mexico (NAFTA) produce 19 %, a 16 % is located in Europe and the rest of it is shared between Middle East, Africa and Latin America. On the contrary, in 2020 plastics production decreased due to the partial shutdown of human activity, although this reduction was limited to 367 Mtons, which implies an actual development of mass production with no significant changes in the distribution. Also, the most developed regions are at the forefront of virgin plastics reduction. As an example, European plastics production without including recycled plastics has decreased from a peak of 64.4 Mtons in 2017 to 55 Mtons in 2020.

On the other hand, the reports offer a clear trend in plastic demand of continuous growth that will lead to almost a threefold increase in plastic use mainly driven by rising populations, incomes and development [55] if intervention is neglected. As a representative case, data from 2020 reflect that the 6 largest countries in Europe concentrate almost 70 % of the plastic market. Moreover, a direct link between this market and industrial activity can be deduced if polymers demand is examined in segments: 40.5 % is concentrated on packaging, 20.4 % is related to building and construction, and 8.8 % is required by the automotive industry and the rest is shared by minor sectors such as agriculture and household.

Two main drawbacks can be ascribed to the massive plastics trade exposed: on one hand, it entails intensive exploitation of petroleum resources, which hampers the decarbonisation goals; on the other hand, the production of plastics has as an inevitable consequence the enlargement of the solid waste amount. Even if secondary plastics markets are boosted and policies are focused on extending plastics service life to curb the production [56], primary plastics production is expected to keep increasing for the incoming years and therefore so will the plastics wastes at their end of life.

1.2.2. Plastics wastes

Plastic waste or pollution comprises all activities that imply a negative impact on the environment of an area in which plastics have begun to be stored. The hazardous effects that plastics disposal has on our ecosystem are wide, as they can directly affect human health (either through the release of toxic substances or acting as carriers for other co-existence pollutants) [57], changing the properties of the environment soils and at the same time affecting to their animals [58], damaging the marine inhabitants [59] and leading to microplastics formation that affects indeed to all the previous circumstances [60].

The elemental composition of some of the majority of plastics found in municipal solid wastes (MSW) blends can be found in Table 1.3. Most of the basic plastics such as HDPE or PP show a high carbon content, the rest of them being mostly hydrogen. These compositions reflect a high calorific value, raising interest in their proper management once their lifespan has ended [61]. Nonetheless, the more complex the molecules designed for the plastic the higher introduction of heteroatoms such as oxygen (PET) or chloride (PVC), which can be dangerous in their treatment or toxic. Note that some of them show sulphur traces despite not having this element in their design composition and as a consequence of the multiple post-fabrication treatments they undergo. All the unknown compounds that might be within the composition of the plastics or have adhered to them during their service life exacerbate the plastic pollution issue.

In addition to the individual composition dilemma, the heterogeneous nature of the plastic blends that can be recovered from the MSW must be considered. The average MSW blends include the following composition regarding plastics [62]: polypropylene (PP), 26 wt%; high-density polyethylene (HDPE), 15 wt%; low-density polyethylene (LDPE), 13 wt%; linear low-density polyethylene (LLDPE), polyvinyl chloride (PVC), 20 wt%; polystyrene (PS), 7 wt%; polyethylene terephthalate (PET), 6 wt%, and; others, 5 wt%. Besides, the recovery of post-consumer plastics is far from complete capture, as the rapid rise of the waste volume in urban areas in developing countries has encountered issues in terms of disposal, collection and management of the discarded materials [63].

Table 1.3. Elemental composition of some plastics recovered from the MSW [64].

Material	C (wt%)	H (wt%)	N (wt%)	O (wt)	S (wt%)
PET	61.4	4.3	0.05	32.7	0.17
HDPE	82.4	15.2	0.06	0.3	-
PVC	35.6	4.9	0.20	4.1	-
LDPE	87.3	15.2	0.06	0.2	-
PP	79.1	14.4	0.40	1.7	0.15
PS	93.5	8.5	0.06	0.2	-

PET: polyethylene terephthalate; HDPE: high-density polyethylene; PVC: polyvinyl chloride; LDPE: low-density polyethylene; PP: polypropylene; PS: polystyrene.

1.2.3. Waste Refinery

The set of processes and technologies that promote the large-scale valorisation of not only plastics but also other discarded materials have been held under the name of Waste Refinery. The concept arises from the necessity of merging conventional units of refineries and new alternative feeds that are otherwise wasted. The integral valorisation of wastes faces noteworthy handicaps such as the huge initial investment that new units would require, the quality standards that the resulting products must fulfil and the competition with the conventional refineries [62]. As a consequence, Waste Refinery processes are proposed to be a combination of a first stage of secondary low-quality streams in conventional refinery units that must be further upgraded with a second stage of versatile units that can absorb not only those streams but also waste materials, as illustrated in Figure 1.3. This way, the refineries would promote the intensification of the actual processes while introducing a valorisation industry in an attempt of maximizing the yields of fuels and chemicals.

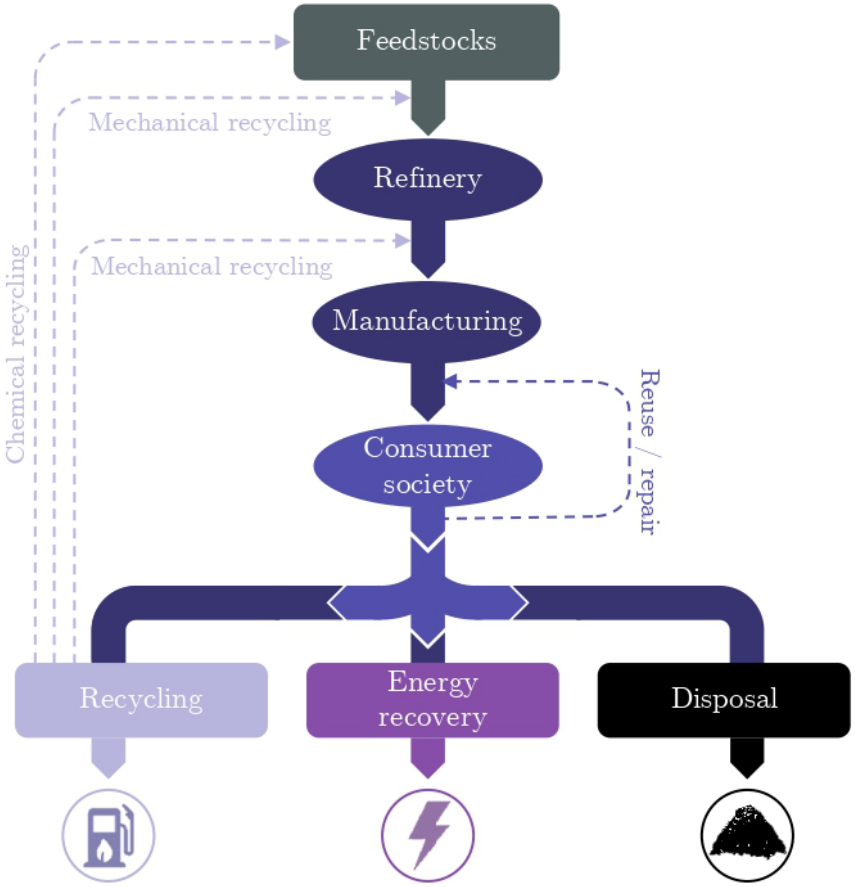

Figure 1.3. General scheme of the Waste Refinery concept.

1.2.3.1. Biofuels

Thermochemical conversion of bio-waste has several pathways depending on the main product that is obtained: they can be converted into gases (e.g. syngas), solids (such as biochars) and liquids (biofuels or bio-oils), thus giving rise to a varied number of processes encompassed in what is called Biorefinery. Raw biomass represents the most abundant organic macromolecular material containing carbon in nature [65] and its main advantage is the carbon-neutral character that is attributed to it due to the amounts of CO_2 related to its development and the energy production derived from it being almost equal [66],

along with other good properties as its renewable nature and its low sulphur concentration.

Conventionally, biomass has been extensively focused on heating facilities through its combustion but the correct utilization of this resource can be directed towards electric, fuels and other chemicals production, especially in countries with a strong share of coal in their primary energy sources [67]. Almost 50 % of global energy demand is expected to be supplied by renewables by 2030, most of these sources having a biomass-derived origin [68].

The most frequent materials used for that conversion include woody biomass, agricultural crop residues, algae, livestock manure, part of the MSW [69] and also materials of animal origin, which are sometimes overlooked when exposing biomass as a potential energy source. In total, bio-waste arising in the European Union (including MSW) has been estimated at 76.5-102 million tonnes, plus 37 million tons from the food and drink industry [70]. As these amounts are predicted to be continuously increasing in the years ahead, the biomass market will thrive and diversify into various energy forms such as electricity, hydrogen, fuels and other chemicals.

Sustainable biofuel production is also required, as the supply impact of first-generation food-based biofuels and second-generation biofuels may imply food insecurity resulting from the diversion of agricultural lands to intensify lignocellulosic energy crops [71]. For that reason, the merging with other sectors, the sustainable exploitation of agricultural lands and preservation of lands for biodiversity and the greenhouse emissions compensation must be encountered through the optimized combination between the biomass available, its properties and the technologies employed.

Apart from bio-waste from various industries such as food and agriculture, the intensification of these processes as well as the dependence of the automotive sector on fossil fuels has led to the identification of CO_2 emissions as an indicator of climate change [72]. Recently, the energy potential of CO_2-derived fuels has been pointed out as an effective way to bend the emissions curve, as they have a

high energy storage capacity while maintaining a near carbon-neutral balance if produced with the help of renewable energies [73]. However, it is sometimes argued that these fuels do not belong to the biofuel group because CO_2 capture can take place in conventional combustion engines, which are not derived from biomass. CO_2-to-fuel technologies are currently being developed in search of an efficient method that combines light and heat in photocatalytic processes to reduce the energy demands of thermocatalytic methods by avoiding or at least reducing the availability of sunlight as a constraint in photochemical processes [74].

1.2.3.2. End-of-life tires

As a consequence of the increasing part of the automotive industry in the development of the economy of many countries, tire production has achieved an essential role. The continuous evolution of these materials and the numerous categories and origin do not affect their general composition, considering them as homogeneous materials mainly composed of [75]: 40-48 % of natural and synthetic rubbers; 22-27 % of carbon black and/or silica; 5-25 % of reinforcing materials (metals and textiles); and 0-8 % of facilitators (oils, waxes, plastics...).

Tires market has been directly related to the growing population and hence to increasing demand. This way, 1.5 billion tires were estimated to be produced in 2017 and the predictions elevate this value up to 2.5 billion units by 2022 [76]. This trend has turned into a worry since the 1960s, in a search of an economical and sustainable way to yield the maximum energy recovery from end-of-life (EOL) tires [77].

As with other wastes, the management of EOL tires can be divided into three main routes, namely material, energy or chemical recovery. Apart from that, consideration must be given to the incomplete correct management of tires. Regardless of the efficiency of recovery through the mentioned methods, landfill and stockpiles must be also considered. The tire disposal in landfills has been drastically reduced over the last years, as they are potentially risky due to the lack of control, the abandoning of most of them and the threats of potential fires

[78]. With respect to stockpiles, they are now the less desirable destination and have been also limited due to their impact on water, soil and air [79]. Currently, global data indicate that 3-15 % of tires are recycled, 5-23 % are reused, 20-30 % of them are landfilled or stockpiled and 25-60 % are incinerated [80].

Coming to the matter of more sustainable options, secondary utilization from EOL tires can be achieved through various alternatives, exposed in Figure 1.4. First, tire retreading is the renewing of the tread of a tire, thus extending its useful life. This reduces the cost required for one tire manufacturing between 30 and 50 % of a virgin tire [81]. However, the strong dependence of the efficiency on the original tire structure, the lack of standardization in the processes and the limited retreading cycles of the tires can be submitted to reinforce the weight of searching alternatives. On the other side, using tires as repurposed construction material (under the so-called civil engineering) has been emplaced at the top of the agenda, as it involves a high-value recovery that requires fewer resources than recycling [82].

With regard to energy recovery, it can be a better way to deal with tire waste if compared to their disposal but should be only performed when recycling is not possible. The combustion of an EOL tire implies just 37 % of the energy required for the synthesis of a new one [83]. Nevertheless, it is not discarded as an option because tires contain a very low moisture content and high content of volatiles and heat, making it a very good option for the partial replacement of fossil fuels in combustion plants [84].

Last, chemical recovery comprises two main processes based on the thermal conversion of EOL tires making advantage of the good compositional properties exposed above: gasification and pyrolysis. Gasification mainly produces syngas (a gaseous blend of CO, hydrogen and hydrocarbons) from carbonaceous materials. The application of this technology to tires waste has been essentially made under laboratory conditions, with fewer results reported in pilot-scale units [85], but exhibiting a good waste management potential, even considering that it has proved to be heavily dependent on the temperature and the gasifier agent [86].

Figure 1.4. Scheme of the circular economy of tires [87].

Alternatively, pyrolysis is the other thermal route to deal with tires that provides a considerable number of valuable products at the same time that it is one of the most environment-friendly and economically viable options within a competitive framework [88]. The maturity of this technology has allowed obtaining very good yields of products of interest while directly and indirectly reducing greenhouse gas emissions and the materials that are not converted during the pyrolysis (metals, rubber, additives...) might be recovered after the process, promoting the circular economy of these materials [89].

The valorisation of the tyre pyrolysis liquid (obtained in a spouted bed reactor) has been studied by Rodriguez et al [90]. In the framework of this research, these authors investigated the effect of the operating conditions (temperature, catalyst-to-oil ratio and contact time) on the cracking of this liquid and then took a further step towards its real introduction in refineries by co-feeding it with vacuum gasoil [91, 92]. As a result, they demonstrated the feasibility of using these residues for the production of high yields of fractions of interest in refineries with compositions equally valuable for the production of liquid fuels. Furthermore, they established the operating conditions necessary for the minimization of lower-value gaseous products, boosting the performance of the FCC units. On the other hand, the use of hydroprocessing units for the valorisation of tyre pyrolysis liquids has been extensively studied by Hita et al. [93–95], who proposed a two-stage strategy in a trickled bed reactor. The most relevant results showed a remarkable reduction of sulphur compounds (the main objective of the research) while obtaining a remarkable conversion of aromatic compounds and the heavier fraction in general.

1.2.3.3. Plastics

The core of the plastics waste issue lies in the mismanagement that has prevailed in dealing with post-consumer materials. The different methods to cope with plastics residuum are the energy recovery processes (mainly incineration), landfill disposal and recycling, which accounted for 42 %, 23.4 % and the remaining 34.6 %, respectively, in 2020. Incineration is the most widely extended process so far mainly due to the energy potential of the materials disposed of [96] and the reduction of the MSW volume. However, the combustion of mixed plastics from MSW is used to produce steam that provides electrical energy and the global process has an efficiency cap of 23 to 40 % [97]. Besides, the rapid increase in plastics consumption and their limited duration of life (from less than 1 month to 35 years [98]) have led inescapably to massive disposal of waste in landfills. This comes with an increasing threat because of its impact on soils, air, water and human safety [99] that reinforces the idea that, from a Global Warming Potential (GWP) and Total Energy Use (TEU) point of view, the best practice to deal with waste plastics is recycling.

Among recycling processes, mechanical recycling is currently the only option deployed at scale, based on the circular economy of these materials without significantly modifying their composition [100]. Even so, mechanical recycling of plastics has several limiting factors such as the heterogeneous nature of the polymers found on MSW, the additives and contaminants related to them and the poorer competitiveness of lower-quality and higher-cost recycling materials. Within this framework, chemical recycling (which only represents 0.2 % of the management distribution) appears as a viable solution to deal with plastics, as it involves the decomposition of the plastic through the chemical break of their bonds, producing blends of hydrocarbons suitable for new plastics or fuel production.

Over the last few years, great efforts have been made to bolster the chemical recycling of waste plastics, putting special emphasis on the economically and environmentally feasible nature of these processes. The variety of technologies studied in this field includes depolymerisation, gasification, pyrolysis, catalytic cracking and hydroprocessing. Depolymerisation is somehow the starting point of plastics chemical recycling, as it entails the addition of a depolymerisation agent (such as glycol or methanol) that makes possible the reconstruction of the original monomers [101]. The main constraints of the application of this method to MSW plastics lie in the different nature if they are divided by their synthesis method into thermoplastics and thermosetting plastics. At the same time, the first group can be divided into addition or condensation polymers. Both addition polymers and thermosetting plastics require a strong chemical attack that moves away the focus due to the wide window of byproducts that can be formed instead of a major yield of the monomer [102].

Gasification of plastics focuses on the production of syngas (and particularly hydrogen) and hydrocarbons as a byproduct, exploiting the high volatile content of some of the usual plastics in waste. Although good yields of the target gases can be achieved, even with technological enhancements such as the usage of plasma gasification, the process demands huge energy investments and alternative

strategies are being explored, for example, the combined co-pyrolysis/gasification [103, 104].

In pyrolysis processes, materials are degraded by heat at moderate temperatures (300-700 °C) in an oxygen-free atmosphere. This degradation can be thermal or catalytic, and the control of temperature, pressure and time of the process determines the yields of the products obtained, which can be divided into liquids (condensable vapours and oil), solids (char) and non-condensable gases [105]. Pyrolysis capacity to absorb plastics of different compositions and multilayer polymers (that are otherwise hard to deal with through mechanical recycling), the maturity of the technique in terms of reactor and catalysts design and the employment of catalysts that notably reduce the power requirements to achieve such temperatures have resulted in the imposition of pyrolysis over the other available technologies [106], at least from a theoretical point of view. Some authors point out that there is a strong correlation between the operating conditions used (including the vast range of determining parameters and catalysts) and the composition and selectivity of products of interest that needs to be refined [107], while others highlight the preliminary nature of the process for its implementation at full scale, considering the operational problems derived from the sticky nature and heat transfer limitations of plastics [108]. Nonetheless, most of the results support pyrolysis as a promising chemical recycling way, some of the ones developed at a laboratory scale being collected in Table 1.4.

From another perspective, chemical recycling also makes use of the refinery units with the highest versatility as catalytic cracking and hydroprocessing. In the same way that pyrolysis, catalytic cracking is presented as a viable alternative to pyrolysis due to its narrower range of products and the reduction of the employed temperatures [109].

Table 1.4. Summary of laboratory scale studies of plastics pyrolysis.

Material	Operating conditions	Ref.
PET	450-560 °C, thermal pyrolysis, spouted bed reactor	[110]
HDPE	500 °C, HZSM-5 + SiO_2/$Al2O_3$, spouted bed reactor	[111]
PS	400-700 °C, zeolites, micropyrolyzer	[112]
LDPE	550 °C, USY and HZSM-5, fixed bed reactor	[113]
Plastics mix (PE, PP, PS, PET, PVC)	440-500 °C, ZSM5, semi-batch reactor	[114]
Plastics mix (PE, HDPE, LDPE, PP, PVC, PS)	390 °C, zeolites and FCC catalysts, fluidized bed	[115]

Catalytic cracking is commonly used to deal with feeds containing large molecules as the catalysts of FCC units are usually acid zeolites adjusted for the proper acidic strength and density and shape selectivity [116]. To understand the virtues of introducing waste plastics in refineries units, the global energy context should be resumed. The growing price of crude oil facilitates the economic feasibility of processes that produce transportation fuels and other chemicals from unconventional materials [117]. Consequently, careful attempts have been realized to upgrade low-value secondary streams of refinery through refining processes such as catalytic cracking. A step beyond limiting these technologies to refinery streams, the inclusion of alternative potential hydrocarbons sources, such as post-consumer plastics, has gained attention recently, as well as the co-feeding of both feedstocks.

Conversely, many of the studies above-referred have been conducted in individual reactors, exhibiting some drawbacks such as the difficulty to recover the catalyst after use, the deposition of foreign compounds adhered to the plastics or the contribution of these materials to catalyst deactivation (e.g. through coke deposition). To face these deficiencies, other authors have called attention to

strategies that separate the polymer degradation and the quality upgrading steps, mainly through a pyrolysis/catalytic cracking system. This way, the yields towards high-value products have been improved as in the production of gasoline, olefins and BTX. Alternatively, using solvents to reduce viscosity has also been considered when feeding plastics to these units. A summary of the most relevant and recent studies of the catalytic degradation of plastics is collected in Table 1.5.

Table 1.5. Summary of studies about catalytic cracking of plastics.

Material	Operating conditions	Ref.
HDPE	350-550 °C, HZSM-5	[118]
HDPE	500 °C, MCM-41 + ZSM-5	[119]
HDPE waxes	500-560 °C, FCC catalyst	[120]
PP	450 °C, clinoptilolite	[121]
LDPE	500 °C, Zn- and H-ZSM-11	[122]

Last, the hydroprocessing of plastics has turned into one of the most promising technologies, as it combines plastic degradation and aromatic and heteroatom compounds reduction. Besides, the products coming from other refinery units are usually refined in hydroprocessing units to remove sulphur, aromatics or even metals, so the union of long-chain hydrocarbons cracking and quality adjustment in one unit presents several benefits. The involvement of many complex simultaneous mechanisms, however, requires a thorough study to comprehend the process and optimize its application to a more sustainable industry.

In this field, Rodriguez et al. studied the introduction of plastic pyrolysis liquid in a simulator of an FCC unit simulating refinery conditions, both separately [120] and by blending with vacuum gasoil [123], the usual feed for these units. The results showed the capacity of this unit for the valorisation of plastic waste through the production of middle distillates and the existence of synergistic mechanisms when both liquids are co-fed. Similarly, a first approach to the co-feeding of plastics with vacuum gas oil has been carried out in hydroprocessing

units using polyolefins and the liquid derived from their pyrolysis liquid, research carried out by Vela et al [124, 125]. By optimising the operating conditions and the catalyst used, results have been obtained that confirm the viability of the process and allow maximising the production of naphtha or LCO with a composition suitable for blending in refinery pools.

1.3. HYDROPROCESSING

Hydroprocessing is a refinery process focused on the conversion of various petroleum fractions at the same time that eliminates heteroatoms and metals through the employment of high temperatures and partial pressures of hydrogen. Hydroprocessing processes often vary within a wide operating condition range depending on the nature and origin of the feed and also on the desired specifications of the products, although all of them are recognized as one of the most advanced methods to upgrade oil streams and produce high-value fuels [126].

The introduction of hydrogen in heavy feeds upgrading was one of the most significant advances in refining technology during the 20^{th} century [127]. By adding hydrogen to the medium, two types of reactions are added to cracking processes: hydrogenation and hydrogenolysis (limited destructive hydrogenation of C-C linkages), which imply the saturation of aromatic compounds and the cleavage of C-X bonds, being X either carbon, sulphur, nitrogen, oxygen or metals. Besides, several advantages are achieved: (i) improving the performance and stability of gasoline; (ii) reducing the corrosion in the refining process; (iii) decreasing smoke formation in kerosene; and (iv) boosting the burning properties of the fuels by reducing the heteroatom content.

The application of hydroprocessing strongly depends on the final goal of each unit, presenting multiple parameters to configure them. The most important variables in these processes are temperature, pressure, space-time (or the synergy between catalyst mass and reaction time in discontinuous reactors) and, to a lesser degree, sulphur and nitrogen content, polynuclear aromatic compounds concentration, hydrogen recirculation rate and water presence.

According to the severity of the conditions, two main processes can be distinguished, namely hydrotreatment and hydrocracking, which produce different levels of conversion among the most common refinery processes, as illustrated in Table 1.6. Hydrotreatment involves only hydrogenation and hydrogenolysis, while the cracking function is added in hydrocracking due to the use of more severe conditions. These reactions, along with the hydrogen presence,

lead to the minimization of polymerization (which would trigger under thermal cracking atmospheres) and of coke condensation. Moreover, isomerization, dehydrogenation and cyclization also happen in hydroprocessing reactors because of the drastic conditions employed.

Table 1.6. Operating framework of the most common processes in the refinery.

Process	**Temperature, °C**	**Pressure, bar**	**Conversion, %**
Coking	480-560	1-6	50-75
Visbreaking	470-500	3-15	5-25
Hydrovisbreaking	455-510	3-20	45-75
Catalytic cracking	480-550	0.7-1.4	60-90
Hydrotreating	270-340	7-207	0-35
Hydrocracking	300-450	60-210	60-95

The applicability of each hydroprocessing depends on the main goal of the treatment, differentiating between contaminant pollutants removal, mild conversion or full conversion. The severity of the operating conditions distinguishes between hydrotreating, mild hydrocracking or severe hydrocracking, each having different conversion ranges and features, as depicted in Figure 1.5.

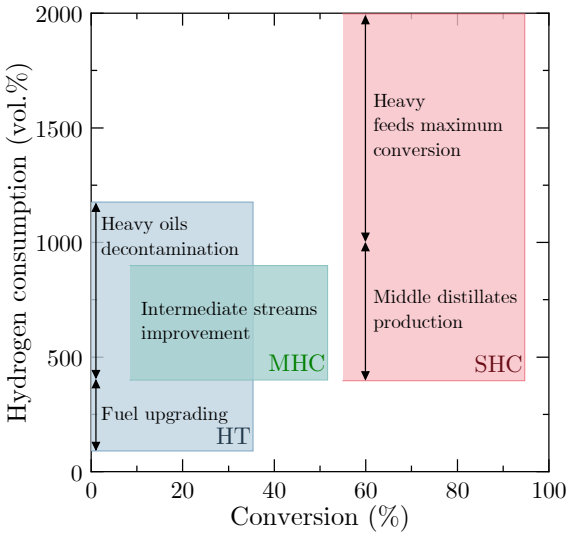

Figure 1.5. Main differences between the conversion range and targets of the principal types of hydroprocessing.

1.3.1. Hydrotreatment

Hydrotreating is aimed at the removal of impurities in crude oil fractions to reduce the related emission of pollutants during the use of the treated products as fuels. In addition, hydrotreating is a common process for enhancing the quality of commercial fuel streams.

The increasing interest in these units lies in the increasingly heavy nature of the available crude oil reserves, which demands further upgrading of the refinery products. Indeed, although a noticeable success has been achieved in improving the hydrotreatment units, the process has been not economically possible until the price and impact of hydrogen have decreased because of its production in refineries through reforming.

As a catalytic process, catalyst selection plays a key role in hydrotreating units. However, this parameter is usually controlled by the feedstock due to the lack of one catalytic system suitable for hydroprocessing feedstocks with different porphyrins content and molecular weight distributions, which are the main

factors affecting the catalyst selection. For that reason, research has focused on the development of new catalysts that reach the broader spectrum of possible scenarios.

Hydrotreating catalysts are usually composed of dispersed oxidized metals such as Co, Mo, Ni and W [128], which later undergo sulphidation, supported on a low-mild acid support. Each combination of metals has a specific target: Ni-Mo catalysts are focused to deal with polyaromatics and nitrogen refractory compounds, Ni-W combinations are used when a high aromatic saturation is required [129] and Co-Mo catalysts have proven to provide the best results in hydrodesulphurization and hydrodenitrogenation, but with lower impact on aromatics concentration.

The structural properties of the catalyst, mainly provided by the support, as well as the acidity, would determine the accessibility to the active sites and the extent of hydrogenolysis reactions, which are undesired in hydrotreating. The common materials used as supports comprehend silica, silica-alumina, carbon nanotubes, titanium oxide, zirconia or even blends of them [130]. However, among the usually proposed supports, γ-alumina shows outstanding mechanical and textural properties [131].

Similar to catalyst selection, catalyst deactivation is regulated by the properties of the feedstock, the operating conditions and their nature. Anyways, the two main phenomena involved in catalyst deactivation are coke fouling and poisoning by metals [132]. The limitation of the severity of operating conditions might minimize the first one due to the lesser extent of cracking/polymerization of aromatics, which are coke precursors. Moreover, the regeneration of the coke deposited on the catalysts under these operating conditions is feasible and can be achieved through oxidation at mild temperatures [133]. However, metal deposition on the catalyst is inherent to hydroprocessing and depends on the original metal amount of the feed, leading to an irreversible deactivation that affects some of the main functions of hydrotreating catalysts [134], thus discarding them.

As previously stated, the main reactions involved in hydrotreating are hydrogenation and hydrogenolysis. The operating conditions of this type of hydroprocessing, however, favour the predominance of hydrodearomatization (HDA). HDA is an exothermic and reversible type of reaction carried out to saturate double bonds and aromatic structures [135]. The hydrogenation of aromatic structures has been proposed to take place ring-by-ring, concluding that there are no partially hydrogenated ring compounds in the final products [136]. Moreover, it is well-established that the higher the aromatic ring number, the higher the HDA reaction rate. Considering the possible species going under hydrotreating within crude oil refining, some representative reactions of hydrotreating are shown in Figure 1.6.

1.3.2. Hydrocracking

The urgency of converting refractory feedstocks into naphtha and jet fuels paved the way for the development of hydrocracking. This process is based on the same principles as hydrotreating but uses more severe conditions to break down high-boiling molecules at the same time that it takes full advantage of the addition of hydrogen. Because of this, the lower limits of the hydrocracking operating framework can overlap with the upper limits of hydrotreating.

Hydrocracking's origins date back to the 1920s in Germany. IG Farben introduced sulphur-resistant catalysts for the hydrogenation of coal and tar to obtain liquid fuels [137]. The catalytic materials used back then were nitrogen compounds mixed with other catalysts such as clays, active silica or alumina [138].

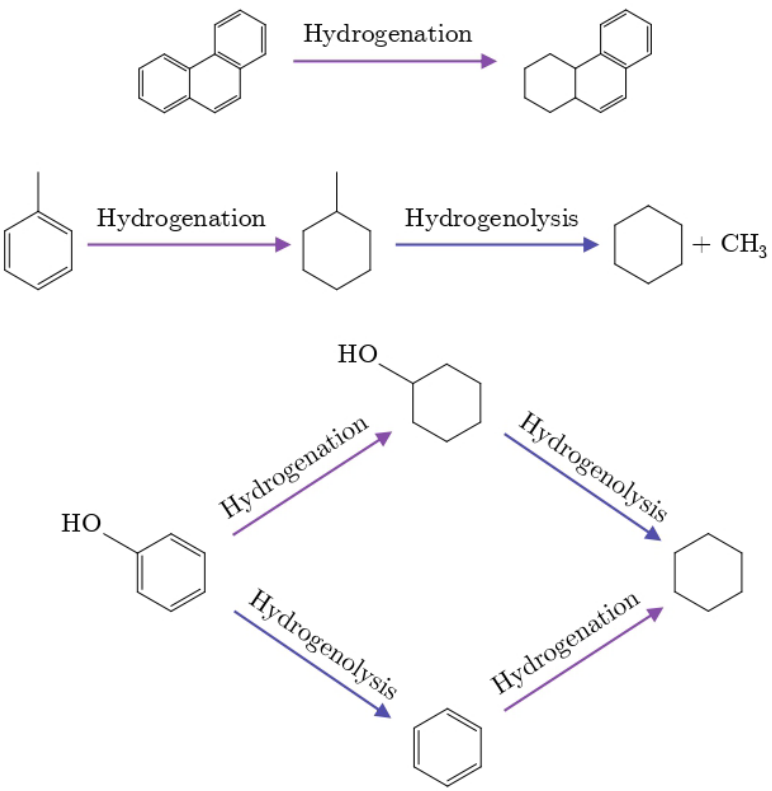

Figure 1.6. Representative reactions of hydrotreatment.

Later on, the intensification of fuels for aviation promoted the application of hydrocracking as an alternative source during World War II, using more advanced materials such as tungsten or molybdenum sulphide as catalysts [139]. However, the emergence of fluid catalytic cracking, which became the major source of high-octane fuels, along with the availability of crude oil in the Middle East, outshone the further development of hydroprocessing technologies as it was not economically competitive [140]. Far from disappearing, hydrocracking technology was continuously investigated during the 1960s and early 1970s and its capacity grew in a moderate but continuous way, especially in the USA but followed by the rest of the world during the following decade [141]. This boost benefited from the development of the automotive industry, the production of lower-value and refractory secondary streams in catalytic cracking units that could be treated in

hydrocracking units and the flexibility of this process that allowed focusing on different fuels according to the evolution of the demand.

In recent years, the increasingly restrictive legal requirements, the development of high-efficiency catalysts, the expansion of the petrochemical industry and the introduction of computation in the calculations of optimum operating conditions have significantly stimulated the development of hydrocracking processes [142]. Consequently, the expansion of this technology covers the direct treatment of crude oil [143], the refining of byproducts coming from other units such as the catalytic cracking and the reforming ones [144] and even absorbing new alternative materials such as wastes or biomass.

The main interest of its application lies in the fact that hydrocracking offers a threefold action: it reduces boiling point to commercial fuel cuts, removes heteroatoms and reduces aromatics, especially polynuclear aromatic compounds, through the characteristic ring-opening mechanism. This phenomenon encompasses a set of series-parallel reactions that begin with the partial hydrogenation of polycyclic aromatics, producing saturated rings that then are cracked into monoaromatics. The scission of the side chains attached to the aromatic rings results in the production of paraffins and isoparaffins [145]. Taking phenanthrene as a representative compound of the polyaromatic compounds found in heavy petroleum streams, Figure 1.7 exemplifies the ring-opening pathways and interactions between the possibly appearing species.

Within this reaction scheme, the main (and desired) products are expected to be formed by saturated compounds or low-ring number aromatics, with no presence of olefins (resulting from the cracking but almost immediately hydrogenated). Due to the isomerization reactions, which occur in a parallel way, the streams obtained from hydrocracking have a high degree of branching, thereby increasing their quality as commercial fuels. Moreover, the presence of hydrogen provides one of the main differences with thermal cracking: the polyaromatic compounds from the feed or formed during the process can be partially converted into lighter species instead of undergoing condensation reactions, lessening the coke formation. It must be bear in mind that, although the saturation of olefins is

practically irreversible, the reactions shown in Figure 1.7 can be reversible if the operating conditions are not favourable, as in the case of a very high temperature that promotes the dehydrogenation of saturated species towards aromatics formation. Similarly, the adjustment of operating conditions will establish the preferred pathway of the feed species, even if it is common that a number of them to take place simultaneously [146].

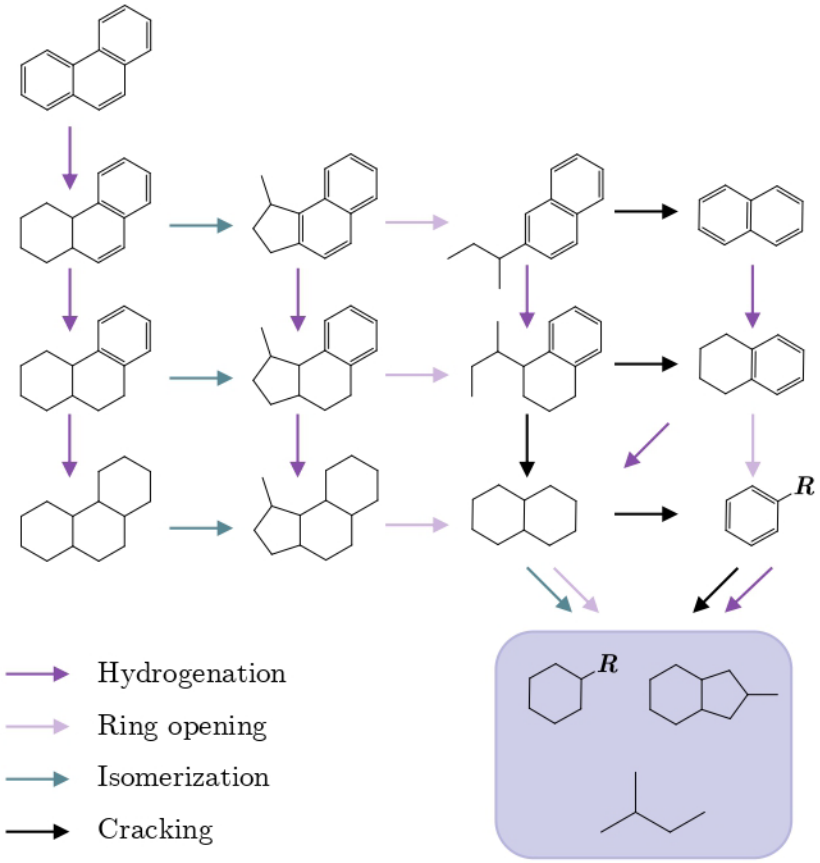

Figure 1.7. Phenanthrene ring-opening mechanism (adapted from [147]).

The most common industrial implementation processes of hydrocracking are one- and two-stage processes. Their popularity comes principally from their flexibility to produce gasoline, jet fuel or diesel, therefore allowing adjusting the production

to the demand at any given moment. Currently, the configuration election depends on the individual economics of the refinery.

The use of a single-stage process is focused on the conversion of vacuum gasoil into medium distillates, with approximate conversions of 50-60 %. The resulting product has good properties such as low sulphur and nitrogen content and can be transferred either to catalytic cracking units or fuel blending pools. Moreover, it is usual to recycle part of the products to maximize the conversion and/or selectivity towards lighter cuts. The recycling rate is determined by the refractory nature of the fresh feed, as the less reactive compounds would promote coke formation and therefore the catalyst deactivation [148].

A two-stage process is designed with two purposes: on one hand, the poisons and impurities free stream coming from the first stage can be further converted in the second one; on the other hand, the total hydrogen consumed in the process is often less than that used in single-stage processes [149]. Regarding the first, it is considered a noticeable advantage due to the formation of great quantities of ammonia and hydrogen sulphide in the first stage, thus minimizing their concentration during the second one. The optimization of the operating framework of the individual units is this way designed to eliminate these compounds under more severe conditions and then to maximize the selectivity in the second stage by using a catalyst with balanced metal and cracking functions.

As there are different configurations for hydrocracking units, various types of reactors can be used [150], the most common being collected in Figure 1.8. Among them, fixed bed reactors are one of the most extended, as soft and mild hydroprocessing units do not suffer from severe catalyst deactivation and therefore can be working in continuous mode for long periods, with hydrogen being produced in other units of the refinery. On the other side, ebullated-bed units are designed to absorb larger quantities of feed. Moreover, catalyst life is not a limiting parameter, as the fresh catalyst is added and the spent catalyst is removed continuously. Last, slurry-phase hydrocracking units stand out due to their flexibility to deal with different feedstocks, usually heavier (even coal tar), by using the most severe operating conditions with low-priced catalysts.

There are numerous commercial applications of hydrocracking technology, some of them being the following: the so-called "residfining" and Residue HydroCracking (RHC) processes, the Asphaltenic Bottom Cracking (ABC) process, CANMET hydrocracking process, HYVAHL F process and LC-Fining process, all of them aimed to the conversion of heavy feeds [30, 151].

The advancement in catalyst design and the improvements in reactor design have allowed in recent years the introduction of new and alternative feeds in hydrocracking units in an attempt of producing liquids suitable for their use as fuels.

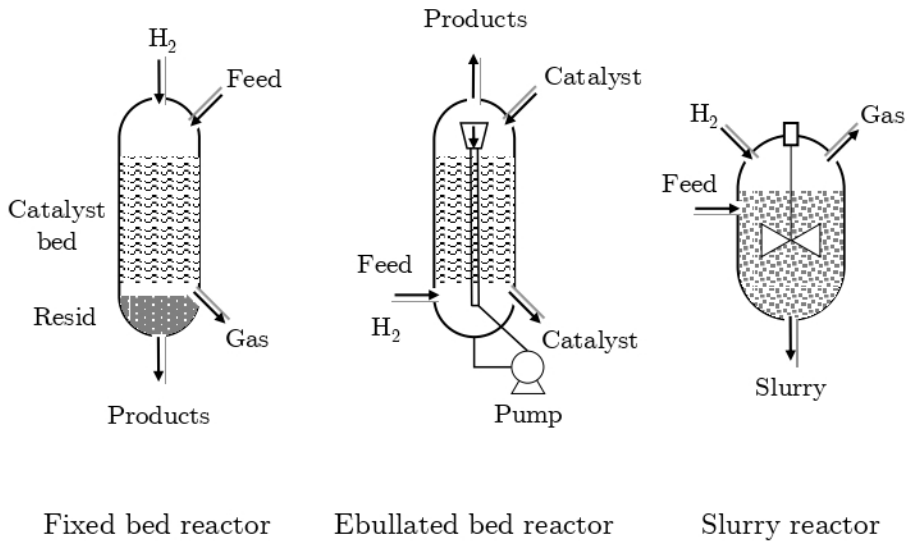

Figure 1.8. Most common hydrocracking reactors.

Some works have focused on the valorisation of secondary streams such as light cycle oil (LCO) to improve its quality and confirm the viability of considering it as the main feed [152, 153]. LCO is a secondary stream of FCC units of refineries, with a boiling point range similar to diesel. However, this stream is not considered as good due to some of its properties such as a low cetane number, a high density and a much higher content of sulphur and nitrogen. A two-stage hydroprocessing

strategy has been confirmed to be feasible for providing acceptable yields of naphtha and middle distillates with adequate quality [154, 155].

Tires pyrolysis oil has also been presented as a suitable alternative to dealing with waste tires. The use of zeolite catalysts allows for obtaining an intermedium stream in the pyrolysis stage that can be focused towards naphtha or diesel production. The resulting product should be fed afterwards in a hydroprocessing unit to adapt its composition to the characteristics of commercial fuels, as its sulphur and aromatic content require a refining process that is sometimes advised to perform by its co-feeding with other materials [156].

The application of hydrocracking to biomass-derived oils has also been proven to be a feasible upgrading route, as the removal of water from these oils is compensated in terms of product total hydrogen content through the surplus of hydrogen used in hydrocrackers [157]. The introduction of these bio-streams appears to be an eco-efficient solution that benefits refinery economics [158]. However, as it occurs with other new materials, the addition of bio-compounds to hydrocracking habitual reactors must be constrained due to the sulphur and composition variations that they might produce. For that reason, the co-feeding of these materials with conventional streams has also been advised [159].

Recently, the introduction of waste materials such as plastics has gained attention due to the good yields of liquid fuels produced in their hydrocracking [160]. In order to reduce the operational problems that introducing solid materials to the reactor may provoke, some modifications such as a previous pyrolysis stage [161] and the addition of a moderate quantity of these plastics [162] have been employed to boost this plastics valorisation strategy. Yet the knowledge about the effects of adding materials with such a heterogeneous nature as the plastics blends is scarce and the process must be further studied.

1.3.3. Additional functions: HDS, HDN, HDO and HDM

Throughout hydroprocessing, hydrogenolysis reactions (involved in both hydrotreating and hydrocracking) also imply the cleavage of σ-type C-X bonds, X being nitrogen, sulphur, oxygen or metals, commonly, leading to what is

sometimes termed "hydropurification". The presence of these atoms is usually harmful, not only because they are limited in commercial fuels due to the hazardous nature of their combustion products but also because of some operational problems derived from their presence and/or transformation in other compounds [163–167]. The hydrogenolysis of compounds containing these heteroatoms behaves similarly in the case of N, S and O atoms (as depicted in Figure 1.9a), the corresponding products being ammonia, hydrogen sulphide and water through hydrodenitrogenation (HDN), hydrodesulphurization (HDS) and hydrodeoxygenation (HDO), respectively. On the other hand, hydrodemetallization (HDM) usually ends up with the deposit of varied metal forms. Figure 1.9b shows a frequent route for HDM based on sulphided catalysts that promote HDM activity [168]. The removal of heteroatoms is this way another reason why these units play a key role in product quality upgrading processes in refineries.

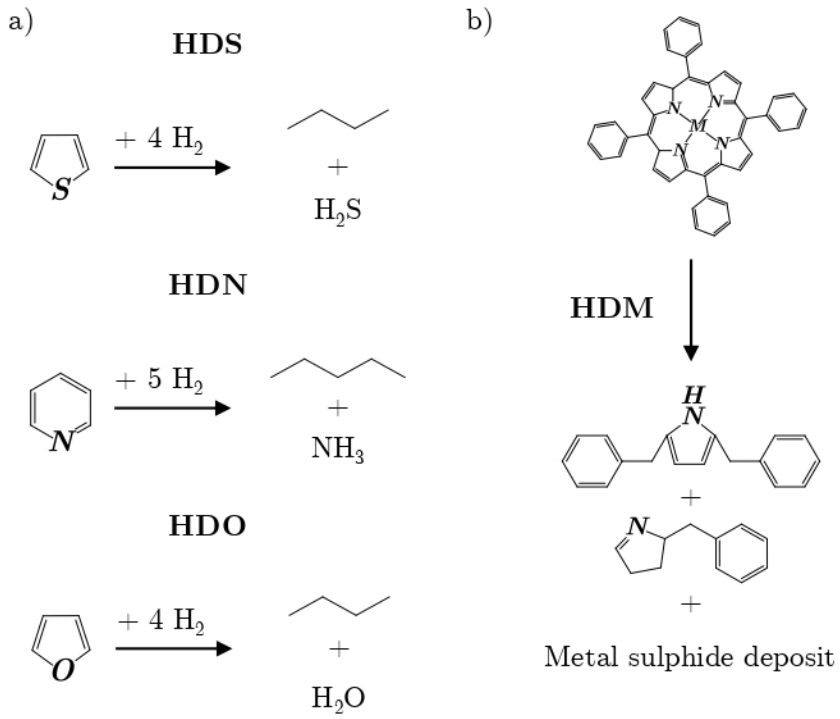

Figure 1.9. General heteroatom removal mechanisms in hydroprocessing.

HDS has been conventionally applied in refineries for some time now in order to produce low-sulphur fuels, as the unhealthy consequences of SO_x compounds productions are well-known [169] (e.g. acid rain, damage to marine and soil life). Moreover, the tightening of environmental regulations has incremented in the last years due to the higher concern about the automotive industry pollution. In crude oils, two main families of sulphides can be found. On one side, active sulphides, which include sulphur, hydrogen sulphide and mercaptans, can be easily removed partially because of their simple structures. On the other side, inactive sulphides such as thioethers, disulphides and thiophenes-derived compounds are more reluctant to be removed due to their aromatic structures and steric hindrances [170].

The optimization of HDS processes focuses on the elimination of the most refractory sulphur-containing molecules. As an example, the conversion of 4,6-dimethyldibenzothiophene (4,6-DMDBT) presents two routes with very different rates, as depicted in Figure 1.10 [171]: one of direct desulphurization (DDS) and another that firstly undergoes the hydrogenation (HYD) of one of the aromatic rings, followed by the sulphur elimination. The final products are dimethylbiphenyl (DMBP) and methyl cyclohexyltoluene (MCHT), respectively. The selectivity towards one or another route is largely influenced by the catalyst, although as a general rule, the presence of methyl substitutes leads to steric hindrance that facilitates sulphur removal through the indirect route. For this reason, the correct identification of the sulphur compounds that heavy streams in a refinery can contain is a matter of study, since HDS catalysts design is conditioned by the selectivity towards their conversion. Historically, HDS catalysts consist of a molybdenum active phase (either in metal or sulphide form) which can be doped with nickel or cobalt. Furthermore, the support significantly affects the HDS in terms of metal dispersion and catalyst stability, the most common ones being gamma-alumina, zeolites and carbon structures [172]. Recently, the modification of conventional catalysts through the addition of phosphorous and iron has exhibited an improvement in HDS performance [173].

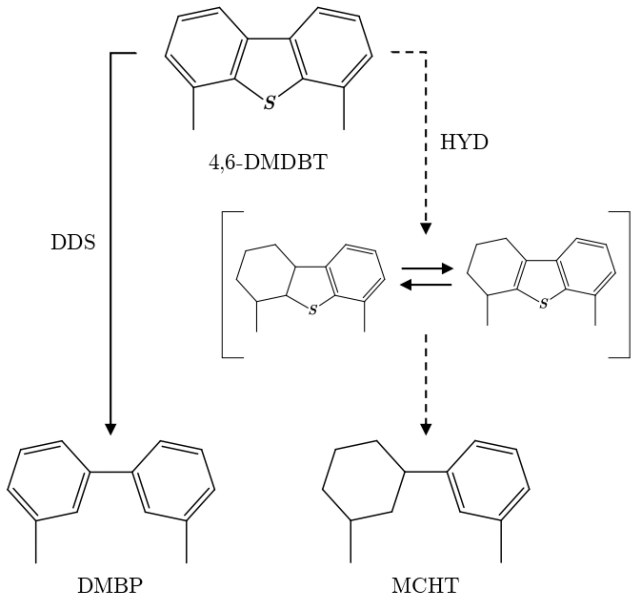

Figure 1.10. HDS routes.

While the industry has focused on the production of ultra-low sulphur streams for fuel blending pools, the presence of nitrogen and the intensification of diesel production has contributed to the formation of NO_x species in the atmosphere that cause health, environmental and economic impacts [174]. Apart from that, nitrogen species are proven to be poisons for hydrotreating and hydrocracking catalysts and inhibit the removal of other heteroatoms in the catalytic conversion of heavy streams [175], exhibiting the most refractory nature among them.

Organonitrogen species can be divided into heterocycles and non-heterocycles [176]. The latter ones are more likely to be eliminated through hydroprocessing and comprehend simpler structures such as anilines and aliphatic amines. However, most of the nitrogen-containing species contain heterocyclic aromatic rings (the most representative of them being pyrrole and carbazole-derived structures) which are difficult to remove directly through cracking reactions as in the case of the non-heterocycles [177]. The application of HDN is currently based on the same metals that those of HDS catalysts due to their high efficiency and supports that provide high specific surface area and volume, easy modification

and open and concentrated pore distribution [178], as they are mesoporous silica materials (MCM-41, SBA-15, FDU-12).

Since petroleum contains noticeably less oxygen than sulphur and nitrogen, HDO reactions have received comparatively less attention. However, the absorption of new materials that contain this heteroatom (such as some plastics or bio-streams) by hydrocrackers has returned this issue. Oxygenated compounds appear in the mentioned materials in diverse forms such as methoxyl (R-O-CH_3), phenolic noncyclical benzyl ether (R-O-R) and carbonyl groups (R-C=O) [179]. Besides, the removal of oxygen from these molecules does not occur in one way, as the breakdown of C-O-C- and C-O-H bonds that takes place implies a complex reactions system (that involves hydrogenation, hydrogenolysis, decarbonylation and hydrolysis) and results in increasing the fuel stability. Globally, HDO reactions usually produce water and the corresponding hydrocarbon after deoxygenation, although hydrogen consumption is high due to the formation of water and the proton supply to complete the formed molecule [180]. With this purpose, HDO catalysts are usually made up of sulphides or noble metals supported on acidic materials (e.g. γ-alumina, activated carbon or silica-alumina) [181].

Last, the importance of HDM has risen because of the increasing content of undesired metals in the heavier oils that are now being exploited. Those metals (including vanadium, nickel, lithium, iron and chromium, among others) form the so-called porphyrins, which are part of larger colloidal aggregates responsible for the catalyst deactivation due to the pore blockage and, in the worst cases, for the sedimentation of particles that affect the quality of the products of refineries [182]. Consequently, refineries' hydroprocessing units usually have a guard-bed HDM catalyst (of lower price) consisting of meso- and macro-porous supports (Al_2O_3) with metals (Ni, Mo, Co) oxides as active phase [183].

1.3.4. Hydrocracking catalysts and catalytic deactivation

The multiple reactions involved in hydrocracking require a catalyst capable of promoting two main functions: hydrogenation and cracking. Previous studies in

the development of catalytic cracking catalysts had introduced the concept of two functions happening at the same time. In a similar way, in the 1960s, the first approaches to a consecutive cracking and isomerization mechanism were introduced [184]. Later, the observation of unsaturated compounds' behaviour in hydroprocessing introduced the importance of metallic materials in the catalyst. The refinement of the catalyst design and the deepening of the hydrocracking mechanisms' knowledge led to the establishment of bifunctional catalysts as the preferred option for this process.

1.3.4.1. Bifunctional catalysts

Bifunctional catalysts are composed of a support that is involved in cracking reactions and a metal dispersed over the support that promotes hydrogenation-dehydrogenation reactions. While metals are chosen due to their activity levels, the support must provide a large surface that favours a uniform metal dispersion, good pore distribution and acidic properties, and thermal stability. The ideal hydrocracking mechanism of an n-alkane over a bifunctional catalyst is shown in Figure 1.11. First, the long paraffin is dehydrogenated in the metal sites; then the corresponding alkene intermediates diffuse to the acid sites of the support and are either isomerized or cracked. The resulting products can be hydrogenated to form final species or further cracked through secondary scission reactions that promote the formation of lighter species once they undergo hydrogenation back in the metal sites. If hydrocracking is not ideal, the largest fragments formed during primary cracking will undergo secondary cracking reactions, although the formation of C_1 and C_2 hydrocarbons does not take place as their primary carbenium ions are energetically disfavoured. Moreover, the formation of non-symmetrical hydrocarbons distribution when the carbon number is high enough (at least 12 carbons) is very likely to happen if the primary scission products are not rapidly desorbed, which only occurs under ideal conditions.

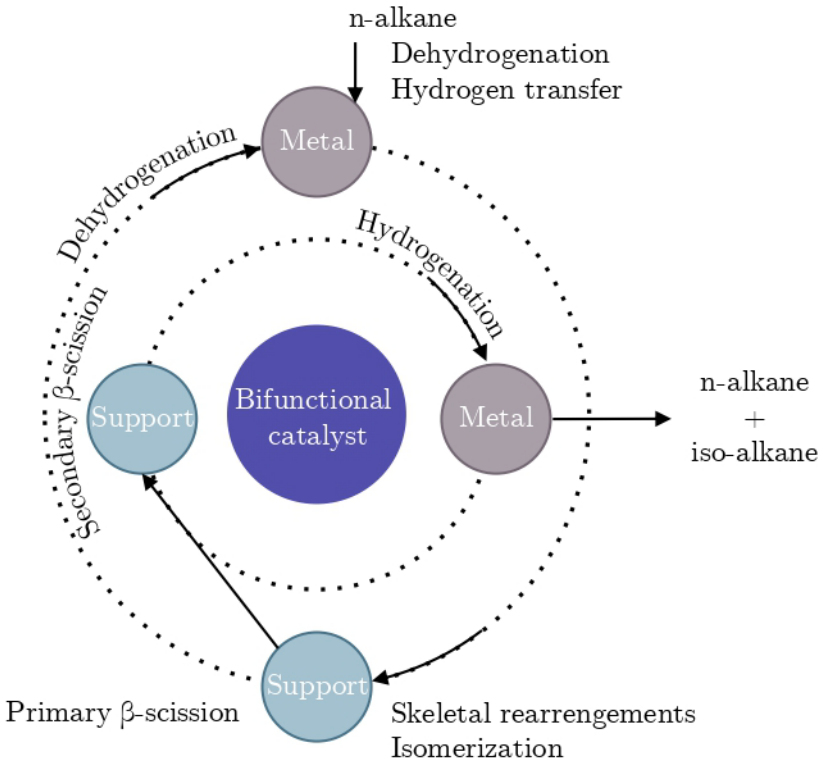

Figure 1.11. Ideal hydrocracking mechanism of an n-alkane over a bifunctional catalyst.

Possible combinations of acidic supports and metals for soft hydroprocessing have already been discussed in the previous subsection. However, the support of hydrocracking catalysts must contribute to a higher extent to the cracking function at the same time that provides isomerization activity [185]. The material employed for supporting the active phase must provide a pore distribution that facilitates the rapid diffusion of the branched isomer to the bulk phase before overcracking takes place. Moreover, it should allow the metal to be dispersed as close as possible to the acid sites (especially in the zeolite catalysts), as it has been proved that the intimacy between the metallic and acidic sites favours the hydrocracking sequential mechanisms [186]. The selectivity towards desired products depends not only on the acidic strength but also on the nature of the acidic sites, benefiting from the presence of Brønsted sites [145]. Taking all into

consideration along with the particular needs of each feed, mesoporous materials such as MCM-41 [187], alumina [188] or silica-alumina [189] and microporous materials such as zeolites [190] have been widely studied.

Regarding the metallic function, there are two variants of metal types used for the catalyst design, namely non-noble and noble metals. The first group include molybdenum, tungsten, cobalt and nickel and different combinations of them and their respective catalysts have been extensively used in the oil industry [191, 192]. Compared to these, noble metals (Pt, Pd, Ir, Ru) based catalysts have shown better performance in terms of activity and selectivity [193], although their use is contingent on the poisoning species (especially sulphur) present in the feed [194], as these metals are extremely sensitive to the presence of poisons and can be rapidly deactivated. To avoid this, common strategies in refineries are the addition of materials that protect the catalyst components [143] and, more often, the utilization of a double system with an HDS pretreatment [195], either in separate reactors or independent beds in the same reactor. Recently, the introduction of oil-soluble dispersed catalysts (like Mo, Ni, Co and Fe salt) has been studied, as they supply a high exposure to active sites and low mass transfer resistance of the high molecular weight molecules [196].

1.3.4.2. Catalyst deactivation

Aside from activity and selectivity, stability is a mandatory feature of industrial catalysts. Catalyst deactivation may occur due to various causes in hydroprocessing: (i) coke deposition, (ii) poisoning metals, (iii) active phase sintering and (iv) attrition [197–199]. The extent of each cause depends in a great manner on the operating conditions and the feed, although the main deactivation causes are the first two, with special concerns about coke deposition. Generally, in the industry three stages of catalyst deactivation are distinguished, as first there is a rapid deactivation due to coke deposition on the surface, then metals are deposited at a slower rate and finally both of those materials lead to the pore obstruction. Commercial catalysts are designed to last longer and therefore their visible deactivation is very gradual, with cycles comprehended between a few

months and up to two years [200]. The understanding of each of the mentioned phenomena allows for creating more stable catalysts.

Carbonaceous particles precipitation does not occur only over the catalyst surface but also can affect the equipment, leading to its fouling [201]. Although the coke formation mechanisms are not globally settled because of their complexity, researchers agree on the two main routes for its formation: on one side, the precipitation of the partially hydrocracked asphaltenes; on the other side, the condensation of coke precursors [202]. In industrial operations, coke formation is mainly related to primary and secondary asphaltenes [203]. The nature of these molecules has a great impact on their behaviour during hydrocracking, as the higher presence of metals that may not be removed promotes the formation of colloidal aggregates. With respect to coke condensation, the nature of its mechanism is more well-established, mainly composed of (i) hydrogen transfer at acid sites, (ii) dehydrogenation of adsorbed hydrocarbons and (iii) polycondensation reactions [204]. Using the example of the ring opening mechanism depicted in Figure 1.7, whose pathways were already told to be reversible, coke formation takes place through consecutive stages as follows [205]: alkanes which are being cracked form olefins that can be either saturated in presence of hydrogen or undergo oligomerization reactions, forming firstly dienes and then naphthenes by cyclization reactions. If hydrogen transfer reactions persist, aromatics are formed from these naphthenes and polyaromatics are produced sequentially. The primary form of these aromatics is soluble aromatics, which are usually confined in the support (as in zeolite cages), and condense into insoluble structures that develop until they reach the catalyst surface, leading to a massive clogging of the pores structure. Although under hydrocracking conditions the formation of olefins is rare, the formation of naphthenes is an inherent stage that could be directed towards their further cracking or starting the condensation towards coke structures skipping the olefins cyclization step. The severity of the operating conditions (temperature, the acidity of the catalyst...) and the nature of the compounds in the feed (as aromatics have a higher interaction with active sites that facilitate their conversion into coke structures) are essential in the understanding of coking processes [206, 207].

Catalyst deactivation due to metals deposition is evidenced more progressively than coke formation but has gained attention in recent years due to the deterioration of the quality of heavy oil feedstock. Current processes demand a more efficient HDM that avoids clogging issues in hydrocracking units, as catalyst deactivation by metals (unlike coke deposition) is irreversible [143]. Oppositely to the coke deposition deactivation mechanism, poisoning metals sediment is fundamentally based on diffusion and adsorption phenomena. The efficiency of HDM catalysts will be measured in terms of HDM activity and retention capacity, both of them dependent on structural and morphological properties. Some authors have argued that a large average pore diameter provides greater activity and stability to the catalyst [208], while others suggest that pore distribution and its optimization is crucial for maintaining a commitment between activity and stability [209]. Additionally, the behaviour of organometallic species is diverse, as some metals like vanadium are mostly deposited over the surface while others like nickel are preferentially distributed through the pores [210]. Hitherto, HDM is carried out in guard-bed reactors before even HDS reactors to prevent HDS catalysts deactivation [166]. Thus, metals deposition contribution to the catalyst deactivation should not be undervalued, particularly when refineries are about to integrate new feeds that can contain unknown metals coming from their manufacture.

1.3.5. Hydrocracking modelling

Control of hydrocracking units in terms of yields, selectivity and quality standards (such as environmental restrictions) is decisive for the refinery economics. The development of models that can predict and simulate the effect of changing the operating conditions and feeds of these units allows this way maximizing economic profits. However, the nonlinearity and sensitivity to feed changes of hydrocrackers considerably complicate the establishment of a universal tool for their optimization [211]. Heretofore, hydrocracking models have been performed through two methodologies, i.e. discrete and continuous lumping modelling. Apart from those, there are two more innovative and complex model types, which are structure-oriented and single-event models [212]. Conventionally,

the discrete lumping procedure has been more frequently used, as it is considered simpler, even if the increase in the studied lumps and mechanisms involved have significantly increased their number of parameters (and therefore their difficulty) in recent years [213]. On the other hand, continuous modelling is used for predicting the composition of the resulting products by taking into account the numerous compounds appearing in petroleum cuts. For that same reason, its application is yet limited.

Discrete lumps models are presented as a solution to the difficulties that catalytic processes inherently carry due to their complex reaction networks involving hundreds of hydrocarbons. The utilization of such an approximation allows for quantifying more easily phenomena such as diffusional limitations of the components in the reaction media and catalyst deactivation [197] that are usually empirically quantified. Lumps grouping is based on the consideration of pseudo-components with similar kinetic behaviour, which can be established according to two different criteria. On one side, the boiling point criterion distinguishes between dry gas (DG), liquefied petroleum gases (LPG), naphtha, light cycle oil (LCO), heavy cycle oil (HCO) and coke (carbon deposited on the catalyst), and determines the appropriate reaction network [214], perform the sensibility analyses that grant the simplification of the models [215], and relate the kinetic parameters with those obtained in literature [216]. On the other side, SARA (saturates, aromatics, resins and asphaltenes) composition [217, 218] has also been used for separating models to predict liquid, gas and coke yields [219].

Various approaches to the modelling of heavy streams hydroprocessing have been carried out with diverse degrees of complexity, ranging from direct conversion to products [220] to more complex systems that consider from 4-5 lumps [221, 222] and even parametric studies that analyse the expansion to 22 lumps [223]. In order to provide confidence to the kinetic parameters obtained, it is common for the resolution of these models to be solved by progressive sub-models that start with simpler reaction networks and evolve towards the final proposed models, following the methodology well-explained by Ancheyta-Juárez and Sotelo-Boyás [224]. Regarding the literature about modelling the hydrocracking of plastics,

there are several fewer studies. These studies are usually based on experimental works that do not treat directly plastics but instead work with plastic pyrolysis waxes or solutions [161, 225]. The modelling of LDPE has been proposed by Bin Jumah et al. [218], who established 4 lumps involved and a reaction system similar to those proposed by other authors for heavy streams hydrocracking. This study found the limiting step in plastics conversion and constituted a precedent for introducing these alternative lumps into conventional models. The limited experimental studies about the co-feeding of plastics with heavy streams result in limited knowledge about the modelling of the hydrocracking of these blends. As an example, Vela et al. [162] have realized a successful fitting of a 6 lumps model for an HDPE and VGO blend hydrocracking, considering a general formula for the catalyst deactivation related to coke deposition, proposing the kinetic model depicted in Figure 1.12.

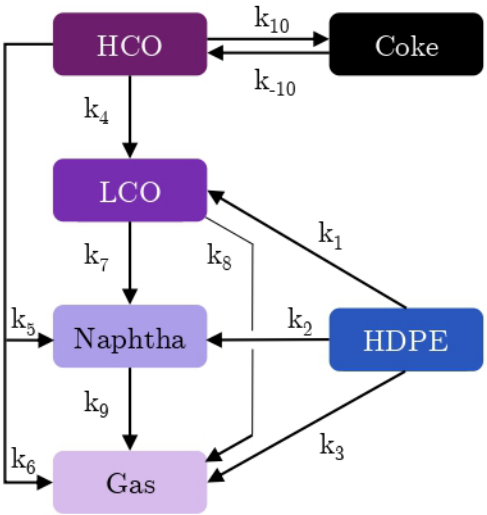

Figure 1.12. Reaction network for HDPE/VGO hydrocracking proposed by Vela et al. [162].

On the other hand, as discrete models cannot describe hydrocracking processes at a molecular level, continuous models emerge as an alternative directed to the understanding of the underlying physicochemical properties to take advantage of

computational development for describing and optimizing the hydrocracking process in a more advanced level [226]. Moreover, they present other advantages such as predicting the boiling point curve of the products and the distribution of heteroatoms [227] First attempts to apply continuous models to hydrocracking resulted in better fittings of discrete models when analysing VGO hydrocracking [222], even considering different parallel and in-series reaction pathways. The most recent advances have been performed in the hydrotreating field, with accurate predictions about the distribution of heteroatom concentration over time and as a function of boiling point [228]. However, these models still present some limitations such as the production of many samples and the non-exclusive dependence of species that belong to heavy oil fraction to boiling point or molecular weight, as explained by Ancheyta [229].

1.4. OBJECTIVES

Given the current situation of plastics consumption and annual growth rates, large-scale recycling of plastics is a priority to avoid the environmental problems of landfilling and direct combustion for energy generation. In this scenario, there is an interest in integrating refineries in this final stage of recycling and final production and marketing of plastic-derived fuels. This initiative increases the feasibility of large-scale recycling using devalued refinery units as part of the progress towards Sustainable Refinery (in this case through the enhancement of Waste Refinery).

The concept of the Sustainable Refinery was created in response to the need for change and innovation in refineries in the face of current circumstances: i) progressive decline in the quality of crude oil; ii) increased fuel quality requirements due to environmental legislation; iii) growing demand for fuels in the short term and for streams of increasing consumption such as olefins; iv) socio-economic changes and uncertainties; and v) coexistence with other energy sources (both fossil and renewable). The Sustainable Refinery pursues the development of new thermochemical processes to be integrated into refines and the adaption and intensification of processes already in place to obtain fuels. Consequently, it aims to achieve an intensifying recovery of oil, progressively integrating the exploitation of other fossils (coal, natural gas) that of renewable resources (such as biomass through Biorefinery) and the recovery of waste from the consumer society (through Waste Refinery, by absorbing materials such as plastics or tyres).

Due to their volume of implementation in refineries, the catalytic processes considered potentially suitable for the new feedstocks to be studied are the cracking (FCC) and hydroprocessing units. The hydroprocessing of plastic waste is an initiative that has been little studied in the literature and mainly involves work on small-scale slurry reactors. Hydroprocessing aims to produce fuels with the right composition for commercialisation, which is not achieved directly in the FCC (a unit that is more versatile and simpler than hydroprocessing units). Furthermore, given the difficulties in physically separating the different types of

plastics, dissolving them in other refinery streams such as fuel oil and vacuum gas oil or mixing them with other materials such as coal or lubricating oil can be an object of study for conventional refinery processes.

The general objective of the thesis project is to develop plastics hydroprocessing to obtain automotive fuels (petrol and diesel) with the appropriate composition in order to progress towards the implementation of this initiative in refinery units. The results (catalyst, operating conditions, kinetic modelling) obtained at a laboratory scale will be key information for subsequent proposals for pilot plants development. Thus, progress towards hydroprocessing units implementation is key to covering the demand for automotive fuels in the short term, intensifying the recovery of oil and complying with environmental requirements in terms of its composition, and thus responding to the challenge of achieving Clean, Safe and Efficient energy. On the other hand, the proper and integrated management of plastics (and their hydroprocessing meets these conditions) is considered a priority to contribute to curbing or reversing Climate Change.

Concerning the specific objectives, they extend into the scientific and applied fields. Thus, the contribution to knowledge on topics such as hydroprocessing mechanisms, the role of catalysts, kinetic modelling and the methodological contributions to these reactions (little studied due to their complexity) are aspects of great interest to the international scientific community. The objectives of the research are:

1. To establish the appropriate conditions for the different feeds (PS, PET, PMMA, in all cases together with VGO), based on the compromise of reaction rates (activity, selectivity and quality of the products, and resistance to catalyst deactivation).
2. To evaluate the impact and synergy of co-feeding plastics for VGO hydroprocessing in the results.
3. To study in depth the reaction mechanisms of a catalytic process with a complex reaction system and a wide range of species involved.
4. To establish a kinetic scheme for the individual reactions involved in the hydroprocessing of the different blends and reach a reasonable level of

knowledge of the reaction and deactivation mechanisms, which is adequate to establish kinetic equations for the different stages on a mechanistic basis.

5. To obtain kinetic equations that quantify the reactions' progress, allow calculating the concentrations of the product fractions of the corresponding kinetic scheme over a wide range of operating conditions and enable the simulation and optimisation of the processes.

Chapter 2

EXPERIMENTAL

This Chapter details the methodological information on the materials, equipment and analyses used. Here, the characterization of the feeds used, the equipment and reaction procedure and the conditions of the analytical methods used for the characterization of the catalyst, the reaction products and the deactivated catalysts are detailed.

2.1. FEEDSTOCKS

2.1.1. Vacuum gasoil (VGO)

The vacuum gasoil (VGO) used in this work is the base product of the vacuum distillation tower of a Petronor refinery located in Muskiz, Spain. The main physico-chemical properties of VGO have been measured by different techniques and are collected in Table 2.1.

Table 2.1. Properties and elemental composition of the VGO.

Properties	VGO
density at 15 °C (g mL^{-1})	0.9213
viscosity at 40 °C (cSt)	72.57
average molecular weight (g mol^{-1})	413
IBP–FBP (°C)	408–503
Asphaltenes (wt%)	0.1
GHV (kJ kg^{-1})	61.6
Elemental analysis (wt%)	
C	82.3
H	12.1
N	2.8
O	2.6
S (ppm)	2240

Density has been calculated by digital density meter, following the procedure described in the ASTM D4052 Standard. Viscosity (ν) has been determined following the procedure 11A4.2 of API Technical Data Book. This procedure consists of the utilization of an Ubbelohde Viscometer 53832 type IIC at 37.8 °C utilizing a thermal bath. The measurement is repeated 6 times and the average time is used to calculate this parameter according to Eq. 2.1.

$$\nu = K(t - \lambda) \tag{2.1}$$

where K is the constant dependent on the capillarity of the viscometer, t is the measured time in seconds and λ is a correction factor that is tabulated and provided by the manufacturer.

The average molecular weight, as well as the chemical composition (saturated and aromatics concentration, shown in Table 2.3) have been determined through SAR analysis with an HPLC, and the content of asphaltenes has been determined following the ASTM D3279 Standard.

For the calculation of initial and final boiling points (IBP and FBP, respectively), the simulated distillation curve, which is shown in Figure 2.1, has been carried out on an Agilent Technologies 6890 gas chromatograph equipped with a DB-2887 semi-capillary column (length, 10 m; inner diameter, 0.53 mm) and a FID detector, following the ASTM D2887 Standard.

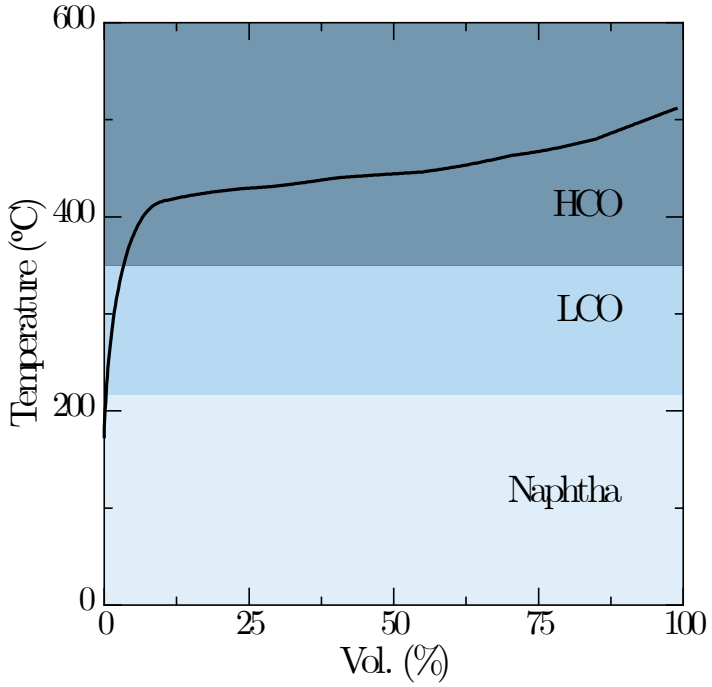

Figure 2.1. Simulated distillation curve of the VGO.

The conditions used for this analysis are shown on Table 2.2.

Table 2.2. Chromatographic analysis conditions for simulated distillation analysis.

Section	Variable	Value
Oven	T_0 (°C)	40
	t_0 (min)	5
	R_1 (°C min^{-1})	10
	T_1 (°C)	125
	t_1 (min)	0
	R_2 (°C min^{-1})	5
	T_2 (°C)	155
	t_2 (min)	0
	R_3 (°C min^{-1})	10
	T_3 (°C)	300
	t_3 (min)	30
Injector	T (°C)	350
	P (bar)	0.078
	Column flow (mL min^{-1})	9.4
	Split ratio	2.5:1
FID	T (°C)	320
	H_2 flow (mL min^{-1})	40
	Air flow (mL min^{-1})	450
	Make up flow (mL min^{-1})	20

Last, elemental composition and gross heat value (GHV) have been determined in a LECO TruSpect CHN Macrom equipment, the second one being determined by the Dulong formula (Eq. 2.2), where the concentration of each element (C, H, O, S) is in weight percentage and the heating value is obtained on kcal/kg. Sulphur content has been determined through X-Ray Fluorescence.

$$HV = 0.01\left[8.08C + 34.5\left(H - \frac{O}{8}\right) + 2240S\right] \tag{2.2}$$

The differentiation between fractions in Figure 2.1 has been carried out according to the boiling point criteria: naphtha (35-216 °C), light cycle oil (LCO, 216-343 °C) and heavy cycle oil (HCO, > 343 °C). Table 2.3 collects this fraction definition as well as the chemical composition of the VGO.

Table 2.3. Composition of VGO.

Composition	VGO
Lumps (wt%)	
naphtha	0.81
light cycle oil	0.97
heavy cycle oil	98.22
Chemical groups (wt%)	
paraffins	49.0
naphthenes	21.9
aromatics	
1-ring aromatics	2.1
2-ring aromatics	2.5
3+-ring aromatics	24.5

2.1.2. Plastics

Polystyrene (PS), polymethyl methacrylate (PMMA) and polyethylene terephthalate (PET) have been purchased from Dow Chemical, Altuglas International Arkema Group and Artenius, respectively. They all have been obtained in pellet form so, before their use, they have been ground to a particle size ($d_p < 0.5$ mm) by cryogenic methods. The main properties of the three plastics are collected in Table 2.4.

Average molecular weight, polydispersity and density have been provided by the suppliers. The elemental composition as well as the heating value have been determined in the apparatus described in Section 2.1.1.

Table 2.4. Main properties of the plastics.

	PS	PMMA	PET
Average MW, kg mol^{-1}	311.6	-	25-30
Polydispersity	2.39	-	2
Density, kg m^{-3}	1030	1165	-
Elemental composition, wt%			
C	92.1	64.0	67.5
H	7.9	7.5	4.0
O	0	28.5	28.5
HV, kJ kg^{-1}	43	27	24

Finally, the three plastics have been pyrolyzed at programmed temperature to study their thermal behaviour, as collected in Figure 2.2. For this purpose, a temperature ramp has been carried out for each plastic in a TA Instruments TGA Q5000 IR Thermogravimetric apparatus.

Figure 2.2a shows the weight loss with temperature of the studied polymers, noticing that both PS and PMMA start to degrade at 200 °C, although PMMA shows the lowest thermal resistance as its weight is < 1 wt% at 410 °C, while it takes 60 °C more to PS to be fully degraded. Regarding PET; the mass rapid loss is observed at the same temperature than that of PS, although it is noticeable that PET remains constant at ca. 15 wt% at temperatures above 475 °C.

Figure 2.2b shows the derivative weight loss profiles of the combustions observed in Figure 2.2a, observing that PS and PET peaks match at 432 °C, with a minor

signal of PET due to the fraction of the plastic that is not converted. PMMA peak, on its side, is located at a lower temperature (378 °C).

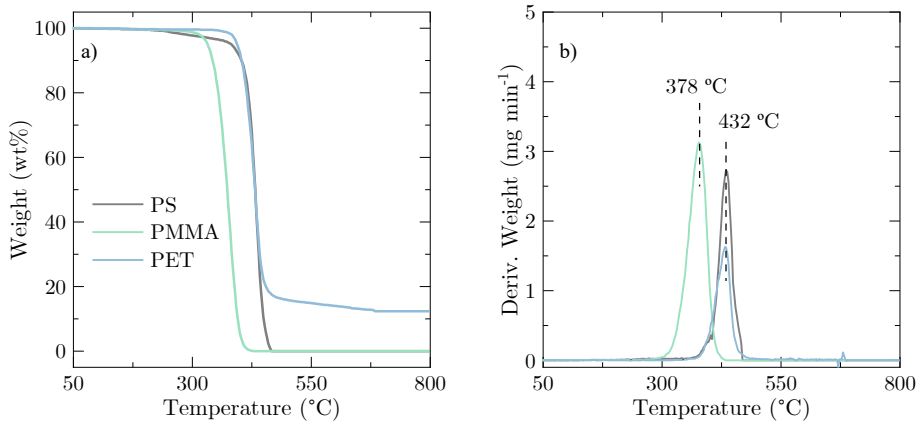

Figure 2.2. Thermogravimetric analysis of PS, PMMA and PET: a) weight loss and b) weight loss derivative.

2.2. CATALYST SYNTHESIS AND CHARACTERIZATION

Hydrocracking runs have been carried out using an in-house prepared bifunctional catalyst. The synthesis procedure, established by Gutiérrez et al. [230], follows the scheme described in Figure 2.3.

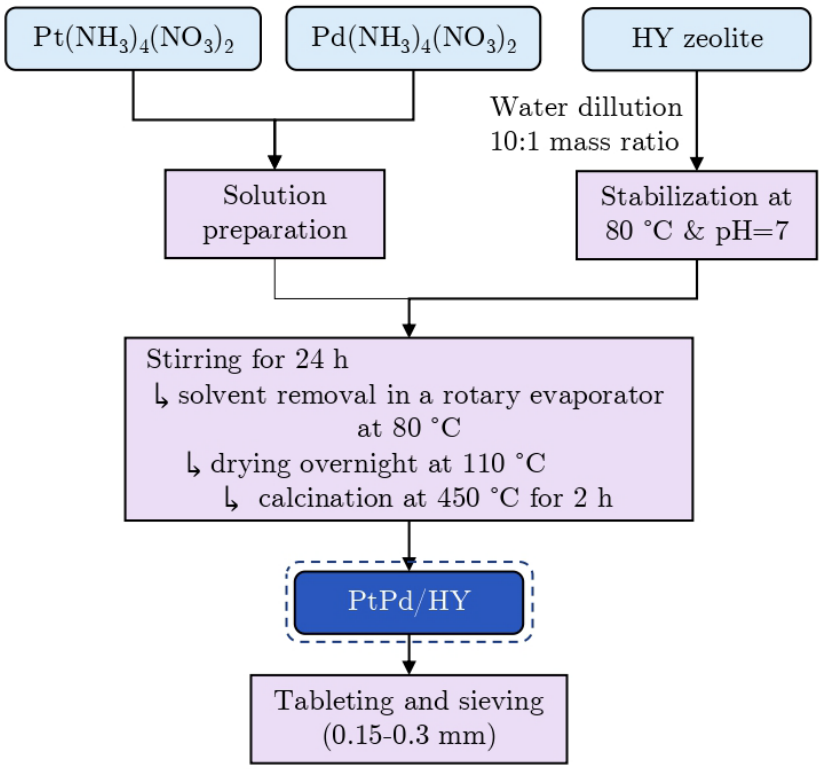

Figure 2.3. Schematic of the catalyst synthesis procedure.

Platinum and palladium precursors (both in nitrate form) have been supplied by Alfa Aesar and Strem Chemicals, respectively, and have been used to prepare two solutions of established concentrations (ca. 2500 ppm) by diluting them in distilled water. Zeolite support consists of an ultrastable zeolite supplied by Zeolyst International (CBV 712) and has been calcined prior to the synthesis as follows: (i) 2 h at 400 °C (5 °C min^{-1}), (ii) 15 h at 500 °C (5 °C min^{-1}), and (iii) 2 h at 550 °C (5 °C min^{-1}).

The procedure consists of the dilution of the zeolite in distilled water, with a mass ratio of 10:1 of solvent-zeolite. Then this solution is stabilized at 80 °C and pH=7 by using NH_3 and NH_4NO_3 when necessary to adjust the pH. Once it is stabilized, the metals solutions are added to achieve the final concentration, which in this case is a nominal content of 0.5 wt% of each metal. This election is based on the positive results obtained by Keogh et al. [231] when analysing the effect of platinum content on hydrocracking of hexadecane and the major selectivity to the fractions of interest obtained by Gutiérrez et al. [232] when performing a platinum-palladium based catalysts screening.

2.2.1. N_2 adsorption-desorption isotherms

Surface properties of the catalyst have been determined from the nitrogen adsorption-desorption isotherms obtained with a Micromeritics ASAP 2010 apparatus. The specific surface has been determined according to the BET procedure, whereas pore volume has been obtained from the *t*-plot method [233]. The average pore diameter has been estimated applying the BJH model The analysis has been carried out at -196 °C using N_2 after the samples degasification at 150 °C for 8 h and vacuum pressure ($2.7 \cdot 10^{-6}$ bar) in order to remove impurities and humidity from the sample.

2.2.2. Temperature programmed desorption (TPD)

The acidic properties of the catalyst have been measured by means of temperature-programmed desorption of ammonia (NH_3-TPD) in a Micromeritics AutoChemII 2920, equipped with a thermal conductivity detector (TCD). The utilization of ammonia as a base to measure the acidity of micro-mesoporous catalysts presents no diffusional limitations and neutralizes centres in a wide range of acid strength. Thus, the application of this method for measuring similar catalysts has been corroborated by other authors [234].

The procedure is as follows: (i) sample is swept with a 20 mL min^{-1} flow of He and heated up with a temperature ramp of 15 °C min^{-1}, then maintained for 10 min; (ii) then the sample is cooled down to 150 °C; (iii) and stabilized at that temperature with a continuous flow of He of 50 mL min^{-1}; after that, the sample

is saturated with continuous injection of ammonia (750 μL min^{-1}); (iv) after sample flow is changed to 20 mL min^{-1} again, and the physisorbed fraction of adsorbate is eliminated; (v) finally, the temperature programmed desorption is carried out up to 550 °C with a 5 °C min^{-1} ramp.

2.2.3. Fourier transform infrared (FTIR)

Brønsted/Lewis (B/L) acid sites ratio has been estimated by pyridine adsorption in a Specac high-temperature high-pressure cell couple in-line with a Nicolet 6700 FTIR spectrometer. From FTIR spectra, Brønsted and Lewis bands are located at 1515-1565 cm^{-1} and 1435-1470 cm^{-1}, respectively. This occurs because of C-C stretching vibrational frequencies associated with the protonated pyridine that forms pyridinium ions on Brønsted sites and the coordinated pyridine on Lewis sites [235]. The molar extinction coefficients (ε_B and ε_L, 1.67 and 2.22 cm μmol^{-1} respectively), the surface of the sample disk (S_d, 1.69 cm^2), its weight (W_s) and the area of each peak (A) are applied then by using Eq. 2.3, which allows calculating the pyridine concentration ($C_{pyridine}$) adsorbed on each type of acid site [236].

$$C_{pyridine} = \frac{A\,S_d}{\varepsilon\,W_s} \tag{2.3}$$

The analysis follows an established procedure: (i) the catalyst sample is milled to powder and around 20 mg are placed into a press to obtain a wafer, (ii) the sample disk is placed inside the measurement cell and evacuated under vacuum pressure and a temperature up to 450 °C with a 5 °C min^{-1} ramp, (iii) after moisture has been removed from the sample and the corresponding spectrum has been checked, the cell is cooled down and stabilized at 150 °C when the first analysis spectrum is taken; (iv) pyridine pulses are injected for 2 min, then the sample is stabilized for 2 min and evacuated under vacuum pressure for 5 min, after which a new spectrum is taken; (v) this process is repeated until the saturation of the sample is achieved, and the last spectrum is the one used for the calculations explained above.

2.2.4. Inductively coupled plasma with atomic emission spectroscopy (ICP-AES)

Metal content on the fresh catalyst has been measured by inductively coupled plasma with atomic emission spectroscopy (ICP-AES) at the Geology Department of the University of the Basque Country UPV/EHU. A Thermo quadrupolar mass spectrometer (XSeries 2 model) from Perkin Elmer with a plasma source equipped with Xt interphase, shielded torch and concentric nebuliser has been used for the analysis. The calibration of the equipment has been carried out by using multi-elemental solutions of 100 ppm.

The analysis is performed by adding a blend of HNO_3:HF to a sample of 50 mg of the catalyst in closed containers of PFA (Savillex) for 24 h at 90 °C. Additional $HClO_4$ is added during the evaporation of the resulting solution in order to avoid the formation of insoluble fluorides. Then HF is introduced on the samplers and heated overnight at 90 °C, dried and HNO_3 is introduced and diluted into a 1:450 ratio to perform the analysis.

The deposited metals content on the spent catalysts has been determined by ICP-AES as well in King Abdullah University of Science and Technology (KAUST) Core Labs. The methodology changes with respect to the previous one: first, samples are digested in an HNO_3 (5 wt%), HCl and HF blend in a 3:1:1 ratio using an Ultra WAVE instrument (Milestone) at 250 °C and 130 bar for 40 min, and then diluted according to the appropriate proportion taking into account the total concentration and the calibration curves before being submitted to analysis.

2.2.5. Metal dispersion

Metal dispersion of the catalysts has been measured by CO pulse chemisorption in a Micromeritics AutoChem II apparatus coupled in line with a Blazer Instruments mass spectrometer. CO purity is 20 vol.% diluted in He. Metallic dispersion (D) is calculated following Eq. 2.4, as N_S is the number of metal atoms over the catalyst surface and N_T is the total number of metal atoms.

$$D = \frac{N_S}{N_T} 100 \tag{2.4}$$

The amount of total atoms is determined by the sum of the atoms of each metal, calculated by means of their concentration, measured by ICP-AES, the sample mass, their molecular weight and Avogadro's number. The total atoms over the surface are calculated by determining the amount of CO retained on the catalyst and assuming the stoichiometry ratio of CO/Pt and CO/Pd chemisorption of unity [237].

The analysis is carried out as follows: a sample of 100 mg is reduced at 300 °C for 1 h while a 50 mL min^{-1} flow of 10 vol.% H_2 in Ar is going through the reactor in order to remove the impurities of the sample at the same time that metals turn into their reduced form. Then, the sample is stabilized at 60 °C and consecutive CO pulses are performed until the sample is saturated.

2.2.6. Pt and Pd ligands

The arrangement of the Pt and Pd ligands has been assessed by means of CO adsorption at 25 °C in the FTIR spectrometer described in Section 2.2.3. The loading procedure is the same as that explained above, although the operating methodology differs.

Vacuum pressure is applied to take a spectrum in order to ensure that the infrared beam is going through the sample. The vacuum pump is switched off, and a H_2/Ar flow of 120 mL min^{-1} goes through the cell for 1 min, then regulated at 40 mL min^{-1}. The cell is heated up to 250 °C (5 °C min^{-1}) and the system is stabilized at this temperature for 30 min. Then the gas flow is switched to 120 mL min^{-1} of He for 1 min and stabilized at 60 mL min^{-1}. The system is cooled down to 25 °C and He flow is stopped. After sweeping with 120 mL min^{-1} of CO/He (20 vol.%) for 1 min, this flow is regulated at 20 mL min^{-1} and fed for 10 min. After this time, a new sweeping with 120 mL min^{-1} of He is repeated for 1 min and then spectra are taken with a flow of 60 mL min^{-1} each 10 min until two sequential spectra are the same. That last spectrum is the one used for the data treatment.

Data treatment has consisted of comparing the percentage areas of the different bands collected from literature [238–240] for both platinum and palladium: 1865 cm^{-1}, multibonded CO-Pt; 1911 cm^{-1}, multibonded CO-Pd; 1920, 1936 and

1982 cm^{-1}, bridging CO (adsorbed on the face); 2075 cm^{-1}, linear Pt-CO. The area corresponding to each band has been normalized for all samples with respect to their mass.

2.2.7. XRD

The crystallinity of the catalyst has been determined by powder X-ray diffraction (XRD) in a Philips X'Pert Pro automatic diffractometer operating at 40 kV and 40 mA, in theta-2theta configuration and equipped with a secondary monochromator with Cu-Kα radiation (wavelength, 1.5318 Å) and a PIXcel solid state detector (active length in 2ϑ, 3.347 °). Data have been collected at room temperature from 10 to 90 ° in the 2ϑ range (step size, 0.026°; time per step, 60 s). A fixed divergence and antiscattering slit giving a constant volume of sample illumination have been used.

2.2.8. Scanning electron microscope (SEM) images

Scanning electron microscope (SEM) images have been obtained in the Advanced Research Facilities (SGIker) of the Faculty of Science and Technology of the University of the Basque Country UPV/EHU by means of a Schottky-type field emission scanning electron microscope (JEOL JSM-7000F) equipped with a secondary electron detector at 10 kV.

2.3. REACTION EQUIPMENT AND PROCEDURE

2.3.1. Catalyst activation

Prior to the runs, the catalyst has been reduced *ex-situ* in a fixed bed unit consisting of a stainless fixed bed reactor equipped with three parallel rotameters, a heating jacket controlled by a TOHO TTM-005 controller and a 0.1 M NaOH solution located at the gases exit to prevent the emission of H_2S. The gases controlled by the three rotameters are (i) 99.9995 % purity nitrogen, supplied by *Carburos Metálicos*; (ii) 99.999 % purity hydrogen provided by Air Liquide; and (iii) a 10 vol.% blend of H_2S/H_2 supplied by Air Liquide.

The pre-treatment operation is carried out as follows:

i. **Reactor loading.** A blend of catalyst ($0.15 < d_p < 0.3$ mm) and silicon carbide is equally weighted in order to have an amount slightly higher than the one needed for the reaction, using this CSi to avoid the formation of preferential routes of the gas flow. Before putting it into the reactor, wool glass is placed at the bottom of the reactor to prevent the dragging of solid material with the gas and then silicon carbide is placed below and above the catalyst/CSi bed itself for the same purpose. CSi is previously sieved to have a particle size above 500 μm to ease the posterior separation of the catalyst.

ii. **Catalyst reduction.** Hydrogen is used to activate the catalyst. The flow of this gas is that of 30 mL min^{-1}, diluted in a 50 mL min^{-1} nitrogen flow. At the same time, the temperature is raised to 400 °C (5 °C min^{-1}) and then maintained for 4 h to ensure the complete metals activation.

iii. **Cooling down and catalyst recovery.** The system is cooled down and once it is at ambient temperature, the system is unloaded and the blend of CSi and the activated catalyst is recovered. Then the catalyst is separated by sieving and added to the batch reactor.

2.3.2. Hydrocracking reactors

2.3.2.1. Units description

PS/VGO hydrocracking runs have been carried out in an Autoclave Engineers Microclave™ reactor specifically designed for laboratory-scale heterogeneous catalytic processes. This unit allows working at temperatures and pressures up to 454 °C and 345 bar, respectively, which allows operating at the operating conditions window corresponding to industrial hydroprocessing.

A scheme of this unit is collected in Figure 2.4. The setup can be divided into four different zones: (i) feeding zone, (ii) reactor, (iii) gas product sampling zone, and (iv) condenser system.

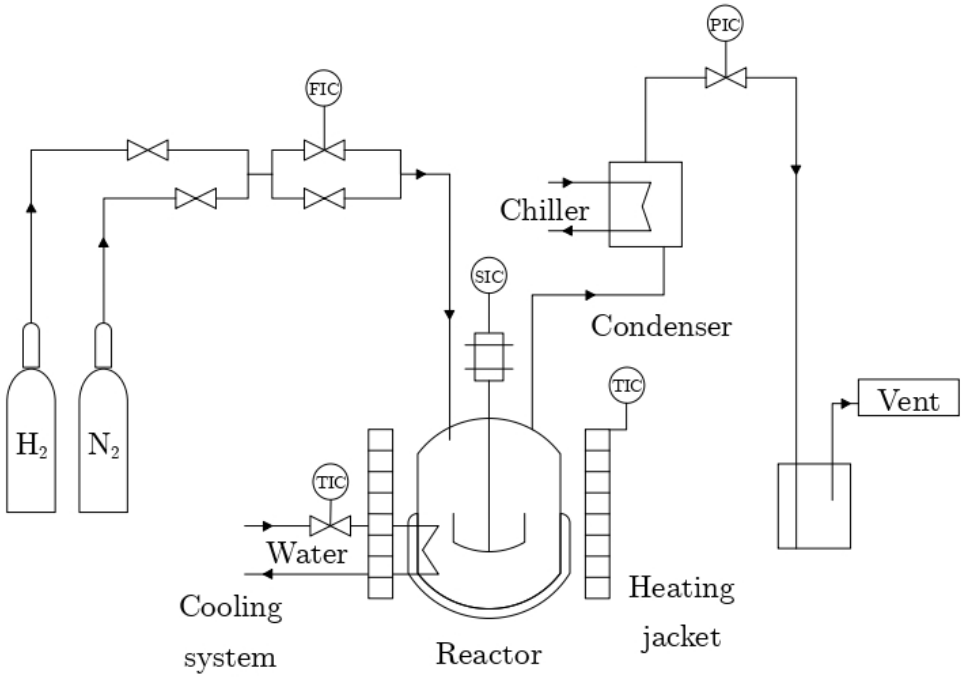

Figure 2.4. Reactor system scheme.

(i) Feeding zone. The equipment has two different gas input lines. Each of them is provided with a Bronkhorst High-Tech B.V. mass flow controller, as well as a shutoff valve and a check valve to prevent the reverse flow through these lines. The gases used are:

- Nitrogen. Used for the conditioning of the reactor (leak testing and inertizing). It is supplied by *Carburos Metálicos* with a purity of 99.9995 wt%. Nitrogen flows up to 100 mL min^{-1}.
- Hydrogen. Used as reactant. It is provided by Air Liquide (purity of 99.999 wt%). Hydrogen flow up to 100 mL min^{-1}.

(ii) Reactor. The reactor is a stirred tank reactor consisting of a HASTELLOY® C-276 alloy cylindrical vessel, with an internal diameter of 1.6 cm, length of 11 cm and volume of 50 mL. It is provided with 3 deflector plates that prevent the

formation of vortices during stirring and thus favour the dispersion of the gas within the blend and the contact between the three phases.

Mixing is regulated by a MagneDrive™ magnetic stirrer that allows operating at stirring speeds up to 5000 rpm. Reactions have been carried out at 1300 rpm in order to minimize external diffusion, as it has been proven that speeds over 800 rpm do not influence conversion and allow neglecting external diffusion effects in batch reactors [219]. The stirring impeller is provided with a 6-flat-blade disc-turbine designed by Dispersimax™, which provides high-speed radial flow stirring and supplies the gas into the system through a hollow located on the central part of the turbine, maximizing the perfect blend between the gas and the other phases. Finally, the stirring system is supplied with a heat exchanger that uses cool water for keeping an adequate stirrer temperature.

The reacting system is designed to operate isothermally, being provided with an external furnace of 2000 W of maximum power and a refractory material that covers the resistance. Two K-type thermocouples are used for this purpose, one located inside the vessel and another one located between the refractory material of the heating jacket and the external surface of the reactor. This heating system is controlled by an IB50 control unit that also provides real-time monitoring. A surrounding coil is also placed around the vessel and can be fed with cooling water once the reaction time has ended up.

(iii) Gas product sampling zone. The reactor gas outlet is connected at the upper side of the reaction vessel, that reaches a three-way valve that allows collecting gas at the end of the reaction in external collecting sampling bags of 500 mL or directing the flow to a NaOH- solution scrubber to adsorb H_2S before venting it out.

(iv) Condenser system. The equipment is provided with a Huber Minichiller 600 OLÉ that provides continuous flowing of an organic refrigerant at -10 °C in order to prevent the volatilization of light compounds, thus collecting only $< C_5$ compounds in gas products. The condenser is designed as concentric tubes of

2 m high (to achieve an efficient condensation), the inner one being the gas above explained and the external one being the refrigerant line.

A very similar system has been used for oxygenated plastics/VGO hydrocracking but the unit employed for those experiments is a PID Engineering & Tech reactor of 100 mL. The reasoning behind the use of a different unit for analogous experiments with the different plastics is the experimental observation of some corrosive compounds when feeding oxygenated plastics that provoke the corrosion of the 50 mL reactor gasket.

2.3.2.2. Procedure

Prior to each reaction, reactor needs to be weighted every time one of the materials is added, as well as a previous measurement when it is empty. Then, the usual operating conditions lead to weight: (i) 2 g of reduced and sieved catalyst; (ii) 2 g of plastic; (iii) 18 g of VGO. Then the reactor vessel is connected to the setup, tighten up and surrounded around with the heating jacket. The steps of the reactions are then the following:

Phase 1. Valves are checked to be in the correct position and gas cylinders to be open and with pressure enough to carry out the reaction.

Phase 2. Reactor is fed with a nitrogen flow of 100 mL min^{-1} during 5 min for inertizing. Then it is pressurized up to 5 bar and then released for two repeated times. After that, leak test is performed by pressurizing up to 30 bar, flow is then stopped and pressure is checked to be constant for 30 min. If leak test is successful, pressure is released and the initial procedure of feeding gas up to 5 bar and released is repeated with 100 mL min^{-1} of hydrogen in order to remove nitrogen.

Phase 3. The system is conditioned by feeding hydrogen with a 100 mL min^{-1} flow until pressure reaches half of final pressure value, to prevent the partial vaporization of the blend while temperature is rising. Then, flow is stopped and heating is started by control unit until reactor temperature reaches a value

around 50 °C below the set point. At this point, hydrogen flowing is once again started until both temperature and pressure reach the reaction set point values.

Phase 4. Once operating conditions have been reached, the stirring is activated and this time is counted as time zero. At this moment, the cooling system of the stirring system is switched on to avoid the overheating of the stirrer.

Phase 5. After the established reaction time, the stirrer, the heating system and the hydrogen flow are turned off. Gas sample is collected at this point by releasing around 5 bar of inner pressure. The system remains pressurized while cooling down to room temperature, maybe helping by switching on the cooling system through the external coil around the reactor when it is at 100 °C.

Phase 6. The system is depressurized with a constant rate, low enough to avoid dragging the liquid through the gas vent line.

Phase 7. All the valves are switched to safe positions again and the vessel is dismounted and weighted.

2.4. PRODUCT COLLECTION, IDENTIFICATION AND ANALYSIS

2.4.1. Product separation

The product separation process is collected in Figure 2.5.

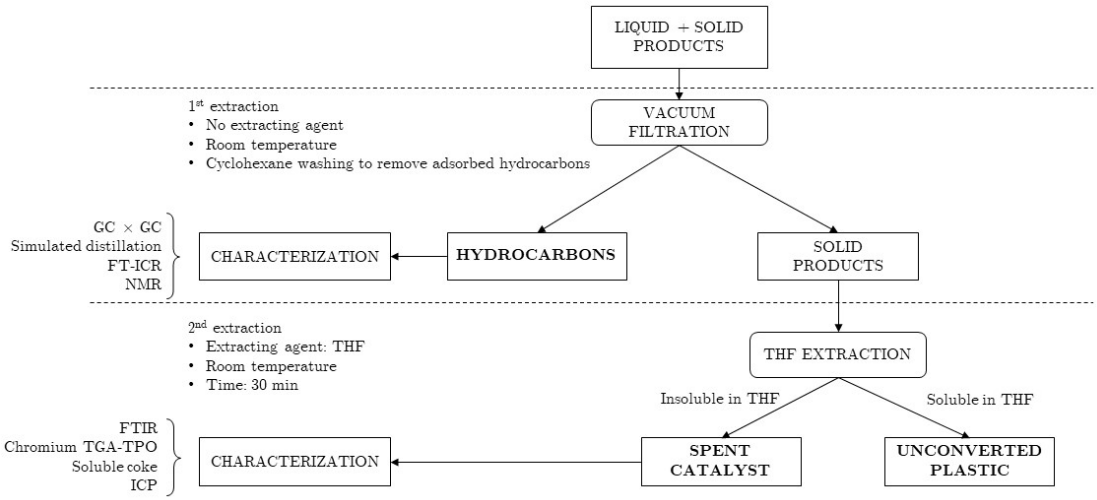

Figure 2.5. Product filtration and separation system scheme.

Once the reactor has been dismounted from the setup, the liquid product is obtained employing a first vacuum filtration at room temperature, separating it from the unconverted plastic and deactivated catalyst. In cases of viscous product blends, directly attributed to low plastic conversions, cyclohexane has been used as diluting agent in 1:3 feed:cyclohexane mass ratio, ensuring that chromatograms peaks are not masked by the cyclohexane peak in posterior analyses. The solid products are dried at 110 °C overnight to evaporate the remaining cyclohexane. Afterwards, unconverted plastic and deactivated catalyst are separated by filtration at room temperature, previous addition of tetrahydrofuran (THF). The required amount of this solvent is calculated as a 1:20 dilution ratio of the foreseeable plastic mass, considering that the amount of catalyst remains constant along the procedure. The spent catalyst is then once again dried overnight at 110 °C and subsequently collected to analyse it. Dissolved plastic has also been collected for possible analysis of their degradation during hydrocracking.

Once the separation of the products has been explained, the mass balances have been determined as follows: (i) gas product amount is calculated as the mass difference between the reactor weights before and after the reaction; (ii) coke amount is calculated using thermogravimetric techniques that will be detailed at the end of this Section and its total amount is determined taking into account the amount of catalyst recovered from the subsequent filtrations; (iii) unconverted plastic amount is obtained from the weight of the solid products after the first filtration (once they are dried) and the one of the final recovered catalyst; (iv) liquid fraction weight is calculated by the difference of initial loading and the catalyst and the other products.

2.4.2. Gas products

Two different chromatographic techniques have been used for characterizing gas products, according to the system that has been used. For the 50 mL reactor, gases have been analysed in an Agilent Technologies 6890 cryogenic gas chromatograph equipped with a capillary column HP-PONA (length, 50 m; internal diameter, 0.2 mm), a FID detector and a CO_2 detector for reaching cryogenic temperatures (-30 °C) to ensure the lightest compounds. Gas samples of 2 μL are taken from the sampling bag by means of a Hamilton syringe and then manually injected into the gas chromatograph. The analysis conditions used in the equipment are collected in Table 2.5.

On the other side, gas products of the 100 mL reactor have been analysed in a Varian CP-4900 gas micro-chromatograph provided with four analytical modules: (i) a molecular sieve (MS-5) for the quantification of Ar, N_2, O_2, CO and methane; (ii) Porapak Q (PPQ), for differentiating between CO_2, methane, ethane, propene and propane; (iii) Al_2O_3 to separate propene, propane, isobutane and n-butane; and (iv) CPSiL to separate C_5-C_{10} hydrocarbons. Note that due to the utilization of a chiller operating at -10 °C, the last modulus is not used. The addition of Ar to the system is performed with a controlled mass flow of 10 mL min^{-1}, measured before each experiment, in order to have a pattern for the real-time monitoring of both qualitative and quantitative analyses of gases. The method for this analysis is established as follows: sample time, 20 s; run time, 180 s; stabilizing

time, 5 s; sample line temperature, 110 °C, acquisition delay, 5 s. The conditions of each modulus are listed on Table 2.6.

Table 2.5. Chromatographic analysis conditions for gas product analysis.

Section	Variable	Value
Oven	T_0 (°C)	-30
	t_0 (min)	5
	R_1 (°C min^{-1})	15
	T_1 (°C)	235
	t_1 (min)	1
	R_2 (°C min^{-1})	30
	T_2 (°C)	275
	t_2 (min)	0
Injector	T (°C)	300
	P (bar)	0.85
	Column flow (mL min^{-1})	0.9
	Split ratio	100:1
FID	T (°C)	320
	H_2 flow (mL min^{-1})	40
	Air flow (mL min^{-1})	450
	Make up flow (mL min^{-1})	20

Table 2.6. Chromatographic analytical conditions for continuous analysis of gaseous products.

Modulus	MS-5	PPQ	Al_2O_3
Column temperature (°C)	45	95	110
Injector temperature (°C)	110	110	110
Injection time (ms)	40	20	20
Backflush time (s)	10	10	25
Initial pressure (bar)	1.38	1.72	1.59

2.4.3. Liquid products

2.4.3.1. Simulated distillation

Liquids have been characterized by simulated distillation according to the ASTM D2887 Standard in an Agilent Technologies 6890 chromatograph, following the same method as described in 2.1.1.

2.4.3.2. Liquid product composition

Liquid product composition has been characterized by means of bi-dimensional chromatography. The conditions used for the method are listed in Table 2.7.

Table 2.7. Chromatographic analytical conditions for bidimensional chromatographic analysis of liquids.

Section	Variable	Value
Oven	T_0 (°C)	50
	t_0 (min)	1
	R_1 (°C min^{-1})	2
	T_1 (°C)	260
	t_1 (min)	40
Injector	T (°C)	300
	P (bar)	1.83
	1st column flow (mL min^{-1})	0.75
	2nd column flow (mL min^{-1})	35
	Split ratio	50:1
FID	T (°C)	350
	H_2 flow (mL min^{-1})	20
	Air flow (mL min^{-1})	450
	Make up flow (mL min^{-1})	20

The analyses were carried out on an Agilent Technologies 7890A gas chromatograph equipped with: (i) one non-polar capillary column DB-5 ms J&W 122-5532 (length, 30 m; internal diameter, 0.25 mm; thickness, 0.25 μm); (ii) one

polar capillary column HP-INNOWAX (length, 5 m; internal diameter, 0.25 mm; thickness, 0.25 μm); (iii) a flame ionization detector (FID); (iv) an Agilent Technologies 7683B series autosampler, provided with 8-sample slots and a 10 μL syringe.

2.4.3.3. Fourier-transform ion cyclotron resonance – mass spectrometry (FT-ICR MS)

Fourier-transform ion cyclotron resonance – mass spectrometry (FT-ICR MS) coupled with atmospheric pressure photoionization (APPI FT-ICR MS) characterization has been carried out in a Bruker SolariX XR 9.4 Tesla instrument (Bruker Daltonics, Bremen, Germany) coupled in line with an Apollo-II ion source operated in positive-ion mode. Nitrogen at 220 °C has been used as a drying agent with a 4 L min^{-1} flow. Nitrogen has also been used as nebulizing agent, at a pressure of 1.2 bar. Photons have been produced with a krypton lamp with energies of 10.0 and 10.6 eV.

Prior dilution of the samples in toluene is required and has been done through a syringe pump, then infused into the ionization source by direct infusion with a rate of 20 μmL min^{-1}. Spectra have been calibrated by using homologous series, data treatment has been performed by Bruker Data Analysis V4.5 software, and chemical formula assignments have been done by means of the Composer software by Sierra Analytics (CA, U.S.A). DBE number is defined in Eq. 2.5 and has been determined with the following elemental constraints: C = 0-200; H = 0-1000; N = 0-4; O = 0-4; S= 0-4.

$$DBE\left(C_cH_hN_nO_oS_s\right)=c-\frac{h}{2}+\frac{n}{2}+1 \tag{2.5}$$

2.4.3.4. Nuclear magnetic resonance (NMR)

NMR spectra have been recorded using a Bruker 700 AVANAC III spectrometer equipped with a Bruker TCI multinuclear CryoProbe (BrukerBioSpin, Rheinstetten, Germany). Analyses have been performed at room temperature, collecting 32 scans for 1H spectra, 1024 scans for 13C spectra, and 8 scans for both HSQC and HMBC spectra. Recycle delay is 2 s for one-dimension analyses

and of 1 s for two-dimension spectra. Data treatment has been done using MestreNova (MNova) software, processing each spectrum 5 times and using the average value for each assignment. Structural assignments for 1H and 13C spectra have been done according to the one selected by Poveda and Molina [241]. These assignments are collected in Table 2.8. Samples have been prepared by diluting 20 mg of sample in 1 mL of deuterated chloroform ($CDCl_3$) in 5 mm NMR tubes (NORELL ©).

Table 2.8. Structural assignments in ^{1}H and ^{13}C NMR.

Region		Structural assignation
9.0-12.0	H_1	Aldehydic and carboxylic hydrogen
7.2-9.0	H_2	Aromatic hydrogen linked to aromatic carbons in di or poliaromatic rings
4.5-6.0	H_3	Aromatic hydrogen linked to monoaromatic rings
6.0-7.2	H_4	Olefinic rings
2.0-4.5	H_5	Paraffinic and naphthenic hydrogen CH, CH_2 and CH_3 type linked to aromatics systems in a position, other groups can be appear in this region (-OH and –SH)
1.5-2.0	H_6	Naphthenic hydrogen, CH_2 type, b to aromatic systems
1.0-1.5	H_7	Paraffinic hydrogen, b to aromatic systems, alkyl termination
0.1-1.0	H_8	Paraffinic hydrogen CH_3 type, g and more to aromatic systems
190.0-220.0	C_1	Aldehydic and cetonic carbons
178.0-190.0	C_2	Quinoloinic carbons
160.0-178.0	C_3	Carboxylic carbons
137.0-160.0	C_4	Non protonated aromatic carbons
154.0-157.0	$C_{4.O}$	Benzo and dibenzo aromatic carbons type, alpha to oxygen atom
137.0-140.5	$C_{4.SN}$	Alpha carbon to sulphur or nitrogen atom in benzo, dibenzotiophene and benzopyridine type structures

Table 2.8. (continued)

129.2-137.0	C_5	Aromatic carbons linked to methyl groups and head bridge between aromatic rings
129.7-131.7	$C_{5.1}$	Only aromatic carbons head bridge between aromatic rings
85.0-129.2	C_6	Protonated aromatic carbons olefinic and carbons in benzonaphthenic and alkylic systems and aromatic carbons bridge of three aromatic rings
60.0-78.0	C_7	Paraffinic and naphthenic carbon alpha to OH
50.0-60.0	C_8	Tertiary (CH) and quaternary (C) paraffinic carbons
21.5-60.0	C_9	Naphthenic and paraffinic carbons, CH_2 and CH type
32.9	$C_{9.0}$	Methyne carbons (CH-CH_3)
23.0	$C_{9.1}$	Alpha methylene (CH_2) to terminal methyl in alkyl chains
30.0	$C_{9.2}$	Methylenic carbons (CH_2) in long chains, three and more carbons to final of chain
32.0	$C_{9.3}$	Methylenic carbon, third carbon atom from the end of chain or beta to aromatic rings
37.0	$C_{9.4}$	Methyne carbons to aromatic systems (CH_2 bencylic)
39.0-43.0	$C_{9.5}$	Methylene carbons in alpha position to two aromatic ring
18.5-21.5	C_{10}	Methyl carbons in alpha position to aromatic rings
3.0-18.5	C_{11}	CH_3 carbons atoms type

2.4.3.5. GC/FID-PFPD analysis

Sulphur analysis was performed on a gas chromatograph (Agilent Technologies 7890A) equipped with a FID detector and a pulsed flame photometric detector (PFPD). The GC has a HP-PONA capillary column (length, 50 m; inner diameter, 0.20 mm; film thickness, 0.50 μm). The equipment uses helium as a carrier with a constant flow rate of 0.85 mL min^{-1} and the sample analysed is 0.3 μL. The conditions of analysis are given in Table 2.9.

Table 2.9. Chromatographic analysis conditions for sulphur compounds speciation.

Section	Variable	Value
Oven	T_0 (°C)	40
	t_0 (min)	3
	R_1 (°C min^{-1})	15
	T_1 (°C)	235
	t_1 (min)	1
	R_2 (°C min^{-1})	30
	T_2 (°C)	320
	t_2 (min)	25.17
Injector	T (°C)	250
	P (bar)	2.47
	Column flow (mL min^{-1})	1.2
	Split ratio	60:1
FID	T (°C)	340
	H_2 flow (mL min^{-1})	30
	Air flow (mL min^{-1})	400
	Make up flow (mL min^{-1})	25
PFPD	T (°C)	250

2.4.3.6. Research octane number (RON)

The RON of every sample has been determined following the methodology developed by Anderson et al. [242]. This method is based on chromatographic characterization of naphtha, dividing 31 different groups (some of them single components) that are separated according to their chemical nature, boiling point and retention time. A specific factor is attributed to each of these groups and RON is calculated as the sum of the multiplication of each group percentage and its corresponding factor.

2.4.3.7. Cetane index (CI)

Cetane index is based upon the density and volatility of light cycle oil fraction, and has been determined using the calculation proposed by ASTM D-4737 Standard, as follows:

$$CI = 45.2 + 170B + 0.0892T_{10N} + (0.131 + 0.901B)T_{50N} + (0.0523 - 0.42B)T_{90N} + 0.00049(T_{10N}^2 - T_{90N}^2) + 60B^2 \quad (2.6)$$

where

$$B = e^{-3.5}(\rho - 0.85) - 1 \quad (2.7)$$

Note that T_{10N}, T_{50N} and T_{90N} are the modified values from simulated distillation as distillation temperatures of 10, 50 and 90 vol.% minus 215, 260 and 310, respectively. The density of LCO fraction, ρ, is estimated through GCxGC analysis described in Section 2.4.3.2, by using the average blend taking into account the amount of each carbon number and compound type and their corresponding individual densities.

2.4.4. Coke amount

The amount of coke deposited on the spent catalysts has been determined by temperature-programmed oxidation by thermogravimetric analysis (TG-TPO) on a TA Instruments thermobalance (TGA Q500).

Apart from quantifying the total coke amount deposited on the catalyst, the procedure is modified based on the methodology developed by Wang et al. [243] in order to differentiate between the internal and external coke deposits. The preparation of the sample consists of mixing 20 mg of deactivated catalyst sample with 0.4 mg of CrO_3 by means of an extra addition of a few drops of water to ensure the correct blend of chromium, the final content of which is assumed to be 1 wt%. Once the sample is placed on the balance, a pretreatment with 50 mL min^{-1} of nitrogen at 50 °C is held for 10 min. Then the oven is heated up to 550 °C (10 °C min^{-1}) and held for 5 min in order to remove the moisture content of the sample as well as the adsorbed light organic compounds that can be swept and therefore are not considered as coke. After that, the sample is cooled down to 50 °C, stabilized for 10 min and then the nitrogen inlet is switched to air.

Then, the temperature is risen to 550 °C (5 °C min^{-1}) and held for 60 min to assure the complete combustion of coke molecules.

2.4.5. Reaction indices

In order to follow the extent of the reactions, different indices have been defined.

2.4.5.1. Yields

Taking into account the formation of gas, liquid and solid products, the evolution of the different lumps defined in the hydrocracking runs need to be done through a comparable variable. Thus, the yield (Y_i) of each i lump is defined as the mass of each lump (m_i) with respect to the total mass of the products, as defined in Equation 2.8.

$$Y_i = \frac{m_i}{\sum m_i} 100 \tag{2.8}$$

2.4.5.2. Conversions

Two different conversions have been defined as two different feeds can be distinguished. Hydrocracking conversion (X_{HC}) is defined based on the conversion of the heaviest lump of VGO, i.e. HCO, in mass basis, as described in Equation 2.9.

$$X_{HC} = \frac{m_{HCO,0} - m_{HCO,t}}{m_{HCO,0}} 100 \tag{2.9}$$

being $m_{HCO,0}$ the initial mass of HCO lump and $m_{HCO,t}$ the mass of HCO lump at the end of a reaction of t duration time.

In the same way, plastic conversion relates the initial loaded amount of plastic with the unconverted amount of solid plastic, as depicted in Equation 2.10.

$$X_{plastic} = \frac{m_{plastic,0} - m_{plastic,t}}{m_{plastic,0}} 100 \tag{2.10}$$

where $m_{plastic,0}$ is the initial plastic amount added to the reactor and $m_{plastic,t}$ is the amount of solid plastic recovered at the end of reaction.

2.4.5.3. Selectivity

With the aim of quantifying the target lumps (i.e. naphtha and LCO) yields and measuring the catalytic activity, a selectivity (S_i) has been used based on an already used parameter [125].

$$S_i = \frac{m_{i,t}}{(m_{HCO,0} + m_{plastic,0}) - (m_{HCO,t} + m_{plastic,t})} \tag{2.11}$$

where $Y_{naphtha}$, Y_{LCO}, Y_{DG}, Y_{LPG}, $Y_{plastic}$ and Y_{coke} are the yields of naphtha, LCO, DG, LPG, HCO, plastic and coke, respectively.

Chapter 3

PS/VGO HYDROCRACKING

This Chapter gets a first approach to the non-olefinic plastics and vacuum gasoil blends hydrocracking. The characterization of the PtPd/HY catalyst used here is detailed, as well as the deactivation mechanisms involved in the process that are used in the last Chapter to explain the kinetic model development. In this context, the study of the influence of the operating conditions on the hydrocracking performance has been carried out with the final goal of obtaining high yields of fuel-like streams, i.e. naphtha and middle distillates. The effect of temperature, time and pressure is assessed on product distribution, liquid composition and plastic conversion. The results obtained in this Chapter formulate the optimal operating framework as well as the possibilities of regenerating the catalyst to contribute to a more sustainable process while valorising plastic wastes. Part of the results in this Chapter have been published in *Fuel Process. Technol.* **2021**, 224, 107010.

3.1. CATALYST CHARACTERIZATION

The properties of the catalyst used for the reactions have been determined according to the procedures described in Section 2.2.2. Nitrogen isotherm as well as the ammonia TPD are collected in Figure 3.1. Moreover, the textural properties of the catalyst properties can be found in Table 3.1. Figure 3.1a shows a type IV isotherm with a characteristic hysteresis loop (H3-type), which corroborates the presence of a well-developed mesoporous structure along with slit-shaped (and usually narrow) pores according to the IUPAC [244]. This structure is reflected in the high capacity of nitrogen adsorption (178 cm^3 g^{-1}) at low relative pressures, as well as the high surface of the catalyst and the average pore diameter.

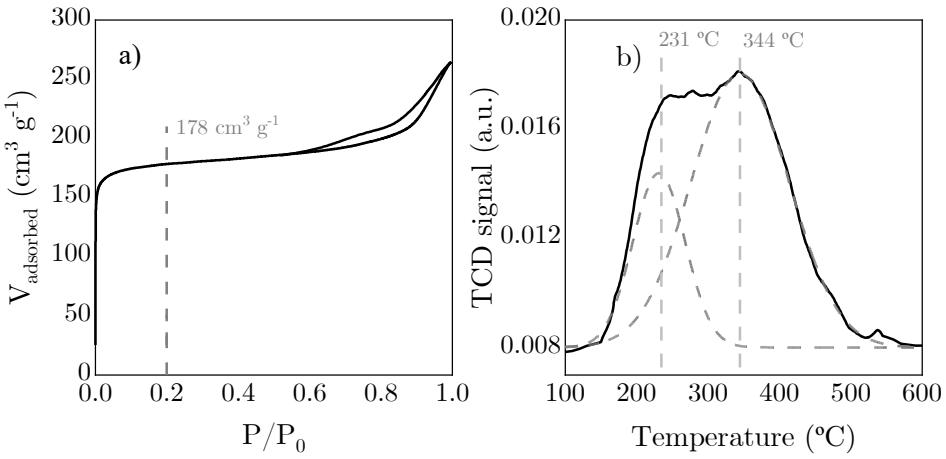

Figure 3.1. a) N_2 adsorption-desorption isotherms and b) NH_3 TPD of the PtPd/Y catalyst.

Concerning the acidic properties, the TCD signal of the catalyst (Figure 3.1b) shows a bimodal distribution that represents two different types of acid sites (100-300 °C region associated with weak acid sites and 300-500 °C region attributed to strong acid sites [245]) and total acidity of 0.465 mmol NH_3 g^{-1}, a remarkable value related to the support. The ratio between the area of the first and second peaks resulting from the signal deconvolution indicates that there is a higher amount of strong acid sites. Apart from that, the pyridine adsorption

FTIR spectrum is collected in Figure 3.2a. Following the procedure previously explained (Section 2.2.3), the determination of the B:L sites ratio has been carried out, finding a value very close to the unity, as can be seen in Table 3.1.

Table 3.1. Properties of the PtPd/Y catalyst.

Textural properties	
S_{BET} ($m^2\,g^{-1}$)	548
$S_{micropores}$ ($m^2\,g^{-1}$)	368
$V_{micropores}$ (mL g^{-1})	0.163
D_{pore} (nm)	7.9
Acidic properties	
total acidity (mmol NH_3 g^{-1})	0.465
B/L ratio	0.98
Metallic properties	
Pt content (wt%)	0.44
Pd content (wt%)	0.50
dispersion (%)	47.8

In Figure 3.2b, the spectrum from the CO adsorption FTIR analysis is collected, resulting in a higher concentration of Pt linear bonds (68.4 %) at 2075 cm^{-1} and the remaining one corresponding to multibonded Pd atoms (found at 1982 cm^{-1}). Figure 3.2b also shows a signal corresponding to the 1650 cm^{-1} wavelength that is usually attributed to interactions between the adsorbed gas and the support [246]. The importance of the Pt arrangement lies on the direct relationship between the ratio of bridging/linear bonds and the size of the particles, which can explain not only their dispersion but also their activity [247].

Last, the XRD pattern of the catalyst is collected in Figure 3.3. The characteristic peaks of the zeolite are easily noticeable [248], as it is the main composing material. In the same way, the alumina diffraction peaks can be observed in the regions between 45-50 ° and 65-70 ° [249], as well as the broad shift on the baseline comprehended between 15 and 35 ° can be attributed to the SiO_2 of the material [250]. Moreover, noble metals' signal can be attributed to the peak observed at

40 °, although their dispersion and low concentration can hinder their detection [251].

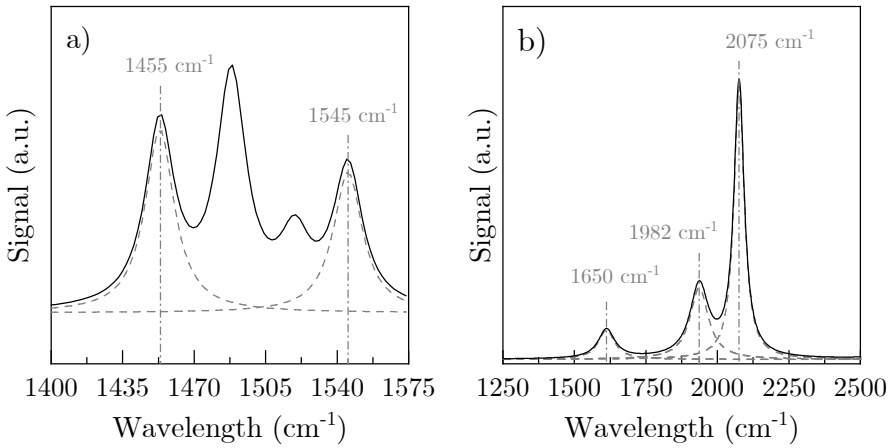

Figure 3.2. a) Pyridine adsorption FTIR spectrum and b) CO adsorption FTIR spectrum of the PtPd/Y catalyst.

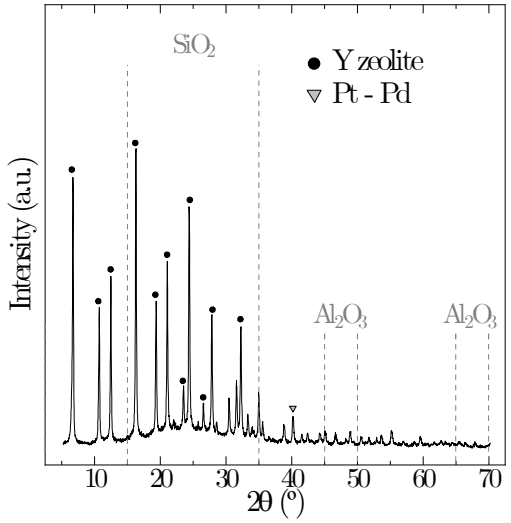

Figure 3.3. X-ray diffraction pattern of the PtPd/Y catalyst.

3.2. YIELDS DISTRIBUTION

PS/VGO hydrocracking reactions have been carried out in a 50 mL batch reactor unit (described in Section 2.3.2.1) using the PtPd/Y catalyst under the following conditions:

- Feedstock: PS (10 wt%) blended with VGO
- Temperature: 380-420 °C
- Pressure: 50-110 bar
- Reaction time: 30-300 min
- Catalyst-to-feed ratio (mass basis): 0.1
- Stirring speed: 1300 rpm

To properly evaluate the feasibility of hydrocracking of plastic/VGO blends, the performance of the different lumps established must be studied, as well as the influence of each property on their evolution. Thus, the objectives are to maximise the formation of lumps of commercial interest (i.e. naphtha and LCO) as well as HCO and PS conversion and minimise if possible the formation of low-value-added products such as gases.

3.2.1. Effect of temperature and time

Figure 3.4 displays the effect of temperature and reaction time on the product yields distribution obtained in the hydrocracking of the PS/VGO blend at 80 bar. Note that lines describe the trends followed by the experimental points. Firstly focusing on the results obtained at 380 °C, the major fraction in the feed, i.e. HCO, decreases from an initial 88.4 wt% to a 62.3 wt% at 30 min and then to a 60.4 wt% at 60 min. From that time, the catalyst activity is inhibited and the conversion of this lump is stopped, at the same time that other lumps' formation also ends. Specifically, LCO and naphtha yields, which show their intermediate nature in these systems, increase during the first hour from values close to 1 wt% to 9.6 and 18.1 wt%, respectively. With respect to the gaseous fractions, their content is very limited and only a 5.0 wt% of LPG is appreciated.

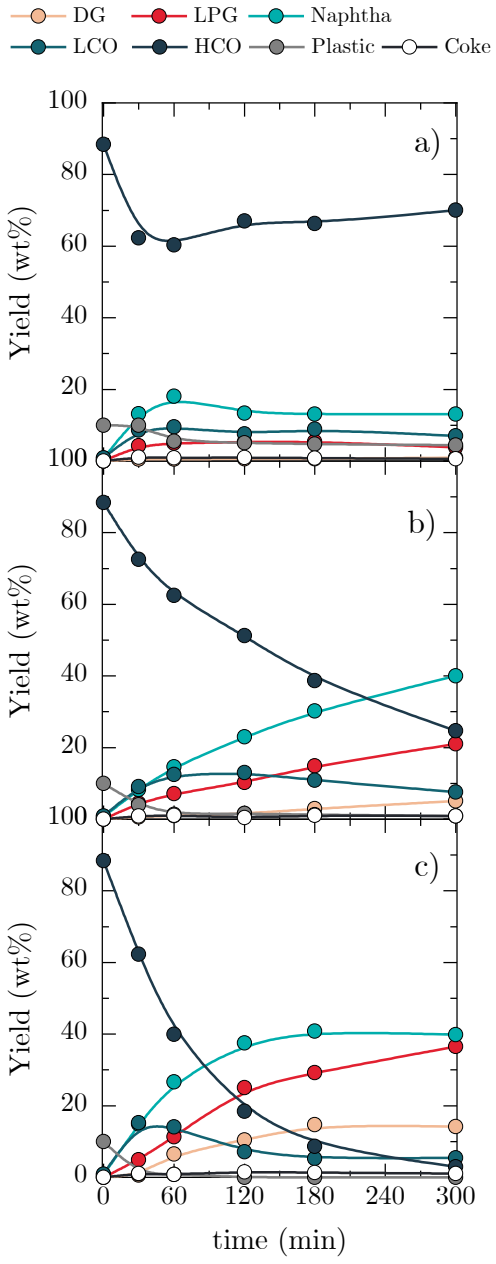

Figure 3.4. Evolution with reaction time of the yields of the products resulting from the PS/VGO hydrocracking at a) 380, b) 400 and c) 420 °C.

Also, a certain degree of condensation from the naphtha and LCO lumps can be observed at 380 °C, as the HCO yield achieves a final value of a 70.0 wt% at 300 min, while the yield of the aforementioned lumps decreases due to the inhibition of the catalytic activity. Similarly, PS decreases from the initial 10.0 wt% to a 5.6 wt% at 60 min and then the decrease of this feed is practically non-existent. This means that plastic conversion at this temperature does not overcome 55 wt% at 300 min.

On the other hand, the results observed at 400 and 420 °C show a very different behaviour as this activity decays within the first 60 min of reaction is not observed, and the conversion of both HCO and PS continues along the reactions. This way, the HCO lump at 400 °C goes down to 24.7 wt% at 300 min, with final contents of naphtha and LCO of 40.0 and 7.6 wt%. This focus on naphtha increasing and the limited content of LCO confirms the intermediate nature of this lump, which is immediately converted into lighter products and goes through a maximum at 120 min (13.0 wt%). In the same way, at 400 °C gas formation becomes significant, producing 5.1 wt% of DG and 21.0 wt% of LPG in the longest reaction. Alongside, at this temperature, the conversion of PS is not limited and from 60 min forward the yield of the unconverted PS is very close to 1 wt%.

The increase of temperature up to 420 °C favours the hydrocracking reactions extent in a way that the HCO lump yield reaches 3.0 wt% at 300 min, which represents a conversion of 98.5 %. However, as the temperature increase has a major effect on cracking reactions, the naphtha and LCO yields are limited to values similar to those obtained at 400 °C (39.8 and 5.5 wt%, respectively), at the expense of higher gas formation, with final DG and LPG yields of 14.2 and 36.5 wt%, respectively. Also, the conversion of PS is boosted such that at 30 min unconverted PS yield is already close to zero.

As a result of this, it can be established that a temperature of 380 °C is not high enough to totally convert the PS. This hinders the conversion of the heavy molecules of HCO due to the deposition of the partially degraded PS molecules over the surface of the catalyst, avoiding the contact between the other reactants and the active sites. Bin Jumah et al. proposed a mechanism of PS hydrocracking

[252] consisting of three stages for its conversion into ethylbenzene: (i) the initiation stage in which polymeric chains are broken into smaller chains on the acid sites of the zeolite and formed olefins are hydrogenated on the Pt and Pd particles; (ii) the propagation of the hydrocracking reactions that form oligomers and monomers; and (iii) the hydrogenation stage that leads to the formation of ethylbenzene. The high content of hydrogen within the reactor acts as a stabilizing agent for PS, as it inhibits the chain unzipping responsible for the depolymerization of PS that expels styrene monomers [253].

Thus, the explanation for the activity decay observed at 380 °C (Figure 3.4a) lies on the incapacity of the catalyst at that temperature for promoting the second stage of the PS hydrocracking mechanism, as the initial conversion of this material confirms that the initiation stage has indeed taken place. On the contrary, the high conversion levels found at 400 and 420 °C reflect the progress of this mechanism towards the second and even the third stage due to the hydrogen excess that promotes an easy hydrogenation, favoured by the presence of the noble metals of the catalyst.

3.2.2. Effect of pressure

As an additional parameter of study, the effect of pressure on hydrocracking reactions has been also studied. The experiments (Figure 3.5) have been carried out under pre-set conditions of 120 min and 420 °C, as the corresponding reaction shows a good catalyst performance (Figure 3.4c) in terms of naphtha and LCO yield and plastic conversion. A hydrogen pressure increase seems to entail a direct reduction of the formation of gases, even when the conversion of the HCO lump is similar. The composition of the liquid fraction obtained from the simulated distillation manifests only a ± 5 wt% difference in the HCO content, so the differences observed in Figure 3.5 can be attributed to the lesser extent of DG and, especially, LPG formation. This major influence of hydrogen pressure on the vaporization of heavy feeds has already been observed [254], reporting that the higher hydrogen pressure implies a gas-liquid equilibrium displacement in favour of the liquid, as it takes less space.

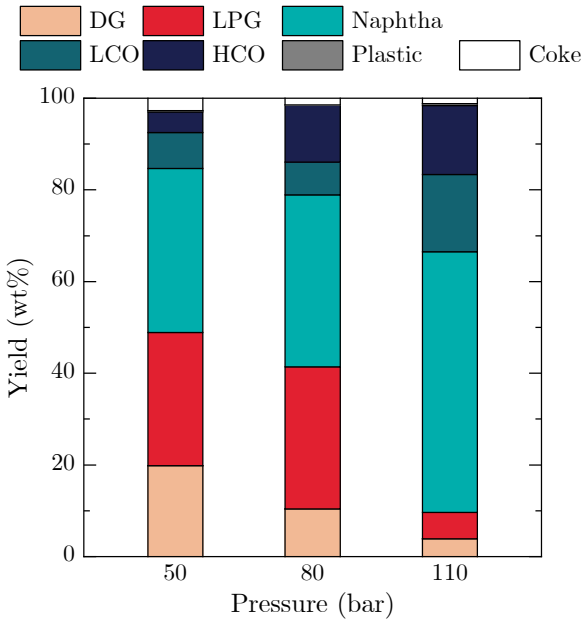

Figure 3.5. Effect of hydrogen pressure on products yield distribution of the PS/VGO hydrocracking at 120 min and 420 °C.

Concerning the formation of lumps of interest, it can be seen that even with not too different yields of HCO (from 4.5 wt% at 50 bar to 15.0 wt% at 110 bar), both yields of naphtha and LCO escalate up to values of 56.9 and 16.9 wt%, respectively. This, along with the decrease in gas yields, can be explained through the promotion of hydrocracking mechanisms over thermal cracking ones, as the presence of hydrogen attenuates the formation of free radicals. Plastic yields have residual values (lower than 0.5 wt%) whose evolution cannot be attributed to the real effect of pressure on plastic conversion but to insignificant experimental differences within the context of full conversion aforementioned for the reference reaction. Finally, it must be noticed that the hydrogen pressure has a clear effect on coke deposition, as its yield decreases along the pressure increase from a 2.7 wt% to 1.2 wt% at 110 bar. The reduction of the deposited coke amount is a direct consequence of the lessening of the coke precursor formation derived from the hydrogen pressure increase [255].

3.3. LIQUID COMPOSITION

The production of fuel-like streams is subject to the suitability of these fractions to be blended into motor fuel blends commonly found in refineries, so careful compositional analysis is necessary to determine the effect of operating conditions on liquid properties. As naphtha and LCO have been set as preferred products, their individual composition for the PS/VGO hydrocracking products has been determined and analysed in this Section.

3.3.1. Effect of temperature and time

Figure 3.6 collects the evolution of naphtha composition over reaction time at different temperatures. As the naphtha fraction contains only compounds with a boiling point below 216 °C, aromatics of three or more rings do not belong to this fraction and therefore have not been considered. It can be observed that the influence of temperature on chemical composition is strong, although the effect of this parameter affects each group differently. Accordingly, the concentration of isoparaffins, naphthenes and monoaromatics seem to be greatly influenced by increasing temperature and time course, while normal paraffins and diaromatics are not so much affected.

The results obtained at 380 °C (Figure 3.6a) are appreciably conducted by the aforementioned PS fouling mechanism (Figure 3.4a). Thus, the usual hydrocracking mechanisms that would lead to the hydrogenation of aromatics in favour of naphthenes and paraffinic compounds [145, 147] are inhibited, observing steady values of these families up to 120 min. Then, once the catalytic activity has been fully inhibited, monoaromatics concentration increases in the same quantity that naphthenes and isoparaffins decrease, which leads to conclude that hydrogen-transfer reactions have been suppressed and dehydrogenation reactions are promoted instead. Furthermore, hydrogen-transfer reactions are commonly followed by the construction of scaffolds that lead to the formation of cyclic molecules [256], so the boost of the opposite reactions explains not only the formation of monoaromatics from naphthenes but also the cyclization of isoparaffins.

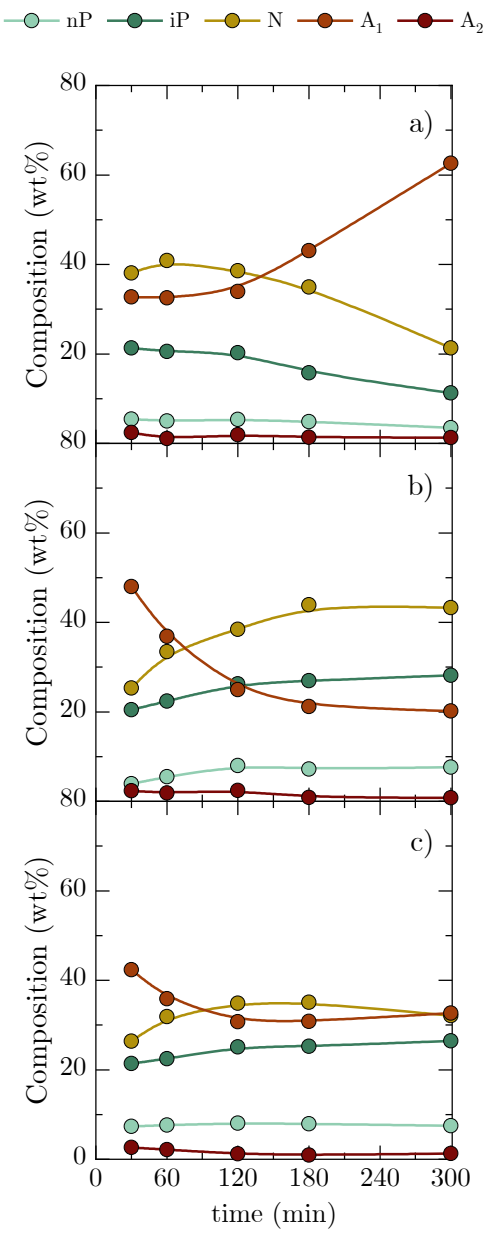

Figure 3.6. Evolution over time of the naphtha composition obtained in the hydrocracking of PS/VGO blends at a) 380, b) 400 and c) 420 °C.

This mechanism can be explained through the hydrogen-donor nature of alkyl groups of isoparaffins, especially methyl groups, in hydrogen-transfer reactions,

in which the formed carbocations act as hydrogen acceptors [257]. Consequently, the resulting carbonium ion from the isoparaffins will undergo the cyclization reaction mentioned before, increasing the content of naphthenes that will be subsequently transformed into monoaromatics. Apart from that, hydrogen-transfer reactions are not only induced under a surplus of hydrogen but also take place in absence of it, as may be the case, as polystyrene is continuously being converted from 60 min onwards. These elementary reactions are promoted for example at high temperatures in other processes such as catalytic cracking [258], thereby taking place on the acid sites of the support once the degraded PS molecules have covered the metallic sites of the catalyst surface.

On the other hand, the trends displayed at 400 and 420 °C (Figure 3.6b and 3.6c, respectively) for the reacting families are the opposite of those observed at 380 °C. Essentially, monoaromatics concentration decreases in favour of an increase of isoparaffins and naphthenes. Temperature is the controlling parameter in these reactions, as the maximum hydrodearomatization is achieved at 400 °C, as monoaromatics concentration reaches a minimum at this temperature and 300 min (20.2 wt%). At that same reaction time, the content of 1-ring aromatics at 420 °C is 32.3 wt%. Concurrently, a maximum of 43.3 wt% of naphthenes concentration has been obtained at 400 °C against the 32.1 wt% produced at 420 °C. This effect of temperature on the composition is directly related to the thermodynamic limit of monoaromatics hydrogenation to naphthenes, as the equilibrium of this reaction has its critical point at ca. 380 °C which shifts towards dehydrogenation reactions once has been overpassed [259]. With respect to isoparaffins, the effect of temperature at 400 and 420 °C is almost negligible, as final contents are almost identical (28.2 wt% at 400 °C and 26.5 wt% at 420 °C). The decrease observed by rising the temperature is coherent with the promotion of cracking reactions that take isoparaffins as reactants for the formation of smaller molecules that belong to DG and LPG lumps [260].

LCO composition has been also analysed, as displayed in Figure 3.7. In this case, a higher number of chemical families have been affected by both temperature and reaction time, as normal paraffins do not show a stationary behaviour at 400 and

420 °C. However, the activity decay phenomenon observed at 380 °C is also reflected in this fraction. This way, monoaromatics concentration has the maximum value at this temperature (as well as the concentration of total aromatics) and it goes to a minimum at 180 min. The fact that the PS molecules hinder the contact between the reactants and the catalyst active sites is reaffirmed at this point. The higher initial amount of aromatics occurs due to the low catalytic activity as a result of the difficult access that HCO and hydrogen (liquid and gaseous) would have due to the deposition of PS molecules (solid) in the medium (diffusional problems) [143]. In addition, both isoparaffins and naphthenes concentrations show exactly the opposite trend, passing through a maximum at 180 min and then decreasing. In a similar way that dehydrogenation mechanisms have been explained before, the hydrogenation activity is therefore suppressed. Hence, the reactions that take place in the acidic sites of the catalyst are the controlling mechanisms from 180 min onwards.

Regarding the results obtained at 400 and 420 °C (Figure 3.7b and 3.7c, respectively), the trends followed by the different families of compounds have been maintained over time. As shown, both normal and branched paraffins raise with reaction time while the concentrations of naphthenes and aromatics diminish. Attending to each group of aromatics, first, it must be noticed that the total concentration of aromatics only increases by a 3.8 wt% from 400 to 420 °C. The distribution among the aromatic compounds is illustrative of the aforementioned thermodynamic equilibrium in hydrogenation reactions, as it can be observed that there is a higher 1-ring aromatics and lower 2-ring aromatics concentration, which is explained through the consecutive hydrogenation mechanism of polyaromatics. These reactions begin with the easy hydrogenation of polyaromatics present in the HCO fraction, producing di- and poly-aromatics corresponding to the LCO fraction, which go then under further hydrocracking reactions until they turn into monoaromatics (known for being more refractory [261]) and naphthenes [262].

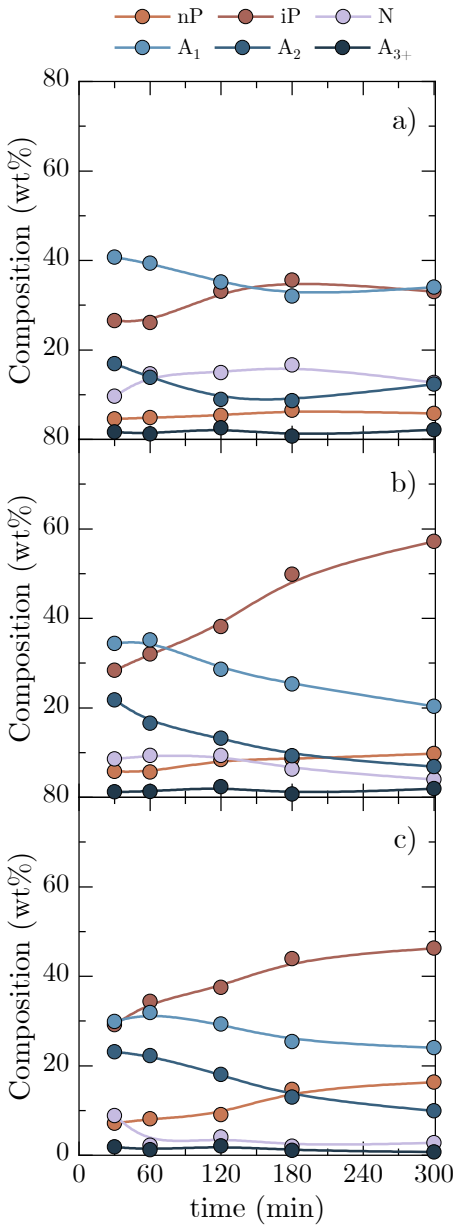

Figure 3.7. Evolution of LCO composition over reaction time obtained in the PS/VGO hydrocracking at a) 380, b) 400 and c) 420 °C.

Focusing on aliphatic compounds, a strong impact of temperature can also be observed on their concentrations. This way, at 420 °C the higher content of

n-paraffins results as a direct consequence of the higher development of cracking reactions that break both isoparaffins and naphthenes, promoted by the temperature increase. However, the major concentration of isoparaffins and naphthenes observed at 400 °C implies a change in the ongoing mechanisms, as hydroisomerization/hydrocracking reactions have a dominant role at this temperature [263].

Lastly, research octane number (RON) and cetane index (CI) have been also calculated to complement the understanding of the time and temperature effect on the quality of the naphtha and LCO fractions, displaying these results in Figure 3.8. Note that the values corresponding to 380 °C reactions (Figure 3.8a) do not follow any trend as a consequence of the activity decay due to PS fouling and the changes observed in the liquid composition that have been discussed above. Apart from that, RON values obtained at 400 and 420 °C (within the 91.9-104.3 range) allow establishing that the naphtha obtained is adequate for being used as a blending component of commercial gasoline. Also, the effect of temperature on this index is subtle, as it is quite similar for both temperatures, although there is a slight decrease in RON with increasing temperature due to the effect of temperature on cracking reactions. With respect to CI, the values obtained at both 400 and 420 °C are also attractive for the inclusion of the fraction obtained here into the refineries blending pools. The trends show opposite directions along the time at the different temperatures, observing an increase of this index at 400 °C and a clear decrease at 420 °C. Although the decrease in isoparaffins should improve the value of the index, the distribution of this compositional change is equally divided into normal paraffins and aromatics when comparing 400 and 420 °C samples at 300 min. The contribution difference between branched and normal paraffins is quite lower than the CI loss produced by the increase in aromatics [264], thus explaining these contradictory trends. Considering all the above, and even if the values of the samples are generally below commercial standards, the quality of the streams obtained is considered good enough to be added to the blending pools.

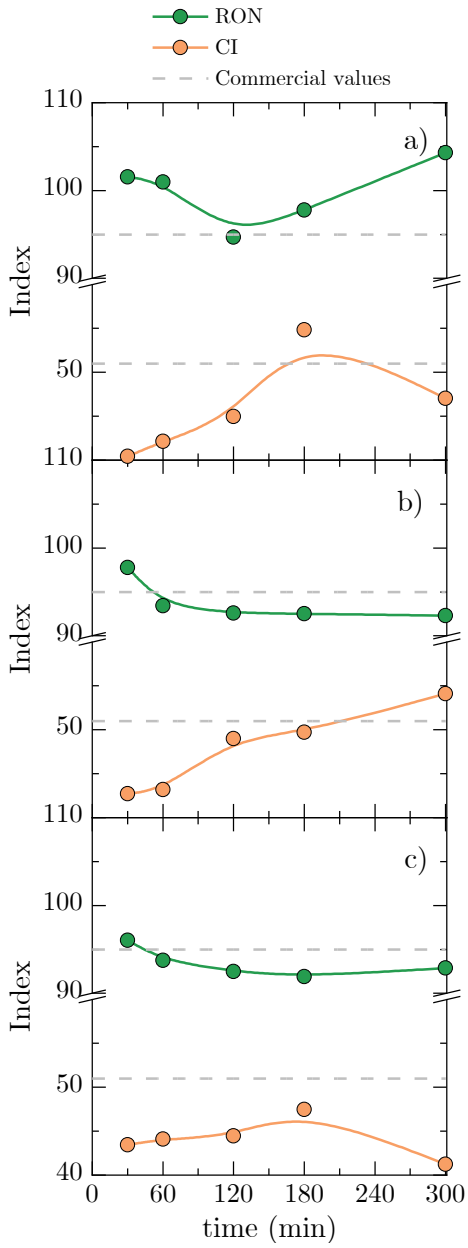

Figure 3.8. Evolution of RON and CI of the products resulting from the PS/VGO hydrocracking at a) 380, b) 400 and c) 420 °C.

3.3.2. Effect of pressure

Figure 3.9 displays the naphtha composition change along the studied hydrogen pressure values. Under 50 bar, aromatics account for up to 45.3 wt% of the naphtha, being reduced to 32 wt% by increasing the pressure up to 80 bar, while the further increase to 110 bar only reduces the total aromatic content by an additional 2.4 wt% (29.6 wt%). In all cases, the hydrogenation of aromatics produces an increase in naphthenes content (from 22.7 wt% at 50 bar to 34.9 and 39.7 wt% at 80 and 110 bar, respectively), as expected based on the typical ring-opening mechanism [265].

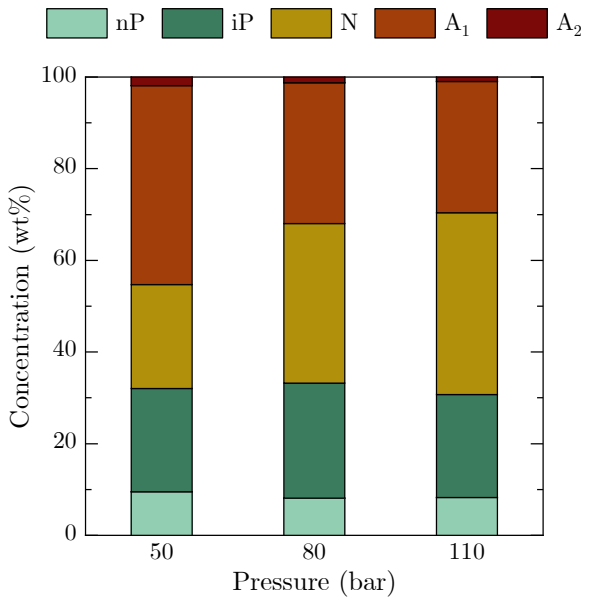

Figure 3.9. Effect of hydrogen pressure on naphtha composition of PS/VGO hydrocracking products at 420 °C.

On the other hand, even though there is a visible decrease in normal paraffins when increasing pressure, this change is limited to 1.3 wt%. Meanwhile, the isoparaffins do not follow a clear trend, their content being between 22.5 wt% and 25.1 wt%. Condensation of the small compounds that are formed (discussed in Section 3.2.2) may be responsible for this limitation in the capacity of hydrogen

pressure to promote hydrocracking reactions. This way, the cyclization of paraffins would increase the number of naphthenes present in the medium and not only those produced by the hydrogenation aromatics, whose thermodynamic equilibrium would be affected by this alternative formation of saturated cyclic compounds.

As well as naphtha composition, LCO composition has also been studied and the results are shown in Figure 3.10.

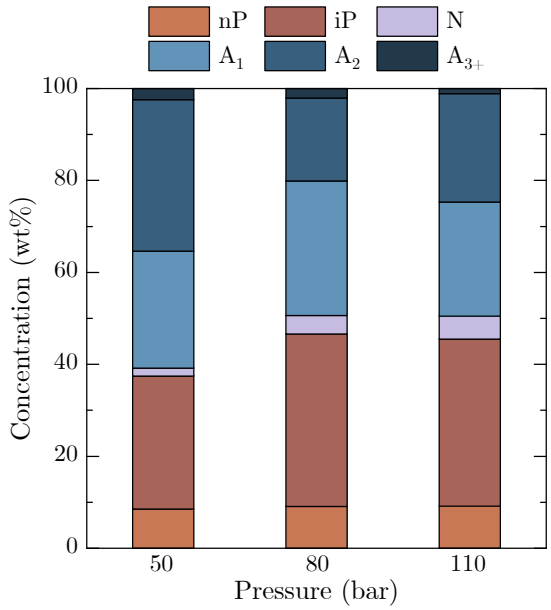

Figure 3.10. Effect of hydrogen pressure on the LCO composition of PS/VGO products obtained at 420 °C.

The same effect of hydrogenation of aromatics when increasing pressure from 50 bar to 80 bar is observed here, obtaining a reduction of total aromatics of 11.4 wt%. However, there is a stagnation when increasing pressure up to 110 bar, which is probably a result of the further hydrogenation of the most refractory polyaromatic structures found on the heaviest fraction, which now are being hydrogenated into LCO compounds. This can be related to the behaviour also observed in naphtha composition (Figure 3.9), since the mechanism of cascade

hydrogenation of polyaromatics (and posterior hydrocracking) would explain the increase in saturated species while producing a similar concentration of monoaromatics. In fact, LCO composition shows a higher amount of diaromatics but also of naphthenes that can be the straight result of those polyaromatics hydrogenation.

With respect to paraffins belonging to the LCO fraction, a similar effect to that observed on naphtha composition is noticed when attending to normal paraffins, with a slight effect of pressure on their concentration (whose change is less than 1 wt%). However, there is a noticeable boost in isoparaffins when increasing pressure from 50 to 80 bar, which is consistent with the ring-opening mechanism as final products resulting from the hydrocracking of aromatics in the absence of a catalyst with high selectivity towards normal paraffins [266].

3.4. CATALYST DEACTIVATION

Catalyst deactivation is a crucial issue nowadays in industry, as the activity decay in catalytic processes requires compensation that usually proceeds by a temperature increase or other alternative that shortens the service life of the catalyst. In hydroprocessing, one typical approach to characterize the catalyst deactivation is based on the determination of the coke and metals deposited on it [200]. However, the introduction of new materials in hydroprocessing units can change the scenario, as the deactivation strongly depends on the properties of the feeds, operating conditions and even the structure of catalysts. In this Section, a diligent characterization of the spent catalysts has been carried out to enhance the knowledge of the catalyst.

3.4.1. Coke characterization

Coke deposition is the main cause of catalyst deactivation related to hydrocracking processes and, consequently, there is extensive literature delving into the issue [267, 268]. However, as the hydrocracking of plastics and refinery streams blends has been studied far less [269], the deposited coke characterization of these systems needs to be performed by the combination of different and complementary techniques.

Table 3.2 collects the amounts of coke deposited (per 100 g of catalyst) in the catalyst at different temperatures over the reaction time. Catalysts of short reactions do not show a clear trend, probably as a consequence of the plastic deposition over the catalyst that enlarges the amount of carbonaceous material that can be oxidized during TPO analyses. Otherwise, the effect of time and temperature can be summarized in two statements: (i) for long reactions, the effect of temperature is that of promoting the deposition and development of polyaromatics inside the support of a bifunctional catalyst [270]; and (ii) the high hydrogen pressure and catalytic activity can compensate the formation of carbonaceous deposits by enhancing the hydrocracking reactions of coke precursors, as observed during the hydrodeoxygenation of bio-oil [271], which results in the initial deposition of higher amounts that are gradually converted

over time, thus explaining the lower contents observed at 180 and 300 min compared with the preceding ones.

Table 3.2. Coke content (wt%) deposited on the spent catalysts used in PS/VGO hydrocracking.

	30 min	60 min	120 min	180 min	300 min
380 °C	10.6	9.2	9.6	8.4	6.2
400 °C	8.7	10.6	4.5	11	9.1
420 °C	10.4	8.3	14.9	13.7	10.9

The methodology followed to carry out the TPO analyses allows not only to measure the quantity of the deposited coke but also to distinguish between the amount of coke deposited on the external and the internal parts of the catalyst, as exposed in Figure 3.11 for one of the samples.

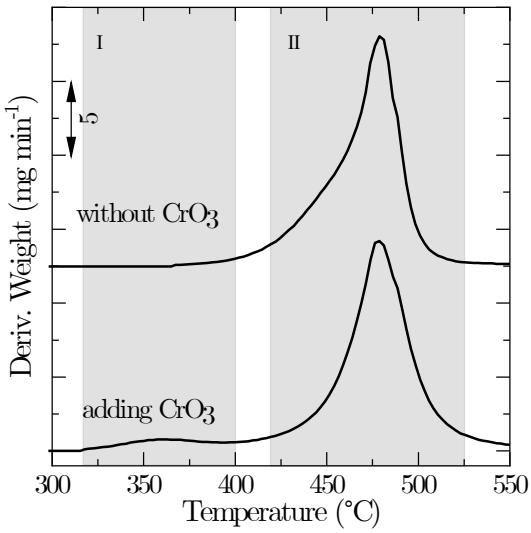

Figure 3.11. TPO profiles of the sample obtained at 420 °C and 300 min with and without the chromium addition.

The addition of chromium (see Section 2.4.4) is proven effective to perform an actual deconvolution of the peaks integrated at close temperatures by catalysing

the combustion of the external coke. In this context, Figure 3.12 displays the evolution over time of the internal and external coke at different temperatures.

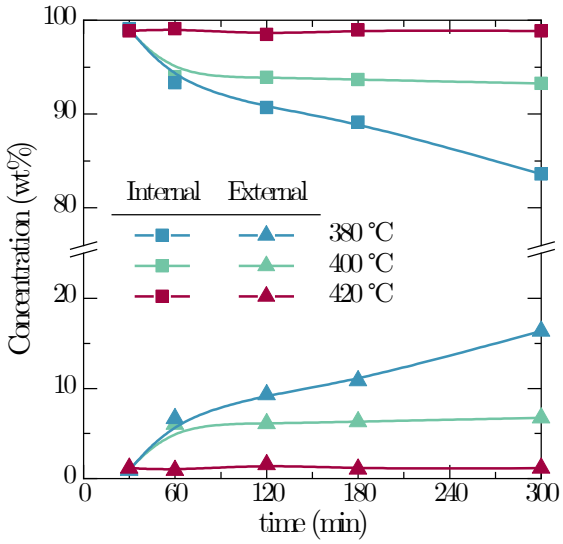

Figure 3.12. Evolution over reaction time of the internal and external coke obtained in the hydrocracking of the PS/VGO blend at the studied temperatures.

Independently of the temperature, internal coke is the predominant type of carbonaceous deposit. However, there are clear trends in the evolution of coke according to the effect of temperature and reaction time. Thus, the temperature rise is reflected by a consequent increase in the relative amount of internal coke. This, along with the general increase of coke deposited in the catalysts aforementioned, is attributed to the coking reactions that take place in the acid sites of the zeolites and are promoted at higher temperatures [272]. The formation of internal coke is the result of the condensation into PAHs of small aromatic molecules [177] that can be found in the liquid products obtained at 420 °C (Figure 3.6c and 3.7c), which present a high concentration of monoaromatics.

With respect to the influence of reaction time on the evolution of the two types of coke, the trend followed by samples obtained at 400 and 420 °C is identical, achieving steady values after one hour because of the equilibrium between the condensation and hydrogenation forces that are involved into the coke formation

mechanisms, thus remaining constant for the 300 min. On the contrary, the samples obtained at 380 °C show a growing deposition of external coke. This observation is linked to the phenomenon of PS molecules deposition that has been already explained, as their behaviour and the one attributed to asphaltenes are very similar in terms of being somehow composed of high molecular weight alkyl-bridged aromatic and cycloalkyl groups [273]. As stated before, the catalyst is not capable of converting the chains of PS, whose degraded molecules end up being insoluble within the liquid products [274]. The sedimentation of these molecules is the PS fouling phenomenon described in Section 3.2, causing the corresponding activity decay. Moreover, there is a possible chemical pathway in which these molecules undergo several chemical transformations and form aggregates via Van der Waals interactions, leading to the formation of species that can be classified as coke [275]. PS aggregates and the deposited compounds defined as coke have not entered the channels of the zeolite and therefore they are later recovered as external coke when dissolved in THF, in which PS is indeed highly soluble.

The nature of the deposited coke has been studied through FTIR analysis and the spectra are displayed in Figure 3.13. Although the spectra have been collected for the complete spectral range (550-4000 cm^{-1}), only the regions with distinguishable signals are shown on the graphs, according to the aliphatic and aromatic vibration regions. Based on that, the structures that can be observed on the deposited coke correspond to bulky aromatics and branched alkanes [276]. More specifically, the following regions have been established according to the literature [271, 277]: (i) 3000-2800 cm^{-1}, attributed to the aliphatic C-H stretching, with two maxima at ca. 2856 and 2925 cm^{-1}, which correspond to symmetric and asymmetric stretching, respectively; (ii) 2000-1650 cm^{-1}, related to aromatic C-H stretching; (iii) 1650-1600 cm^{-1}, corresponding to olefinic C=C stretching; and (iv) 1600-1550 cm^{-1}, which is attributed to aromatic C=C ring breathing and usually has a maximum around at 1585 cm^{-1}.

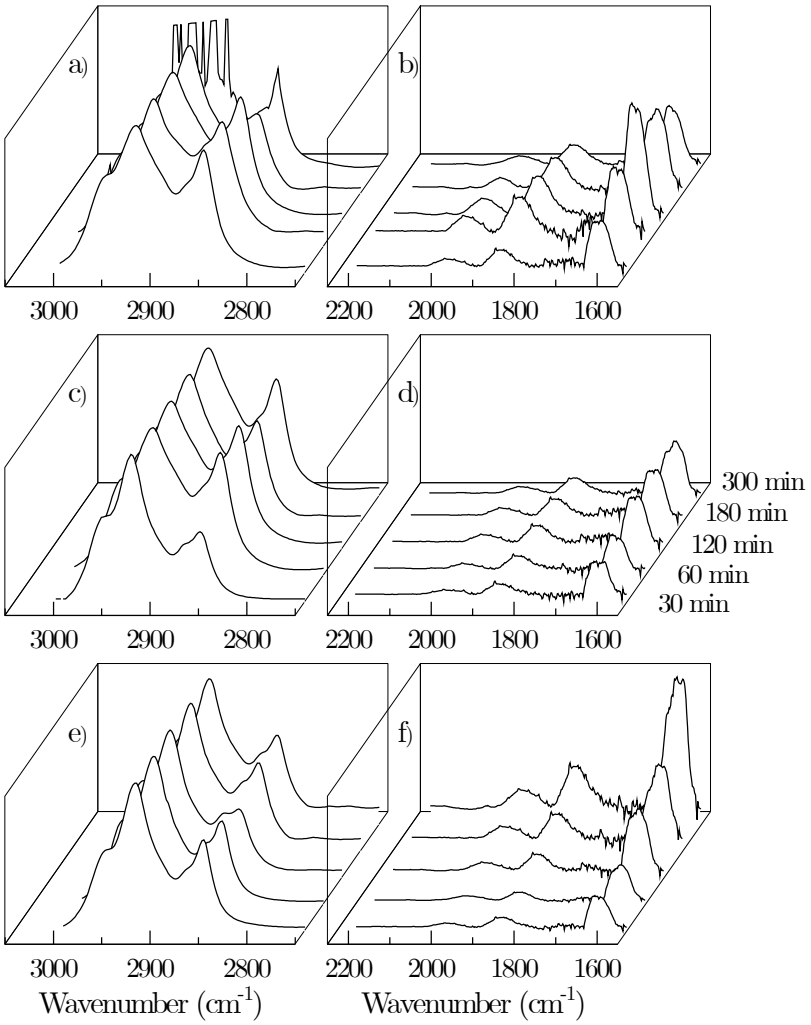

Figure 3.13. FTIR analysis evolution in (a, c and e) the aliphatic and (b, d and f) aromatic regions of the coke obtained at (a and b) 380 °C, (c and d) 400 °C and (e and f) 420 °C in the hydrocracking of PS/VGO blends.

Considering the aforementioned, it can be deduced that the main species in the coke deposited on the catalyst in all the cases are mainly aliphatic, since the intensity of the signals belonging to this region is noticeably higher for all the samples. However, an increase in temperature results in a progressive decrease in the aliphatic band. Moreover, the distribution of this region is different depending

on the reaction temperature. This way, at 380 °C, an increase in the asymmetric stretching band can be observed, even saturating the detector at 300 min (Figure 3.13a). However, these signals are reduced at 400 °C (Figure 3.13c), obtaining that the symmetric stretching band increases up to 60 min and remains constant for the rest of the time, while the asymmetric band is virtually constant for all the samples. A very similar behaviour is observed in the aliphatic region for the samples collected at 420 °C (Figure 13e), although the general intensity of the signals is lower than the previous ones, especially in the case of the symmetric band.

On the other hand, a strong influence on the temperature and reaction time can be extracted from the aromatic vibration bands. At 380 °C (Figure 3.13b), the samples go through a maximum of intensity 120 min, so a clear trend cannot be established. Despite that, a general increase in aromatic regions can be appreciated, along with an increase in the olefinic C=C stretching signal. At this temperature, the effect of the PS degraded chains on the changeable coke nature is exposed, as it has been already commented that the partially converted plastic molecules change their chemical composition over time and, therefore, so do the carbonaceous deposits [278]. At 400 °C (Figure 3.13d), the intensity of the aromatic band is constant along the reaction time, as a consequence of the equilibrium between the hydrogenation and condensation reactions, as commented before. If the temperature is increased up to 420 °C (Figure 3.13c), there is an obvious effect of the dehydrogenation mechanism that leads to the formation of more condensed structures and that takes place through hydride transfer and methylation of aromatics, which are promoted at high temperature and long reactions [279].

The results of the extraction and characterization of the soluble fraction of the deposited coke are displayed in Figure 3.14.

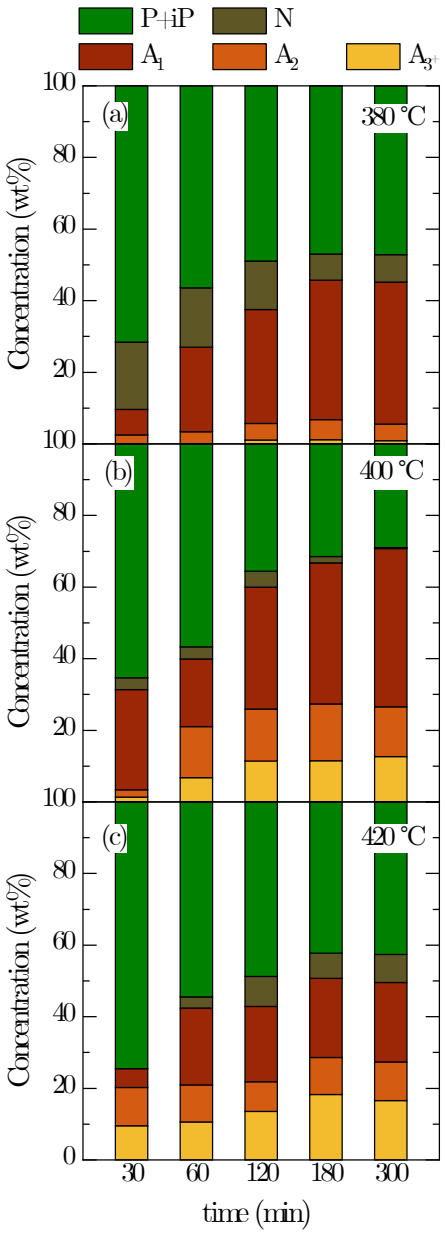

Figure 3.14. Evolution of the soluble coke composition of the PS/VGO hydrocracking spent catalysts obtained at a) 380, b) 400 and c) 420 °C.

Note that there is a strong dependency of the fraction of coke that can be extracted following the methodology used, as at 380 °C the weight fraction of this

soluble coke accounts up for a 70 wt% and it decreases down to a 28 wt% at 420 °C. The effect of time on the composition of soluble coke is evident and constant at all temperatures, as the species turn into more aromatic compounds, especially during the first 120 min. In the same way, and more noticeably at 400 and 420 °C, the aromatics species condensate into more complex compounds as reflected in the increasing amount of polyaromatics. This is in line with the conventional effect attributed to the temperature on condensation and cokization reactions, which are promoted when this parameter is risen [199].

Taking into account the above-mentioned condensation phenomenon, it is interesting the fact that aliphatics achieve a minimum concentration in the soluble coke at 400 °C, even more so considering that the concentration of heavy species and the weight of the insoluble coke is higher in the samples obtained at 420 °C. It is precisely for this reason that such a deviation in the trend is observed, as the insoluble fraction is usually composed of PAHs [280] and the concentration of these compounds is higher at 420 °C, while the aromatics representing the major fraction of the composition obtained at 400 °C are 1-ring compounds. Thus, the aromatic fraction of the coke is remaining at a higher degree in the insoluble coke, therefore offering the illusion that the coke obtained at 420 °C is less aromatic than that obtained at 400 °C.

3.4.2. Plastic covering and metals deposition

The coke deposited on the catalyst as well as the poisoning metals and the degraded PS that precipitates when not properly converted lead to the deterioration of the physicochemical properties of the catalyst. With the aim of illustrating a full picture of the deactivated catalysts and comprehending the reasons for the degradation of their properties, some additional methodologies have been applied to perform their full characterization.

SEM images of some of the spent catalysts are shown in Figure 3.15, which allow identifying the incidence of the different causes of deactivation. This way, Figure 3.15a reveals a smooth covering over the catalyst particles that, employing EDX analysis, is confirmed to be carbonaceous and different from other dark

particles found on the spent catalysts (coke). Because of this, it can be concluded that this material corresponds to the degraded PS that has been reported as the main deactivation agent in the reactions carried out at 380 °C. Furthermore, this covering has been not observed at the other studied temperatures, which is coherent with the different activity behaviour exhibited at 400 and 420 °C (Figure 3.15b and 3.15c).

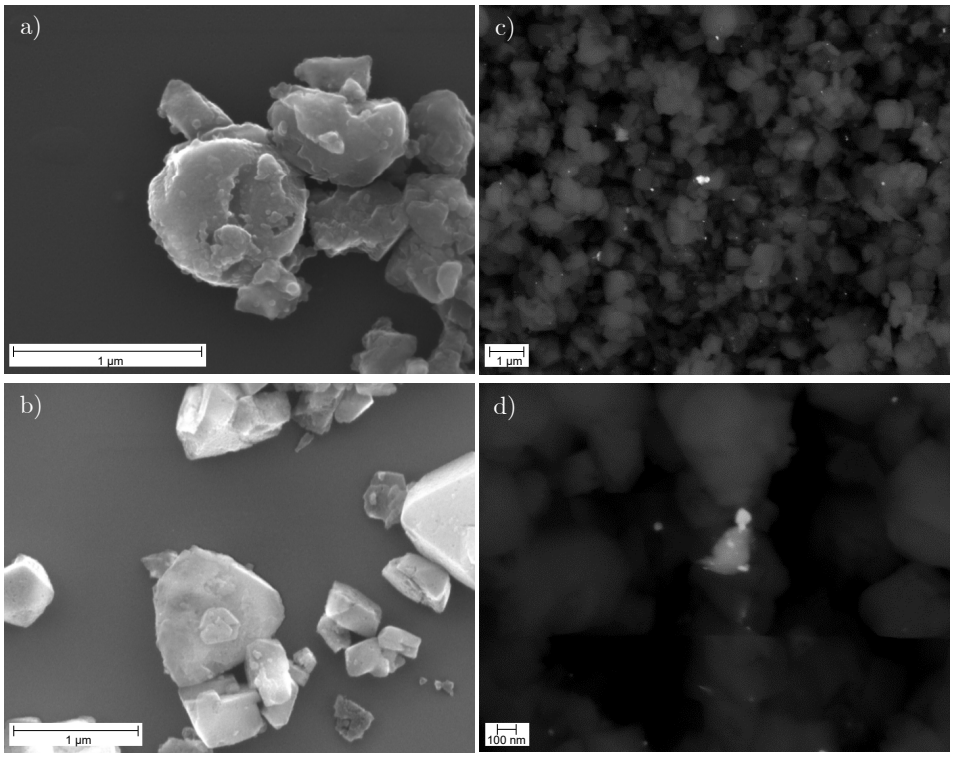

Figure 3.15. SEM images of the spent catalysts obtained at a) 380 °C, b) 400 °C, and c and d) 420 °C.

At 420 °C (Figure 3.15c and 3.15d), the deposition of poisoning metals is exposed, as it is a known phenomenon that takes place in the hydroprocessing of heavy streams [281]. By application of contrast, the particles showing higher bright levels in the images correspond to high molecular weight atoms, which stand out from others of lower molecular weights. The noble metals inherent to the catalyst have a moderate brightness and a very low particle size as the dispersion achieved

is high. However, there are some materials with a higher shine that, by means of EDX, have been assigned to Fe and Ni particles, which are usually found in VGOs [91]. Furthermore, these highly brilliant particles can constitute a sort of alloy whose formation is possible at high temperatures [282, 283], as manifested in Figure 3.15d. The formation of these alloys can noticeably affect the catalyst deactivation not only by pore blockage but also due to their deposition on the catalyst metals.

The existence of undesirable metals in the feed (and so in the spent catalysts, as seen in Figure 3.15) creates the necessity of monitoring them, as they can substantially affect both the catalytic activity and the condition of the equipment [166]. Figure 3.16 shows the metal loading evolution of the identified metals in the spent catalysts (Fe, Ni), that have been measured through ICP-AES, at the three studied temperatures.

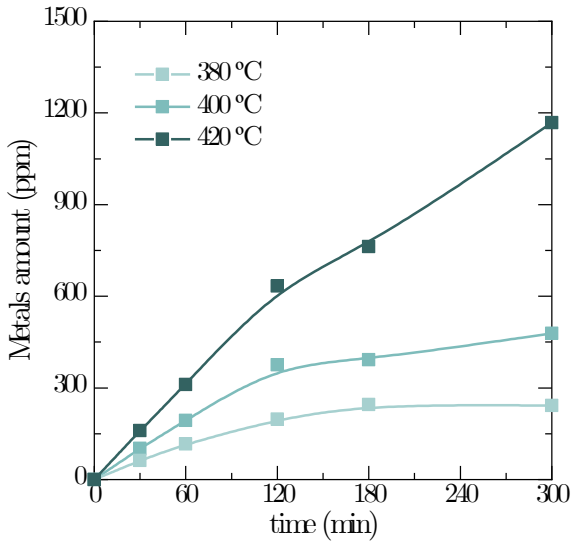

Figure 3.16. Evolution of deposited metals amount over time at the three studied temperatures on the spent catalysts of PS/VGO hydrocracking.

The trends show a boosting effect of temperature on the hydrodemetallization capacity of the catalyst [284], as the uptake of the catalyst increases at 400 and 420 °C. However, there are different tendencies observed along the reaction time.

At 400 °C, the metals deposited on the catalyst seem to achieve an asymptotic value up to a maximum (246 ppm) at 180 min that is maintained onwards. As the metal retention capacity is mainly based on the textural properties [285], the catalytic inhibition provoked by the PS molecules that clog the pores can prevent not only hydrocracking but also hydrodemetallization to carry on. On the contrary, at 400 and 420 °C the metal loading on the catalyst keeps increasing over time. Here, a strong effect of temperature is observed when increasing it up to 420 °C, as the maximum of metals accumulation in the catalyst is moderately above the one observed at 380 °C (479 ppm), while this amount escalates at 420 °C even at lower times (from 120 min), ending up at 1168 ppm.

3.5. CATALYST REGENERATION

Each process and the reactions involved have intrinsic mechanisms that trigger catalyst deactivation, a major concern for the industrial application of catalytic processes due to economic and practical aspects. Considering coke deposition as the main cause of catalyst deactivation, the usual process to partially or fully recover its initial activity is coke oxidation. However, the regeneration method can be incomplete or, even in the case that the combustion is complete, the initial properties of the catalyst might not be recovered. Indeed, the regeneration method can also affect some of the properties of the material, modifying this way the catalytic performance. In this Section, the regenerability of the catalyst is explored through different methodologies and the one that offers the best results has been applied over different time conditions to ensure the proper behaviour of the regenerated catalyst.

3.5.1. Regeneration methods screening

Based on the results obtained in Section 3.2, the selection of the optimum operating conditions has been done in a search of maximizing plastic conversion and naphtha yield at the same time that gas production is contained. For that reason, the regenerability study of the catalysts has been performed at 400 °C, 180 min and 80 bar, as a full conversion of PS and naphtha yield of 34 wt% is achieved under those conditions.

Figure 3.17 presents the yields distribution of the products from the PS/VGO hydrocracking with the fresh catalyst and the regenerated ones using different methods referenced in the literature [204]. Such processes consist of controlled combustion with diluted air (20 mL min^{-1} of air and 80 mL min^{-1} of pure nitrogen), hydrogen (30 mL min^{-1} diluted in 50 mL min^{-1} of nitrogen) and CO_2 (30 mL min^{-1} and 50 mL min^{-1} of nitrogen); all of them carried out at reaction temperature in an attempt to minimize the catalyst modifications that can take place during the regeneration process.

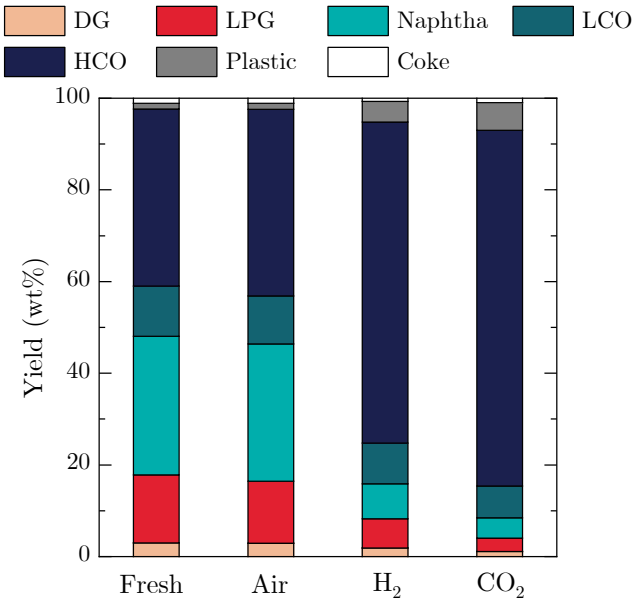

Figure 3.17. Products yield distribution obtained in the hydrocracking of PS/VGO with fresh and regenerated catalysts through different methodologies. Operating conditions: 400 °C, 180 min, 80 bar.

Comparing the results with those obtained with the fresh catalyst, it is evident that only the controlled oxidation of the spent catalysts provides a similar activity under the studied conditions. The utilization of hydrogen for removing the deactivating species or carbon dioxide to promote their oxidation seems to be unfeasible, as the conversion of HCO fraction is minimal and even the PS is not converted. This low reactivity of PS can be responsible for the low hydrocracking activity of VGO in the same way that it was observed when operating at 380 °C (Section 3.2.1). Hydrogen incapacity for regenerating the catalyst can be attributed to the formation of coke species in that same atmosphere with higher partial pressures, so this agent is incapable of converting and sweeping those compounds. Concerning CO_2, the regeneration possibilities provided by this gas have been proven in other processes that involve lighter species with higher regeneration temperatures due to the highly endothermic character of coke gasification. However, an increase in temperature could affect the support in

terms of thermal stability, so a further study about this possibility might be suggested to involve CO_2 valorisation in the whole process.

With respect to coke combustion, the yields of interest barely decrease when regenerating the catalyst by these means (less than 0.5 wt%), observing that the higher HCO yield corresponds to a decrease in LPG, although this difference only accounts for 2 wt%. This slight decrease in catalytic activity can be assigned to the irreversible deactivation related to metals deposition at this temperature (Figure 3.16c and 3.16d). As the deactivation due to metal deposition is often described in terms of an implicit maximum capacity of metal removal [197], it can be assumed that this catalyst deactivation has limitations once the catalyst is saturated with metals. This way, it is logical to establish that there is a limit for the magnitude of the activity decay linked to this phenomenon.

3.5.2. Effect of air combustion regeneration on system performance

To confirm the feasibility of catalyst regeneration through air combustion, various reactions at 400 °C and 80 bar have been performed with the catalysts regenerated under this method. Figure 3.18 displays the effect of this regeneration on the product distribution over reaction time, with very similar yield distribution, the difference accounting for less than 2 wt%. On the contrary, at 300 min the conversion of the heavy fraction is surprisingly higher than the one obtained with the fresh catalyst, obtaining 10.9 wt% of HCO, lower than the 25.8 wt% obtained with the fresh catalyst. The fact that this decrease of ca. 15 wt% does not match with the slight increase of 3.3 wt% of gas production leads to conclude that the hydrocracking reactions development is changing and not only an increase in cracking force has taken place. Although the thermal stability of zeolites is well-established, an exothermic reaction as it is the coke combustion can result in thermal stress via local hot spots on these materials [286], therefore altering their properties and thus explaining the changes observed in Figure 3.18. Moreover, the explained equilibrium between the hydrogenation and condensation of aromatic structures results in a higher monoaromatics content (Figure 3.14b) in the coke fraction. The production of a fraction with a

higher volatile content can significantly increase the flammability and combustion stability during coke combustion [287], thus enhancing its exothermicity.

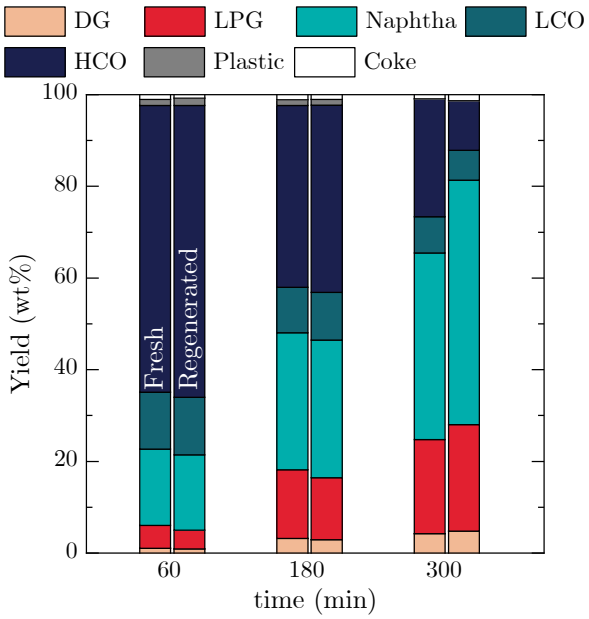

Figure 3.18. Yields distribution over reaction time at 400 °C by using the catalyst regenerated with controlled air combustion for the PS/VGO hydrocracking.

As the combustion of coke has revealed itself as an effective treatment for recovering the catalytic activity, the composition of the target fractions has been studied. This way, the naphtha composition of the products resulting from the PS/VGO hydrocracking with regenerated catalysts is displayed in Figure 3.19. Two main differences can be observed in the naphtha composition of the samples obtained with fresh and regenerated catalysts, each of them being attributable to one phenomenon. First, the samples obtained at 60 and 180 min show a slight decrease in hydrodearomatization capacity, with paraffins and naphthenes contents ca. 5 wt% below the concentrations obtained with the fresh catalyst. Since the hydrogenation function is promoted by the metallic sites of the catalyst and these are more affected by the irreversible deactivation related to deposited metals, this slight decrease is undoubtedly owed to the noble metals poisoning.

On the other hand, it has been already commented that the cracking activity of the catalyst used for 300 min has increased, which can be directly related to its acidic properties. Even though the metals precipitate with maximum catalyst uptakes, the change in the support can suppose an increase in the adsorption strength of aromatics, therefore enabling a higher HDA activity [288].

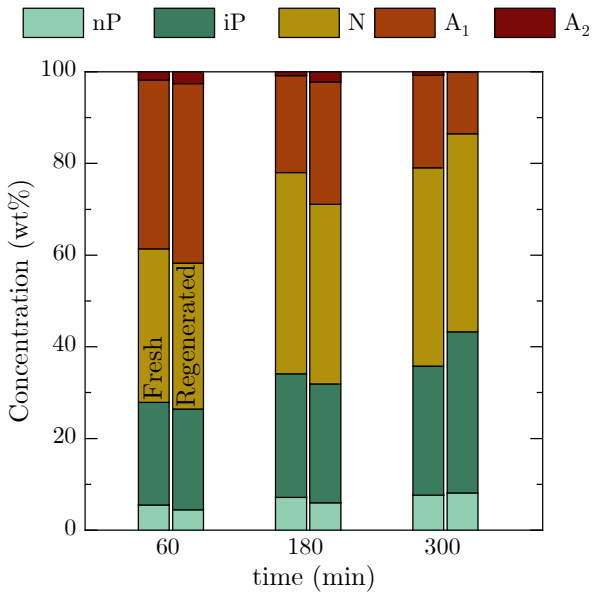

Figure 3.19. Naphtha composition from the PS/VGO hydrocracking products obtained with fresh and regenerated catalysts at 400 °C and 80 bar.

On the other side, Figure 3.20 shows the LCO composition of PS/VGO hydrocracking products with fresh and regenerated catalysts. A similar behaviour that the one observed on naphtha composition can be appreciated, as the general effect of the catalyst regeneration is slightly lessening its hydrogenation capacity. This way, the saturated species concentration diminishes between 2 and 7 wt% when using the regenerated catalysts, mainly due to the minor concentration of naphthenes. The direct relationship between the hydrogenation potential of a catalyst and the hydrogenation of 1-ring aromatics has already been discussed, therefore concluding that the hindering of these reactions is the logical consequence of the deterioration of the hydrogenation function. Regarding

paraffins, isoparaffins are also modified as a result of the minor formation of naphthenes. On the contrary, the non-selective cracking of aliphatic chains during the ring-opening makes that normal paraffins content remains steady after the regeneration.

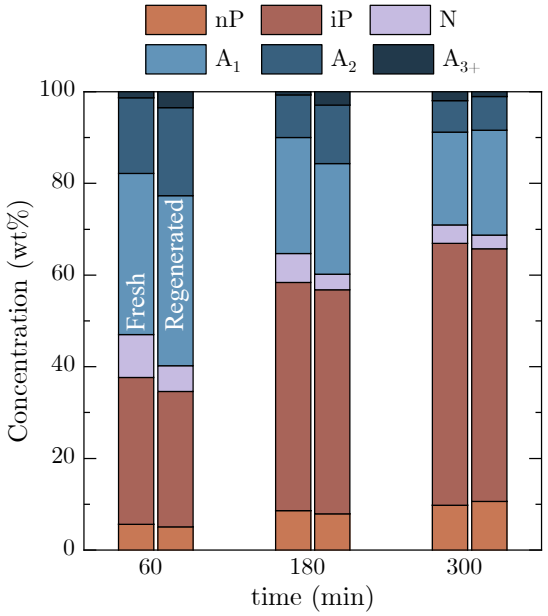

Figure 3.20. LCO composition from the PS/VGO hydrocracking products obtained with fresh and regenerated catalysts at 400 °C and 80 bar.

3.5.3. Effect of air combustion regeneration on coke deposition.

Figure 3.21 shows the TPO profiles of the spent catalysts used in PS/VGO hydrocracking reactions after their regeneration in the oxidative atmosphere. Note that shaded areas indicate the zones corresponding to the denominated as external (first) and internal (second) coke.

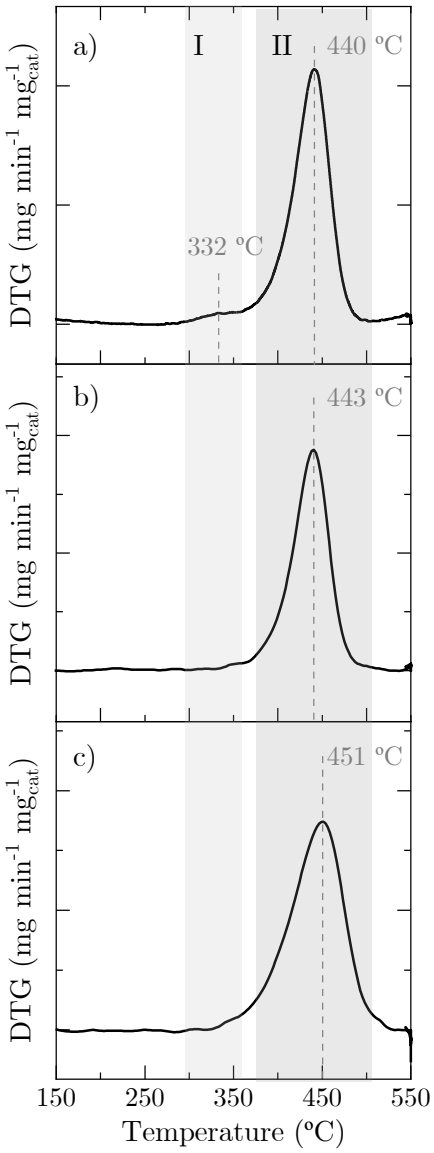

Figure 3.21. TPO profiles of spent catalysts recovered from PS/VGO hydrocracking after regeneration for a) 60 min, b) 180 min and c) 300 min.

The apparition of external coke only at 60 min differs from the results obtained with the fresh catalyst (Figure 3.12), as some external coke deposition was observed for times higher than 30 min at all temperatures. As the external coke

at 400 °C with the fresh catalyst accounts only for 5 wt%, its fading (probably due to its condensation into more complex structures) can be related to the hydrogenation activity loss related to irreversible deactivation. In fact, it has been observed in Section 3.5.2 the same impact on the hydrogenation function is reflected in the aromatics increase, so this can be another consequence of the metals poisoning.

Apart from that, there is an increase in the combustion peak as reaction time goes on, which corresponds to the condensation of coke structures. The change in the combustion peak is more pronounced in the 300 min sample, which is a result of the increment of cracking reactions extent [289] also commented on in Sections 3.5.1 and 3.5.2. Regarding the total coke deposited on the catalyst, the trend also changes with respect to that observed in fresh catalyst reactions. As can be appreciated in Figure 3.18, the coke amount continuously increases from 0.8 wt% yield at 60 min to 1.3 wt% yield at 300 min. This lack of coke attenuation that was observed with the fresh catalyst due to the compensation between hydrogenation and condensation reactions is in line with the promotion of cracking forces here observed, which lead to a higher extent of the second reaction type. In fact, the broadening of the signal observed in Figure 3.20c when compared to Figure 3.20a and 3.20b also indicates a wider spectrum of coke species that take longer to undergo complete combustion, meaning that condensation of coke precursors still takes place at 300 min.

Chapter 4

HYDROCRACKING OF OXYGENATED PLASTICS AND VGO BLENDS

In this Chapter, the co-feeding of oxygenated plastics and VGO within a hydrocracking process has been studied using the PtPd/Y catalyst characterized in the previous Chapter. Polyethylene terephthalate (PET) and polymethyl methacrylate (PMMA) have been selected due to their representation among non-olefinic plastics in the usual municipal plastic waste. The effect of adding different polymers to the feeding blend on product distribution and composition has been assessed, with special attention to the changes observed in the hydrocracking mechanisms. This way, the results obtained are used for introducing the analyses of heteroatom-containing structures as well as that of heavy molecules. As in the previous Chapter, the influence of each plastic on coke formation has been investigated, contributing to the foundations for the kinetic modelling development.

4.1. EFFECT OF OPERATING CONDITIONS ON PRODUCT DISTRIBUTION

VGO, PMMA/VGO and PET/VGO hydrocracking reactions have been performed in a 100 mL batch reactor unit using the PtPd/Y catalyst characterized in Chapter 3 under the following operating conditions:

- Feedstock: plastics (10 wt%) in VGO, and neat VGO
- Temperature: 400-420 °C
- Pressure: 50-110 bar
- Reaction time: 30-300 min
- Catalyst-to-feed ratio (mass basis): 0.1
- Stirring speed: 1300 rpm

The need for the utilization of a different reactor arises due to the production of potentially dangerous and corrosive compounds from the hydrocracking of carboxylic acids that can be obtained from these plastics [290]. In fact, a few initial tests with PMMA and PET blends confirmed the damage to the reactor gasket of the 50 mL reactor. As the catalytic performance over temperature and time has been discussed in the previous Chapter, the results when feeding PMMA and PET along with VGO focus on product distribution in terms of selectivity towards products of interest and the effect of different plastics on the optimization of the operating conditions.

4.1.1. Influence of temperature and time

Figure 4.1 displays the conversion of the heaviest fraction, i.e. HCO (Figure 4.1a), and plastics (Figure 4.1b) along with reaction time on the hydrocracking of the neat VGO, PMMA/VGO (PMMA) and PET/VGO (PET) blends at 400 and 420 °C. It can be observed that higher reaction times favour both HCO and plastics conversion in all cases and conversion of the plastic is higher than that of HCO through the studied reaction time (30-300 min). By an initial comparison between the conversion levels, it can be observed that HCO conversion depends on the combination of feed and temperature. Thus, at 400 °C HCO conversion is higher for the plastics blends, as the good conversion of the polymers

(Figure 4.1b) and the need for a higher cracking force for converting HCO polyaromatics constraint VGO conversion (73.3 wt% at 400 °C and 300 min). However, the increase up to 420 °C improves both VGO and PMMA/VGO blends, with final conversions of 95.9 and 94.6 %, respectively, while PET/VGO blend conversion of HCO is limited to 79.5 %. This highlights that, at a given time and temperature, the PMMA/VGO blend has a greater conversion than the PET/VGO blend, which is likely related to the refractory nature of aromatics, which hampers its conversion [291].

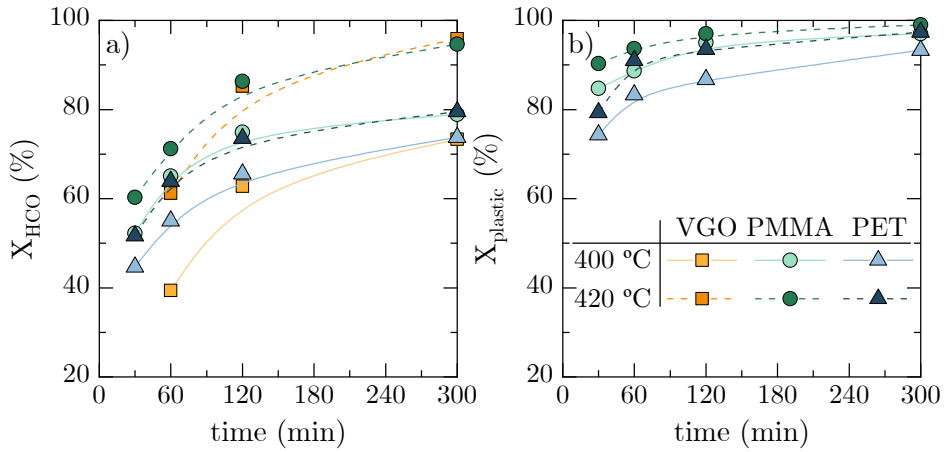

Figure 4.1. Hydrocracking conversion of a) HCO and b) plastics over reaction time at 400 °C and 420 °C. Reaction conditions: 80 bar, C/F = 0.1.

Attending plastics conversion (Figure 4.1b), it can be noticed that after 30 min, both plastics are already converted in over 70 %, and almost complete conversion (> 90 %) is attained at 300 min. The remaining PET obtained at 400 °C, which presents a lower and slower conversion than PMMA, explains the parallel lower conversion of HCO observed in Figure 4.1a. As exposed in Chapter 3, it has been demonstrated that the unconverted plastic can act as a barrier between the active sites of the catalyst and the molecules of the co-fed materials [252, 253], therefore hindering their conversion. Temperature effect on cracking reactions seems evident, as the higher plastics conversion observed can be related to the higher scission of the long polymers chains [124].

Figure 4.2 depicts the selectivity towards the different gaseous products, as they present distinct behaviour over time and temperature and diverse conclusions are extracted from the results of the different feeds. Total gas selectivity remains in the 0.17-0.45 range, which represents a maximum of ca. 40 wt% of the products for PMMA/VGO products and less than 30 wt% when feeding the other materials. Note that, taking into account the oxygen contained in the plastics and based on the products obtained from their pyrolysis [292, 293], CO and CO_2 have been identified as products and quantified along with the other gaseous fractions. Overall, the selectivity of gas products is higher when processing plastic/VGO blends compared to VGO alone. For a better understanding of the mechanisms involved, individual analyses of the gas fractions have been performed.

The evolution of the DG selectivity is shown in Figure 4.2a. It can be noticed that the production of this lump is never over 0.1, exposing the limited overcracking activity of the bifunctional catalyst. That being said, the effect of temperature seems to affect differently to each feed. The addition of plastics to the feeding blend promotes the formation of these lighter species at 400 °C, probably due to the formation of C_4 compounds as a result of the PMMA cracking and C_2 compounds coming from PET cracking, as these groups can be found on the corresponding monomers and, as it has been seen on Figure 4.1b, the polymers' conversion is quite high since the very beginning. However, when the temperature is increased, both VGO and PMMA/VGO selectivity towards DG escalates as a result of the thermal cracking activity [294], while PET/VGO dry gas amount over time barely changes after 60 min (thus observing a selectivity decrease). Due to its aromatic nature, PET hydrocracking can be assumed to occur through a carbocation mechanism [295], as the thermal cracking of this polymer has been explored at much higher temperatures [296], therefore explaining the restrictions on its conversion and DG formation at the studied temperatures.

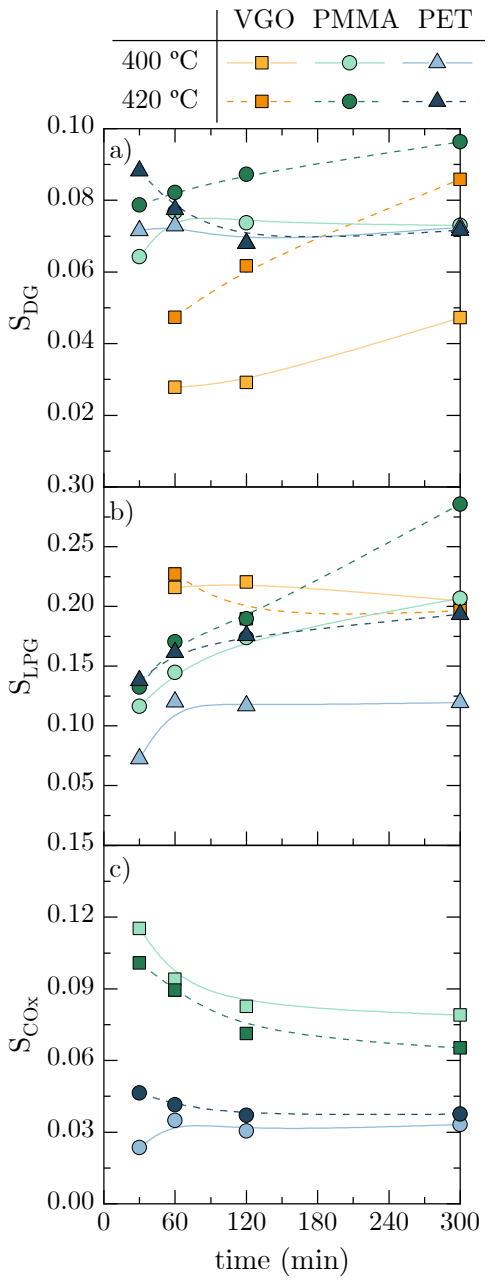

Figure 4.2. Selectivity of a) DG, b) LPG and c) CO_x of hydrocracking products. Reaction conditions: 400-420 °C, 30-300 min, 80 bar, C/F = 0.1.

In Figure 4.2b, LPG selectivity advancement over time is collected at 400 °C and 420 °C for each blend's products. The greater extent observed in LPG formation with respect to that observed in DG corresponds to the cracking mechanism that produces C_3-C_4 as primary products [297] during the hydrocracking of medium streams. Two factors must be considered to fully understand LPG selectivity. On one hand, the temperature increase results in a general increase of the selectivity towards LPG, as it promotes the cracking reactions that produce gaseous compounds. The exception to this trend is observed in VGO products, as similar initial and final points are found in LPG selectivity. This behaviour is due to the simultaneous formation of higher amounts of LPG and the boost of secondary cracking reactions [298], therefore a fraction of LPG that is formed is converted into DG. On the other hand, and related to this, the effect of time is also that of promoting the formation of C_3-C_4 compounds. However, there seems to be a linear relationship between LPG and reactants conversion, therefore explaining the almost and fully steady values of LPG selectivity over time for VGO and PET/VGO hydrocracking products. In the case of PMMA/VGO, the predominance of cracking reactions leads to an increasing trend that is boosted with temperature.

Last, the influence of HCO conversion, temperature and feed on the formation of CO/CO_2 is followed in Figure 4.2c. Here, the effect of time and temperature is pretty clear on the evolution of this lump, as the selectivity towards these compounds seems to be strongly limited by the plastic that is being fed into the reactor. The PMMA/VGO blend is more easily converted into gaseous hydrocarbons and also into CO/CO_2 than the PET/VGO blend, especially when the reaction is carried out at 420 °C and for 300 min, when overcracking is promoted. As a result, it can be deduced that all the CO_x fraction that can be produced from this polymer is obtained at low reaction times, thus its selectivity decreases with time because no more CO_x but other products are being produced. Temperature rise indeed improves the production of CO_x from PET at 420 °C and 30 min, but its selectivity then decreases as a consequence of the formation of other products when feeds conversion increases. As the oxygen content is analogue in both polymers, we observe that the CO/CO_2 formation is half of that

produced by the PMMA/VGO blend. Since the levels of polymer conversion achieved by each blend are similar at high conversion levels and the total oxygen content supplied by them should be similar, it seems logical to expect that more oxygenated liquid products can be found in the PET/VGO blend hydrocracking products.

In Figure 4.3, the selectivity of the hydrocracking of VGO, PMMA/VGO and PET/VGO blends towards the fractions of higher interest, those being naphtha and LCO, is shown at different temperatures over time. The evolution of the naphtha selectivity (Figure 4.3a) shows the final product character of this lump, as its formation is always promoted by a higher conversion of the feeds. This, along with the fact that the final values of selectivity obtained for all the systems are between 0.35 and 0.65, remarks the good performance of the catalyst for producing streams suitable for their mixing with the gasoline pools in refineries, especially if reactions are carried out for long enough times.

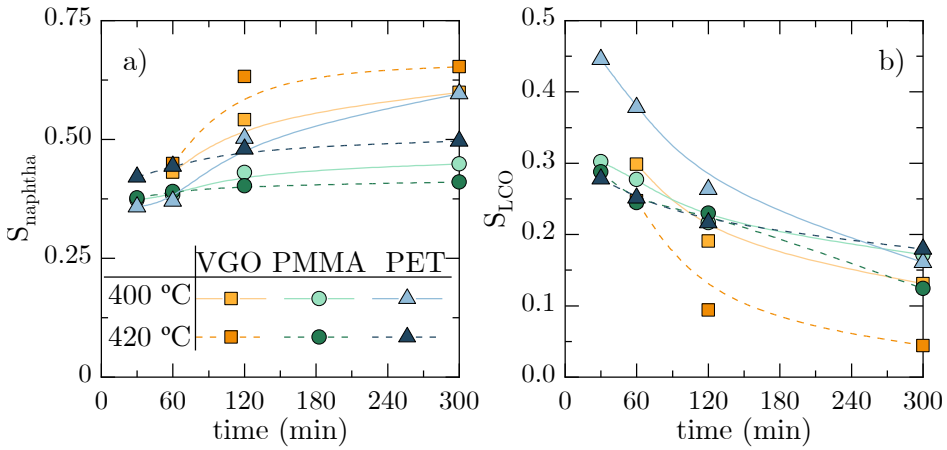

Figure 4.3. Selectivity towards a) naphtha and b) LCO of VGO, PMMA/VGO and PET/VGO hydrocracking products. Reaction conditions: 400-420 °C, 30-300 min, 80 bar, C/F = 0.1.

Here, the effect of increasing the temperature only benefits the selectivity towards naphtha when feeding VGO, as the promotion of lighter species for PMMA/VGO and PET/VGO blends avoids the maximization of this lump. The explanation is

concurrently found in the increment of VGO heavy compounds conversion and the promotion of secondary cracking of plastic blends products [298]. In fact, as these secondary cracking reactions are hindered by PET's lower conversion when compared to PMMA, it can be seen that the naphtha selectivity of the first blend is higher than that of the second at 400 °C (0.60 vs 0.45, respectively).

With respect to LCO selectivity (Figure 4.3b), the intermediate character of this fraction is easily recognizable when attending to the trends over time, as it is formed in the first place but when conversion is further advanced it decreases in favour of lighter fractions. This way, the selectivity towards LCO is favoured when HCO conversion is lower (i.e. VGO and PET/VGO hydrocracking at 400 °C) and decreases with the conversion escalation (as observed at 420 °C in Figure 4.1a). The rapid conversion of PMMA/VGO into final products is reflected in its minor selectivity for this intermediate fraction. In the case of PET/VGO products, the increment in conversion is observed by the lower LCO fraction obtained at 420 °C, although the harder conversion of the blend can be appreciated by a higher LCO production compared to the other blends.

4.1.2. Effect of pressure

The role of hydrogen pressure has been proven to be important to adjust the composition of liquid products, but its effect on product distribution can be limited depending on the medium, as discussed in Chapter 3. By changing not only the reactor but also the feeds, the pressure effect on product distribution must be reviewed and is depicted in Figure 4.4. The hydrogen effect on liquid-gas equilibrium is once again confirmed, as an increase in hydrogen pressure results in a decrease in the selectivity towards gas (Figure 4.4a). The production of a major liquid fraction when hydrogen pressure is increased corresponds to the termination of the cracking mechanisms, which primarily form cations on the acid sites of the catalyst that can be further cracked or (and as in this case) saturated and transported to the bulk phase without being converted in lighter species [299]. When comparing the feeds, this effect is more noticeable in PET/VGO gaseous products selectivity, probably due to the aromatic nature taking advantage of a more reducing atmosphere and the general effect of a higher pressure above

commented. The cutback in gas formation for that blend is also reflected in a higher increase in fuel selectivity when pressure is incremented (Figure 4.4b), which confirms that the greater conversion of PET can produce compounds belonging to fuel fractions.

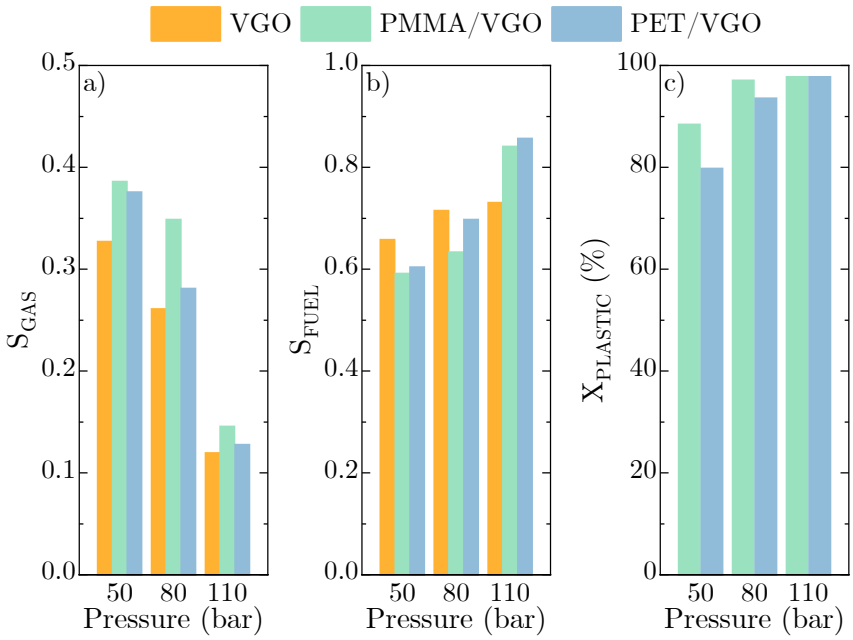

Figure 4.4. Effect of pressure on a) gas selectivity, b) fuel selectivity and c) plastic conversion. Reaction conditions: 420 °C, 120 min, C/F = 0.1.

Precisely attending to fuel selectivity (Figure 4.4b), PMMA/VGO products confirm this direct relationship between the gas and liquid fractions and the hydrogen pressure, following the same trend that was observed in PET/VGO samples. In general, a fuel selectivity increase is observed with the pressure increment because of the two factors discussed: on one side, the displacement of gas-liquid equilibrium in favour of the liquid [254]; on the other side, the fast hydrogenation of intermediate species formed during cracking reactions that avoids their subsequent cracking into gaseous compounds [299]. If individual increments are focused, PMMA/VGO products increment from 80 to 110 bar can be attributed to the latter phenomenon exposed, as its branched nature turns out to be the ideal starting point for secondary cracking mechanisms [300]. For

PET/VGO reactions, not only this effect should be taken into consideration but also the higher conversion of the aromatic rings of the polymer, which leads to major conversion levels of the plastic (Figure 4.4c) through the enhancement of hydrogen transfer reactions within the scheme of the hydrocracking of aromatic molecules [301].

With respect to plastic conversion (Figure 4.4c), the synergy between the hydrogen pressure and each plastic's nature has already been pointed out due to its connection to gas and fuel selectivity. If the classical mechanisms of isomerization and hydrocracking are considered [302], a lower hydrogen pressure can shift the preferential mechanisms to beta-scission reactions that afterwards will be hydrogenated on metal sites, thus forming light isoparaffins, which is consistent with the high gas selectivity (Figure 4.4a). On the contrary, if hydrogen pressure is increased, the reversible pathway can be followed in the first stage, resulting in the formation of larger iso-C_iH_{2i+2} compounds that possibly belong to fuel fractions. Similarly, PET is converted through similar mechanisms, considering a preliminary ring opening mechanism of the aromatic molecules that, as it is consolidated in hydrocracking, benefits from the hydrogen increment. In this matter, the effect of temperature should be re-examined, as it is the main driving force in the polymers conversion initiation. For example, the promotion of the formation of mono- and di- branched alkylcarbenium ions from PMMA by increasing the temperature can be deduced from the high content of CO/CO_2 quantified within the gas products [303].

4.2. LIQUID COMPOSITION

4.2.1. Influence of temperature, time and feed

Figure 4.5 depicts the changes in the naphtha composition of the VGO, PMMA/VGO and PET/VGO hydrocracking products with reaction time for products obtained at 400 and 420 °C. To study the effect of each variable in this composition, the individual effect is analysed and then the relationship with other variables is established. The effect of time is that of promoting the ring-opening mechanism, observing that the main changes produced within this fraction are related to monoaromatics, naphthenes and isoparaffins. The sequential transformation of aromatics into naphthenes and then into paraffins is also conditioned by the adsorption strength of each type of compound [304], therefore being the aromatics and naphthenes the most reactive compounds, regardless of the thermodynamics equilibrium of hydrogenation reactions. Therefore, the higher advance in HCO conversion when feeding VGO results in a higher content of isoparaffins as the final product of the ring-opening reactions.

Anyways, the displacement of this equilibrium at different temperatures is also exposed. It can be seen that at 400 °C hydrogenation reactions are favoured, with higher contents of naphthenes and isoparaffins that behave differently according to the feed for VGO and PMMA/VGO products, while PET/VGO products seem to be severely affected by the aromatic nature of this plastic. Even in that case, the trend observed over time is that of hydrogenating the monoaromatics produced in favour of saturated species. Once the temperature has risen to 420 °C, the equilibrium of hydrogenation has been shifted towards the aromatization of the compounds through the cyclization and dehydrogenation of the compounds formed from the enhancement of the cracking forces. For example, a higher initial content of isoparaffins can be appreciated in the VGO hydrocracking products, which then decrease either because of the formation of gases through cracking or due to the cyclization towards naphthenic structures.

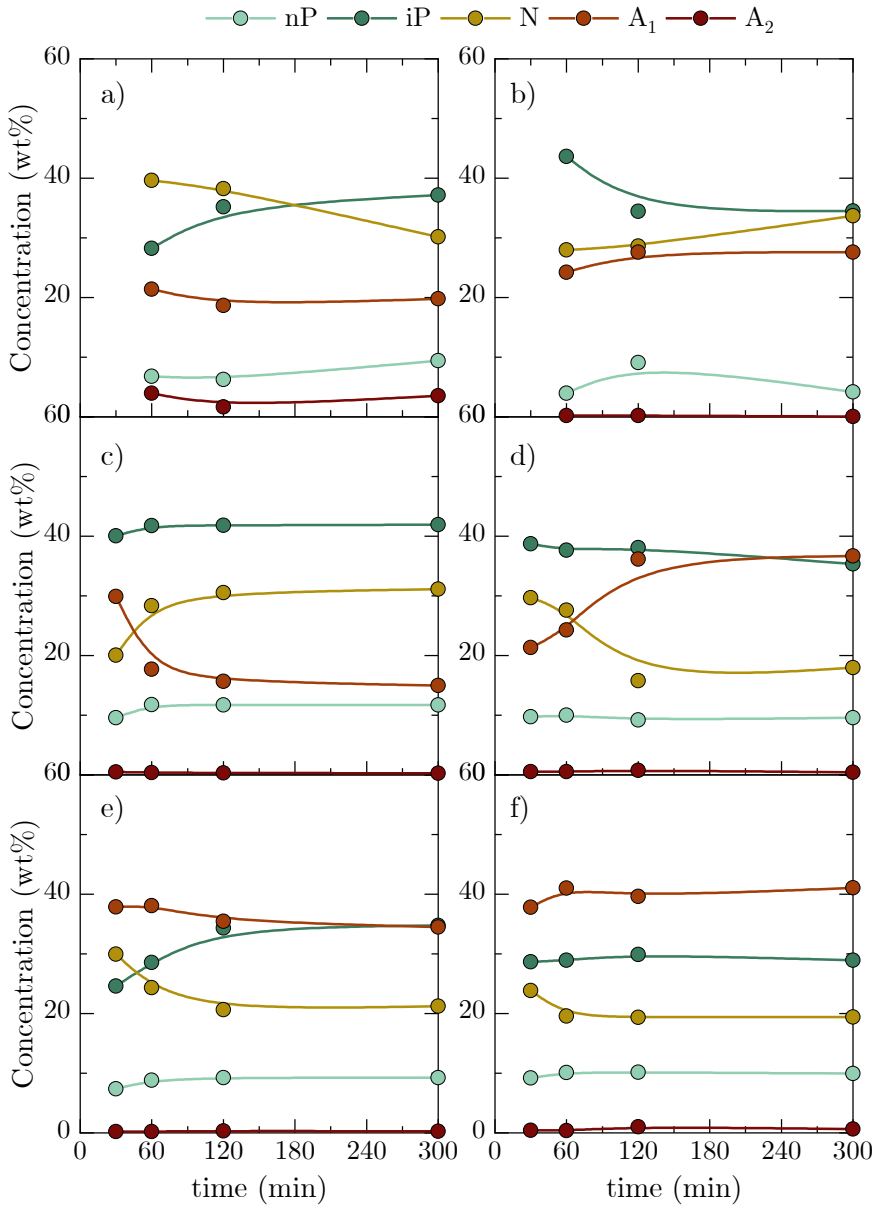

Figure 4.5. Evolution of naphtha composition for VGO, PMMA/VGO and PET/VGO hydrocracking products over reaction time at 400 (a, c and e, respectively) and 420 °C (b, d and f, respectively). Reaction conditions: 80 bar, 30-300 min, C/F = 0.1.

This reverse reaction is more evident in PMMA/VGO products, which directly interrelate the isoparaffins content decrease over time with the parallel increase in monoaromatics. The latter can be explained through the role that hydrogen-transfer reactions play when the hydrogenation equilibrium is not favoured, as isoparaffins are converted into carbonium ions that are likely to undergo cyclization reactions [256, 257]. This effect is also detectable when feeding the polymers' blends, although the changes, as well as the concentration distribution of each chemical family, are strongly influenced by the nature of each feed.

Regarding the effect of the blend on the composition of the naphtha fraction, the rapid conversion of the polymers at the beginning of these reactions (seen in Figure 4.1b) can explain the different starting points of this composition. By these means, and at 400 °C, the higher hydrogenation of the polyaromatics present in the VGO leads to a content of naphthenes of 39.6 wt% at 60 min, while this group is limited to a 28.4 and a 24.3 wt% in PMMA/VGO and PET/VGO products, respectively. In the same way, isoparaffins concentration at that time is higher when looking at the PMMA/VGO products (41.8 wt%) and monoaromatics are preferentially formed from PET/VGO blend (38.1 wt% at 60 min). Precisely, the higher content of monoaromatics with respect to those obtained in VGO and PMMA/VGO products cannot be explained only through the addition of PET, as the total content of aromatic groups should be equal or less than the 10 wt% of co-fed polymer. Two simultaneous phenomena taking place lead to this situation: (i) on one side, the lower conversion of both HCO and PET can partially explain the lesser advance of aromatics hydrocracking reactions and the lower contents of naphthenes and, consecutively, of isoparaffins, according to the ring opening classical mechanism [147, 301]; (ii) on the other side, the hydrogenation reactions that affect aromatics from both VGO and PET are hindered by the competitive adsorption of their molecules on the catalyst and the more difficult conversion of the polymer [125].

Figure 4.6 shows the evolution of LCO composition over reaction time for VGO, PMMA/VGO and PET/VGO hydrocracking products at 400 and 420 °C.

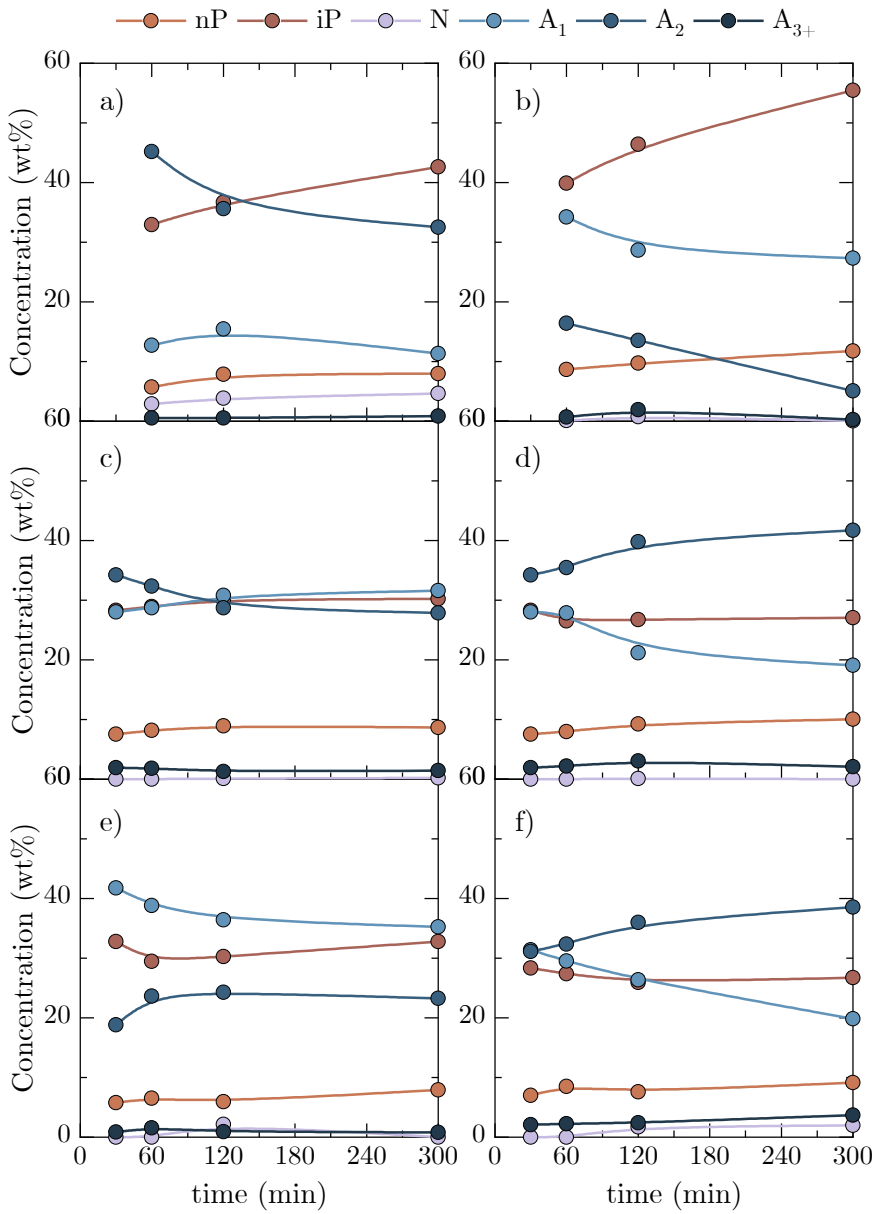

Figure 4.6. Evolution of LCO composition of VGO, PMMA/VGO and PET/VGO hydrocracking products over reaction time at 400 (a, c and e, respectively) and 420 °C (b, d and f, respectively). Reaction conditions: 80 bar, 30-300 min, C/F = 0.1.

In this fraction, the influence of reaction time on the distribution of the lumps is less noticeable at 400 °C, since, in general, all of them achieve steady values at 120 min. At 420 °C, however, the development of the reactions does not reach a steady state and continues modifying the composition of each product with the reaction time. The differences observed over temperature are dependent on the co-feeding of a polymer, as two different trends can be observed according to the presence or lack of a polymer in the initial blend. On one hand, the extensive conversion of HCO when feeding VGO facilitates the conversion of first the polyaromatics in HCO fraction, thus rising their content in LCO, and then their further conversion in lighter species. This way, the content of diaromatics severely decreases at expense of an increase of monoaromatics, contrary to what is expected if attending to the hydrogenation equilibrium thermodynamics, as an increase of temperature favours the cracking of intermediate products, displacing the thermodynamic equilibrium of hydrogenation [294]. On the other hand, similar compositions and distributions can be found in PMMA/VGO and PET/VGO products. This indicates that the conversion of plastics through hydrocracking at 420 °C is so fast that the compounds that possibly belong to the LCO fraction are rapidly converted into naphtha species. Concerning the trends observed here, the effect of temperature on aromatics hydrogenation is the one that could be expected. The displacement of operating conditions towards dehydrogenation conditions leads to a reversal of diaromatics behaviour, as they increase at the same time that monoaromatics content is reduced. Under competitive adsorption conditions, VGO compounds are expected to reach the active sites more easily [304]. For that reason, the compounds derived from the polymers cannot be cracked in lighter products and end up being dehydrogenated towards polyaromatic structures.

Last, it has already been commented that greater differences in the products obtained from each feed can be found at 400 °C on LCO composition for low-time reactions. The higher content of diaromatics (45.2 wt%) in VGO products at the early stages of the reaction reflects the higher conversion of the polyaromatics present in this material, while PMMA/VGO and PET/VGO hydrocracking products have major contents of isoparaffins (28.3 wt%) and monoaromatics

(31.4 wt%), respectively, when compared with the other products. Furthermore, the advance of hydrocracking reactions is also perceptible with close attention to polyaromatics' behaviour. That is so that this lump increases on VGO products at 120 min and then decreases, which can be attributed to the conversion of heavier structures in HCO fraction to LCO compounds that then undergo further hydrocracking. In the same way, PET/VGO products show a final increase at 300 min, when plastic is almost fully converted and thus so increases HCO conversion. In fact, the formation of polyaromatic species from the PET cannot be discarded, as the conversion of this plastic could begin with the formation of HCO molecular weight chains [305].

To evaluate the quality of the naphtha fraction produced through the hydrocracking of each blend, the RON and CI have been assessed, and results are collected in Figure 4.7. The behaviour of RON is observed to be more similar when co-feeding plastics and VGO than that obtained by only feeding VGO. This way, the changes observed in the products of the latter are more noticeable than the others, which barely change over time and temperature. However, the effect of temperature is the same for VGO and PET/VGO products, as the RON of samples at 420 °C and 300 min overpasses the one at 400 °C, even when lower reaction times provide lower RON values. The explanation of these trends lies in the contribution of each of the groups considered for the calculation of the RON value. For example, 9 carbons aromatics and 10 carbons isoparaffins (among other groups) and naphthenes have a remarkable contribution and have a greater presence in VGO products at both temperatures, thus improving the RON when compared to those from the blends.

On the other hand, the CI also follows almost an identical trend for the blends hydrocracking products and a slightly different one for VGO hydrocracking products. That is so that this index depends strongly on both the composition of the LCO fraction and the heaviness of the samples (in terms of density). Therefore, the low conversion of VGO at 400 °C explains the particularly low range of CI of VGO products, while PMMA/VGO and PET/VGO products

present an LCO fraction with similar CI values, only differentiated at high reaction times due to their composition.

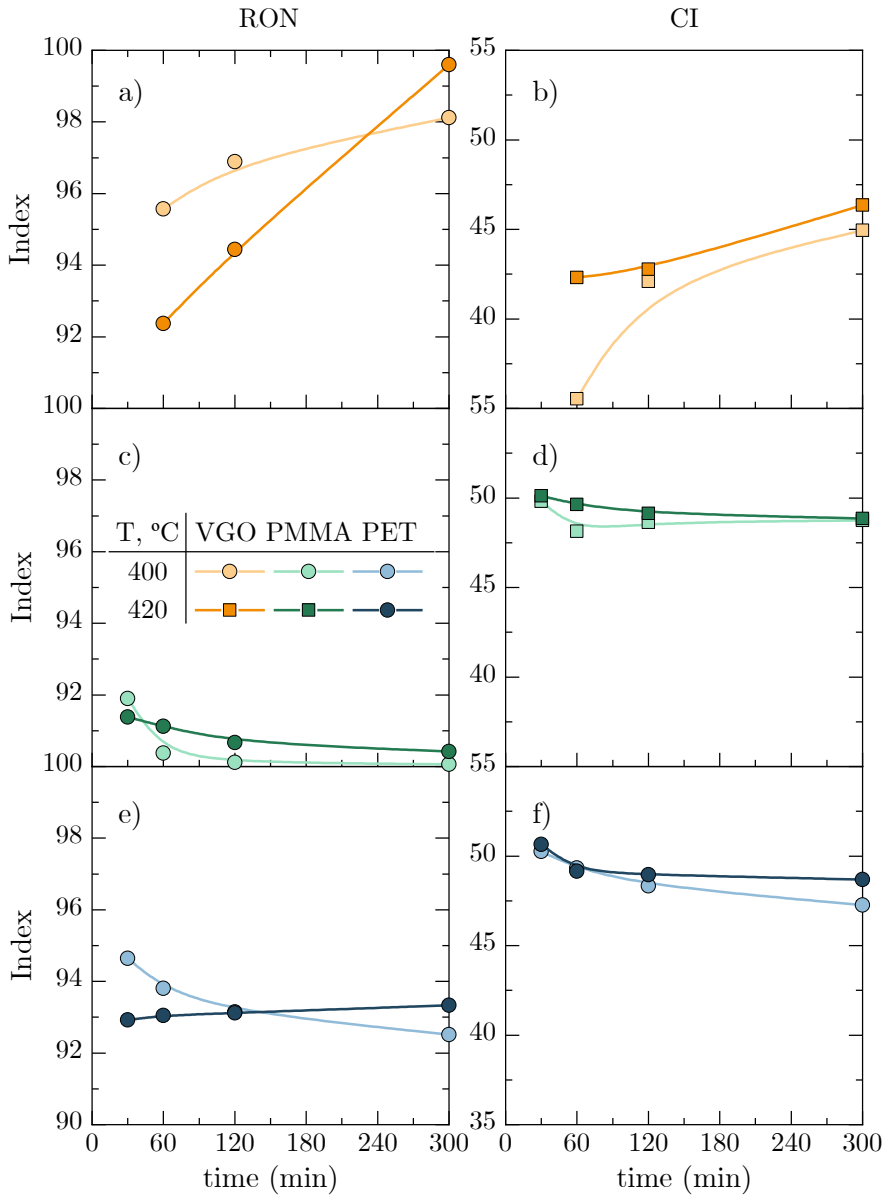

Figure 4.7. Evolution of RON and CI of the products resulting from VGO (a, b), PMMA/VGO (c, d) and PET/VGO (e, f) hydrocracking. Reaction conditions: 400-420 °C, 30-300 min, 80 bar, C/F = 0.1.

Moreover, the effect of temperature is clear, as at 420 °C the CI of the VGO hydrocracking products is raised and those of the blend hydrocracking products are maintained over those obtained at 400 °C due to the shift towards a more aromatic composition reflected in both blends. It has been previously reported in the literature that ring-opening mechanisms are not a straightforward way to obtain products with better CI values, since for this, this mechanism should be very selective for the scission of substituted C-C bonds in naphthenic structures in order to minimize the branching degree of the formed products [306].

4.2.2. Effect of pressure.

The naphtha composition changes observed when varying the hydrogen pressure between 50 and 110 bar are collected in Figure 4.8 for each blend, as well as the RON of each sample. It can be noticed that the VGO products show the opposite trend on saturated/aromatic species to that observed for plastic blends. As all the hydrogen is consumed by the polyaromatics found on the VGO, it is reasonable to deduce that the continuous increment in hydrogen pressure leads to further hydrogenation of those compounds that end up being monoaromatics, as their hydrogenation is more unlikely than that of rings from polycondensed structures [261]. This way, the content of total aromatics in the naphtha of VGO products goes from 19.6 to 48.0 wt% when increasing from 50 to 110 bar, compared to the decrease of PMMA/VGO and PET/VGO products, and are converted from 46.8 and 54.6 wt% to 29.2 and 41.8 wt%, respectively. A higher amount of total aromatics in PET/VGO products is this way observed since the utilization of low hydrogen pressures, meaning that part of the hydrogen is being captured by the aromatic molecules that form the polymer structure.

When comparing the products of the different blends, the presence of long chains of hydrocarbons that need to be firstly hydrogenated to be then converted into smaller molecules by cracking, appears to result in the assimilation of part of that extra hydrogen by the polymers, therefore impeding the further hydrogenation of those polyaromatics of VGO. Also, the increase up to 110 bar on PET/VGO products corroborates somehow that part of the hydrogen is being transferred into the plastics, as the content of monoaromatics is similar to that on

PMMA/VGO products at 80 bar (ca. 39 wt%) but then the hydrogenation of these aromatics only occurs on the latter. The formation of monoaromatics due to the saturation of the aromatics molecules from the PET could explain the prevalence of this concentration. Also, the preferential formation of isoparaffins from the aromatics ring opening can be appreciated, both at low hydrogen pressure on VGO products and high pressures on plastic blends products. The selective hydrocracking of both aromatics and n-paraffins (main components of the feed of these blends) has isoparaffins as the final product, favoured by an increase of the carbon atoms number of the initial molecules [307] and also by an increase in hydrogen pressure [308].

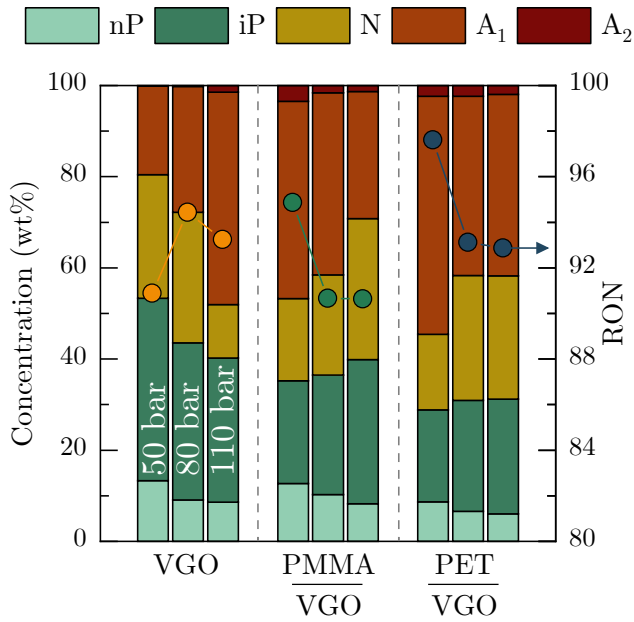

Figure 4.8. Effect of pressure on the naphtha composition of the VGO, PMMA/VGO and PET/VGO hydrocracking products. Reaction conditions: 420 °C, 120 min, 80 bar, C/F = 0.1.

RON changes in different ways according to the feed, as the VGO hydrocracking products go through a maximum after their RON increase by increasing the pressure from 50 to 80 bar and the blends' RON initially decrease and then stalls. The RON increase when working at pressures up to 80 bar observed in the VGO

products is consistent with previous experiments [309], while the further increase up to 110 bar has a direct effect on the concentration of some of the highest contributing compounds, such as the alkylbenzenes. With respect to PMMA/VGO and PET/VGO hydrocracking products, their initial monoaromatics content produces the high RON values observed (noticing a direct relationship between these parameters) that then decrease along with that concentration. In PMMA/VGO hydrocracking products, the equilibrium between the isoparaffins and the monoaromatics on naphtha composition makes this value stable, while the similar concentration obtained with PET/VGO blend causes the same effect on RON.

As has been done with naphtha, changes in LCO composition and CI values with increasing pressure have been collected in Figure 4.9. Note that the effect of pressure on normal paraffins production is barely appreciated, while isoparaffinic and aromatic species transformation are the main mechanisms affected.

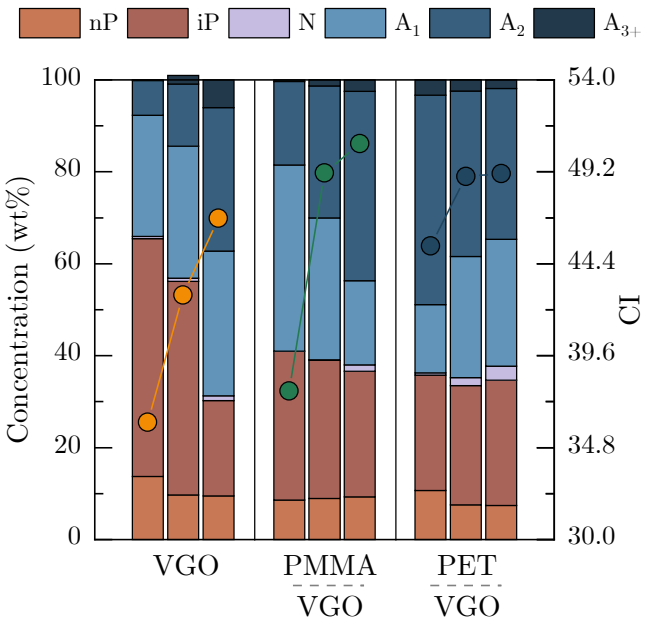

Figure 4.9. Effect of pressure on the LCO composition of the VGO, PMMA/VGO and PET/VGO hydrocracking products. Reaction conditions: 420 °C, 120 min, 80 bar, C/F = 0.1.

The transient nature of LCO fraction and the multiple pathways of polyaromatics hydrogenation focus attention on the evolution of these mechanisms instead of those of paraffins formation and isomerization. Indeed, these reactions are subject to the formation of different aromatic species before paraffins start to form [310], along with the stronger influence of hydrogen pressure on hydrogenation function rather than on cracking mechanisms.

The trend of aromatics hydrogenation is shared by VGO and PMMA/VGO products, observing a progressive increase in diaromatics concentration in their composition while PET/VGO products' amount of diaromatics decreases. This different behaviour is related to both conversion and the behaviour anticipated on naphtha composition: as VGO and PMMA/VGO blends only deal with polyaromatics from HCO fraction, the sequential hydrogenation of those compounds gives increasing amounts of di- and then mono-aromatics [147]. An increase in hydrogen pressure leads to the logical increment of these species, this effect being more appreciated in VGO products due to the highest hydrogenation activity of the heaviest compounds already observed in Figure 4.8. Oppositely, PET/VGO products show an increasing production of monoaromatics that is less pronounced when increasing from 80 to 110 bar. Similarly to what is observed in naphtha composition, a further increase in the hydrogenation of PET molecules would explain this trend, and the cracking of these compounds into lighter monoaromatics leads to the monoaromatics behaviour observed in Figure 4.8.

Concerning the composition differences between the products of each blend, there is a clear contrast between VGO hydrocracking products and the polymers' blends hydrocracking products. While aromatics in LCO from VGO hydrocracking increase up to 69.4 wt%, aromatics in LCO from PMMA/VGO and PET/VGO hydrocracking are limited to 62.8 and 64.3 wt%, respectively, at 110 bar. The change in this total concentration along with the increase in hydrogen pressure is only noticeable on VGO hydrocracking products, as a direct consequence of the continuous hydrogenation of polyaromatics and the formation, to a higher extent, of fuel-like streams (Figure 4.2b). The total aromatics in the LCO from PMMA/VGO hydrocracking seem to barely vary from 80 to 110 bar,

which also justifies the decrease in monoaromatics that belong to naphtha. Regarding LCO from PET/VGO hydrocracking, the total content of aromatics is not that much influenced by hydrogen pressure, although the change in their distribution can be related to the parallel and cascade hydrogenation of polyaromatic species that form both HCO and unreacted PET.

CI behaviour follows the same trends regardless of the feed, unlike those observed in RON, the values of hydrocracking products of the polymers' blends being higher than those of the VGO hydrocracking products. The CI of VGO products continuously increases when pressure is elevated, probably as a consequence of the noticeable formation of aromatics with alkyl chains through ring opening mechanisms, which present a favourable set of properties to ignite in a compression ignition setting [311].

Concerning the plastic blends, the higher content of monoaromatics of PMMA/VGO products seems to impoverish their CI at 50 bar due to their stable nature, which hinders their ignition. When pressure is increased, this relationship is confirmed, as a minor content of monoaromatics is observed in PMMA/VGO products and, consequently, a higher CI is obtained. The relationship between the stability of aromatics and their influence on the boiling point depending on the branching degree must be therefore carefully assessed, as also stated by other authors [264].

4.3. COKE CHARACTERIZATION

The role of the feeding blend, as well as that of the reaction temperature, on the amount of coke deposited is analysed using the data collected in Table 4.1, showing the coke concentration of the catalysts used in the hydrocracking of VGO, PMMA/VGO and PET/VGO blends for 300 min. As evidenced, the extent of the reactions is directly related to the coke formation in terms of the deposited amount. As the cracking reactions advance, the formation of dienes from the primary cracking of large hydrocarbons can turn into saturated species or oligomers that then will evolve into coke precursors [205]. Hence, at higher cracking levels is coherent to obtain higher coke amounts as a result of condensation mechanisms. Moreover, plastics can play a key role in coke formation and development, as the hydrogen acceptor nature of some of them can hamper the hydrogenation and cracking of coke precursors. This way, the addition of branched hydrocarbons [312] as in the case of PMMA/VGO and the higher conversions of these reactions lead to the highest coke deposits at both temperatures.

Table 4.1. Coke concentration (wt%) of the spent catalysts used on the hydrocracking of VGO, PMMA/VGO and PET/VGO blends for 300 min.

Temperature (°C)	VGO	PMMA/VGO	PET/VGO
400	10.5	15.8	12.6
420	16.5	16.5	15.9

To fully understand the formation of coke and, attending to its nature, TPO profiles of the spent catalysts of reactions carried out at 300 min, both temperatures and for the three blends are collected in Figure 4.10. The deconvolution of VGO and PMMA/VGO catalysts profiles is also included, while there is no evidence of this dual nature in the PET/VGO profile. A direct relationship between the location of the combustion peak and the conversion level achieved can be noticed, as the higher the conversion the higher the maximum temperature of combustion. In this matter, the effect of temperature is

particularly noticeable in VGO and PMMA/VGO profiles. As can be seen, the deconvolution gives a higher signal in the second peak in both cases at 420 °C (Figure 4.10b), which represents a major concentration of a more developed coke than the one less condensed. It is well-established that zeolites can lead to polyaromatic structures development that forms coke due to the hydrogen transfer reactions and the steric limitations for releasing the condensed structures once formed [313]. Apart from that, it can be deduced from the location of the peaks (which have similar temperatures for both feeds) that the coke structures formed must be similar, so the coke formation mechanism takes place in similar ways.

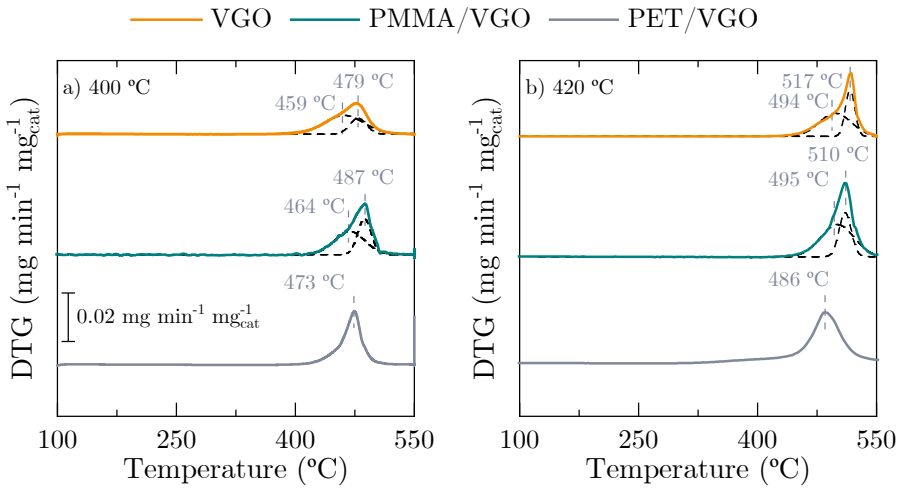

Figure 4.10. TPO profiles of the spent catalysts recovered from VGO, PMMA/VGO and PET/VGO hydrocracking reactions at a) 400 °C and b) 420 °C. Reaction conditions: 80 bar, C/F = 0.1, 300 min.

With respect to the PET/VGO profile, which is somehow different from the others, mainly because of the predominance of low combustion temperatures. This can find its explanation in the lower development of the hydrocracking mechanisms that also lead to the development of coking reactions and vice versa. The competitive adsorption on the active sites of VGO and PET molecules can lead to a lower conversion due to the lower PET hydrocracking capacity observed.

Moreover, the occupation of those sites on the surface of the catalyst (in which the plastic would be deposited first) would modify the posterior activity of the catalyst [312, 313], thus explaining that even if the polymer is progressively converted the evolution of hydrocracking mechanisms is slower. At the same time, the introduction of heteroatom-containing and aromatic molecules, such as the ones provided by PET hydrocracking, can have a notorious impact on the development of coke formation reactions [314]. However, the development of a less condensed coke and the minor quantities reflected in Table 4.1 lead to conclude that the catalyst deactivation should be less severe in the PET/VGO system than that observed in PMMA/VGO reactions.

In order to confirm some of the possible coking mechanisms above mentioned, the effect of pressure on coke formation through the measurement of their content and profiles are collected in Table 4.2 and Figure 4.11. First, it can be seen that the trends followed by the coke amounts on the spent catalysts (Table 4.2) are as would be expected because the enhanced hydrogenation due to the higher hydrogen pressure promotes the hydrogenation of both coke and its precursors [315].

Table 4.2. Coke concentration (wt%) of the spent catalysts of VGO, PMMA/VGO and PET/VGO hydrocracking at 420 °C and 120 min.

Pressure (bar)	VGO	PMMA/VGO	PET/VGO
50	20.8	22.0	19.2
80	16.3	16.4	15.7
110	12.7	12.0	12.6

The effect of pressure on TPO profiles is collected in Figure 4.11. It can be seen that the general trend when increasing hydrogen pressure is that of reducing the temperature of combustion of the deposited species on the spent catalysts, so it is conclusively proved that the hydrogen favours not only the reduction of coke amount but also its hardness.

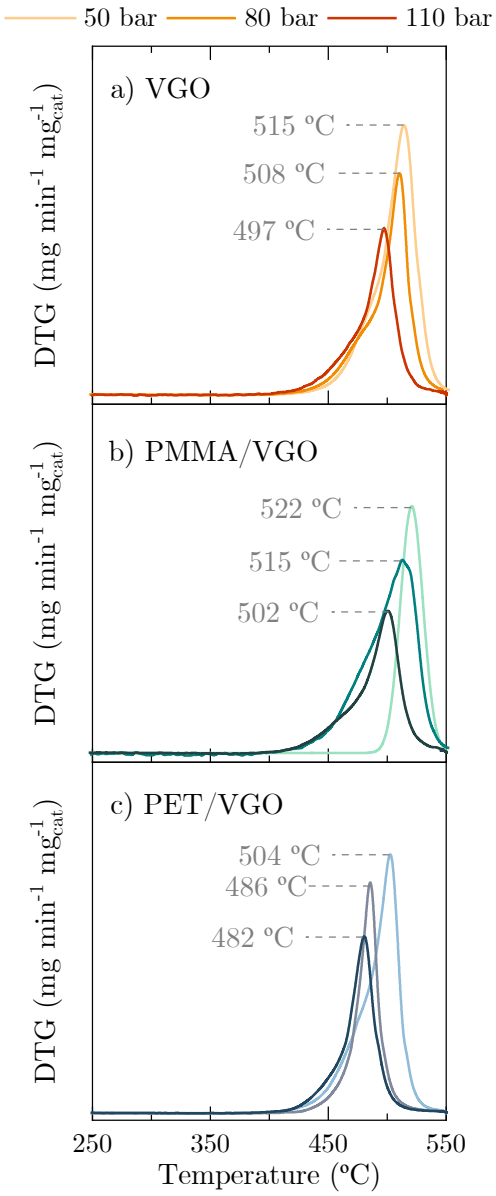

Figure 4.11. TPO profiles of spent catalysts used in a) VGO, b) PMMA/VGO and c) PET/VGO hydrocracking at studied pressures. Reaction conditions: 420 °C, 120 min, C/F = 0.1.

However, it must be noted that the displacement on the combustion peaks is similar for both types of coke (one peak at a higher temperature and one shoulder

at a lower value), therefore not affecting selectively the coke formation. Thus, because of the increasing hydrogen pressure, the mechanisms of coke formation are globally palliated through the hydrogenation of coke precursors that inhibits the development of condensed species that appear at lower pressures. Moreover, the utilization of higher hydrogen pressures is associated with higher residual activity of the catalyst, with regard to both the equilibrium between the coke formation and hydrocracking forces and the reduction of other deactivation mechanisms such as the sulphurization of the metallic phase [309].

Attending to the differences found on each blend, it must be pointed out that the combustion temperature of the peaks pivots around the 80 bar peak in a range similar to that observed in Figure 4.10. Yet a different distribution can be observed on VGO and PMMA/VGO catalysts profiles when compared to those of PET/VGO. This way, the bimodal distribution previously commented on is more noticeable in Figure 4.11a and Figure 4.11b, while the combustion peak of PET/VGO coke seems to be sharper. The latter can be attributed to a higher concentration of aromatic species (in coherence with the nature of the plastic and its influence on the general composition, as concluded in Section 4.2) even when they present lower combustion temperatures due to the minor development of the hydrocracking reactions.

4.4. CATALYST REGENERATION VIABILITY

On account of a different reaction system has been used when feeding the oxygenated plastics along with the VGO, the regeneration method previously proved shown to be efficient in Section 3.5 (diluted air atmosphere at reaction temperature) has been tested using this reaction system to verify the applicability of the procedure selected. This way, Figure 4.12 collects the yield distribution of the products from the PMMA/VGO and PET/VGO hydrocracking when using the fresh catalyst compared to those obtained after that catalyst is regenerated in an oxidizing atmosphere. As occurs when feeding a PS/VGO blend, almost a full recovery of the catalytic activity can be observed due to the broadly similar distribution, with very slightly lower yields of the products of interest due to some less extent of hydrocracking reactions attributed to the irreversible deactivation mechanisms.

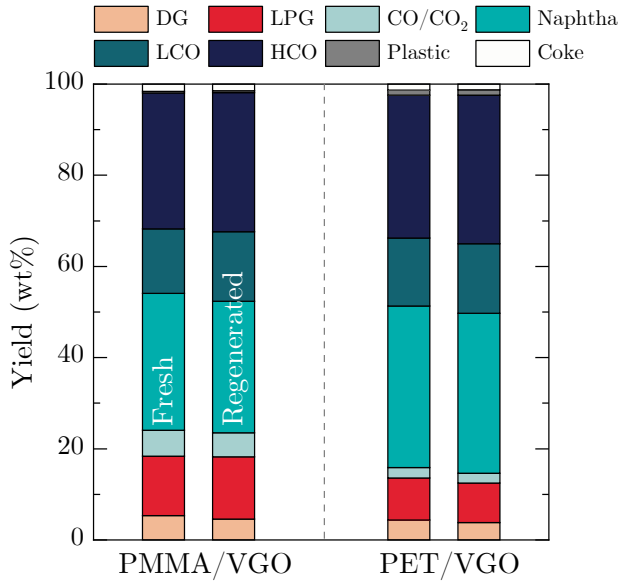

Figure 4.12. Product yields distribution of PMMA/VGO and PET/VGO hydrocracking using fresh and regenerated catalysts. Reaction conditions: 420 °C, 120 min, 80 bar, C/F = 0.1.

When comparing both systems, it can be noticed that the activity decay when using fresh and regenerated catalysts is almost identical, so the reversible deactivation phenomena are equally overcome, as the coke, sulphide materials

and even some basic nitrogen-containing compounds can be removed through an oxidizing atmosphere [316] when regenerating hydroprocessing catalysts. On the contrary, the lesser reactions extent that can be appreciated in Figure 4.12 is a consequence of irreversible mechanisms such as metal deposition, as explained in Sections 3.4.2 and 3.5.1. The mere use of hydrogen and a hydrocracking catalyst already trigger the HDM mechanisms [198], regardless of the materials that are being fed, as virgin plastics are supposed to be poisoning metals free. This, along with the fact that those metals only come from the VGO in the systems that have been employed here, can induce to establish a similar behaviour of the HDM function on PMMA/VGO and PET/VGO reactions, therefore resulting in a similar activity decay.

Catalyst regeneration has the same repercussion on naphtha composition as it has on yields distribution, as depicted in Figure 4.13.

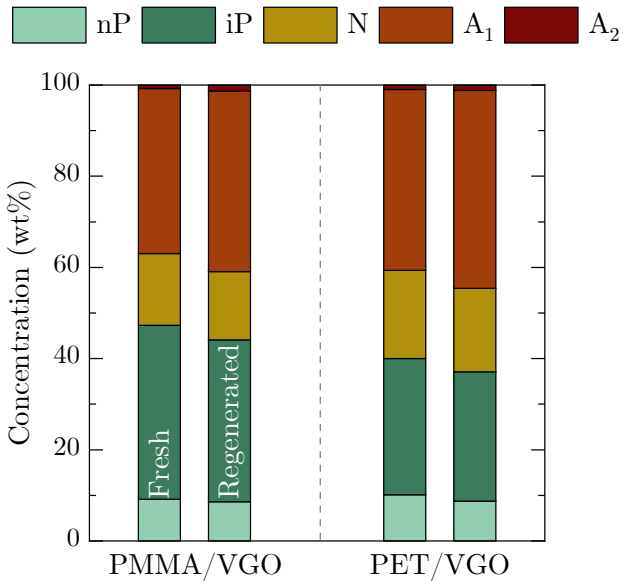

Figure 4.13. Naphtha composition of PMMA/VGO and PET/VGO products using fresh and regenerated catalysts. Operating conditions: 400 °C, 120 min, 80 bar, C/F = 0.1.

A trivial ($<$ 5 wt%) change in the concentrations of each group can be noticed when the regenerated catalyst is used for both blends. The affection of poisoning

metals to the metallic function has been already referred to [281], with a simultaneous probability of causing a pore blocking of the catalyst (and more specifically the support) that could lead to an inferior cracking activity. As the higher concentration of aromatics in the products is supposed to be a result of a minor hydrogenation activity and not from cyclization of the produced paraffins as there is a considerable recovered activity, the decreasing amounts of paraffins can be explained through the modification of the support by these metals [317]. In fact, the development of dehydrocyclization reactions is strongly influenced by the operating conditions (temperature, space-time) [318] and is given a secondary role with respect to hydrocracking reactions when only the properties of the catalysts are modified. Anyhow, the regenerating method can be considered as efficient as the metal storage capacity of the catalysts is limited and once this amount has been achieved through consecutive reaction-regeneration periods the composition of the naphtha obtained is expected to remain constant along these cycles.

The effect of the regeneration of this catalyst on LCO fraction when PMMA/VGO and PET/VGO blends are hydrocracked has also been studied, as depicted in Figure 4.14. The same effect that the regeneration has on yield distribution and naphtha composition can be here noticed, with minor differences between the concentrations obtained (less than a 3 wt%). In this case, the hampering of aromatics hydrogenation cannot be definitively established as the origin of these variations, as it has already been commented that the hydrogenation of polyaromatics is much easier than that of monoaromatics. Note that the exact quantification of all the compounds present in these samples can admit some analysis error so the discrepancies between these contents do not allow to establish a real impoverishment of the quality of the LCO fraction produced, concluding that a good-quality LCO can be obtained through the controlled regeneration of the catalyst.

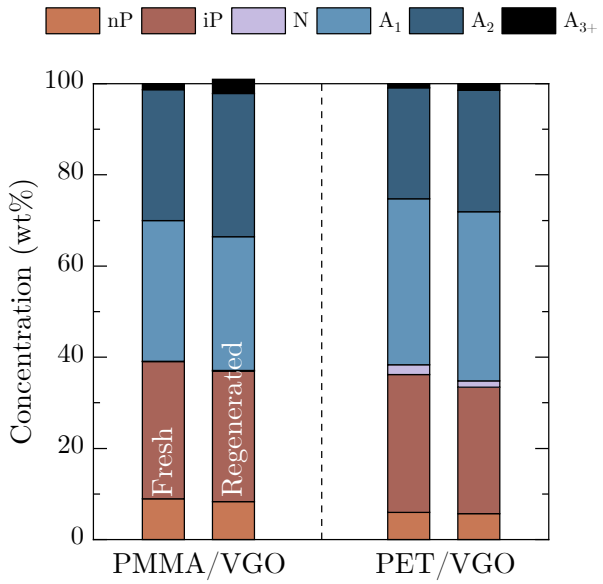

Figure 4.14. LCO composition of PMMA/VGO and PET/VGO products using fresh and regenerated catalyst. Reaction conditions: 400 °C, 120 min, 80 bar, C/F = 0.1.

Chapter 5

ANALYSIS OF HYDROCRACKING MECHANISMS

This Chapter deepens the mechanisms involved in the reactions of the previous Chapter, those being the hydrocracking of VGO, PMMA/VGO and PET/VGO blends. The composition analysis is commonly performed in terms of the fractions of interest, paying attention to naphtha and LCO fractions' composition. However, neat VGO and heavy products contain several heavy structures that are usually disregarded. Moreover, the importance of the heteroatomic molecules present in crude oil derivatives has been repeatedly reported throughout Chapters 3 and 4. In addition, the co-feeding of heteroatom-containing plastics reinforces the weight of side hydroprocessing routes (such as HDO for PMMA and PET hydrocracking). Thus, NMR, PFPD and FT-ICR techniques have been used in this Chapter to establish more developed and comprehensive mechanisms.

5.1. ANALYTICAL TECHNIQUES

Hydrocracking runs have been performed according to those conditions exposed in Chapter 4. Shortly, they are the following:

- Feedstock: plastics (10 wt%) in VGO, only VGO
- Temperature: 400-420 °C
- Pressure: 80 bar
- Reaction time: 300 min
- Catalyst-to-feed ratio (mass basis): 0.1

For this part of the study, pressure and time have been set to fixed values due to the amount of data to be processed considering all the available samples obtained in Chapter 4.

Bearing that in mind, the basis for using additional characterization techniques must be pointed out. Figure 5.1 schematizes the range of a simulated distillation chromatogram that can be trustfully used for identifying species with each type of technique. NMR analyses are particularly useful when analysing mixtures with a large number of components with wide molecular weight distribution (MWD) [319], while FT-ICR extends the range of GC×GC/MS for an in-depth compositional characterization [320]. The interest in analysing the heaviest fractions lies in virgin VGO composition, which is almost fully represented by HCO, as well as the yield of this fraction in the hydrocracking products, which sometimes account for almost 50 wt%.

FT-ICR improves the insights into crude oil composition providing information within a wide range of m/z values, although this range should be bounded for accurate structure elucidation [321]. Even considering that the information provided by this technique is considered qualitative, the mere presence of heteroatomic compounds can be confirmed by an initial approach.

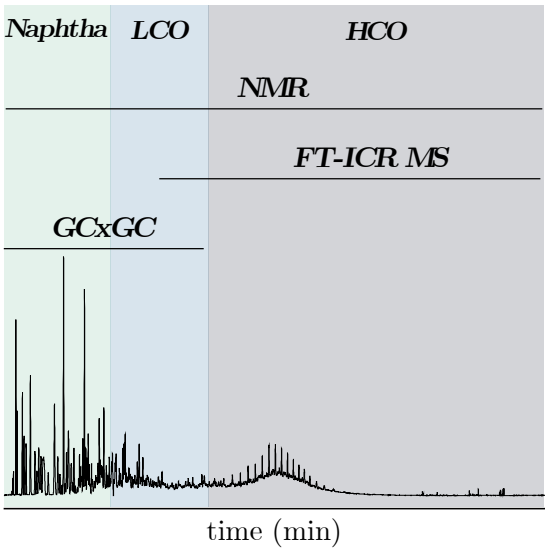

Figure 5.1. Scheme of the range of analytical techniques on a sample simulated distillation chromatogram sample.

Figure 5.2 depicts the FT-ICR chromatograms of virgin VGO for the main classes of compounds found in crude oil products, namely hydrocarbons, nitrogen, sulphur and oxygen compounds.

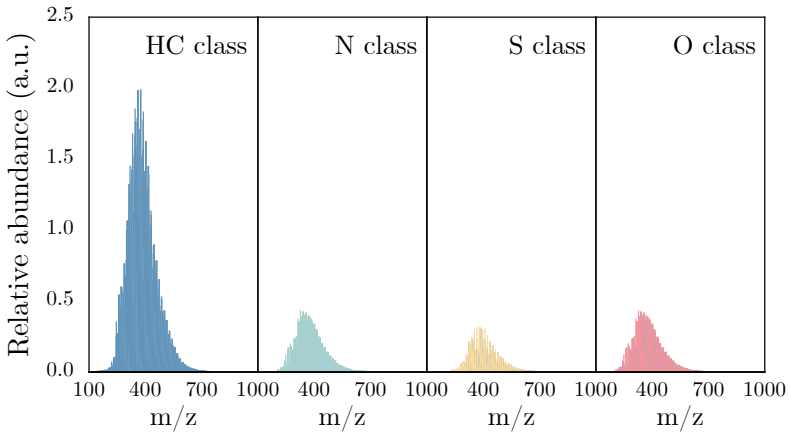

Figure 5.2. Relative abundance of each class of compounds found in VGO.

Although the major quota of free-heteroatom compounds can be appreciated, the relative abundance distribution and maximum location confirm the presence of typical refractory compounds whose presence needs to be followed. This way, the extent of HDN, HDS and HDO functions and their relationship with the catalytic performance seen in Chapter 4 can be endorsed [322].

Regarding the abundance distribution, the concentration of the main structures can be found between m/z = 300 and m/z = 500 for all the classes. This signal concentration range has been previously reported in other MWDs [323], mainly composed of four and five rings aromatics. Note that the utilization of APPI (+) FT-ICR has some limitations regarding the type of compounds that can be identified and some additional species can be found if different ionization sources are used [324]. Besides, the non-polar nature of long lineal paraffins locates them out of the detection range of this equipment. Anyways, the width of the signal of the HC class indicates that the heaviest compounds (highest m/z values) belong to this class, with final values approaching m/z = 700. On the other side, the lowest signal values correspond to both HC and N classes, while S and O classes are limited to a more constrained m/z window. This might be a consequence of the VGO primary treatment (prior to the supply), which can eliminate some light-reactive sulphur and oxygen species, while nitrogen compounds are known for being more refractory [175] and therefore have not been strongly affected.

Due to the size of the data and the different mechanisms that affect each of the classes found in the VGO and its hydrocracking products, the families observed in Figure 5.2 are hereunder analysed separately.

The species number of the distinct families is considered and its evolution at different temperatures for each blend is depicted in Figure 5.3. Non-heteroatomic compounds are the most prominent in both VGO and hydrocracking products regardless of the feed. The number of HC species in the original VGO and the products is shown in Figure 5.3. As depicted, the number of species has the opposite trend according to each combination of feed and temperature. This way, at 400 °C VGO and PET/VGO hydrocracking products present a larger number of HC species than those of original VGO. This could indicate an intermediate

character of those species since the amount of such species is reduced at 420 °C. Moreover, the higher advance of the hydrocracking reactions observed for PMMA/VGO could lead to a higher number of light species not reflected here, therefore fulfilling this trend. The formation of more reactive species such as reaction intermediates has been already observed in hydrocracking [325], concluding that in absence of a very strong cracking function, other pathways such as isomerization take place.

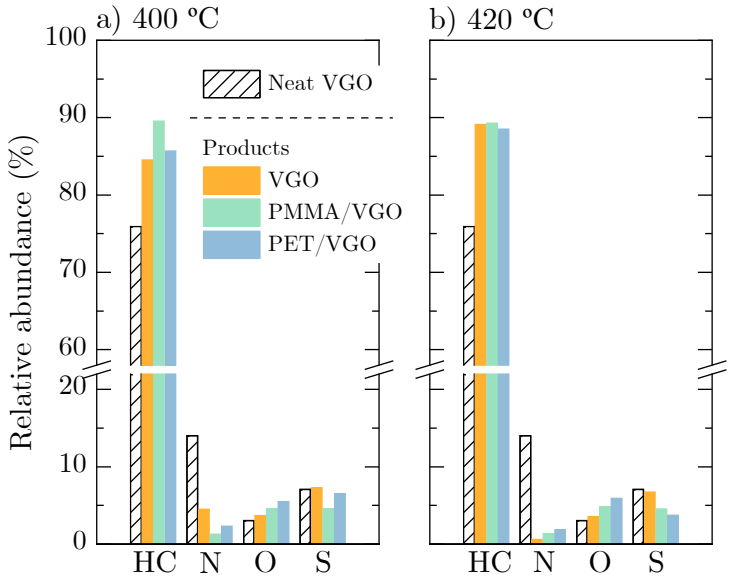

Figure 5.3. Distribution of the different species families of the feed and hydrocracking products at a) 400 and b) 420 °C. Reaction conditions: 300 min, 80 bar, C/F = 0.1.

The appearance of these species is conditioned both by the progress of the reactions and by the introduction of plastics, since it can be seen that at 400 °C there are more HC species in the products of the blends than in those of neat VGO hydrocracking. However, when the conversion of VGO is higher at 420 °C this number is equalized, indicating a more similar compositional space due to the higher severity of the reactions, which favour the conversion when feeding only VGO. Regarding the heteroatom species, the reduction of nitrogen species

seems to be directly related to the conversion of the original feed, favoured both by the introduction of plastics (due to the absence of nitrogen in them) and by the temperature. Regarding the other families, the reduction of nitrogen species seems to be directly related to the conversion of the original feed, which is favoured by temperature, especially when feeding only VGO. The increasing number of oxygenated compounds, which is noticeably more remarkable in PMMA/VGO and PET/VGO products, confirms the introduction of singular compounds coming from plastics. Indeed, the higher abundance of oxygenated compounds in PET/VGO products at both temperatures confirms the hypothesis stated when analysing the oxygen mass balance in Chapter 4. Finally, the reduction of sulphur species seems to be facilitated by the introduction of plastics, while the VGO products show values similar to those of neat VGO. This indicates that the sulphur species present in VGO are probably very refractory, corresponding to condensed aromatics typical of asphaltene-type structures that are subject to mass transfer limitations in HDS reactions [326].

5.2. HYDROCARBON (HC) CLASS

In order to resolve the composition of the liquid product at a molecular level, APPI (+) FT-ICR MS has been applied to the samples. HC class iso-abundance plots of double-bond equivalent (DBE) versus carbon number are collected in Figure 5.4 for untreated VGO and hydrocracking products at 400 °C and 420 °C, and 300 min. DBE is a method used to calculate the degree of molecular unsaturation with assigned formulas, indicative of the number of aromatic rings and double bonds present in those molecules. Dashed lines represent the planar limits, which are usually interpreted as the maximum DBE values for given carbon numbers [327]. These lines should not be crossed by natural compounds and, generally, they give an approach to the level of condensation of aromatic structures. Concerning the untreated VGO, its contour plot presents an island shape with a maximum centre of DBE values between 9 and 11 and carbon numbers of 25-28. This type of structure is representative of anthracene and pyrene species. The evolution of this plot observed in the hydrocracking products reinforces the evidence of the hydrocracking mechanisms taking place through some reaction intermediates. This way, the evolution of hydrocracking can be appreciated by attending to the samples of growing levels of conversion: at 400 °C, first it can be appreciated in VGO products how the species are hydrogenated by the increase in lower DBE structures concentration. Then, in PET/VGO products, the general carbon number is reduced (through cracking mechanisms of those saturated species), obtaining as final products (whose concentration is more pronounced in PMMA/VGO products) species close to the planar limit, a DBE of ca. 12 and a carbon number around of 18-20, which corresponds to highly refractory species such as pyrene, that usually are considered as soluble coke or coke precursors [328].

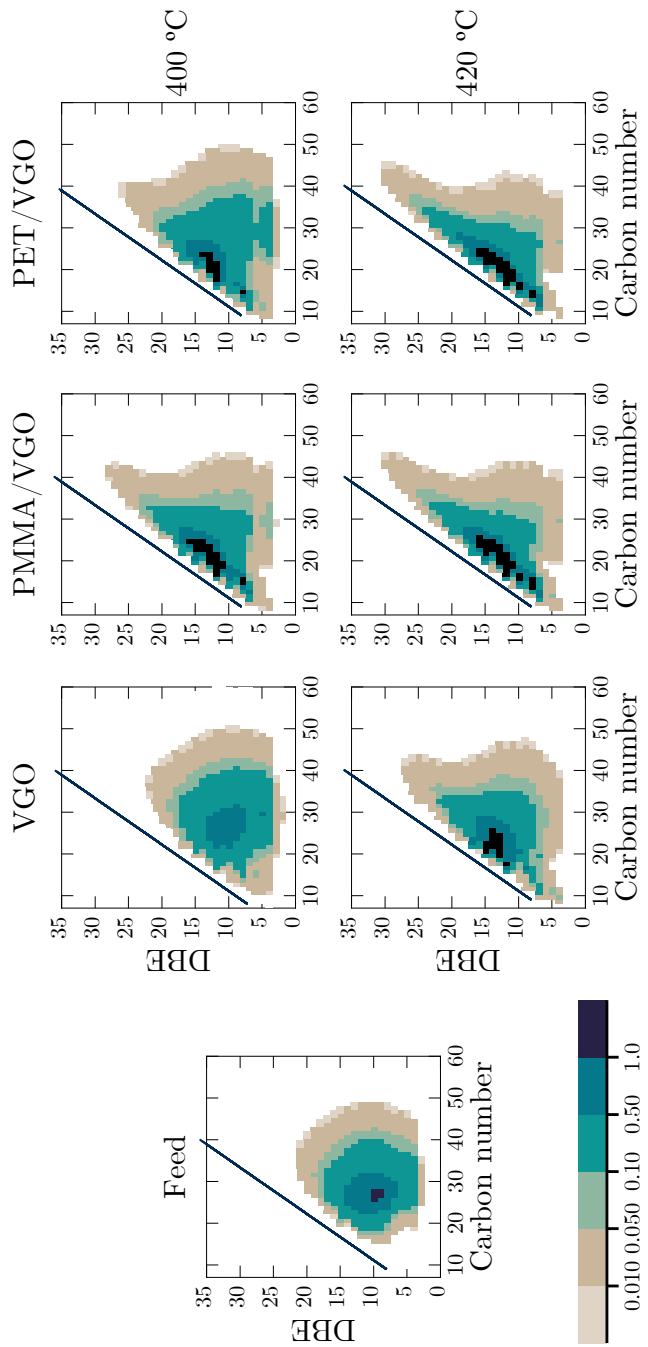

Figure 5.4. Contour plots of DBE versus carbon number of feed and VGO, PMMA/VGO and PET/VGO hydrocracking products at 400 and 420 °C. Reaction conditions: 300 min, 80 bar, C/F = 0.1.

At 420 °C, the plots indicate a different shape in polymer blends products than that obtained for VGO hydrocracking products. The elongation of the compositional space corresponds to compounds with the highest DBE values. This is especially remarkable in PET/VGO products, with a higher concentration of condensed structures, concluding that the mechanism of PET hydrocracking might be involved in the formation of this type of structure. This observation is consistent with some previous studies that also inform about the plastics' potential to form PAHs [329], particularly those containing aromatics in their structures (as in the case of PET).

The quantification of the different C-containing linkages in the liquid hydroprocessing products has been conducted through NMR. The structural assignments have been based on those established by Poveda and Molina [241]. As an example, the ^{13}C NMR spectrum of one of the samples (PMMA/VGO products at 400 °C) is shown in Figure 5.5. It shows the regions that have been integrated with their corresponding groups and two example molecules to illustrate the position of the type of carbons to which each refers. While analysing ^{13}C NMR spectra it should be taken into account that, when working with complex mixtures, the integration is conditioned by the correct separation of peaks with a sufficient signal-to-noise ratio [330], so those regions that presented peaks with sufficient resolution in all the samples were chosen. Spectra were symmetrised and baseline-corrected and then the curve of the peaks appearing in each of the selected regions was integrated. These regions can be classified according to the aliphatic or aromatic nature of the carbons. Of the first group, emphasis has been placed on paraffinic and naphthenic carbons of the CH_2 type (21.5-50.0 ppm), in which the methine carbons are included but which, due to the strongly hydrogenating nature of the reactions, have been found to have no value; methyl carbons in alpha position to aromatic rings (18.5-21.5 ppm) and carbons of the CH_3 type (3.0-18.5). Regarding the aromatic carbons, the regions of interest and with an acceptable signal for their integration are the non-protonated aromatic carbons (137.0-160.0 ppm), from which the regions associated with bonds with oxygen atoms (154.0-157.0 ppm) and sulphur or

nitrogen (137.0-140.5 ppm), and protonated aromatic carbons (85.0-129.2 ppm) have been subtracted.

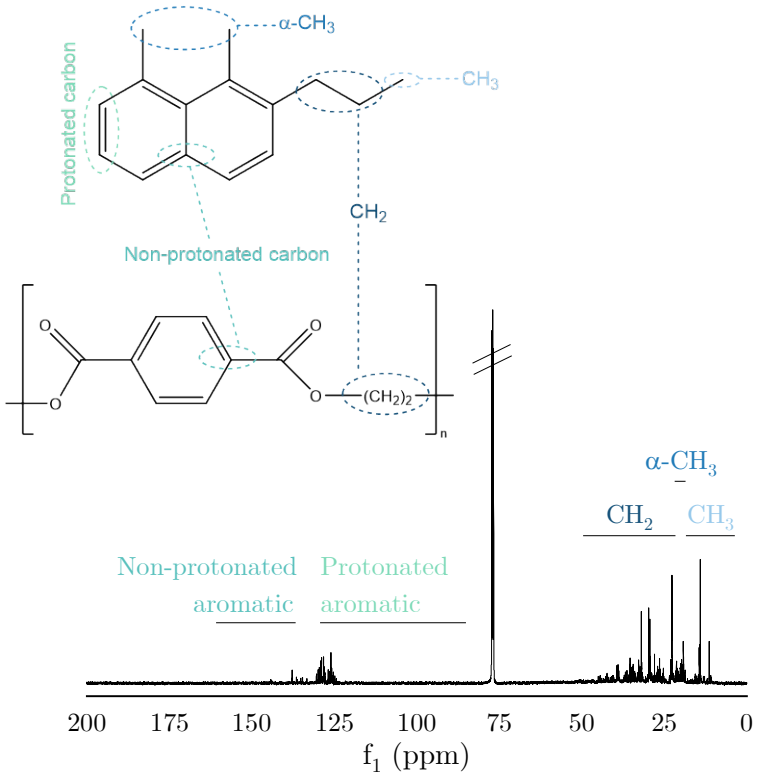

Figure 5.5. ^{13}C NMR spectrum of an exemplary sample and regions to be integrated.

The results obtained from the integration of these regions are pictured in Figure 5.6. Overall, when adding a plastic to the VGO, the aromaticity of the liquid product mixtures is affected to a greater extent in comparison to the aliphaticity. In Figure 5.6a a reduction of aliphatic CH_2 carbons is observed in the products of the blends at 400 °C due to the shortening of the side chains of aromatic compounds, which in turn leads to a global higher content of aliphatic CH_3 groups. In addition, there is a slight parallel increase of CH_3 groups which is limited in the products of the blends with plastics by the increased gas formation (Figure 4.2). This is in line with the shift of the signals in Figure 5.4 to compounds

with lower carbon number. In addition, the higher content of protonated aromatic carbons (Figure 5.6b) corresponds to ring-opening reactions intrinsic to hydroprocessing reactions, which are more advanced in the products of the mixtures at 400 °C [147].

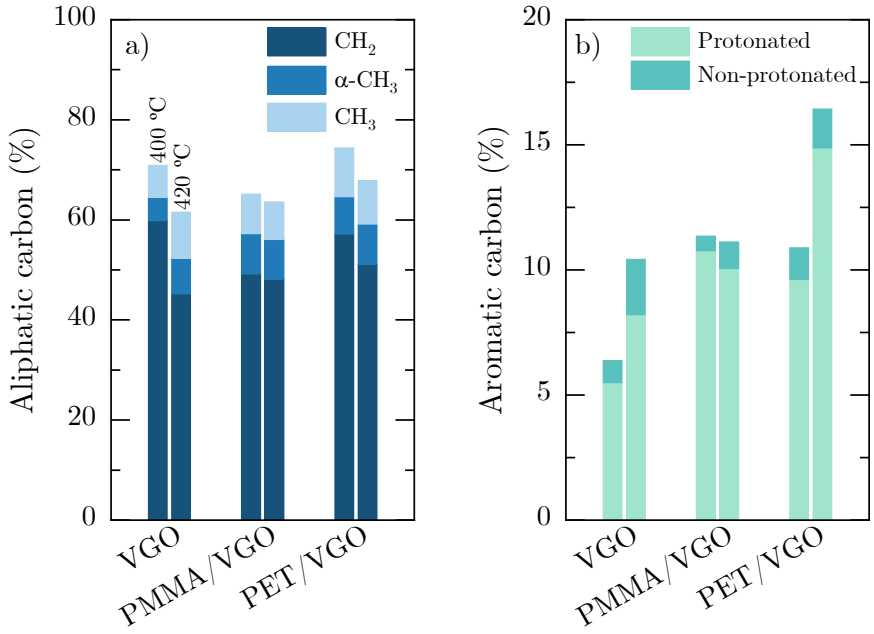

Figure 5.6. ^{13}C NMR relative intensity of the selected regions of a) aliphatic and b) aromatic carbons of VGO, PMMA/VGO and PET/VGO hydrocracking products at 400 and 420 °C. Reaction conditions: 300 min, 80 bar, C/F = 0.1.

The higher conversion of polyaromatics as well as the aromatic nature of PET explain the higher concentration of aromatic protonated carbon at 420 °C. The content of non-protonated carbons, associated with fused aromatic ring structures [331], is lower for the PMMA/VGO products compared to VGO and PET/VGO, as a consequence of the higher conversion of HCO (from which the polyaromatic structures originate) when co-feeding PMMA and due to the absence of aromatic structures in this polymer. Also, the higher conversion achieved at 420 °C promotes the production of less condensed aromatics, hence the growth of protonated aromatic carbons. Although the same growth is observed in the PET/VGO products (both by the formation of aromatics and by the contribution

of these groups when hydrocracking the polymer), in the blend products an increase of the non-protonated aromatic carbon is also observed, which can be related to the structures with higher DBE (near 30) shown in Figure 5.4 and, as stated previously, attributed to the aromatic nature of the PET molecule. The value obtained for PET/VGO products is not only related to a lower conversion (Figure 4.1) but also to the contribution of the PET molecule to benzene-type structures [332].

In addition to one-dimension analyses, the assignments of cross-signals in both Heteronuclear Single Quantum Coherence (HSQC) and Heteronuclear Multiple Bond Correlation (HMBC) spectra, collected in Figure 5.6, are a useful tool when elucidating structures and model compounds of complex mixtures. In this scheme, arrows are representative of the groups (indicated by capital letters) interactions through HSQC NMR, and the carbon-hydrogen cross points elucidated through HMBC (with apostrophes) are depicted by remarking those atoms with black and white spheres.

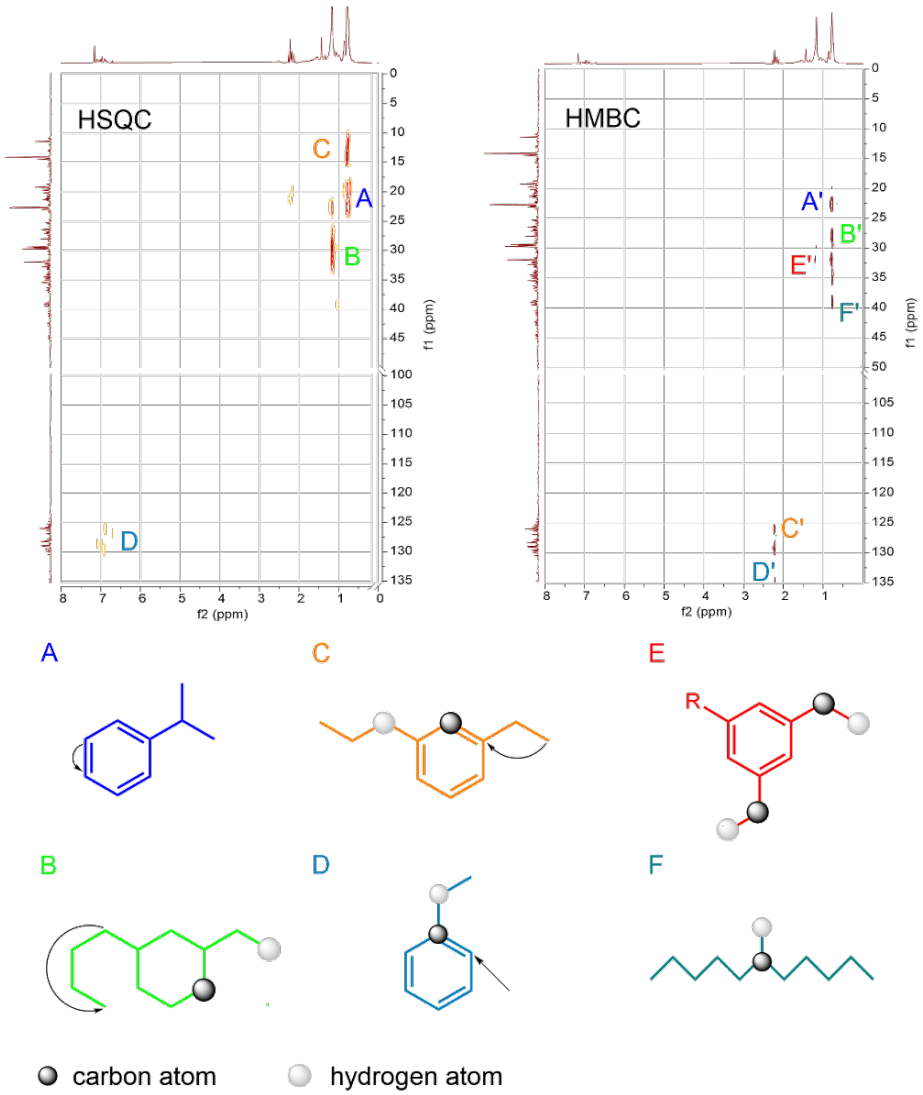

Figure 5.7. Scheme of 2D NMR cross points: HSQC relationships are indicated by arrows and HMBC correlated atoms are highlighted.

The application of the selected regions exemplified in Figure 5.7 and the calculation of the percentage areas corresponding to each of them for the hydrocracking products of VGO, PMMA/VGO and PET/VGO samples lead to their comparison, collected in Figure 5.8. By analysing the interactions between different types of bonds and functional groups, the development of ring-opening

mechanisms and the effect of temperature on the cracking and condensation functions can be verified.

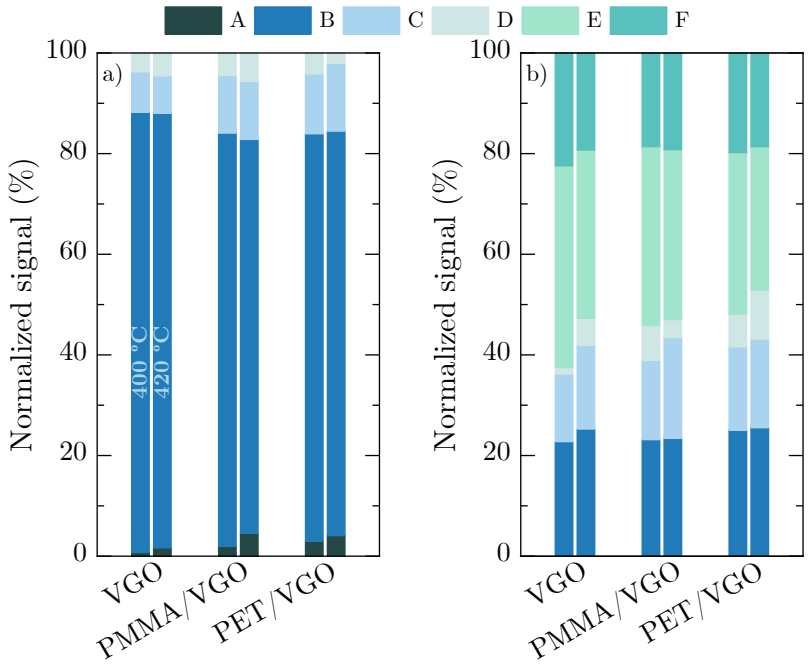

Figure 5.8. Comparison of 2D NMR regions of the VGO, PMMA/VGO and PET/VGO products for a) HSQC and b) HMBC results at 400 and 420 °C. Reaction conditions: 300 min, 80 bar, C/F = 0.1.

On the one hand, the hydrocracking mechanism favours the opening of polyaromatic rings to give rise to lighter aromatic compounds, which is reflected in the increase of the relative intensity of the D region in both HSQC and HMBC. The former is a consequence of the formation of monoaromatics in naphtha (as seen in Figure 4.5) and diaromatics in LCO (Figure 4.6), while the latter corresponds to the shortening of side chains resulting from the increased cracking function attributable to the temperature rise. In fact, this shortening (related to the decrease of region B and an increase of region C) and even the elimination of side branches linked to aromatics (increasing region A and reducing region E) is favoured with increasing temperature. This effect of temperature is consistent with what is observed in Figure 5.4 since the general shift of the compositional

space towards compounds with lower carbon number but partly maintaining the DBE indicates the reduction of the side chains for compounds that maintain their degree of aromaticity.

Finally, the F region is related to the degree of isomerization of the paraffins produced. Thus, the promotion of side-chain cracking reactions, the formation of more aromatic products by dehydrogenation (Figure 4.5) and the formation of gases from the cleavage of small chains attached to other functional groups (especially in the case of PET/VGO products) explain the detriment of the peaks in this region for VGO and PET/VGO products. For their part, PMMA/VGO products exhibit a small increase in this region which may be due to the nature of the polymer (whose degradation would be enhanced at high temperatures).

5.3. NITROGEN (N) CLASS

A great variety of heteroatomic molecules have been detected in both VGO and hydrocracking samples (Figure 5.3). For knowing the effect of hydrocracking under the studied operating conditions, nitrogen Van Krevelen diagrams have been plotted and collected in Figure 5.9, relating the hydrogen/carbon and nitrogen/carbon ratio of the formulated species. In addition, lines depict the core molecules of each family of compounds, namely indole (In), carbazole (Cz), benzocarbazole (BCz) and dibenzocarbazole (DBCz). Note that APPI (+) source has been positively applied to detect basic compounds [333], with less sensitivity than other ionization sources towards neutral compounds such as pyrroles. It can be seen that, generally, there is a considerable hydrodenitrogenation (HDN) of the samples, as the abundance of the compositional space diminishes in all the samples. Moreover, the range that encompasses the indole species is completely removed. When the temperature is increased, two effects can be appreciated on the nitrogen-containing species removal. On one side, the cracking reactions enhance the reduction of aromatic branches. On the other side, the narrowing of the compositional space indicates the simultaneous elimination of light aromatic structures (such as carbazoles, with relatively high H/C ratio values) and the reduction of low H/C and N/C ratio species. The stability of carbazoles core molecules has been previously reported and explained through the steric hindrance that may inhibit the catalyst action on them [334]. Regarding the differences between the samples of each feed, it can be observed that the addition of plastic seems to slightly hinder the HDN function at 420 °C, as the compositional space contraction is less noticeable in those cases. As the polymers virtually contribute with no nitrogen, it could be assumed that the total amount of nitrogen species would be less when adding them to the initial blends at the expense of VGO. The observation of the contrary effect indicates that the development of this function is essentially related to the general conversion of the VGO, thus explaining the different evolutions observed at 400 °C (when the species window is wider for VGO products) and 420 °C.

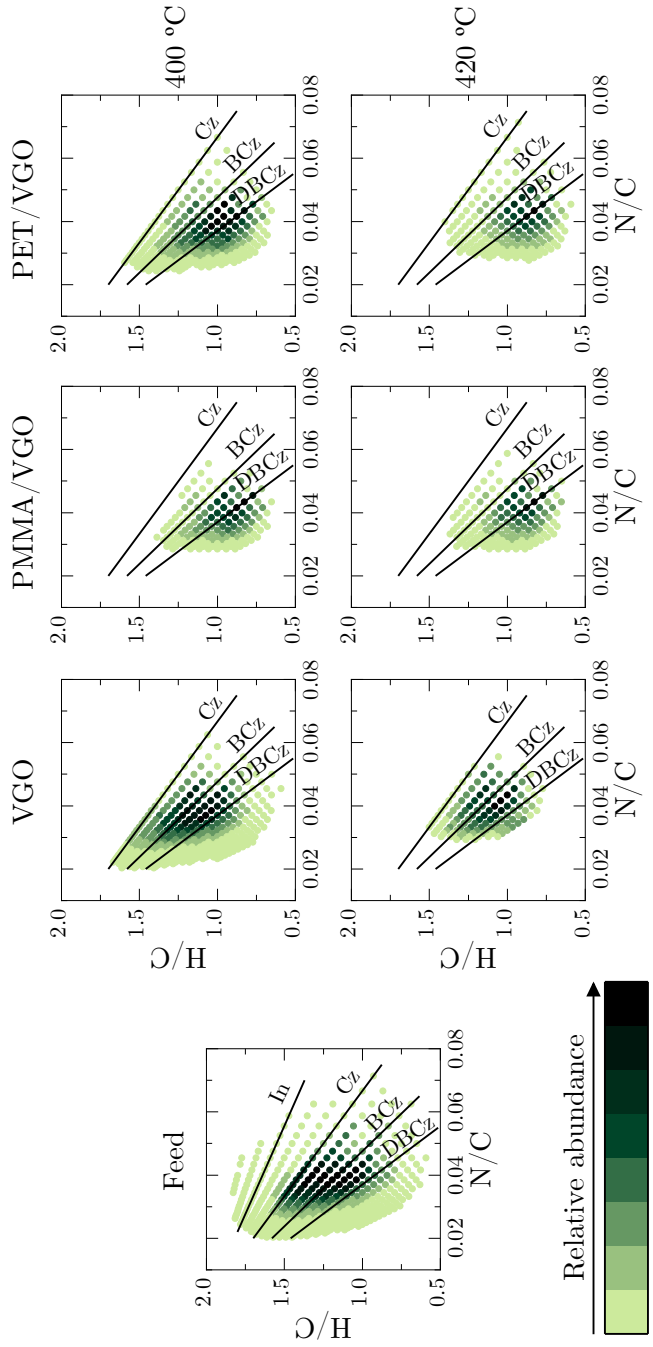

Figure 5.9. Iso-abundance plots of H/C aromatic ratio versus N/C ratio obtained by APPI (+) FT-ICR MS of feed and VGO, PMMA/VGO and PET/VGO samples at 400 and 420 °C. Reaction conditions: 300 min, 80 bar, C/F = 0.1.

For a better understanding of the HDN mechanism and its evolution in each of the systems, Figure 5.10 collects the distribution of the core molecules for each blend's products at 400 and 420 °C. The relative abundance is calculated as the relative intensity of each compound with respect to the most abundant one, thus not representing the total intensity of the compounds of this class but the relative distribution of the compounds and their evolution during the hydrocracking process. This way, it can be seen that the more equal distribution corresponds to the PMMA/VGO products compounds, which is coherent with the fact that they present the highest advance in the reactions. Moreover, it can be appreciated that these products only show compounds with DBE = 12 and DBE = 15 remaining even at 400 °C. This removal of the light nitrogen-containing species is justified by the sequent mechanism of C-N bond cleavage. In presence of an acidic catalyst, the breaking of this bond to form nitrogen-free species requires the previous hydrogenation of polyaromatic structures [335]. These compounds have been proven to be more refractory [336] and the thermodynamical restrictions attributable to the hydrogenation equilibrium also interfere with their transformation.

Here, temperature plays a key role in terms of nitrogen removal, as the increase to 420 °C exhibits a great narrowing of the compositional space, especially for VGO and PET/VGO products. This behaviour is owed to the shortening on both sides as follows: on one hand, the cleavage of C-C bonds affects side chains, this effect being promoted at high temperatures [337]. On the other hand, the preferential removal of high DBE and low carbon number compounds takes place under hydrotreating conditions [338]. Note that the remaining nitrogen acts as a hydrogenation and ring-opening inhibitor, thus strongly retarding the hydrocracking mechanisms development [147], as well as acting as a self-inhibitor for hydrodenitrogenation and hydrodesulfurization mechanisms [339].

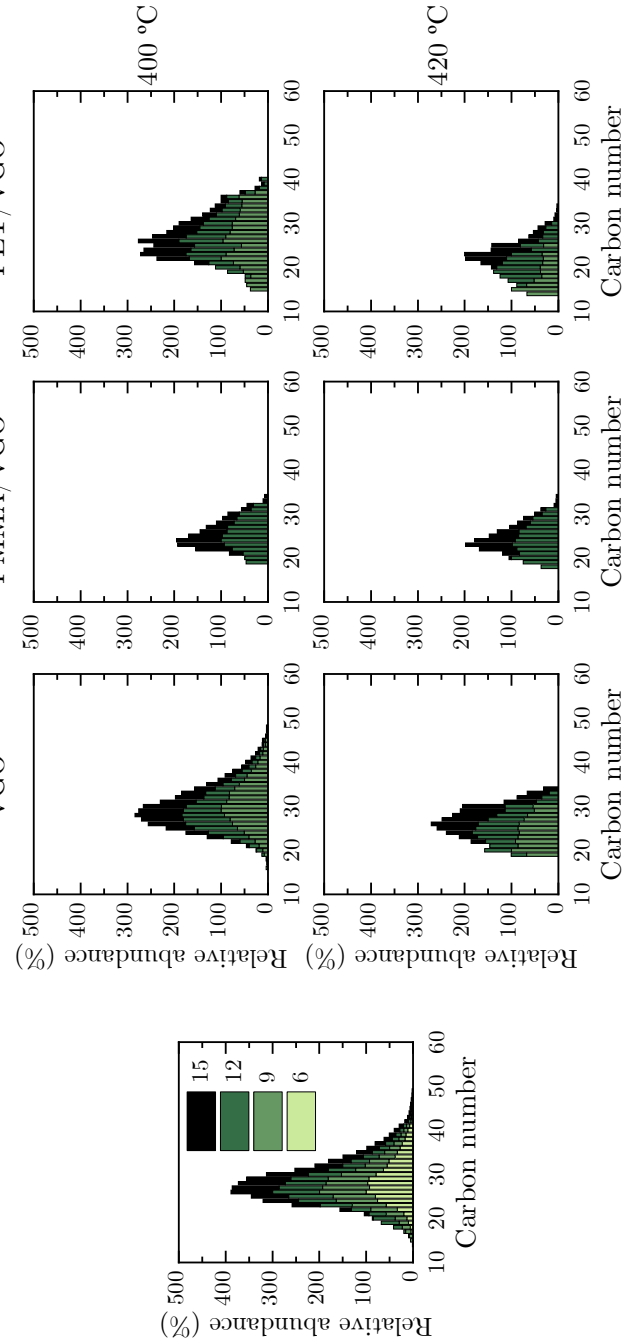

Figure 5.10. Relative abundance of the nitrogen core molecules (indole, carbazole, benzocarbazole and dibenzocarbazole) found in VGO and VGO, PMMA/VGO and PET/VGO hydrocracking products at 400 and 420 °C. Reaction conditions: 300 min, 80 bar, C/F = 0.1.

Bearing all this in mind, the hydrodenitrogenation mechanism that takes place under the studied conditions follows the following pattern: first, the light nitrogen-containing species are removed and the lateral chains are split from the heavy carbazole-derived molecules. Next, the more refractory species, corresponding mainly to DBE values of 12-15, disappear (due to the lower nitrogen content and relative abundance found in the products, as in Figure 5.3) at a similar ratio, therefore maintaining the distribution observed with increasing the temperature (especially in PMMA/VGO products). This equilibrium between the ratio of hydrogenation of heteroatom-containing polycyclic aromatic hydrocarbons and the direct cleavage of the C-N bonds of these molecules has been determined to be a function of both the catalyst and the operating conditions and has been previously observed in the hydrodenitrogenation of quinoline [340].

5.4. SULPHUR (S) CLASS

Increasingly stringent restrictions on the amount of sulphur in commercial fuels mean that there is particular interest in the evolution of these compounds during hydrocracking. Figure 5.11 exemplifies the FID and PFPD chromatograms of the original VGO and the products of the VGO hydrocracking at 400 °C and 300 min.

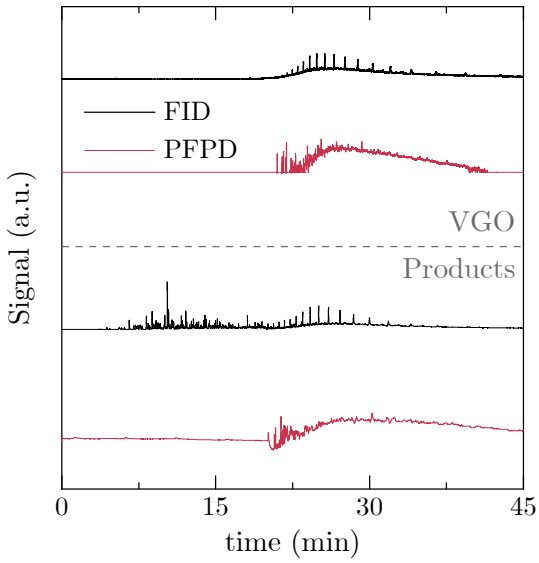

Figure 5.11. Sulphur analyses of untreated VGO and VGO hydrocracking products at 400 °C and 300 min.

It must be pointed out that the results of the products are representative of all the samples that have been analysed in terms of the location of sulphur peaks over the analysis time. In Figure 5.11 it can be appreciated how the hydrocracking affects the hydrocarbon distribution, producing many lighter compounds than those found in the untreated VGO. However, the desulphurization pathway seems to produce the cleavage of C-S bonds with relative ease, as there are no peaks found in the light zones, which correspond to naphtha and LCO fractions by contrast with the VGO FID chromatogram. Moreover, from the products chromatogram, it can be deduced that the desulphurization is not complete, since

sulphur compounds remain after the hydrocracking with respect to those found in the VGO.

A first approach to the effect of hydrocracking in the sulphur class compounds can be made by observing the intensity decay in the first peaks appearing in the VGO chromatogram. This way, it is logical to hypothesize that the compounds remaining in the products will be those with a higher number of aromatic rings, which have been confirmed to be the most refractory ones in other studies [153].

To deepen the compositional window of the sulphur class compounds in each blend after undergoing hydrocracking at 400 and 420 °C, the sulphur Van Krevelen diagrams of original VGO and VGO, PMMA/VGO and PET/VGO products are depicted in Figure 5.12. As with the nitrogen diagrams, the lines have been assigned to the species derived from the most representative sulphur compounds in petroleum-derived mixtures. This way, lines indicate the compounds derived from benzothiophene (BT), dibenzothiophene (DBT) and naphtobenzothiophene (NBT).

The catalyst HDS capacity observed in general at 400 °C is limited, as the concentration of some compounds remains in the high relative abundance range. Moreover, the removal of benzothiophenes is not fully achieved for VGO and PET/VGO blends, even when they are not considered to be highly refractory species. The restricted capacity of the catalyst to remove sulphur compounds is usually attributed to the sensitivity of noble metal catalysts to the presence of sulphur [341]. However, the temperature increment to 420 °C improves HDS performance, since most of the light species are completely removed, as anticipated by PFPD analysis (Figure 5.11). Indeed, the relative abundance of the most abundant compounds is reduced to less than 50 % of the original concentration in the VGO.

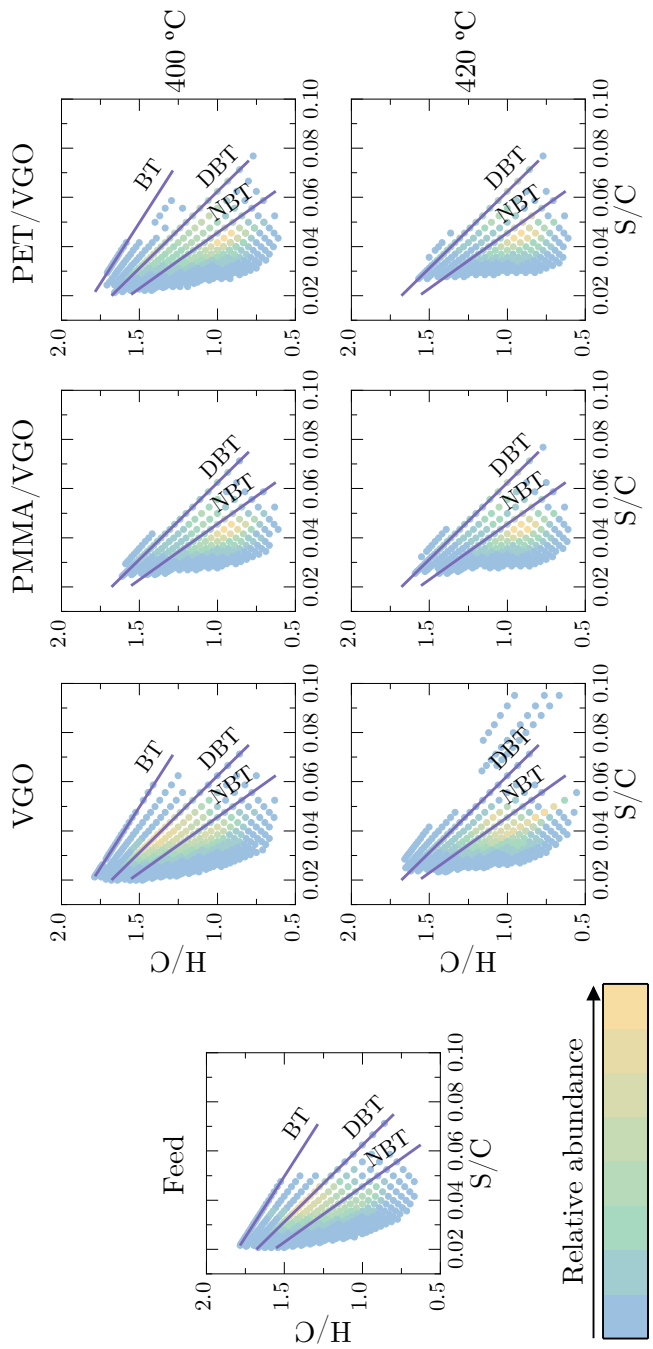

Figure 5.12. Iso-abundance plots of H/C aromatic ratio versus S/C ratio obtained by APPI (+) FT-ICR MS of feed and VGO, PMMA/VGO and PET/VGO samples at 400 and 420 °C. Reaction conditions: 300 min, 80 bar, C/F = 0.1.

On the contrary, most refractory compounds (with a low S/C ratio) are barely affected by the hydrocracking activity. Noble metals catalysts have been previously reported to provide low efficiency in removing refractory sulphur compounds, with an upper limit over the temperature in terms of HDS performance [342]. This has been associated with the poisonous character of sulphur towards these metals. Besides, the compounds with multiple aromatic rings present a steric hindrance, making it even more difficult for catalysts to remove them [343]. So much so that the compounds observed in Figure 5.12 are not limited to some usual model compounds used as refractory compounds (such as NBT) [344], but more aromatic species can be appreciated because of the lower S/C ratio. Apart from that, it has already been mentioned that the presence of other heteroatomic compounds (especially nitrogen) has also a significant influence on the development of HDS reactions [339].

Concerning the main differences observed between the products of each blend, the HDS behaviour can be somehow related to the hydrocracking activity, since the width of the compositional space becomes narrower as the samples show a higher level of conversion. However, a noticeable difference can be appreciated at 420 °C: VGO hydrocracking products are concentrated on BT-derived species with higher S/C ratios, which are not seen in the products of PMMA/VGO and PET/VGO blends. This can confirm that the preferred HDS route when using this catalyst is the one undergoing the primary hydrogenation of polyaromatic structures, leaving as a result the simplest benzothiophene form, which is then converted into a sulphur-free hydrocarbon. This is also supported by the effect of temperature on the hydrogenation equilibrium, which can hinder the rapid transformation of aromatic species, as well as by the cracking reactions (promoted at high temperatures) that form aromatic rings with no ramifications (and therefore with low H/C ratios).

Figure 5.13 illustrates the histograms of the distribution of the core molecules' relative abundance versus the carbon number of the sulphur species. The HDS performance of the catalyst previously commented on is somehow more appreciable in terms of the DBE = 6 species still being present after the

hydrocracking at 400 °C, except for the products of PMMA/VGO hydrocracking. The major conversion of this blend due to the light nature of the polymer has already been remarked when analysing other parameters affected by the reaction extent, maintaining this way the coherence between the introduction of an easy-conversion material and the advance of the hydrocracking mechanisms.

Regarding the influence of the hydrocracking on the product distribution in the sulphur compounds, it can be appreciated (especially in the plastics blends' products) that there is a displacement towards compounds with lower carbon numbers. This confirms the assumption made about the preferred route of HDS in the analysis of Figure 5.12. The proposed mechanism (ring-opening) involves the first opening of a ring, the resulting branch of which can be cleaved if the aromatic is very refractory. In this way, the cracking function of the catalyst favours the dealkylation of the branches formed during this mechanism or those of the original compounds [345]. Dealkylation reactions can relieve the steric hindrance of these compounds, so that once these compounds have been transformed, the sulphur compounds can be more easily converted, as may be the case with the results observed for PMMA/VGO products.

When performing the hydrocracking at 420 °C, a narrowing of the compositional window is observed, as the reduction of the long carbon number is a logical consequence of the enhancement of cracking reactions [346]. In this case, the effect of ring-opening and cracking reactions is almost equally observed in both PMMA/VGO and PET/VGO products, with an evident displacement of the compounds towards lighter species. In fact, the major difference is seen at 420 °C when analysing the effect of the plastic addition.

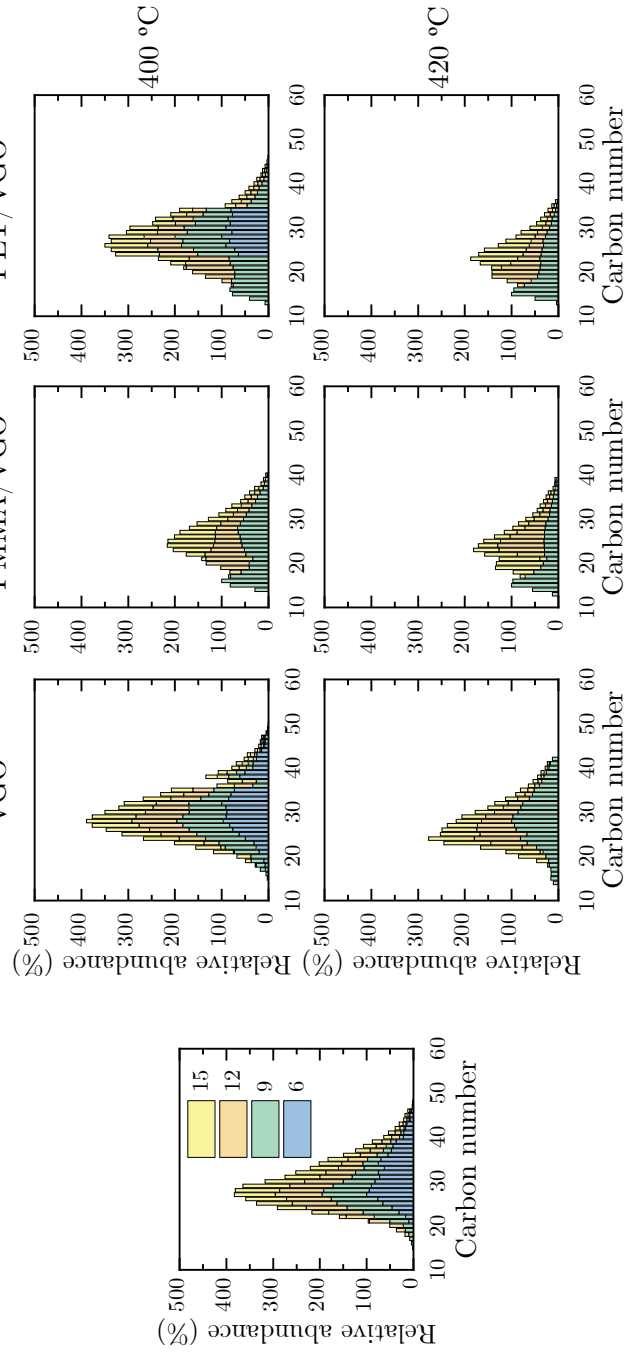

Figure 5.13. Relative abundance of the sulphur core molecules (benzothiophene, dibenzothiophene, benzonaphtothiophene and dinaphthothiophene) found in VGO and VGO, PMMA/VGO and PET/VGO hydrocracking products at 400 and 420 °C. Reaction conditions: 300 min, 80 bar, C/F = 0.1.

VGO hydrocracking products present a more homogeneous distribution that is more highly remarkable for DBE = 9 compounds and a carbon number around 25-30. This much alike distribution in the VGO products does not necessarily mean that sulphur compounds abundance is higher in that sample. Indeed, the major advance of hydrocracking reactions when compared to the one obtained for PMMA/VGO and PET/VGO samples leads to conclude that the higher peak of relative abundance observed for DBE = 9 and carbon number of ca. 15 in the latter are reaction intermediates in the HDS mechanism. Once they are also converted, the most refractory families remaining in the samples have a similar distribution that the untreated VGO (which was pre-treated in the refinery). It has been previously established that DBT species with alkyl-substitutes are hardly removed in HDS processes [347], thus observing the higher concentrations around a carbon number of 25-30 instead of 12-15, which is the number of the core molecule.

All in all, the introduction of plastics seems to affect the dynamics of the HDS mechanisms. As a hypothesis, for very similar conversion levels, the lower removal of sulphur compounds in VGO/polymer blends could be due to their competitive reactivity with polymer-derived compounds. In this way, the compounds obtained by hydrocracking the plastics (free of heteroatoms) would have preferential access to the active sites of the catalyst, thus slowing down other functions within the hydrocracking.

5.5. OXYGEN (O) CLASS

As a final point, the introduction of plastics with a composition not based exclusively on hydrogen and carbon highlights the need to track the evolution of compounds derived from the breaking of oxygen-containing bonds. It was discussed in Section 4.1 that the mass balance was not closed for oxygen when considering CO/CO_2 as products, and therefore some of the oxygen was expected to be in the form of heavier hydrocarbons found in the liquid. In order to locate these compounds and to check the different behaviour of the HDO function of the catalyst on each of the feeding blends, the Van Krevelen diagrams for the oxygenated compounds are shown in Figure 5.13. In this case, the model compounds considered for depicting the indicative lines are dibenzofuran (DBF), benzonaphtofuran (BNF) and dinaphthofuran (DNF).

Although they are not usually given much attention, oxygenated compounds are also present in VGO [348]. However, the first observable differences in Figure 5.14 are obtained in the products at 400 °C, where a compositional range can be seen appearing exclusively when co-feeding plastics with VGO in the range between O/C ratios of 0.06-0.10 and H/C ratios of 0.6-1.25. From the molecular formula of the compounds corresponding to this compositional space, the H/C and O/C ratio values correspond to structures with two oxygen atoms. The appearance of these compounds in the hydrocracking products of PMMA/VGO and PET/VGO suggests that they are structures derived from the cracking of these polymers.

The use of a higher temperature causes greater changes in the distribution of oxygenated compounds, as the amplitude of the compositional space is reduced in areas with a high H/C ratio and a low O/C ratio. This narrowing indicates a preferential removal of the lighter oxygenated compounds. At the same time, it can be observed that the additional compositional space appearing in the products of the PMMA/VGO and PET/VGO blends is maintained at 420 °C, although the species in this zone located further to the left disappear as the temperature increases due to the cracking of the branches attached to the aromatic structures.

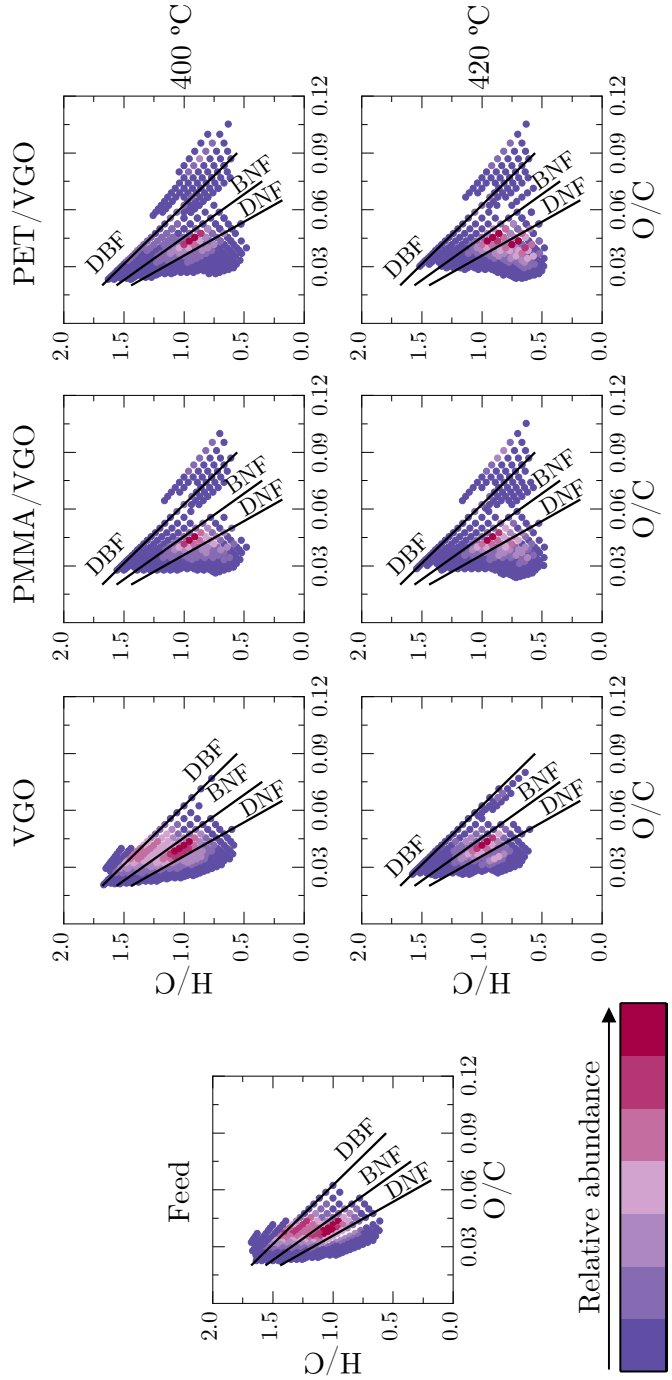

Figure 5.14. Iso-abundance plots of H/C aromatic ratio versus O/C ratio obtained by APPI (+) FT-ICR MS of feed and VGO, PMMA/VGO and PET/VGO samples at 400 and 420 °C. Reaction conditions: 300 min, 80 bar, C/F = 0.1.

Finally, a thickening can be seen in the PMMA/VGO and PET/VGO products in the low H/C and O/C range, perhaps attributable to the building blocks of the polymers. Their production may come from the higher cracking function which gives smaller units than those obtained at 400 °C, hence they appear only at 420 °C. Catalyst design has been established as a fundamental parameter in the development of HDO reactions. The choice of one or two metals, their dispersion on the surface, their strength for the hydrogenation function or the equilibrium with a high acidic strength favouring fast cracking of the C-O bonds have to be taken into account to conclude which is the preferred route [349]. In the case of bifunctional Pt and Pd catalysts, it has been reported that the hydrogenation route before (and thus ring-opening) oxygen scission is facilitated by the high hydrogenation activity of these metals.

For a better understanding of the evolution of the oxygenated compounds, histograms of the relative abundance distribution of the core compounds versus carbon number are illustrated in Figure 5.15. It is evident that both the development of HDO and the effect of temperature on it are strongly feed-dependent, with quite different behaviours and product distributions observed. On the one hand, the core molecules of VGO hydrocracking products at 400 °C hardly show any variation in their distribution concerning that of the untreated VGO. However, at 420 °C the promotion of the cracking function is evident by the general shift of the histograms towards a lower carbon number, the most refractory compounds being those with a carbon size in the range of 28-30. On the other hand, the high conversion in the hydrocracking of the PMMA/VGO blend results in a higher disappearance of heteroatomic compounds. This is reflected firstly in the complete elimination of the benzofuranic compounds and the simultaneous concentration of the other compounds in a lower carbon range (between 20 and 30 compared to 40 in the untreated VGO). Interestingly, the accumulation of compounds with a carbon number between 20 and 25 corresponds to the structures assignable to the points observed in Figure 5.14 only in the hydrocracking products of PMMA/VGO and PET/VGO blends. The formation of those compounds whose formation may derive from the hydrocracking of PMMA and PET could be explained by two different routes.

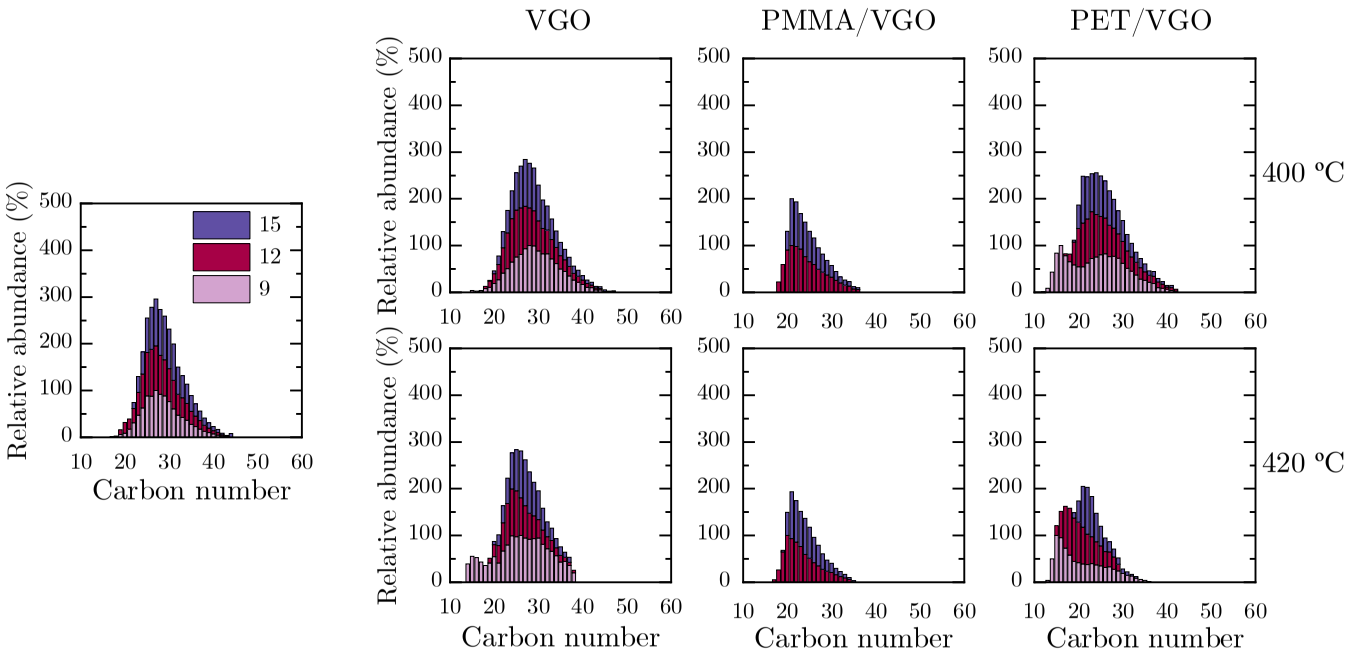

Figure 5.15. Relative abundance of the oxygen core molecules (dibenzofuran, benzonaphtofuran and dinaphthofuran) found in VGO and VGO, PMMA/VGO and PET/VGO hydrocracking products at 400 and 420 °C. Reaction conditions: 300 min, 80 bar, C/F = 0.1.

On the one hand, the direct cracking of the polymer chain, which can occur through the oxygenated groups or randomly while maintaining a certain oxygen content [350], and which, if not completely degraded to hydrocarbons, could be assigned to structures with the DBEs observed here. On the other hand, in the pyrolysis degradation of this polymer, the cyclisation of some segments produced by the breakage of its long chains has already been observed [351]. This, along with the hydrogen transfer phenomena that take place at the metal sites of the bifunctional catalysts, can give rise to aromatic structures [318] (which would be promoted if the conditions did not favour hydrogenation) that still contain some oxygen content and are therefore included among the species shown in Figure 5.14. Here, the effect of temperature is reflected, albeit less noticeably, in the reduction of hydrocarbon size due to the enhancement of the cracking reactions.

Last, the higher concentration of compounds in the left region of the histogram, as stated in the case of PMMA/VGO products, is even more noticeable here. On one hand, the development of the reactions observed in this system may give rise to intermediate compounds which are visible in this region. On the other hand, it has been stated both in Chapter 4 and in this Chapter that the mass balance of the oxygen introduced by each of the plastics showed a greater deficiency in the gaseous products of the PET/VGO blend. The appearance of different compounds, with a DBE = 9, to those observed in the PMMA/VGO products and which are found with a lower or null concentration in the VGO products leads to the conclusion that the PET hydrocracking involves their formation. As discussed above, these compounds do not necessarily correspond exclusively to furan derivatives but maybe to aromatic compounds with oxygen functional bonds, which is consistent with the polymeric form of PET.

In other studies, it has already been shown that the thermal degradation mechanism of PET results in aromatic chains with a functional group at the end of the chain [352], which could be transformed relatively easily in the presence of high hydrogen pressures. Furthermore, in other processes such as the gasification

of this polymer, it has been proposed that the reaction mechanism of PET gives as a final product, among others, compounds with 2 or 3 aromatic rings [353].

After identifying the compounds of the light and heavy oxygen-containing fractions and observing the differences between the compounds produced by each of the feeds, Figure 5.16 shows the proposed hydrocracking mechanisms for each of the co-fed polymers. On the one hand, the PET hydrocracking route takes 3 paths that change depending on whether oxygen removal takes place first (direct HDO), giving rise to aromatic compounds that can then be hydrogenated, or partially, producing aromatics with oxygen that is later removed by the formation of CO_2. On the other hand, the indirect route involves the cleavage of the polymer molecules into smaller fragments (up to dimers) that become reactive oxygenated branched species that can either give rise to the compounds produced by the other routes or react with the heavier VGO compounds to form oxygenated polyaromatic species corresponding to the structures observed in Figure 5.14.

On the other hand, PMMA, due to its branched structure, takes two different routes that do not depend on the hydrogenation activity of aromatics as in the case of PET. Thus, on the one hand, total scission of the side chain gives rise to radicals that can form long hydrocarbon chains after hydrogenation, or oxygenated particles that form light gases (hence their greater formation when PMMA/VGO is fed) or that are responsible for forming the heavier compounds with up to two oxygen atoms in this case. As for partial side-chain cleavage, the result is polymer segments that can be more easily hydrogenated and have isoparaffins as final product. The cracking of the CH_3-O group resulting from this cleavage can be associated with the formation of light gases after a subsequent secondary cracking, which would partially explain the higher amount of DG and CO/CO_2 observed when co-feeding this blend. For neither of the two polymers can it be established that there is a preferred hydrocracking route since all possible compounds proposed as end products have been detected by the different techniques employed, as well as the formation of CO/CO_2 can occur from multiple deoxygenation reactions.

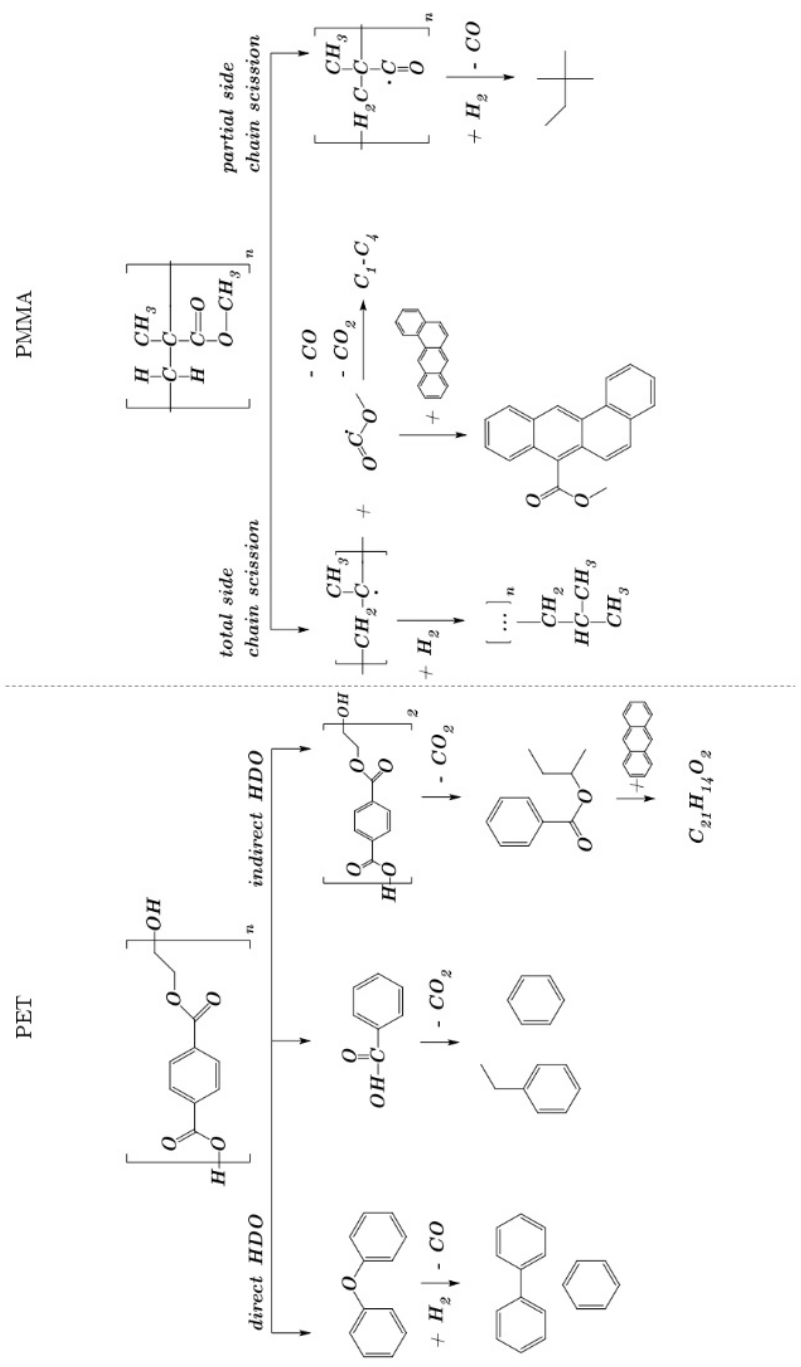

Figure 5.16. Proposed hydrocracking mechanisms of PET and PMMA.

Chapter 6

KINETIC MODELLING OF VGO AND POLYMERS BLENDS HYDROCRACKING

The kinetic modelling of the experiments exposed during Chapters 3 and 4 has been performed. The complexity and the high number of possible reaction pathways necessitate the use of lumps, which is the most common approach to model hydrocracking processes. Moreover, the discrimination between reaction networks and kinetic models has been fulfilled through statistical methods, paying special attention to the hypothetical formation of coke from polymeric materials and the different deactivation phenomena that have been discussed during previous Chapters. The development and selection of best kinetic modelling have been done based on PS/VGO hydrocracking results, and then applied to the other systems to check the validity of the model and compare the results when co-feeding different plastics. Part of the results collected in this Chapter is published in *Chem. Eng. J.*, **2023**, 451, 138709.

6.1. GENERAL ASPECTS

The kinetic modelling of catalytic processes such as the hydrocracking of complex hydrocarbon blends (with intricate reaction networks) presents additional difficulties in fully understanding and representing the deactivation phenomena and their evolution over reaction time. The establishment of an accurate kinetic model allows for: (i) predicting the effect of the operating conditions on the product distribution, (ii) optimizing the operating framework, and (iii) defining the possible revamping requirements of refinery units. With that purpose, lump-based models have been previously used when working with heavy blends that would require a huge experimental base and a very complex calculation methodology [354] if individual components were attended. Moreover, the quantification of the different lumps can be properly done through the usual analysis techniques used in hydrocracking experimental works. To complete the objectives established above, the kinetic model must be supported by the accurate establishment of the lumps involved, the correct assumption of the feasible reaction networks and the introduction of equations that truly describe not only the reaction development of each lump but also the multiple deactivation phenomena that take place in these processes, experimentally measurable.

The reactions that have been submitted to the kinetic models developed here have been shown in the previous Chapters and have been performed under the following operating conditions:

- Feedstock: plastics (10 wt%) in VGO
- Temperature: 380-420 °C for PS and PMMA blends, 400-440 °C for PET/VGO blend
- Pressure: 50- 110 bar
- Reaction time: 30-300 min
- Catalyst-to-feed ratio (mass basis): 0.1
- Stirring speed: 1300 rpm

6.1.1. Reaction network discrimination

The scarce literature about the joint hydrocracking of polymers and heavy streams has led to taking as a basis for the development of the reaction networks some models proposed for the hydrocracking of heavy oil only [355]. The different nature and molecular weight of the heaviest lumps here considered, which match with the main feeds (HCO and plastic), results in the proposal of a parallel-series reactions system based on the reaction network proposed by Martínez and Ancheyta [355], which has been expanded through the introduction of plastic, as collected in Figure 6.1a.

As an initial consideration, for the reaction network called Model A, the formation of coke is only expected from the condensation of the compounds within the HCO lump, although the reversible character of this pathway has been already introduced due to the possible hydrogenation/dehydrogenation of coke compounds.

The enlargement of Model A towards Model B (Figure 6.1b) consists of two main changes that add 6 new kinetic constants (totalling 17): (i) the split of gas lump into LPG and DG separately, as common when exposing hydrocracking results in lumps terms, which provides 5 new kinetic constants related to the formation of this lump from all the heavier ones (except for coke); (ii) the formation of coke from plastic, as the polymerization of large compounds can end up in coke-alike structures, even when the reversible reaction is not considered, since the hydrocracking of coke structures can be encompassed within the HCO lump, regardless the formation mechanism.

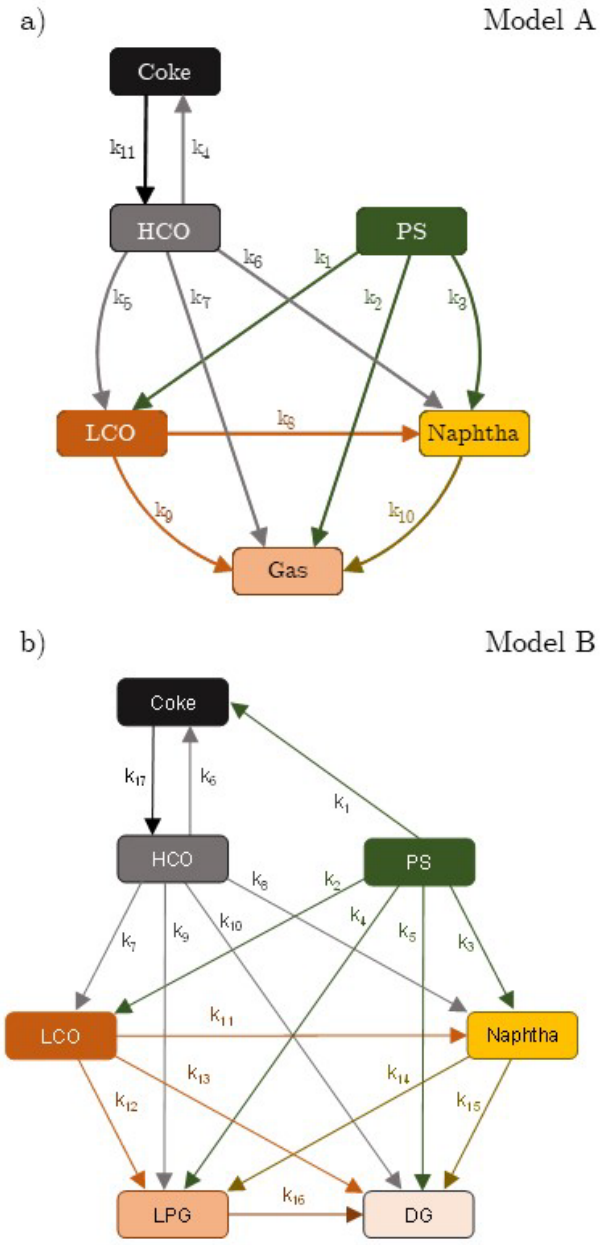

Figure 6.1. Schemes of proposed a) 6-lump (Model A) and b) 7-lump (Model B) reaction networks.

6.1.2. Kinetic modelling development

The kinetic model has been solved based on the resolution of the mass conservation equations. For that purpose, the methodology is supported by the stages and recommendations found in the literature [356] for solving kinetic systems that consider catalyst deactivation.

To define the mass conservation equations for the lumps considered, the following assumptions have been done: (i) external diffusivity is negligible due to the high stirring speed [217]; (ii) gas and liquid phase concentrations are uniform inside the reactor; (iii) a high heat transmission is achieved due to the reactor design, avoiding the formation of temperature gradients in its interior thus considering it as an isothermal system [357]; (iv) the pressure changes along the reaction are negligible due to the excess of hydrogen available since it is continuously fed into the reactor; (v) the catalyst deactivation may occur to different phenomena (as explained in Chapter 3), namely plastic fouling, coke deposition and poisoning by metals, that can be related to individual equations. The foundations of the latter and the significance of its introduction in the model will be explored in this Chapter.

Bearing all this in mind, the evolution over time of the general yield of each lump *i* (Y_i) is defined by the following conservation equation:

$$\frac{dY_i}{dt} = \phi \sum_{1}^{j} k_j (Y_i)^{\alpha_i} \tag{6.1}$$

where ϕ is the deactivation function, k_j is the kinetic parameter of each reaction and n_i is the reaction order. Note that the deactivation function is common for all the lumps conservation equations, as it has been defined as non-selective. Moreover, the reaction order is directly related to the lump involved, in concordance with the literature [358], considering order one ($n_j = 1$) for all reactions except for those of HCO acting as reactant, which are of second order ($n_j = 2$).

To establish the temperature dependence of the kinetic parameter, each of them has been defined following the reparametrized Arrhenius equation [359]:

$$k_j = k_{j,T_{ref}} exp\left[-\frac{E_j}{R}\left(\frac{1}{T}-\frac{1}{T_{ref}}\right)\right] \tag{6.2}$$

where $k_{j,Tref}$ is the kinetic parameter of reaction j at the reference temperature, E_j is the activation energy of the reaction j, R is the universal gas constant, T is the temperature of reaction and T_{ref} is the reference temperature (673 K).

Taking all of this into account, the individual mass balances for each lump are defined as described in Eqs. (6.3-6.9) for the 7-lump model. Keep in mind that the equations for the 6-lump model are very similar, with the suppression of reactions #12 to #17 and the combination of DG and LPG into a gas lump.

$$\frac{dY_{plastic}}{dt} = -\phi\left[k_1 + k_2 + k_3 + k_4 + k_5\right]Y_{plastic}WF \tag{6.3}$$

$$\frac{dY_{HCO}}{dt} = -\phi\left[\left(k_6 + k_7 + k_8 + k_9 + k_{10}\right)Y_{HCO}^2 - k_{17}Y_{coke}\right]WF \tag{6.4}$$

$$\frac{dY_{LCO}}{dt} = \phi\left[k_2Y_{plastic} + k_7Y_{HCO}^2 - \left(k_{11} + k_{12} + k_{13}\right)Y_{LCO}\right]WF \tag{6.5}$$

$$\frac{dY_{naphtha}}{dt} = \phi\left[k_3Y_{plastic} + k_8Y_{HCO}^2 + k_{11}Y_{LCO} - \left(k_{14} + k_{15}\right)Y_{naphtha}\right]WF \tag{6.6}$$

$$\frac{dY_{LPG}}{dt} = \phi\left[k_4Y_{plastic} + k_9Y_{HCO}^2 + k_{12}Y_{LCO} + k_{14}Y_{naphtha} - k_{16}Y_{LPG}\right]WF \tag{6.7}$$

$$\frac{dY_{DG}}{dt} = \phi\left[k_5Y_{plastic} + k_{10}Y_{HCO}^2 + k_{13}Y_{LCO} + k_{15}Y_{naphtha} + k_{16}Y_{LPG}\right]WF \tag{6.8}$$

$$\frac{dY_{coke}}{dt} = \phi\left[k_1Y_{plastic} + k_6Y_{HCO}^2 - k_{17}Y_{coke}\right]WF \tag{6.9}$$

where W is the catalyst-to-feed mass ratio and F is the loading mass.

The global deactivation function is one of the main challenges when developing a hydrocracking kinetic model. The quantification of all the phenomena that can affect the catalyst activity and their interrelationship is hard to measure and it is usually identified as one general formula based on the main deactivation cause, that is, coke deposition. However, the catalyst covering by carbonaceous material is accompanied by the presence of heavy metals in heavy oils that can also deteriorate not only the catalyst metals but the support structure by blockage [197]. In addition to this, the deposition of unconverted plastic over the catalyst surface has been discussed in Section 3.4.2, proving it is an activity inhibitor at low temperatures to the extent that it blocks the catalyst's active sites. The increase in temperature produces a drastic decrease in this deactivation phenomenon effect but rises the importance of the presence of carbonaceous material (coke) in the channels of the zeolite [360] at the same time that promotes the HDM function, bringing with it a higher poisoning metals content on the spent catalyst. Because of all of this, three causes of the catalyst deactivation can be well differentiated: (i) fouling caused by the external deposition of unconverted plastic (at low temperature); (ii) formation and condensation of coke; and (iii) metals poisoning. Hence, three kinetic deactivation equations have been adapted to quantify the individual impact of these phenomena at each temperature of reaction and their expressions have been combined for determining the global deactivation function, ϕ.

The mathematical description of fouling caused by the sedimentation of the partially degraded PS chains (φ_p) has been carried out by the adaptation of a kinetic deactivation model proposed by Elizalde and Ancheyta [361]. Such a model represented sequentially the coverage of the sites and pores blockage by heavy compounds in the feed that could not be converted and that then can be analogously applied to plastic fouling. The corresponding equation has two terms that are applied before (Eq. (6.10)) and after (Eq. (6.11)) the blockage of the pores (t_b) has occurred.

For $t < t_b$:

$$\varphi_{p,1} = \varphi_s + (1 - \varphi_s) e^{-k_{d,p} t} \tag{6.10}$$

For $t > t_b$:

$$\varphi_{p,1} = \varphi_s + (1 - \varphi_s) e^{-k_{d,p} (t - t_b)} \tag{6.11}$$

being $k_{d,p}$ the deactivation kinetic parameter associated with plastic deposition and φ_s the steady-state catalyst activity value, according to the consideration made by Monzón et al. [362]: assuming that catalyst deactivation is rarely complete and the catalyst achieves a pseudo-stable state with constant remaining activity. The plastic fouling expression, φ_p, is thus defined as $\varphi_{p,1}$ when time is lower than the time of pores blockage and as the product of $\varphi_{p,1}$ and $\varphi_{p,2}$ once this time has been achieved.

It has been already commented that coke deposition is the main cause of deactivation in hydroprocessing. The selection of one or another equation to represent it has multiple choices and it is usually made to maintain coherence with the reference material used for the development of the kinetic model. Consequently, in this case, a hyperbolic function (Eq. (6.12)) has been selected according to the methodology proposed by Rodríguez et al. [197] and derived from the Langmuir-Hinshelwood concept. Thus, it introduces a constant α that represents the proportional ratio between the deposited coke on the catalyst (C_c) and the poisoned active sites. Note that this amount, measured through TPO, corresponds to the coke yields shown in Figure 3.4 and are introduced in Eq. (6.12) in form of $g_{coke}\ g^{-1}_{catalyst}$. Those TPO results demonstrate the particular increase in the coke amount deposited on the catalyst when plastic fouling is no longer the main cause of deactivation (400 and 420 °C for PS/VGO system).

$$\varphi_c = \frac{1}{(1 + \alpha C_c)^{m_c}} \tag{6.12}$$

where α is the coke deposition constant, C_c is the fractional content of carbon in the catalyst and m_c is a fitting parameter that represents the order of deactivation of coke deposition.

The activity decay attributed to heavy metals deposition has been described according to an empirical term introduced for describing the kinetic behaviour of hydrocracking in slurry reactors [355]. This formula (Eq. (6.13)) is a function of the concentration of metals in the catalyst (M), calculated through ICP-AES as explained in Section 2.2.4, concerning the theoretically maximum loading capacity of the catalyst (M_0), which is considered as a fitting parameter (with the maximum experimental loading as the lower limit).

$$\varphi_m = 1 - k_{d,m}\left(\frac{M}{M_0}\right)^{m_m} \tag{6.13}$$

where $k_{d,m}$ is the kinetic parameter of deactivation due to metal deposition, M is the metal loading at t time, M_0 is the maximum loading capacity of the catalyst and m_m is the order of this deactivation (fitting parameter).

As a result of combining the explained equations, a global activity function is introduced as in Eq. (6.1), and that takes into account all the possible contributions at different temperatures of the deactivation phenomena with experimental observations foundations [363]. Gayubo et al. [364] considered the synergy between reversible (coke deposition) and irreversible (dealumination) deactivation phenomena as the product of the individual functions in methanol conversion to hydrocarbons, as described in Eq. (6.14):

$$\phi = \sum_{1}^{n} \varphi_k \tag{6.14}$$

being n the number of deactivation causes and φ_k the term that describes each of those causes.

After having analysed each of the deactivation terms, in order to apply Eq. (6.14), the catalyst deactivation has been considered needs to be described at 380 °C with the three deactivation functions, while at 400 and 420 °C the value of steady-

state activity due to plastic fouling is close (or equal) to the unity and therefore only coke and metals deposition are considered for PS/VGO system. It has been checked that, under the operating conditions explored for the reactions involving oxygenated plastics, no plastic fouling has been observed, so the corresponding term is disregarded.

The optimization of all the described fitting parameters (kinetic parameters of reactions, activation energies and deactivation parameters, constants and orders) has been accomplished by adjusting the predicted yields over reaction time at different temperatures to those obtained experimentally. With that purpose, a MATLAB code has been developed, establishing as objective function the sum of squares of the errors between the predicted and experimental data (Eq. (6.15)), introducing a weight factor (Eq. (6.16)) that helps offset the different order of magnitude of the yields, thus providing a higher weight factor to the minority lumps [365].

$$SSE = \sum_{1}^{n_l} \sum_{1}^{n_d} \omega_i \left(Y_i^{exp} - Y_i^{calc} \right)^2 \tag{6.15}$$

being n_l the number of lumps considered, n_d the number of experimental data, Y_i^{exp} the experimentally obtained yield and Y_i^{calc} the one predicted by the model.

$$\omega_i = \frac{1}{\sum_{1}^{n_d} Y_{i,j}} \tag{6.16}$$

where ω_i is the weight factor of each lump i.

The procedure for solving the system of differential equations is summarized in the scheme shown in Figure 6.2. Essentially, the main program reads the experimental data, and, with the initial values provided by the user, initiates the iterative process. The main routine solves the differential equation by means of the function *ode45* and then a subroutine calculates the value of the objective function and minimizes it through two MATLAB functions that have been used successively: *fmincon*, which allows establishing boundaries for the fitting parameters (such as the maximum activity at steady-state or the lower

boundaries for kinetic parameters), and *fminsearch*, which uses the *Levenberg-Marquardt* algorithm, establishing as search direction a cross between the Gauss-Newton direction and the steepest descent direction. The latter has been used in the last optimization steps because it is well-established for solving non-linear least squares minimization problems [366]. Apart from that, one should notice that the lack of literature on the kinetic model of blends of plastics and heavy oils hinders the correct proposal of initial values for this type of program, so several approaches have been made by using the *genetic algorithm* of MATLAB and the selection of the initial ones for the calculations with the above-mentioned algorithms has been made to provide certain coherence with the data available in the kinetic modelling of similar processes [162, 367, 368].

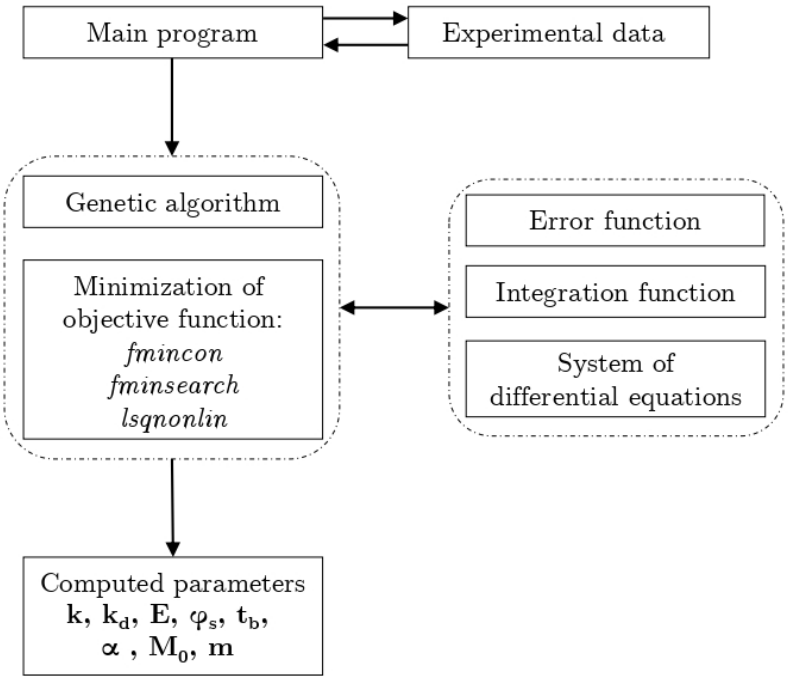

Figure 6.2. Block diagram for the resolution of the lump-based model.

Additionally, the usage of *lsqnonlin* MATLAB function has allowed calculating the residual values for each parameter, the Jacobian matrix and the correlation coefficient matrix, according to the methodology explained by Amin et al. [369].

As the mentioned function requires a user-defined function, another sub-routine has been created in such a way that targets likewise the function defined in Eq. (6.15).

Once the different proposals of reaction networks (Figure 6.1) and models have been optimized, not only the SSE values have been compared to select the best option but also a statistical significance test has been performed based on Fisher's method. This technique is based on the fulfilment of the following criterion:

$$F_{A-B} = \frac{\dfrac{SSE_A - SSE_B}{SSE_B}}{\dfrac{\upsilon_A - \upsilon_B}{\upsilon_B}} > F_{1-\alpha}\left(\upsilon_A - \upsilon_B, \upsilon_B\right) \tag{6.17}$$

where υ are the degrees of freedom of each kinetic model, α is the significance level and it is equal to 0.05 (which represents a confidence level of 95 %), and $F_{1-\alpha}$ is the critical value for Fisher's distribution, calculated by the *finv* function of MATLAB. If the criterion shown above is fulfilled, the improvement that model B provides with respect to model A is considered significant. Note that for the correct application of this method the two models must have different degrees of freedom, which are calculated as follows:

$$\upsilon = n_l n_e - n_p \tag{6.18}$$

being n_l the number of lumps, n_e the number of experiments and n_p the number of parameters.

6.2. PS/VGO HYDROCRACKING MODELLING

6.2.1. Model discrimination

To establish and use the most accurate and appropriate model, four different systems have been tested and compared. This comparison has been carried out when modelling the hydrocracking of the PS/VGO blend, as it has been seen that it represents the most complex blend due to the catalytic deactivation related to plastic fouling, so it is assumed that for less complex systems (PMMA/VGO and PET/VGO) the application of the most appropriate model here found will be valid as well. The first two models considered correspond to the different reaction networks that have been introduced in Section 6.1 (Figure 6.1), and then two more have been developed based on model B. Model B-2 is a modification of model B that takes into consideration the multiple deactivation phenomena that have been exposed, therefore using Eq. 6.14 instead of considering only coke deposition (Eq. 6.12). Moreover, a further modification of model B has been made resulting in what has been called model B-3, which is the significance of thermal routes during the hydrocracking and takes as a basis some other works that have studied this contribution and its magnitude when modelling the kinetic behaviour of hydrocracking systems [370, 371]. The mentioned modifications result in models with a different number of parameters and results after performing the fitting, so the statistical values of each model's parameters have been collected in Table 6.1.

Table 6.1. Statistical comparison between the proposed kinetic models.

Model	Lumps	Deactivation functions	υ	F_{A-B}	$F_{1-\alpha}$	SSE
A	6	1	63	1.22	2.36	19.35
B	7	1	68	-	-	21.22
B-2	7	3	62	16.67	2.25	8.12
B-3	7	3	44	-	1.84	14.76

Firstly, the split of gas lumps into two different lumps and the introduction of another pathway for coke formation from plastic are evaluated by comparing models A and B. The input of a moderate number of new experimental points is not compensated with the establishment of the corresponding new reaction pathways, thus providing higher degrees of freedom when applying Model B. Therefore, model B has been taken as a benchmark to execute the statistical comparison and the test is based on the verification that the reduction of degrees of freedom of model A is significant. Attending to the results, although a lesser error is achieved with model A (21.22 vs 19.35) the criterion of Fisher's test is not fulfilled (Eq. 6.17), thus being Model B a better option.

If the introduction of multiple deactivation equations is examined (Model B vs Model B-2), it can be seen that it considerably reduces the total error of the objective function (21.22 vs 8.12). This is attributed to the accurate description of the phenomenon of plastic fouling, which is hardly described by the hyperbolic function established for coke deposition, as they are two different events, one of them completely stopping the reactions while the other only hinders it partially. This is reflected when analysing the F values, as the value of $F_{A\text{-}B}$ is significantly better than $F_{1\text{-}\alpha}$ (16.67 vs 2.25). For these reasons, the introduction of multiple deactivation equations, i.e. kinetic model B-2, significantly improves the performance of the reaction network established for model B.

As already introduced, the last proposal is a kinetic model that includes the thermal reaction pathways of the best model selected from the previous ones, that is model B-2. The selection of the kinetic equations representative of those routes has been done according to the literature, thus using a potential expression, and maintaining the coherence with reaction order: first-order reactions have been used for all the reaction pathways except for those involving HCO lump as a reactant, in which order 2 equations have been used. In this case, the utilization of such a high number of parameters does not improve the fitting obtained with model B-2, and as it has fewer degrees of freedom and a higher error function value no statistical comparison can be made. Hence, the inclusion of thermal routes cannot be considered, which is in agreement with some results obtained by

other authors that concluded that catalytic pathways have a preferential character and higher orders than those of thermal routes [372].

Bearing all the above in mind, the combination of reaction network B and the kinetic model that includes multiple deactivation equations but only catalytic pathways is considered the best option to represent the results obtained within the hydrocracking of plastics and VGO blends. The subsequent sections explore the fitting of this model for the different blends studied in this Thesis, analysing the predicted values' accuracy, the evolution of the activity function and the performance of simulations to establish the optimal operating conditions.

6.2.2. Fitting and analysis of kinetic parameters

The optimized kinetic parameters of model B-2 used to describe the hydrocracking of the PS/VGO blend, collected in Table 6.2, have been used for describing the evolution of the yields of each lump over time at different temperatures. The comparison between the predicted values and the ones obtained experimentally is shown in a parity plot displayed in Figure 6.3, obtaining an overall good fit. The comparison of the kinetic parameters obtained after the fitting can point out the most relevant steps in the reaction network. This way, the kinetic parameters of steps #7 and #8 reveal the weight that the HCO lump has on the formation of the desired products, i.e. LCO and naphtha. A clear difference can be observed if these two are compared, as the higher value of constant #7 confirms the sequential mechanism established in the literature for the hydrocracking of heavy oils [368]. Thus, the hydrocracking of HCO results in the formation of middle distillates that are later converted into naphtha and light gases. In fact, the constants values of steps #11, #12 and #13 expose that, even if all the paths must be considered, there is a preferential formation of naphtha from LCO, in accordance with this cascade system, which will suffer overcracking towards gaseous species if the conditions promote the cracking forces.

Table 6.2. Apparent kinetic parameters (P) at the reference temperature and corresponding apparent activation energies calculated with model B-2.

Reaction	P	$k_{j,Tref}$	Units	E_j (kJ mol^{-1})
PS → Coke	k_1	(2.47 ± 0.2) 10^{-2}	g_{cat}^{-1} h^{-1}	121.6 ± 10.8
PS → LCO	k_2	(3.19 ± 0.3) 10^{-1}	g_{cat}^{-1} h^{-1}	48.8 ± 3.5
PS → Naphtha	k_3	(1.01 ± 0.1) 10^{0}	g_{cat}^{-1} h^{-1}	223.6 ± 14.8
PS → LPG	k_4	(4.27 ± 0.1) 10^{-2}	g_{cat}^{-1} h^{-1}	355.4 ± 29.8
PS → DG	k_5	(5.17 ± 0.4) 10^{-3}	g_{cat}^{-1} h^{-1}	413.1 ± 4.5
HCO → Coke	k_6	(4.74 ± 1.0) 10^{-5}	g_{cat}^{-1} g_{HCO}^{-1} h^{-1}	0.50 ± 0.01
HCO → LCO	k_7	(1.82 ± 0.2) 10^{-2}	g_{cat}^{-1} g_{HCO}^{-1} h^{-1}	280.9 ± 21.2
HCO → Naphtha	k_8	(1.82 ± 0.1) 10^{-4}	g_{cat}^{-1} g_{HCO}^{-1} h^{-1}	298.0 ± 30.1
HCO → LPG	k_9	(5.19 ± 0.8) 10^{-5}	g_{cat}^{-1} g_{HCO}^{-1} h^{-1}	337.2 ± 4.4
HCO → DG	k_{10}	(2.72 ± 0.1) 10^{-5}	g_{cat}^{-1} g_{HCO}^{-1} h^{-1}	480.1 ± 47.2
LCO → Naphtha	k_{11}	(6.92 ± 0.2) 10^{-1}	g_{cat}^{-1} h^{-1}	114.0 ± 11.3
LCO → LPG	k_{12}	(1.45 ± 0.3) 10^{-1}	g_{cat}^{-1} h^{-1}	120.7 ± 10.2
LCO → DG	k_{13}	(2.19 ± 0.1) 10^{-2}	g_{cat}^{-1} h^{-1}	206.8 ± 3.7
Naphtha → LPG	k_{14}	(9.09 ± 0.5) 10^{-2}	g_{cat}^{-1} h^{-1}	42.8 ± 1.9
Naphtha → DG	k_{15}	(8.03 ± 0.3) 10^{-4}	g_{cat}^{-1} h^{-1}	65.2 ± 2.8
LPG → DG	k_{16}	(2.34 ± 0.3) 10^{-2}	g_{cat}^{-1} h^{-1}	12.1 ± 0.7
Coke → HCO	k_{17}	(6.73 ± 0.5) 10^{-3}	g_{cat}^{-1} h^{-1}	0.42 ± 0.03
Plastic fouling	$k_{d,p}$	(4.29 ± 0.3) 10^{-2}	h^{-1}	-
Coke deposition	$\alpha_{d,c}$	(4.69 ± 0.5) 10^{1}	-	-
Metals poisoning	$k_{d,m}$	(3.66 ± 0.1) 10^{-1}	-	188.0 ± 18.6

Regarding the preferential destination of PS, if the apparent kinetic constants of steps #2 and #3 are attended it can be concluded that naphtha formation from

PS is more likely by the molecules produced in the hydrocracking of this plastic. This is coherent with a previous work [373] in which compounds with a boiling point range within that of the naphtha were obtained in the hydrocracking of neat PS. Indeed, the formation of not only monoaromatics (from the direct hydrogenation of PS monomers) but also the increment of saturated cyclic compounds was observed.

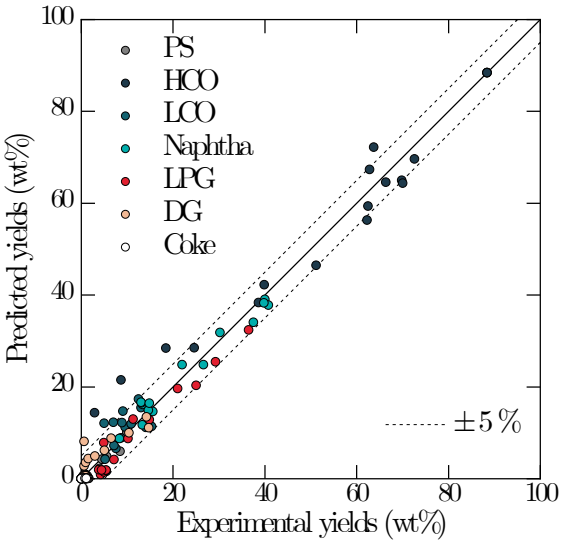

Figure 6.3. Parity plot of experimental vs predicted yields with kinetic model B-2 of PS/VGO hydrocracking.

Another point of interest is the proposed formation of coke from PS hydrocracking in model B-2, as this reaction pathway has been previously reported in the literature [368]. Focusing on the respective constants of coke formation from PS and HCO (steps #1 and #6), it can be deduced that the suggestion is correct, as both of them are of a similar order of magnitude that others involving them as reactants. Although a direct comparison between them is not possible due to the different order of PS and HCO reactions, the favoured nature of step #6 is well-founded on the content of polyaromatics in HCO, which are more likely to form these carbonaceous species. Moreover, and related to this reaction (steps #6 and #17), its reverse character cannot be undervalued, as even if the value is residual

compared to other constants of first-order reactions it has a certain incidence at 420 °C when coke yield goes through a maximum at 120 min.

The apparent activation energies also give information about the feasibility of some of the proposed pathways. For instance, the order of activation energies of the DG formation routes is remarkable: $E_{10} > E_5 > E_{13} > E_{15} > E_{16}$. The effect of temperature on DG formation, which is undesirable, is directly observable in that trend, as the conversion of the reactants (PS and HCO) towards this lump is more unlikely but it results from the hydrocracking of their primary (LCO, naphtha) and secondary (LPG) products.

All this leads to the prediction of the PS/VGO blend hydrocracking product distribution over time and temperature, as depicted in Figure 6.4, showing the experimental points as scatter and the tendencies calculated by the model being represented by continuous lines. Dashed lines indicate a margin of ± 5%. Apart from the good fit observed on the graphs, two main considerations can be extracted from them. The deviations observed on the parity plot are mainly attributed to experimental errors in the measure of the yield of PS at 380 °C, producing a final blend of heavy liquid (due to the low conversion of HCO) and degraded polymer that is hard to separate and quantify. That way, the experimental error at this temperature is noteworthy when attending to HCO and naphtha yields. On the other hand, the fitting obtained at 420 °C shows a lower conversion of the heaviest fraction predicted by the model than the one obtained. The extra gas formation can be attributed to thermal cracking, which has not been considered in the model and is promoted to a greater extent at high temperatures.

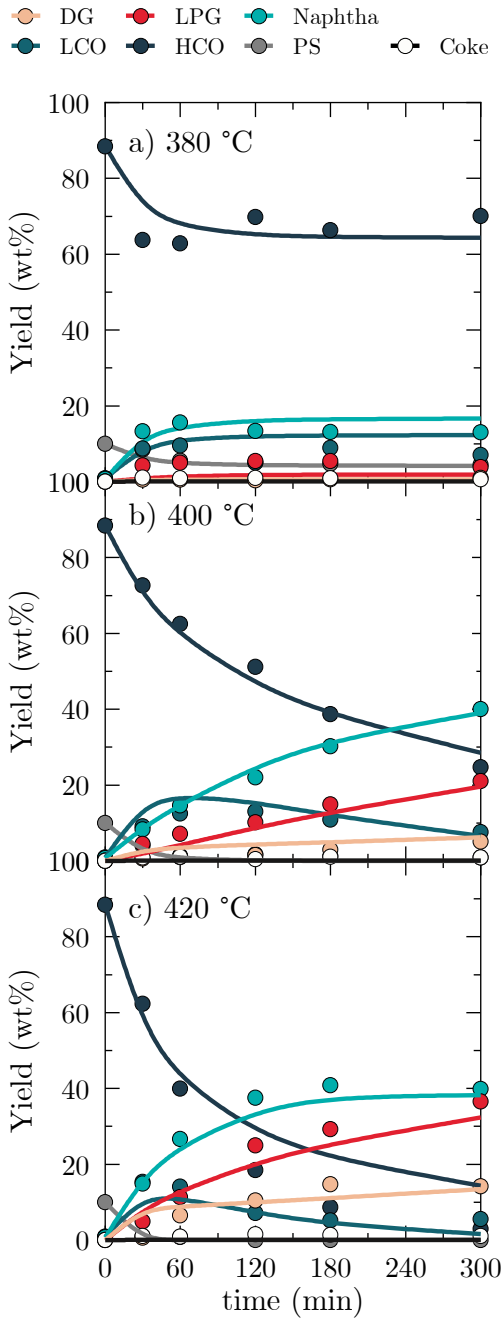

Figure 6.4. Fitting of the predicted values (lines) with respect to the experimental yields (scatter) in the hydrocracking of PS/VGO at a) 380, b) 400 and c) 420 °C.

The correlation matrix, shown in Figure 6.5, allows for establishing the linear relationship between the kinetic parameters and differentiating between the intrinsic correlation between reaction routes because of the process mechanisms and a bad design of experiments that cause an interdependence between parameters that are not legitimately connected [374]. The values of these coefficients are comprehended between -1.0 and 1.0 and the further away the correlation coefficient is from 0, the stronger the linear association between the two parameters involved. Note that the matrix is symmetrical when separated by the diagonal, which is equal to the unity in all cases as they represent the relationship between each parameter with itself.

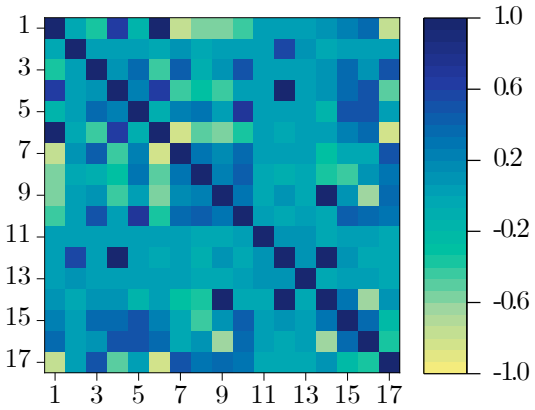

Figure 6.5. Coefficient correlation matrix of the kinetic parameters of model B-2.

From the matrix depicted in Figure 6.5, there are some coefficients close to an absolute value of 1, which means that some of the parameters are strongly interrelated. The individual analysis would allow concluding whether this relationship is inherent to the process or if the system is over-parameterized and some of the proposed routes (and therefore parameters) can be simplified [375]. This way, the most noteworthy coefficients are those involving k_4-k_{12}, k_9-k_{12} and k_{12}-k_{14}, all related to the formation of LPG lump. The main reason for this high interconnection is found in the cascade mechanism that directly relates the formation of one of the reactants and the other (in this case, LCO → naphtha)

with the product, that is LPG. In fact, the formation of naphtha from LCO is one of the most rapid and clear pathways, so the influence of this reaction on LPG formation from both LCO and naphtha is evident. In a similar way, the relationship between those routes and the formation of LPG from PS is conditioned by the prior formation of those intermediate species that, as seen in Table 6.2, is quite faster than the direct formation of gases. Nevertheless, in this case, the suppression of any of the mentioned pathways seems inappropriate as the formation of LPG from any of those reactants has been proven in literature [252].

6.2.3. Activity function

The importance of the introduction of a global activity function that encompasses multiple deactivation causes has been already remarked on. Accordingly, the individual contribution of each of the multiple deactivation functions has been analysed in Figure 6.6.

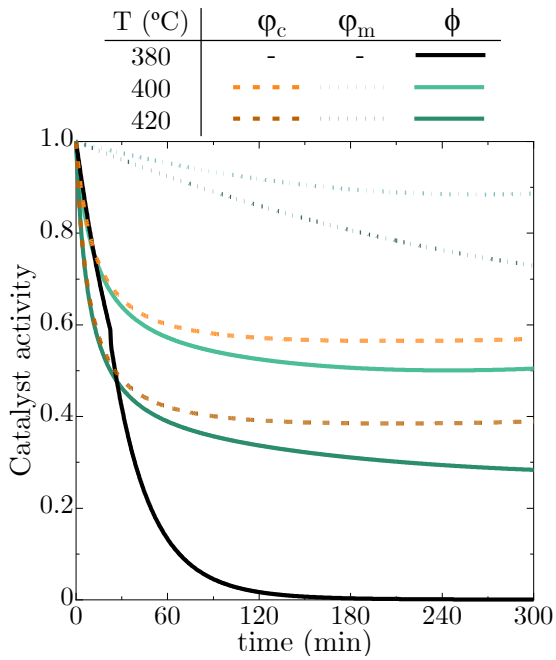

Figure 6.6. Evolution of the catalyst activity functions with reaction time and separate contribution of deactivation by coke deposition and metals poisoning.

Continuous lines represent the global activity function at each temperature (ψ), while dashed lines describe the deactivation functions related to coke (φ_c) and metal deposition (φ_m) as defined in Eqs. (6.12) and (6.13). It must be noted that the individual function related to PS fouling has been not added to Figure 6.6 as its contribution is almost equal to the global activity function at 380 °C when it is the main deactivation, and the value of this function at 400 and 420 °C is very close to the unity.

From the activity profiles, two main conclusions can be extracted. On one side, the activity at 380 °C is confirmed to be ruled by the plastic fouling mechanism, observing a fast activity decay during the first 30 min (halving the catalyst activity to that time) followed by a drastic drop that makes it marginal from 120 min and onwards. The optimization gives as a result a time of pore blockage (as it is defined in Eq. (6.11)) of 28 min, which matches with the experimental observation. As previously stated, the effect of coke and metals deposition on the catalyst has been used for the modelling of the hydrocracking activity at 380 °C but their effect is eclipsed by the one provided by PS fouling and thereby they are not shown in Figure 6.6.

On the other side, the breakdown of the activity functions evolution obtained at 400 and 420 °C confirms the importance and performance of the other two deactivation mechanisms. Even if they are quite different from the very beginning of the reactions, one could notice that coke deposition is confirmed to be the leading deactivation cause. As for metal deposition, the activity decay that it produces doubles its effect when the temperature is increased from 400 to 420 °C, confirming its strong temperature dependence. Moreover, the HDM reactions seem to be hampered at 400 °C, while they seem to have a continuous development at the highest reaction temperature here studied.

Regarding coke deposition, a pseudo-stable remaining activity is observed for both of them despite the temperature increase. This is a consequence of the well-established hydroprocessing mechanisms, which compensate for the rate of condensation of coke precursors with the presence of high-pressure hydrogen that favours the hydrocracking of those precursors. These circumstances have already

been stated in the hydrodeoxygenation of bio-oil [271] and have been considered for the kinetic model of HDO reactions over an acid-activated carbon-based bifunctional catalyst [376].

6.2.4. Simulations

The kinetic model has been used for performing reactor simulations to make an overall portrait of the effect of the operating conditions (time, temperature) on the yield distribution of the most relevant lumps. The simulations have been carried out above 400 °C in order to avoid the critical activity decay related to PS fouling, and time has been extended up to 480 min. This way, Figure 6.7 shows the evolution with temperature and reaction time of the yields of PS, naphtha, LPG and DG.

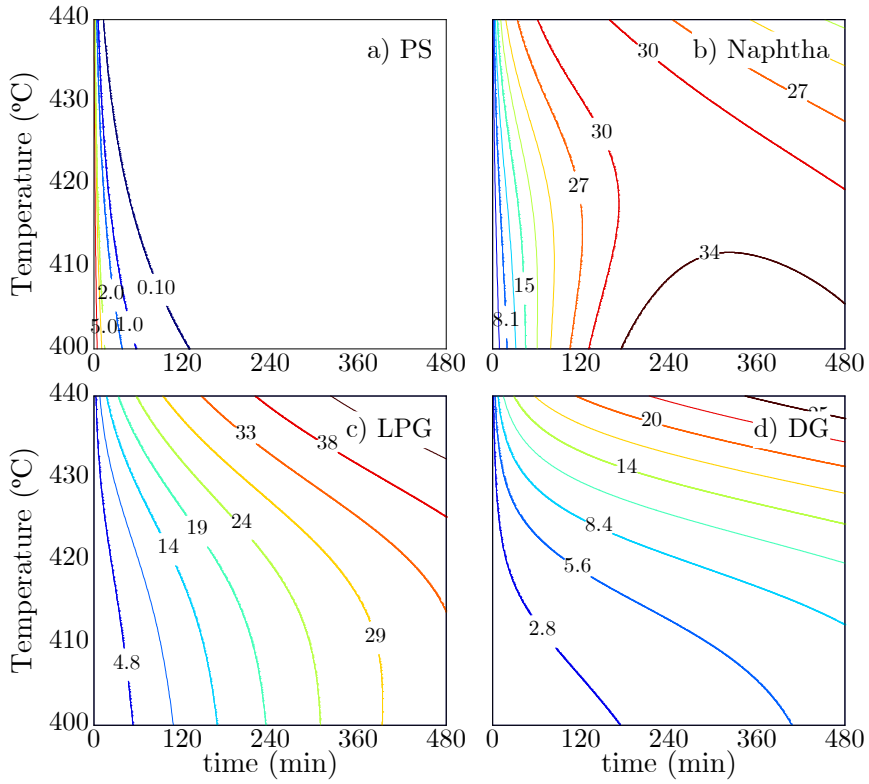

Figure 6.7. Kinetic model prediction of the effect of temperature and reaction time on the yields (wt%) of a) PS, b) naphtha, c) LPG and d) DG.

The selection of the lumps depicted in the operation maps is founded on selecting the ones with the highest interest to be optimized. Thus, plastic yield is represented according to the necessity of maintaining a maximum conversion of the plastic to prioritize the elimination of the wastes and, at the same time, avoid solid deposits that would result in operation stops [105]. Apart from that, naphtha is one of the main targets of this study as the production of high-quality gasoline-like streams from alternative or new materials is gaining attention due to the oil depletion context that the energy scenario is facing over these years [377]. Furthermore, the formation of gas lumps, and more specifically of dry gas as a representative lump of the feed overcracking, must be followed to maximize the selectivity towards fuel-like streams [378].

In Figure 6.7a, the achievement of a plastic conversion up to 90 % (represented by PS yields below a 1 wt%) can be observed for temperatures above 400 °C and times higher than 60 min. The last discernible line (0.1 wt%) corresponds to a conversion of 99 %, demonstrating that even with the lowest simulated temperature an almost full conversion can be achieved within 120 min of reaction. Besides, at 400 °C and for times comprehended between 120 and 180 min, naphtha yield (Figure 6.7b) is maximized up to a 34 wt%. Hence, by increasing either the temperature or the reaction time, a commitment between the naphtha and gas production must be encountered, based on the operating conditions that provide an acceptable conversion of PS. The effect of both temperature and time on gas production is well-established and can be noticed in Figures 6.7c and 6.7d, which evidence the promotion of the lightest species, principally when the temperature is raised. Considering the evolution of gases observed at 400 °C, which are enlarged by almost a 40 wt% in one hour, and that naphtha maximum is achieved around the 180 min of reaction, at which time a full conversion of PS is achieved, the optimum operating conditions for the hydrocracking of PS/VGO blend are established at 400 °C and 180 min.

6.3. APPLICATION TO OTHER BLENDS: PMMA AND PET SYSTEMS

The kinetic modelling methodology developed along Sections 6.1 and 6.2 is now applied to the hydrocracking of oxygenated plastics and VGO blends. The introduction of oxygenated compounds, as seen in Chapter 4, may lead to the formation of new products that require different treatment because of their different nature with respect to that of the considered lumps, so a modification of the reaction network B is necessary, as collected in Figure 6.8.

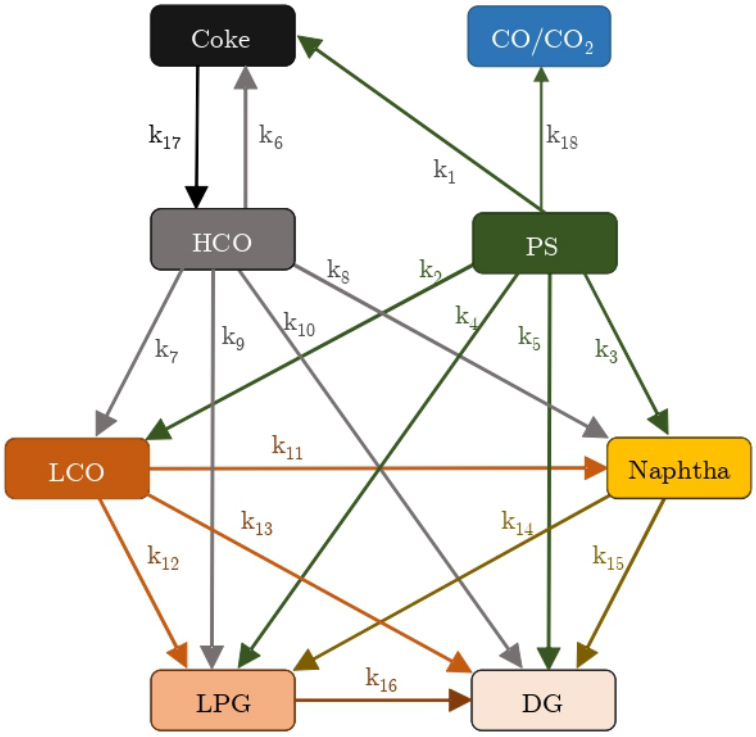

Figure 6.8. Reaction network B adapted to the formation of CO/CO_2.

The absence of CO and CO_2 in the VGO hydrocracking products leads to establishing their production only from PMMA and PET so that only one reaction pathway (reflected in a new kinetic constant and corresponding activation energy) needs to be added.

6.3.1. Fitting and analysis of kinetic parameters

The application of the kinetic model developed along the above sections of this Chapter has been successful in oxygenated plastics and VGO blends hydrocracking, as shown in the parity plot of Figure 6.9.

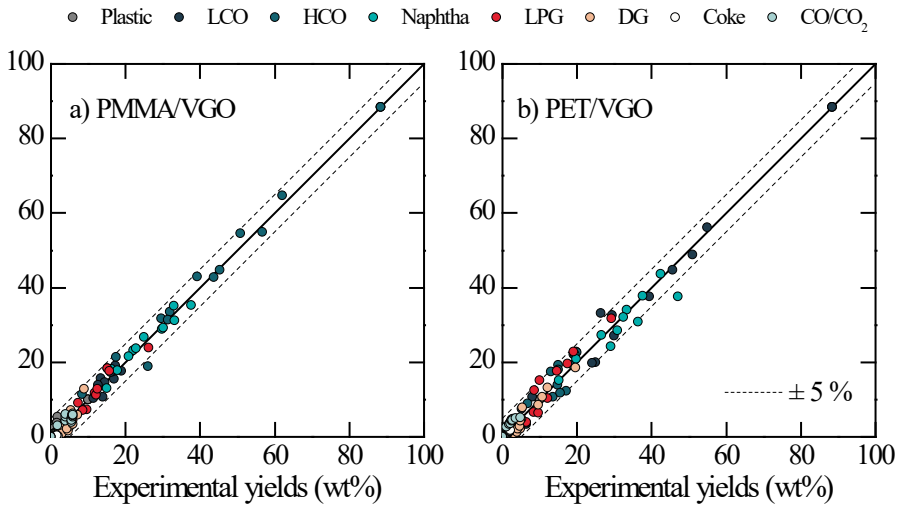

Figure 6.9. Parity plots of experimental vs predicted hydrocracking yields of a) PMMA/VGO and b) PET/VGO.

In fact, the absence of the plastic fouling phenomenon observed on these systems eases the fitting of the predicted points to those obtained experimentally in such a way that the quality of the fitting obtained for both of them can be considered even better than that obtained for PS/VGO hydrocracking. Apart from that, when comparing the fitting for PMMA/VGO hydrocracking (Figure 6.9a) with that for PET/VGO (Figure 6.9b), it can be seen that the former is more accurate than the latter. This may be attributed to the very fast conversion of PMMA; the initial conversion of this lump into others can be easily established, therefore quantifying the final destinations of the polymer and simplifying somehow the resolution of the mass balances of a complex reaction network as depicted in Figure 6.8.

The direct relationship between PMMA and its final products (as CO/CO_2 lump and other gases) reduces by two the number of lumps involved for reaction conditions that provide plastic conversion above 90 %, which are quickly achieved even at 380 °C. The differences between the most relevant reaction pathways of each system can be obtained from the comparison between the kinetic constants once the optimization of each of the systems has been performed. However, as the original blends have a 90 wt% of the same feed and the reaction system is the same in PMMA/VGO and PET/VGO hydrocracking reactions, it is logical to assume that the main changes on the kinetic parameters will be found on the constants related to the polymers.

To confirm this hypothesis, first, the kinetic constants for all the reactions except for those that take plastics as reactants have been collected in Table 6.3. As exposed, almost all the parameters have similar values for both systems, with slight differences that can be attributed either to the error inherent to the different optimization results or the specific development of the reactions in presence of different plastics, since the evolution of the conversion of the heavier fraction shows indeed differences. Nevertheless, there are no changes between them that contradict what was exposed in Section 6.2, such as the cascade reaction scheme through higher values of the main reactions (#7 and #11).

On the other side, the constants related to the plastics are collected in Table 6.4. These results show the preferred reaction pathways for each plastic, as the order of magnitude of the same reaction is different for each blend. This way, the preferential formation of gaseous products from PMMA, observed in Chapter 2, is here reflected, as the higher apparent kinetic constant of PMMA/VGO is that of step #18. Similarly, PET/VGO blend hydrocracking also results in the gain of CO/CO_2, although the pathway towards other gases (step #4) is considerably lesser than that of PMMA/VGO. The higher formation of oxygenated gases from PMMA is therefore reflected in a higher apparent kinetic constant than the one associated with PET, which has been proven to be only partially transformed into CO/CO_2.

Table 6.3. Apparent kinetic parameters at the reference temperature and corresponding apparent activation energies calculated for PMMA/VGO and PET/VGO hydrocracking reactions (R), plastics reactions excluded.

	PMMA/VGO		PET/VGO	
R	$k_{j,Tref}$	E_j (kJ mol^{-1})	$k_{j,Tref}$	E_j (kJ mol^{-1})
6	(3.37 ± 0.9) 10^{-4}	0.4 ± 0.02	(4.57 ± 0.1) 10^{-4}	0.6 ± 0.04
7	(1.99 ± 0.1) 10^{-2}	34.4 ± 1.2	(2.33 ± 0.5) 10^{-2}	12.9 ± 0.1
8	(8.89 ± 0.3) 10^{-3}	154.4 ± 13.1	(8.58 ± 0.8) 10^{-3}	209.7 ± 2.1
9	(1.59 ± 0.8) 10^{-4}	229.6 ± 16.7	(7.21 ± 0.4) 10^{-4}	415.7 ± 20.8
10	(2.59 ± 0.5) 10^{-5}	491.6 ± 33.1	(1.04 ± 0.1) 10^{-5}	436.0 ± 40.9
11	(2.47 ± 0.5) 10^{-1}	0.2 ± 0.02	(3.65 ± 0.3) 10^{-1}	0.1 ± 0.01
12	(1.86 ± 0.9) 10^{-1}	97.6 ± 7.9	(1.66 ± 0.3) 10^{-1}	61.4 ± 1.9
13	(1.41 ± 0.7) 10^{-2}	128.8 ± 14.5	(1.84 ± 0.6) 10^{-2}	69.9 ± 0.8
14	(1.04 ± 0.1) 10^{-2}	23.2 ± 2.2	(1.31 ± 0.3) 10^{-2}	37.6 ± 1.8
15	(7.26 ± 0.8) 10^{-4}	30.2 ± 0.8	(7.48 ± 0.5) 10^{-4}	40.0 ± 0.5
16	(8.58 ± 0.1) 10^{-2}	0.3 ± 0.02	(1.31 ± 0.5) 10^{-2}	0.2 ± 0.01
17	(1.80 ± 0.1) 10^{-4}	191.2 ± 10.5	(2.05 ± 0.4) 10^{-4}	197.0 ± 5.9

$k_{6\text{-}10}$: g_{cat}^{-1} g_{HCO}^{-1} h^{-1}
$k_{11\text{-}17}$: g_{cat}^{-1} h^{-1}

Apart from that, the other main destination of these plastics seems to be naphtha, since the next higher kinetic constant corresponds to step #3 (plastic → naphtha). This is consistent with the rise of monoaromatics concentration on these lumps, as particularly observed experimentally in PET/VGO hydrocracking, due to the hydrocracking mechanism of this plastic.

Table 6.4. Apparent kinetic parameters at the reference temperature and corresponding apparent activation energies of plastics reactions calculated for PMMA/VGO and PET/VGO hydrocracking reactions (R).

	PMMA/VGO		PET/VGO	
R	$k_{j,Tref}$	E_j (kJ mol^{-1})	$k_{j,Tref}$	E_j (kJ mol^{-1})
1	(8.29 ± 0.1) 10^{-5}	8.5 ± 1.0	(9.47 ± 0.9) 10^{-4}	6.2 ± 0.3
2	(1.52 ± 0.1) 10^{-2}	58.4 ± 4.0	(1.27 ± 0.1) 10^{-2}	53.9 ± 10.7
3	(4.02 ± 0.3) 10^{-1}	162.5 ± 12.4	(2.78 ± 0.3) 10^{-1}	130.8 ± 23.4
4	(1.80 ± 0.2) 10^{-1}	194.0 ± 12.6	(1.45 ± 0.8) 10^{-2}	330.4 ± 44.2
5	(2.79 ± 0.5) 10^{-3}	218.3 ± 39.6	(3.23 ± 0.5) 10^{-3}	333.1 ± 13.6
18	(1.13 ± 0.5) 10^{0}	2.5 ± 0.1	(6.76 ± 0.5) 10^{-1}	1.3 ± 0.1

$k_{1\text{-}5,18}$: g_{cat}^{-1} h^{-1}

Last, all the routes except for those of coke formation present activation energies over 120 kJ mol^{-1}, thus corresponding to the range of the reaction-limited regime [162]. The fact that the energies related to coke formation from the plastics are that low can be attributed to the thermal nature of these reactions and therefore they are more unlikely to be strongly influenced by temperature.

The good fitting provided by the optimization of the model and the application of the parameters above collected is displayed in Figure 6.10 for the different operating conditions employed for each system, as indicated in Section 6.1. As can be seen, the mere absence of the plastic fouling phenomenon within the operating framework selected provides smoother tendencies on the experimental data, thus facilitating a higher accuracy on the kinetic modelling of PMMA/VGO and PET/VGO hydrocracking, with an associated error (SSE) of 4.79 and 3.47, respectively.

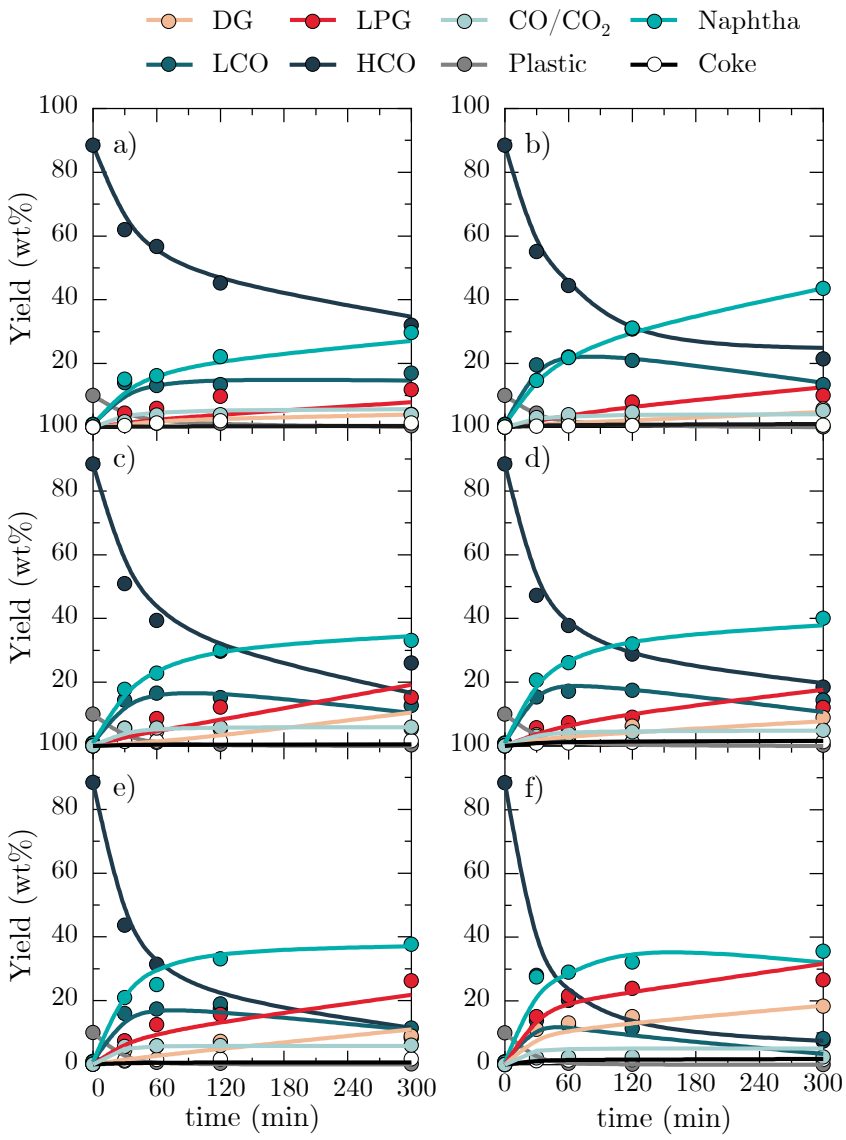

Figure 6.10. Fitting of the predicted values (lines) with respect to the experimental yields (scatter) for PMMA/VGO hydrocracking runs at a) 380, c) 400 and e) 420 °C and for PET/VGO runs at b) 400, d) 420 and f) 440 °C.

6.3.2. Activity function

To fully assess the evolution of the activity function for the two studied systems, the coke content development (shown in Figure 6.10) as well as the metals deposition evolution must be considered. For that reason, the latter is depicted in Figure 6.11 for each feeding blend. Note that the systems have been explored at different temperatures due to the refractory nature of PET, which is harder than PMMA and therefore a higher temperature has been considered as the low boundary.

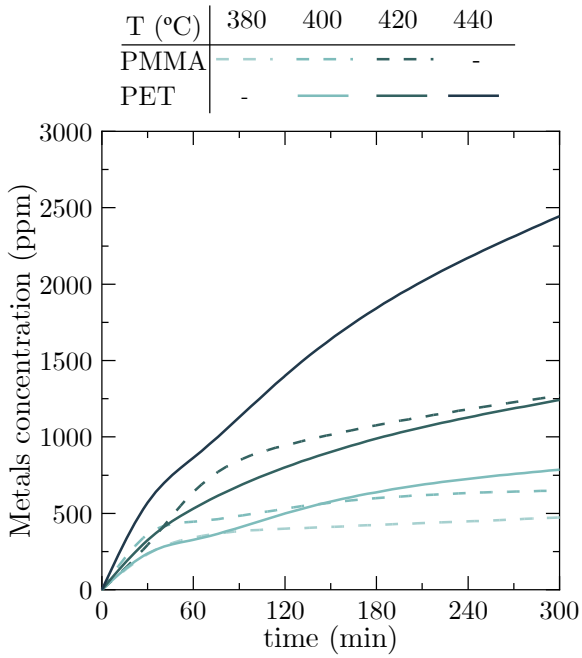

Figure 6.11. Evolution of deposited metals amount over time at the studied temperatures of the spent catalysts of PMMA/VGO and PET/VGO hydrocracking.

A similar HDM performance can be appreciated when comparing the same temperatures of reaction, as this mechanism is mainly driven by temperature, hydrogen pressure and space time [166]. Taking into account that the metals tracked in these systems belong only to the VGO and the reactions are carried out in the presence of the same catalyst, it is coherent that the evolution of the

curves is so similar, as the temperature increases the intraparticle effective diffusivity of the porphyrins through the pores of the catalyst. The escalation of the metal concentration observed at 440 °C for the PET/VGO spent catalyst confirms this effect and the influence of this driving force on the ring-opening mechanism of metal-containing structures in a high-pressure hydrogen medium.

Once the main causes of the catalyst deactivation have been exposed, the progression of the activity function for both systems has been obtained and displayed in Figure 6.12.

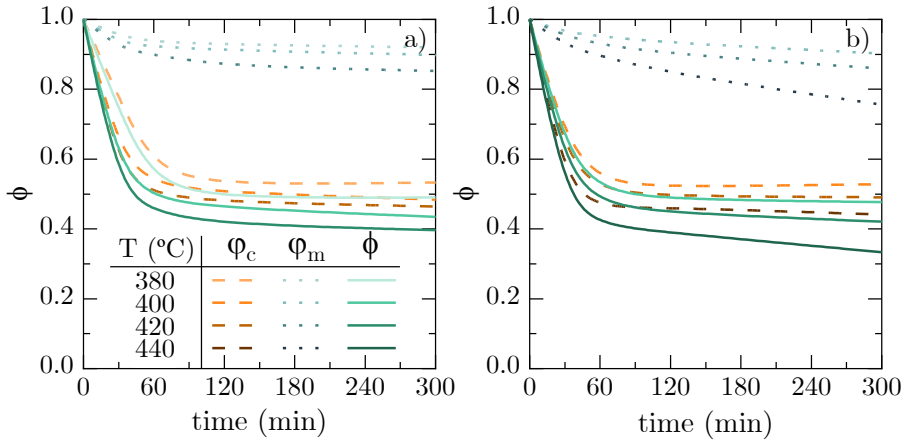

Figure 6.12. Evolution of the catalyst activity functions with reaction time and separate contribution of deactivation by coke deposition and metals poisoning for a) PMMA/VGO and b) PET/VGO hydrocracking.

It can be appreciated that metals deposition-related function is strictly temperature dependent. As discussed before, the mechanism of poisoning metal removal is conditioned by the properties of the catalyst and the reaction temperature, so the fact that, when comparing the same temperatures, the activity functions related to this phenomenon are almost the same is consistent with that fact, which is further supported by obtaining similar parameters in both systems. Moreover, the non-linear gain of the metals deposited on the spent catalyst at 440 °C is here exposed by a greater decrease of the activity function due to this mechanism than that observed when increasing the temperature from

380 to 400 °C or from 400 to 420 °C. Regarding the coke deposition, its activity decay function shows the dependence on its yield, as it reaches lower values for PMMA/VGO runs, which present higher coke yields (as exhibited in Section 4.3), that the ones provided by PET/VGO reactions at the analogous temperatures. Moreover, the effect of temperature on coke deposition is reflected in the increase of this activity decay when working at the highest temperature with PET/VGO. However, one should notice that coke deposition does not depend only on temperature, as different mechanisms are involved above certain temperatures [267]. The wider product distribution of PMMA/VGO compounds, which present higher concentrations of light hydrocarbons, is representative of the higher advance of secondary cracking reactions [379], which are also related to a greater advance of condensation and polymerization reactions that end up in the formation of coke structures.

Bearing all of that in mind, and considering the definition of the global activity function described in Eq. 6.14, Figure 6.12 shows the slightly greater decrease in the activity function observed for PMMA/VGO (Figure 6.12a) runs at 400 and 420 °C, as the activity decay related to coke is higher and metals deposition function value is similar, while the more remarkable activity drop is observed when increasing temperature to 440 °C for PET/VGO runs (Figure 6.12b), because of the parallel evolution of coke and metals deposition mechanisms.

6.3.3. Simulations

The minimization of the error function and the consequent adjustment of the kinetic parameters employed for the kinetic model allow performing simulations of the evolution of the yield of each lump with time and temperature to locate the best operating framework for each blend and to see if they differ according to the plastic that has been co-fed. According to the importance of some specific lumps exposed in Section 6.2.4, PMMA/VGO simulations of plastic, naphtha, LPG and DG yields are displayed in Figure 6.13.

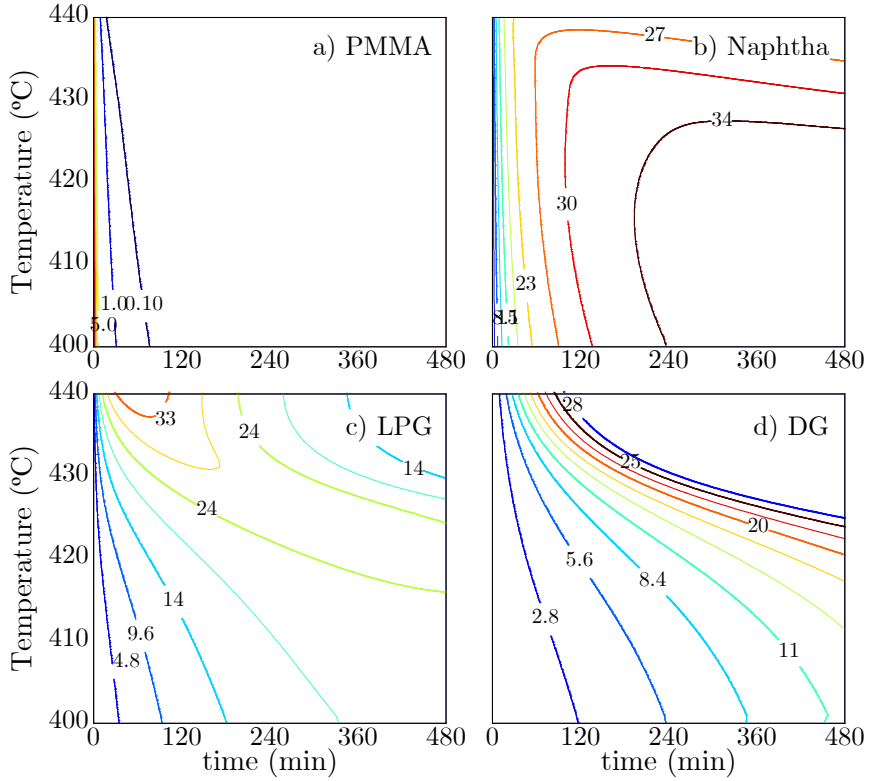

Figure 6.13. Kinetic model prediction of the effect of temperature and reaction time on the yields (wt%) of a) PMMA, b) naphtha, c) LPG and d) DG within PMMA/VGO hydrocracking.

Apart from that, the main effect of temperature on the product distribution is revealed to be that of increasing in greater extents the obtaining of secondary cracking products (LPG and DG), as anticipated before, than that of providing a higher plastic conversion for naphtha production. That being considered, the recommendations for light plastics such as PMMA blended with VGO when being fed in a hydrocracking reactor are to maintain moderate temperatures (~ 400 °C) and short-medium reaction times (≤ 120 min) to avoid the overcracking of primary products, which indeed are of higher interest.

As reflected in the experimental data, the fast conversion of the polymer and its light nature facilitate the formation of light species even at low temperatures and reaction times, achieving yields of the solid polymer below a 0.1 wt% (which

represents the 99 % conversion) at 400 °C and less than 120 min. Moreover, the advance of reactions at that temperature over time only produces an increase in naphtha of ca. 5 wt% at 240 min, while gas production is enlarged to more than double from 7.6 to 19.6 wt% in less than two hours.

Correspondingly, the kinetic parameters obtained have been used for tracking the evolution over time and temperature of those lumps when feeding PET/VGO blends, as shown in Figure 6.14.

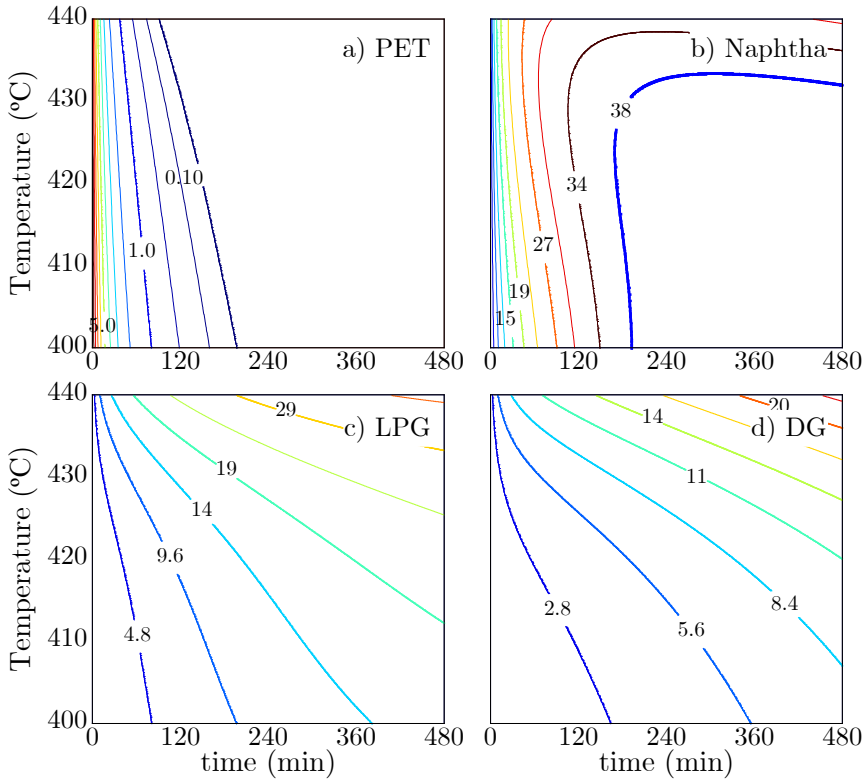

Figure 6.14. Kinetic model prediction of the effect of temperature and reaction time on the yields (wt%) of a) PET, b) naphtha, c) LPG and d) DG within PET/VGO hydrocracking.

In this case, and due to the refractory nature of PET, its conversion is considerably slower, which does not seem to be strongly influenced by temperature when looking for a complete conversion. The temperature has a

similar influence on the development of the simulations, as the vertical contour lines of Figure 6.14a and Figure 6.14b indicate that the increase in temperature does not improve for the same reaction time the conversion of the plastic or the production of naphtha, while the inclination of LPG and DG lines (Figure 6.14c and 6.15d, respectively) confirms the overcracking being favoured. For that reason, in this case, an increase in temperature is also discouraged above 400 °C because no improvement is achieved, while longer reaction times of up to 180 or even 240 min are advised due to the lesser formation of gas products and maximum plastic conversion and naphtha production are achieved, as the global reaction system is slower than that of PMMA/VGO blend.

Chapter 7

CONCLUSIONS

On the upgrading of polystyrene blended with vacuum gasoil through hydrocracking under the activity of a PtPd/Y catalyst

- The production of high-quality products from the PS/VGO hydrocracking has been proven by using an in-lab synthesized catalyst. Naphtha fraction shows high RON values, especially at 400 °C (> 92) due to its low content of monoaromatics (less than 25 wt% from 120 min onwards) and high content of isoparaffins (over 25 wt% after 120 min). The LCO fraction also is considered as suitable for its addition to the commercial diesel pool, exhibiting a clear isoparaffinic nature (almost a 60 wt% at 420 °C and 300 min).
- The effect of the main operating conditions within the hydrocracking scheme have been explored. The temperature can be appropriately established at 400 °C in order to avoid operational issues derived from the introduction of PS, producing high yields of naphtha and LCO (> 40 wt% over 180 min) and maintaining a modest level of deactivation. Time has a remarkable effect on the yields and composition of the naphtha and LCO fractions, diminishing the RON but increasing the CI of the products. However, time reactions above 180 min promote the conversion of PS ($X_{plastic} > 90$ %). Pressure has a minor effect on the product yield distribution as it does not affect to the cracking reactions and hence its major effect is appreciated in the composition of the liquids, enhancing the hydrodearomatization mechanisms.
- The catalyst deactivation is affected by the presence of a plastic since at 380 °C the unconverted PS chains derive in the deposition of carbonaceous material on the surface of the catalyst. On the other side, internal coke is the

main type observed at 400 °C and almost unique at 420 °C and causes a constrained deactivation, allowing for long time reactions. This coke is mainly formed as a consequence of the condensation of polyaromatic structures, especially at 420 °C.

- Catalyst regeneration has been found to be efficient when using an oxygen stream diluted in nitrogen at reaction temperature for the combustion of the deposited coke. The existence of other causes of deactivation with less impact (metal deposition, attrition) results in a lower magnitude of deactivation which can also be considered limited and thus the use of the catalyst in this process in continuous systems is encouraged.

On the hydrocracking of oxygenated plastics blends.

- The plastics and VGO blends hydrocracking feasibility is confirmed when aimed at the production of naphtha and LCO. The addition of plastics to the VGO results in a synergy that favours the conversion of both the polymer and the HCO fraction, this effect being more noticeable at a moderate temperature of 400 °C. Moreover, the nature of the polymer fed conditions the process in terms of higher yields of light fractions ($>$ 35 % of gas selectivity in PMMA/VGO products). Even so, the catalyst maintains a selectivity of the fractions of interest above 50 % in all cases, confirming the feasibility of hydrocracking of any of the feeds tested.
- The operating conditions (time, temperature and pressure) have been analysed when feeding neat VGO as well as when co-feeding PMMA and PET with VGO. Temperature has the effect of improving conversion most notably when feeding neat VGO, since it leads to overcracking of the PMMA/VGO and PET/VGO blends at 420 °C. With respect to time, longer reaction times favour the production of the fractions of interest at 400 °C for polymer blends and at 420 °C when VGO is fed. Regarding pressure, although its effect is to promote hydrogenation reactions, its action on the conversion of the heavier fraction is conditioned by the constraints of equilibrium and by the rapid hydrogenation of intermediate species.

- The effect of PMMA and PET co-feeding on coke deposition is also directly related to the nature of the polymers. While the PMMA/VGO blend and neat VGO presumably develop similar structures (related to the polyaromatics found in the VGO), the addition of an aromatic structure such as that of PET leads to the competitive adsorption at the catalyst centres, explaining both the slightly lower activity and deactivation observed in PET/VGO hydrocracking.
- Catalyst regeneration has also been proven to be efficient in systems with different co-fed plastics. The results indicate a decrease in the yields of the naphtha and LCO fractions as well as in the compositions of these fractions of less than 5 %. This verifies controlled combustion as a suitable method for catalyst regeneration irrespective of whether materials of polymeric nature are fed to common hydroprocessing units.

On the deep analysis of the liquid products of VGO and plastics/VGO blends hydrocracking.

- The application of advanced analytical techniques to the hydrocracking products of VGO and PMMA/VGO and PET/VGO blends allows an in-depth study of the mechanisms involved. In the case of heteroatom-free hydrocarbons, the combination of NMR and FT-ICR allows to confirm the development of ring-opening reactions independently of the presence of polymers. Nonetheless, the formation of compounds exclusively derived from these materials that are associated with structures with a higher degree of unsaturation is confirmed.
- The synergic effect of the polymers co-feeding promotes the conversion of the nitrogenated compounds, especially carbazole-type structures, which result to be more reactive. Moreover, the high refractory species are determined to be 4 rings aromatics that contain a nitrogen atom, as they are the most concentrated ones even using a highest temperature.
- Naphtha and LCO fractions resulting from the hydrocracking of both VGO and PMMA/VGO and PET/VGO blends are sulphur-free, as confirmed through PFPD analyses. Besides, the HDS route is confirmed regardless the

feed to undergo the primary hydrogenation of aromatic sulphur-containing species and its posterior hydrogenolysis.

- Concerning the oxygen, the observation of certain compounds strictly in the blends products and the assignation of their molecular formulas to compounds present in the decomposition of these plastics allow to establish their hydrocracking mechanisms.

On the kinetic modelling of the hydrocracking of plastics and VGO blends.

- A model discrimination has been performed within the PS/VGO hydrocracking, obtaining a 7-lumps model that provides an accurate prediction of the evolution of each lump usually considered in hydrocracking. For that purpose, different deactivation causes (plastic deposition, coke formation and metals poisoning) have been contemplated and mathematically represented.
- Optimisation of the system using the developed model predicts maximum PS conversion and naphtha and middle distillate yields (ca. 50 wt%), which suffer from minimum overcracking, with operating conditions set at 120 min and 400 °C. Moreover, for this reaction time the activity function reaches a pseudo-stable value which represents the arrest of the activity drop.
- This model has been extended to an 8-lump model in order to adapt the existence of oxygenated gases in the hydrocracking of PMMA/VGO and PET/VGO blends, obtaining accurate fittings that allow establishing the optimal operating conditions of these systems at 400 °C and times between 120 (for PMMA/VGO blend) and up to 240 min (for PET/VGO blend).
- The applicability of these models does not only focus on naphtha production but also on targeting different products to be maximized (such as LCO) or minimized (such as gases or coke) while considering the individual deactivation functions of each phenomenon considered as well as the global activity of the catalyst.

Chapter 8

NOMENCLATURE

Capital and lowercase letters

A	area of spectrum peaks
C	carbon content in elemental composition, wt%
C_c	carbon content deposited on the catalyst, $g_{coke}\ g_{catalyst}^{-1}$
$C_{pyridine}$	pyiridine concentration, μmol g^{-1}
D	metal dispersion, %
d_p	particle diameter, mm
D_{pore}	pore diameter, nm
E_j	activation energy of the reaction *j*, kJ mol^{-1}
F	loading mass, g
$F_{1-\alpha}$	Fisher's distribution critical value
F_{A-B}	Fisher's test value
H	hydrogen content in elemental composition, wt%
HV	heating value, kJ kg^{-1}
K	capillarity constant
$k_{d,c}$	catalyst deactivation rate constant related to coke deposition
$k_{d,m}$	catalyst deactivation rate constant related to metals poisoning

k_j	reaction rate constant of reaction *j*
$k_{j,Tref}$	reaction rate constant of reaction *j* at temperature of reference
M	metal loading of the catalyst, kg of metal (kg of catalyst)$^{-1}$
M_0	maximum metal loading of the catalyst, kg of metal (kg of catalyst)$^{-1}$
m_c	coke deactivation rate order
m_i	mass of a certain *i* lump
m_m	metals poisoning rate order
N	nitrogen content in elemental composition, wt%
n_d	number of experimental data
n_e	number of experiments
n_l	number of lumps
n_p	number of experimental data
N_s	number of metal atoms over the catalyst surface
N_t	number of total metal atoms in the catalyst
O	oxygen content in elemental composition, wt%
R	universal gas constant, kJ mol^{-1}
S	sulphur content in elemental composition, wt%
S_{BET}	specific surface area, m^2 g^{-1}
S_d	surface of sample disk, cm^2
S_i	selectivity towards certain *i* lump
$S_{micropores}$	micropores surface, m^2 g^{-1}

SSE	sum of square errors
T	temperature, °C
t	time, min
t_b	catalyst pores blockage time, min
T_{ref}	reference temperature, K
$V_{micropores}$	micropores volume, $cm^3\ g^{-1}$
W	catalyst-to-feed mass, $g_{cat}\ g_{feed}^{-1}$
W_s	weight of a sample, g
X_{HC}	hydrocracking conversion, %
$X_{plastic}$	plastic conversion, %
Y_i	yield of i lump, wt%

Greek letters

α	deactivation constant of coke deposition
ε	molar extinction coefficients, cm μmol^{-1}
ψ	global activity
φ	activity function
λ	viscosity factor
ν	viscosity, cSt
ρ	density, $kg\ m^{-3}$
υ	degrees of freedom
ω	weight factor

Superscripts

n	number of deactivation types
α_j	order of reaction *j*

Subscripts

0	at time = 0
A, B	compared models
c	coke deactivation
i	certain lump
i	certain lump
j	certain reaction
k	certain type of deactivation
m	deactivation by metals poisoning
p	deactivation by plastic deposition
s	steady state
t	at certain t time

Abbreviations and acronyms

A_1	1-ring aromatics
A_2	2-ring aromatics
A_{3+}	3^+-ring aromatics
ABC	Asphaltenic Bottom Cracking

API	American Petroleum Institute
APPI	Atmospheric Pressure Photoionization
ASTM	American Society for Testing and Materials
BCz	Benzocarbazole
BET	Brunauer-Emmett-Teller
BJH	Barret-Joyner-Halenda
BNF	Benzonaphtofuran
BT	Benzothiophene
BTX	Benzene, toluene and xylenes
$CDCl_3$	Deuterated chloroform
CI	Cetane index
CSi	Silicon carbide
Cz	Carbazole
DBCz	Dibenzocarbazole
DBE	Double bound equivalent
DBF	Dibenzofuran
DBT	Dibenzothiophene
DDS	Direct desulphurization
DG	Dry gas
DMBP	Dimethylbiphenyl
DMDBT	Dimethyldibenzothiophene
DNF	Dinaphtofuran
EDX	Energy Dispersive X-Ray Analysis
EOL	End of life

FAME	Fatty acid methyl ester
FBP	Final boiling point
FCC	Fluid catalytic cracking
FID	Flame ionization detector
FT-ICR	Fourier-transform ion cyclotron resonance
FTIR	Fourier-transform infrared spectroscopy
GC	Gas chromatography
GHV	Gross Heating Value
GWP	Global Warming Potential
HCO	Heavy cycle oil
HDA	Hydeodearomatization
HDM	Hydeodesmetallisation
HDN	Hydrodenitrogenation
HDO	Hydrodeoxygenation
HDPE	High-density polyethylene
HDS	Hydrodesulphurization
HMBC	Heteronuclear Multiple Bond Correlation
HPLC	High performance liquid chromatography
HSQC	Heteronuclear Single Quantum Coherence
HYD	Hydrogenation
IBP	Initial boiling point
ICP-AES	Inductively coupled plasma with atomic emission spectroscopy
In	Indole
iP	Isoparaffins

LCO	Light cycle oil
LDPE	Low-density polyethylene
LLDPE	Linear low-density polyethylene
LPG	Liquefied petroleum gases
Max.	Maximum
MCHT	Methyl cyclohexyltoluene
Min.	Minimum
MS	Mass spectrometry
MSW	Municipal solid waste
MW	Molecular weight
NBT	Naphtobenzothiophene
NMR	Nuclear magnetic resonance
nP	Normal paraffins
OECD	Organization for Economic Cooperation and Development
PA	Polyamide
PAHs	Polycyclic aromatic hydrocarbons
PET	Polyethylene terephthalate
PFA	Polytetrafluoroethylene
PFPD	Pulsed flame photometric detector
PP	Polypropylene
PS	Polystyrene
PVC	Polyvinyl chloride
RHC	Residue hydrocracking
RON	Research octane number

SAR	Saturate, aromatic and resin content analysis
SEM	Scanning electron microscopy
TCD	Thermal conductivity detector
TEU	Total Energy Use
THF	Tetrahydrofuran
TPD	Temperature programmed desorption
TPO	Temperature programmed oxidation
VGO	Vacuum gasoil
XRD	X-Ray diffraction

Chapter 9

REFERENCES

[1] Dawn, S., Das, S.S., Gope, S., Dey, B., Márquez, F.-P.G., Global power and energy scenario during COVID-19 pandemic: Lessons from lockdown. *Int. J. Electr. Power Energy Syst.* 2022, *137*, 107757.

[2] Norouzi, N., Rubens, G.Z. de, Choupanpiesheh, S., Enevoldsen, P., When pandemics impact economies and climate change: Exploring the impacts of COVID-19 on oil and electricity demand in China. *Energy Res. Soc. Sci.* 2020, *68*, 101654.

[3] Ma, R.R., Xiong, T., Bao, Y., The Russia-Saudi Arabia oil price war during the COVID-19 pandemic. *Energy Econ.* 2021, *102*, 105517.

[4] Khan, K., Su, C.-W., Khurshid, A., Umar, M., COVID-19 impact on multifractality of energy prices: Asymmetric multifractality analysis. *Energy* 2022, *256*, 124607.

[5] Çelik, D., Meral, M.E., Waseem, M., The progress, impact analysis, challenges and new perceptions for electric power and energy sectors in the light of the COVID-19 pandemic. *Sustain. Energy Grids Netw.* 2022, *31*, 100728.

[6] Wang, Q., Huang, R., Li, R., Towards smart energy systems – A survey about the impact of COVID-19 pandemic on renewable energy research. *Energy Strategy Rev.* 2022, *41*, 100845.

[7] Wang, W., Fan, L., Li, Z., Zhou, P., Chen, X., Measuring dynamic competitive relationship and intensity among the global coal importing trade. *Appl. Energy* 2021, *303*, 117611.

[8] Xia, D., Zhang, L., Coupling coordination degree between coal production reduction and CO_2 emission reduction in coal industry. *Energy* 2022, *258*, 124902.

[9] Andreoni, V., Drivers of coal consumption changes: A decomposition analysis for Chinese regions. *Energy* 2022, *242*, 122975.

[10] Kuzemko, C., Blondeel, M., Dupont, C., Brisbois, M.C., Russia's war on Ukraine, European energy policy responses & implications for sustainable transformations. *Energy Res. Soc. Sci.* 2022, *93*, 102842.

[11] Zhou, X.-Y., Lu, G., Xu, Z., Yan, X., Khu, S.-T., Yang, J., Zhao, J., Influence of Russia-Ukraine War on the Global Energy and Food Security. *Resour. Conserv. Recycl.* 2023, *188*, 106657.

[12] Yang, Q., Scoglio, C.M., Gruenbacher, D.M., Robustness of supply chain networks against underload cascading failures. *Phys. Stat. Mech. Its Appl.* 2021, *563*, 125466.

[13] Fails, M.D., What types of political regimes subsidize fuel consumption? *Extr. Ind. Soc.* 2022, *9*, 101037.

[14] Kochtcheeva, L.V., Renewable energy: global challenges. *E-Int. Relat.* 2016.

[15] Adekoya, O.B., Oliyide, J.A., Fasanya, I.O., Renewable and non-renewable energy consumption – Ecological footprint nexus in net-oil exporting and net-oil importing countries: Policy implications for a sustainable environment. *Renew. Energy* 2022, *189*, 524–534.

[16] Li, F., Zhang, J., Li, X., Research on supporting developing countries to achieve green development transition: Based on the perspective of renewable energy and foreign direct investment. *J. Clean. Prod.* 2022, *372*, 133726.

[17] Ranjbar, M.H., Etemad-Shahidi, A., Kamranzad, B., Modeling the combined impact of climate change and sea-level rise on general circulation and residence time in a semi-enclosed sea. *Sci. Total Environ.* 2020, *740*, 140073.

[18] Cheng, L., Trenberth, K.E., Fasullo, J., Boyer, T., Abraham, J., Zhu, J., Improved estimates of ocean heat content from 1960 to 2015. *Sci. Adv.* 2017, *3*, e1601545.

[19] Zhang, Q., Li, Y.P., Huang, G.H., Wang, H., Li, Y.F., Liu, Y.R., Shen, Z.Y., A novel statistical downscaling approach for analyzing daily precipitation and extremes under the impact of climate change: Application to an arid region. *J. Hydrol.* 2022, 128730.

[20] Bastidas-Arteaga, E., Rianna, G., Gervasio, H., Nogal, M., Multi-region lifetime assessment of reinforced concrete structures subjected to carbonation and climate change. *Structures* 2022, *45*, 886–899.

[21] Minowa, M., Schaefer, M., Sugiyama, S., Sakakibara, D., Skvarca, P., Frontal ablation and mass loss of the Patagonian icefields. *Earth Planet. Sci. Lett.* 2021, *561*, 116811.

[22] Suganuma, S., Katada, N., Innovation of catalytic technology for upgrading of crude oil in petroleum refinery. *Fuel Process. Technol.* 2020, *208*, 106518.

[23] Luz, M.S., Oliveira, P.V., Non-chromatographic method for separation and determination of Fe, Ni and V porphyrins in crude oil. *Talanta* 2019, *199*, 147–154.

[24] Pabón, R.E.C., Filho, C.R. de S., Crude oil spectral signatures and empirical models to derive API gravity. *Fuel* 2019, *237*, 1119–1131.

[25] Draeger, R., Cunha, B.S.L., Müller-Casseres, E., Rochedo, P.R.R., Szklo, A., Schaeffer, R., Stranded crude oil resources and just transition: Why do crude oil quality, climate ambitions and land-use emissions matter. *Energy* 2022, *255*, 124451.

[26] BP p.l.c., Statistical Review of World Energy 2021 | 70th edition. 2021.

[27] Ritchie, H., Roser, M., Rosado, P., Energy. *Our World Data* 2022.

[28] Gates, I.D., Wang, J., Gates, T.D., Su, Y., Kannaiyan, R., Luo, R., Chapter 9 - Heavy oil and extra heavy oil (bitumen) recovery, in: Wang, Q. (Ed.), *Recovery Improvement*, Gulf Professional Publishing, 2023, pp. 533–562.

[29] Ismail, W.A., Raheem, A.S.A., Bahzad, D., Chapter 6 - Biotechnological approaches for upgrading of unconventional crude oil, in: Singh, R.P., Manchanda, G., Bhattacharjee, K., Panosyan, H. (Eds.), *Microbial Syntrophy-Mediated Eco-Enterprising*, Academic Press, 2022, pp. 125–175.

[30] Speight, J.G., Chapter 1 - Feedstocks, in: Speight, J.G. (Ed.), *The Refinery of the Future*, William Andrew Publishing, Boston 2011, pp. 1–37.

[31] Zheng, X., Wang, R., Liddle, B., Wen, Y., Lin, L., Wang, L., Crude oil footprint in the rapidly changing world and implications from their income and price elasticities. *Energy Policy* 2022, *169*, 113204.

[32] Zhang, Z., He, M., Zhang, Y., Wang, Y., Geopolitical risk trends and crude oil price predictability. *Energy* 2022, *258*, 124824.

[33] IEA, World Energy Outlook 2021, IEA, Paris 2021.

[34] Wang, Z., Fan, Z., Zhang, X., Liu, B., Chen, X., Status, trends and enlightenment of global oil and gas development in 2021. *Pet. Explor. Dev.* 2022, *49*, 1210–1228.

[35] Ren, X., liu, Z., Jin, C., Lin, R., Oil price uncertainty and enterprise total factor productivity: Evidence from China. *Int. Rev. Econ. Finance* 2023, *83*, 201–218.

[36] Al-Samhan, M., Al-Fadhli, J., Al-Otaibi, A.M., Al-Attar, F., Bouresli, R., Rana, M.S., Prospects of refinery switching from conventional to integrated: An opportunity for sustainable investment in the petrochemical industry. *Fuel* 2022, *310*, 122161.

[37] Zhang, F., Su, X., Tan, A., Yao, J., Li, H., Prediction of research octane number loss and sulfur content in gasoline refining using machine learning. *Energy* 2022, *261*, 124823.

[38] Ervine, C., Directive 2004/39/Ec of the European Parliament and of the Council of 21 April 2004, in: *Core Statutes on Company Law*, Macmillan Education UK, London 2015, pp. 757–759.

[39] Haruna, A., Merican Aljunid Merican, Z., Gani Musa, S., Abubakar, S., Sulfur removal technologies from fuel oil for safe and sustainable environment. *Fuel* 2022, *329*, 125370.

[40] Uludamar, E., Özgür, C., Optimization of exhaust emissions, vibration, and noise of a hydrogen enriched fuelled diesel engine. *Int. J. Hydrog. Energy* 2022, *47*, 37090–37105.

[41] Zhang, Z., Fan, X., Song, C., Lu, W., Li, H., Wang, P., The effect of dual dielectric barrier discharge non-thermal plasma on the emission characteristics of diesel engine. *Environ. Chall.* 2022, 100652.

[42] Ma, Z., Zhang, K., Xiang, H., Gu, J., Yang, M., Deng, K., Experimental study on influence of high exhaust backpressure on diesel engine performance via energy and exergy analysis. *Energy* 2023, *263*, 125788.

[43] Wang, Q., Li, Y., Benally, C., Li, Y., Chen, C., An, Z., Gamal El-Din, M., Spent fluid catalytic cracking (FCC) catalyst enhances pyrolysis of refinery waste activated sludge. *J. Clean. Prod.* 2021, *295*, 126382.

[44] Varjani, S.J., Gnansounou, E., Pandey, A., Comprehensive review on toxicity of persistent organic pollutants from petroleum refinery waste and their degradation by microorganisms. *Chemosphere* 2017, *188*, 280–291.

[45] Li, J., Xin, W., Liang, J., Shang, P., Song, Y., Wang, Q., Gamal El-Din, M., Arslan, M., Guo, S., Chen, C., Alkaline fermentation of refinery waste activated sludge mediated by refinery spent caustic for volatile fatty acids production. *J. Environ. Manage.* 2022, *324*, 116317.

[46] Guerin, T.F., Phytotoxicity complements chemical assessment for re-use and re-purposing of refinery wastes for soil amendment purposes after bioremediation. *J. Environ. Manage.* 2022, *317*, 115257.

[47] Soares, J., Miguel, I., Venâncio, C., Lopes, I., Oliveira, M., Public views on plastic pollution: Knowledge, perceived impacts, and pro-environmental behaviours. *J. Hazard. Mater.* 2021, *412*, 125227.

[48] Yue, X.-H., Zhang, F.-S., Wu, L., Zhang, C.-C., Qian, P., Upcycling of blending waste plastics as flexible growing substrate with superabsorbing property. *Chem. Eng. J.* 2022, *435*, 134622.

[49] King, S., Locock, K.E.S., A circular economy framework for plastics: A semi-systematic review. *J. Clean. Prod.* 2022, *364*, 132503.

[50] Gao, Y., Neal, L., Ding, D., Wu, W., Baroi, C., Gaffney, A.M., Li, F., Recent Advances in Intensified Ethylene Production—A Review. *ACS Catal.* 2019, *9*, 8592–8621.

[51] Lavrenov, A.V., Saifulina, L.F., Buluchevskii, E.A., Bogdanets, E.N., Propylene production technology: Today and tomorrow. *Catal. Ind.* 2015, *7*, 175–187.

[52] Kuusela, K., Uusitalo, V., Ahola, J., Levänen, J., The transformation of plastics production from net positive greenhouse gas emissions to net negative: An environmental sustainability assessment of CO_2-based polypropylene. *J. CO2 Util.* 2021, *52*, 101672.

[53] Toktarova, A., Göransson, L., Thunman, H., Johnsson, F., Thermochemical recycling of plastics – Modeling the implications for the electricity system. *J. Clean. Prod.* 2022, *374*, 133891.

[54] Plastics - the Facts 2021 • Plastics Europe. *Plast. Eur.* 2021.

[55] OECD, Global Plastics Outlook: Policy Scenarios to 2060, Organisation for Economic Co-operation and Development, Paris 2022.

[56] Report covers sustainability in the plastics supply chain. *Reinf. Plast.* 2021, *65*, 75.

[57] Tong, Y., Lin, L., Tao, Y., Huang, Y., Zhu, X., The occurrence, speciation, and ecological effect of plastic pollution in the bay ecosystems. *Sci. Total Environ.* 2023, *857*, 159601.

[58] Yadav, V., Sherly, M.A., Ranjan, P., Prasad, V., Tinoco, R.O., Laurent, A., Risk of plastics losses to the environment from Indian landfills. *Resour. Conserv. Recycl.* 2022, *187*, 106610.

[59] Wilcox, C., Van Sebille, E., Hardesty, B.D., Threat of plastic pollution to seabirds is global, pervasive, and increasing. *Proc. Natl. Acad. Sci.* 2015, *112*, 11899–11904.

[60] Leterme, S.C., Tuuri, E.M., Drummond, W.J., Jones, R., Gascooke, J.R., Microplastics in urban freshwater streams in Adelaide, Australia: A source of plastic pollution in the Gulf St Vincent. *Sci. Total Environ.* 2023, *856*, 158672.

[61] Bhoi, P.R., Rahman, M.H., Hydrocarbons recovery through catalytic pyrolysis of compostable and recyclable waste plastics using a novel desktop staged reactor. *Environ. Technol. Innov.* 2022, *27*, 102453.

[62] Palos, R., Gutiérrez, A., Vela, F.J., Olazar, M., Arandes, J.M., Bilbao, J., Waste Refinery: The Valorization of Waste Plastics and End-of-Life Tires in Refinery Units. A Review. *Energy Fuels* 2021, *35*, 3529–3557.

[63] Adeboye, B.S., Idris, M.O., Adedeji, W.O., Adefajo, A.A., Oyewusi, T.F., Adelekun, A., Characterization and energy potential of municipal solid waste in Osogbo metropolis. *Clean. Waste Syst.* 2022, *2*, 100020.

[64] Komilis, D., Evangelou, A., Giannakis, G., Lymperis, C., Revisiting the elemental composition and the calorific value of the organic fraction of municipal solid wastes. *Waste Manag.* 2012, *32*, 372–381.

[65] Ouyang, D., Wang, F., Gao, D., Han, W., Hu, X., Qiao, D., Zhao, X., Light-driven lignocellulosic biomass conversion for production of energy and chemicals. *IScience* 2022, *25*, 105221.

[66] Kumari, G., Karmee, S.K., Chapter 22 - Thermochemical routes applying biomass: a critical assessment, in: Sahay, S. (Ed.), *Handbook of Biofuels*, Academic Press, 2022, pp. 435–451.

[67] Vávrová, K., Solcova, O., Knápek, J., Weger, J., Soukup, K., Humešová, T., Králík, T., Bím, J., Economic evaluation of Hemp's (Cannabis sativa) residual biomass for production of direct energy or biochar. *Fuel* 2022, *329*, 125435.

[68] Tezer, Ö., Karabağ, N., Öngen, A., Çolpan, C.Ö., Ayol, A., Biomass gasification for sustainable energy production: A review. *Int. J. Hydrog. Energy* 2022, *47*, 15419–15433.

[69] Wu, Y., Wang, H., Li, H., Han, X., Zhang, M., Sun, Y., Fan, X., Tu, R., Zeng, Y., Xu, C.C., Xu, X., Applications of catalysts in thermochemical conversion of biomass (pyrolysis, hydrothermal liquefaction and gasification): A critical review. *Renew. Energy* 2022, *196*, 462–481.

[70] Jablonský, M., Škulcová, A., Malvis, A., Šima, J., Extraction of value-added components from food industry based and agro-forest biowastes by deep eutectic solvents. *J. Biotechnol.* 2018, *282*, 46–66.

[71] Debnath, D., Das, A., 32 - Third-generation biofuels and food security, in: Jacob-Lopes, E., Zepka, L.Q., Severo, I.A., Maroneze, M.M. (Eds.), *3rd Generation Biofuels*, Woodhead Publishing, 2022, pp. 757–768.

[72] Yang, D., Li, S., He, S., Zheng, Y., Can conversion of CO_2 into fuels via electrochemical or thermochemical reduction be energy efficient and reduce emissions? *Energy Convers. Manag.* 2022, *273*, 116425.

[73] Offermann-van Heek, J., Arning, K., Sternberg, A., Bardow, A., Ziefle, M., Assessing public acceptance of the life cycle of CO_2-based fuels: Does information make the difference? *Energy Policy* 2020, *143*, 111586.

[74] He, Y., Zhou, Y., Feng, J., Xing, M., Photothermal conversion of CO_2 to fuel with nickel-based catalysts: A review. *Environ. Funct. Mater.* 2022, *1*, 204–217.

[75] Shulman, V.L., 4 - Management of end-of-life tires, in: Letcher, T.M., Shulman, V.L., Amirkhanian, S. (Eds.), *Tire Waste and Recycling*, Academic Press, 2021, pp. 43–67.

[76] Martínez, J.D., Campuzano, F., Agudelo, A.F., Cardona-Uribe, N., Arenas, C.N., Chemical recycling of end-of-life tires by intermediate pyrolysis using a twin-auger reactor: Validation in a laboratory environment. *J. Anal. Appl. Pyrolysis* 2021, *159*, 105298.

[77] Al-Salem, S.M., Slow pyrolysis of end of life tyres (ELTs) grades: Effect of temperature on pyro-oil yield and quality. *J. Environ. Manage.* 2022, *301*, 113863.

[78] Artíñano, B., Gómez-Moreno, F.J., Díaz, E., Amato, F., Pandolfi, M., Alonso-Blanco, E., Coz, E., García-Alonso, S., Becerril-Valle, M., Querol, X., Alastuey, A., van Drooge, B.L., Outdoor and indoor particle characterization from a large and uncontrolled combustion of a tire landfill. *Sci. Total Environ.* 2017, *593–594*, 543–551.

[79] Tran, T.Q., Skariah Thomas, B., Zhang, W., Ji, B., Li, S., Brand, A.S., A comprehensive review on treatment methods for end-of-life tire rubber used for rubberized cementitious materials. *Constr. Build. Mater.* 2022, *359*, 129365.

[80] Abbas-Abadi, M.S., Kusenberg, M., Shirazi, H.M., Goshayeshi, B., Van Geem, K.M., Towards full recyclability of end-of-life tires: Challenges and opportunities. *J. Clean. Prod.* 2022, *374*, 134036.

[81] Gaidhane, J., Ullah, I., Khalatkar, A., Tyre remanufacturing: A brief review. *Mater. Today Proc.* 2022, *60*, 2257–2261.

[82] Lamour, M., Cecchin, A., Repurposed materials in construction: A review of low-processed scrap tires in civil engineering applications for disaster risk reduction. *Constr. Build. Mater.* 2021, *293*, 123368.

[83] Formela, K., Waste tire rubber-based materials: Processing, performance properties and development strategies. *Adv. Ind. Eng. Polym. Res.* 2022, *5*, 234–247.

[84] Hwang, J.G., Lee, B.K., Choi, M.K., Park, H.C., Choi, H.S., Optimal production of waste tire pyrolysis oil and recovery of high value-added D-limonene in a conical spouted bed reactor. *Energy* 2023, *262*, 125519.

[85] Oboirien, B.O., North, B.C., A review of waste tyre gasification. *J. Environ. Chem. Eng.* 2017, *5*, 5169–5178.

[86] Santasnachok, M., Nakyai, T., Exergetic and environmental assessments of hydrogen production via waste tire gasification with co-feeding of CO_2 recycled. *Energy Rep.* 2022, *8*, 859–867.

[87] Circular Economy. *ETRMA* 2019.

[88] Al-Salem, S.M., Karam, H.J., Al-Qassimi, M.M., Pyro-gas analysis of fixed bed reactor end of life tyres (ELTs) pyrolysis: A comparative study. *J. Environ. Manage.* 2022, *320*, 115852.

[89] Gao, N., Wang, F., Quan, C., Santamaria, L., Lopez, G., Williams, P.T., Tire pyrolysis char: Processes, properties, upgrading and applications. *Prog. Energy Combust. Sci.* 2022, *93*, 101022.

[90] Rodríguez, E., Palos, R., Gutiérrez, A., Arandes, J.M., Bilbao, J., Production of Non-Conventional Fuels by Catalytic Cracking of Scrap Tires Pyrolysis Oil. *Ind. Eng. Chem. Res.* 2019, *58*, 5158–5167.

[91] Rodríguez, E., Palos, R., Gutiérrez, A., Arandes, J.M., Bilbao, J., Scrap tires pyrolysis oil as a co-feeding stream on the catalytic cracking of vacuum gasoil under fluid catalytic cracking conditions. *Waste Manag.* 2020, *105*, 18–26.

[92] Rodríguez, E., Izaddoust, S., Valecillos, J., Bilbao, J., Arandes, J.M., Castaño, P., Epelde, E., Elordi, G., Lessening coke formation and boosting gasoline yield by incorporating scrap tire pyrolysis oil in the cracking conditions of an FCC unit. *Energy Convers. Manag.* 2020, *224*.

[93] Hita, I., Gutiérrez, A., Olazar, M., Bilbao, J., Arandes, J.M., Castaño, P., Upgrading model compounds and scrap tires pyrolysis oil (STPO) on hydrotreating NiMo catalysts with tailored supports. *Fuel* 2015, *145*, 158–169.

[94] Hita, I., Palos, R., Arandes, J.M., Hill, J.M., Castaño, P., Petcoke-derived functionalized activated carbon as support in a bifunctional catalyst for tire oil hydroprocessing. *Fuel Process. Technol.* 2016, *144*, 239–247.

[95] Hita, I., Rodríguez, E., Olazar, M., Bilbao, J., Arandes, J.M., Castaño, P., Prospects for obtaining high quality fuels from the hydrocracking of a hydrotreated scrap tires pyrolysis oil. *Energy Fuels* 2015, *29*, 5458–5466.

[96] He, J., Hong, Y., Kong, L., Dan, Z., Lv, X., Chen, G., Tang, O., Chen, D., Spatial distribution and management of the energy potential of municipal solid waste incineration: A case study of Lhasa, China. *J. Environ. Manage.* 2022, *322*, 116094.

[97] Cudjoe, D., Wang, H., Plasma gasification versus incineration of plastic waste: Energy, economic and environmental analysis. *Fuel Process. Technol.* 2022, *237*, 107470.

[98] Panda, A.K., Singh, R.K., Mishra, D.K., Thermolysis of waste plastics to liquid fuel. A suitable method for plastic waste management and manufacture of value added products-A world prospective. *Renew. Sustain. Energy Rev.* 2010, *14*, 233–248.

[99] Ferdous, W., Manalo, A., Siddique, R., Mendis, P., Zhuge, Y., Wong, H.S., Lokuge, W., Aravinthan, T., Schubel, P., Recycling of landfill wastes (tyres, plastics and glass) in construction – A review on global waste generation, performance, application and future opportunities. *Resour. Conserv. Recycl.* 2021, *173*, 105745.

[100] van der Hulst, M.K., Ottenbros, A.B., van der Drift, B., Ferjan, Š., van Harmelen, T., Schwarz, A.E., Worrell, E., van Zelm, R., Huijbregts, M.A.J., Hauck, M., Greenhouse gas benefits from direct chemical recycling of mixed plastic waste. *Resour. Conserv. Recycl.* 2022, *186*, 106582.

[101] Crippa, M., Morico, B., Chapter 12 - PET depolymerization: a novel process for plastic waste chemical recycling, in: Basile, A., Centi, G., Falco, M.D., Iaquaniello, G. (Eds.), *Studies in Surface Science and Catalysis*, Elsevier, 2020, pp. 215–229.

[102] Chanda, M., Chemical aspects of polymer recycling. *Adv. Ind. Eng. Polym. Res.* 2021, *4*, 133–150.

[103] Acomb, J.C., Wu, C., Williams, P.T., Control of steam input to the pyrolysis-gasification of waste plastics for improved production of hydrogen or carbon nanotubes. *Appl. Catal. B Environ.* 2014, *147*, 571–584.

[104] Tian, W., Song, P., Zhang, H., Duan, X., Wei, Y., Wang, H., Wang, S., Microplastic materials in the environment: Problem and strategical solutions. *Prog. Mater. Sci.* 2023, *132*, 101035.

[105] Dogu, O., Pelucchi, M., Van de Vijver, R., Van Steenberge, P.H.M., D'hooge, D.R., Cuoci, A., Mehl, M., Frassoldati, A., Faravelli, T., Van Geem, K.M., The chemistry of chemical recycling of solid plastic waste via pyrolysis and gasification: State-of-the-art, challenges, and future directions. *Prog. Energy Combust. Sci.* 2021, *84*, 100901.

[106] Martínez-Narro, G., Prasertcharoensuk, P., Diaz-Silvarrey, L.S., Dixon, L., Phan, A.N., Chemical recycling of mixed plastic waste via catalytic pyrolysis. *J. Environ. Chem. Eng.* 2022, *10*, 108494.

[107] Inayat, A., Fasolini, A., Basile, F., Fridrichova, D., Lestinsky, P., Chemical recycling of waste polystyrene by thermo-catalytic pyrolysis: A description

for different feedstocks, catalysts and operation modes. *Polym. Degrad. Stab.* 2022, *201*, 109981.

[108] Lopez, G., Artetxe, M., Amutio, M., Bilbao, J., Olazar, M., Thermochemical routes for the valorization of waste polyolefinic plastics to produce fuels and chemicals. A review. *Renew. Sustain. Energy Rev.* 2017, *73*, 346–368.

[109] Lima, R.B., Neto, M.M.S., Oliveira, D.S., Santos, A.G.D., Souza, L.D., Caldeira, V.P.S., Obtainment of hierarchical ZSM-5 zeolites by alkaline treatment for the polyethylene catalytic cracking. *Adv. Powder Technol.* 2021, *32*, 515–523.

[110] Niksiar, A., Faramarzi, A.H., Sohrabi, M., Kinetic study of polyethylene terephthalate (PET) pyrolysis in a spouted bed reactor. *J. Anal. Appl. Pyrolysis* 2015, *113*, 419–425.

[111] Artetxe, M., Lopez, G., Amutio, M., Elordi, G., Bilbao, J., Olazar, M., Cracking of High Density Polyethylene Pyrolysis Waxes on HZSM-5 Catalysts of Different Acidity. *Ind. Eng. Chem. Res.* 2013, *52*, 10637–10645.

[112] Ojha, D.K., Vinu, R., Resource recovery via catalytic fast pyrolysis of polystyrene using zeolites. *J. Anal. Appl. Pyrolysis* 2015, *113*, 349–359.

[113] Marcilla, A., Gómez-Siurana, A., Valdés, F.J., Evolution of the deactivation mode and nature of coke of HZSM-5 and USY zeolites in the catalytic cracking of low-density polyethylene during successive cracking runs. *Appl. Catal. Gen.* 2009, *352*, 152–158.

[114] López, A., de Marco, I., Caballero, B.M., Laresgoiti, M.F., Adrados, A., Aranzabal, A., Catalytic pyrolysis of plastic wastes with two different types of catalysts: ZSM-5 zeolite and Red Mud. *Appl. Catal. B Environ.* 2011, *104*, 211–219.

[115] Lin, Y.-H., Tseng, C.-C., Wei, T.-T., Hsu, C.-T., Recycling of dual hazardous wastes in a catalytic fluidizing process. *Catal. Today* 2011, *174*, 37–45.

[116] Thivasasith, A., Rodaum, C., Nunthakitgoson, W., Assavapanumat, S., Wattanakit, C., Fine-tuning the catalytic cracking-assisted synthesis of plastic-derived MWCNTs-supported metal oxides for methanol electrooxidation. *Carbon Trends* 2022, *7*, 100158.

[117] Socci, J., Osatiashtiani, A., Kyriakou, G., Bridgwater, T., The catalytic cracking of sterically challenging plastic feedstocks over high acid density Al-SBA-15 catalysts. *Appl. Catal. Gen.* 2019, *570*, 218–227.

[118] Artetxe, M., Lopez, G., Amutio, M., Elordi, G., Bilbao, J., Olazar, M., Light olefins from HDPE cracking in a two-step thermal and catalytic process. *Chem. Eng. J.* 2012, *207–208*, 27–34.

[119] Ratnasari, D.K., Nahil, M.A., Williams, P.T., Catalytic pyrolysis of waste plastics using staged catalysis for production of gasoline range hydrocarbon oils. *J. Anal. Appl. Pyrolysis* 2017, *124*, 631–637.

[120] Rodríguez, E., Gutiérrez, A., Palos, R., Vela, F.J., Arandes, J.M., Bilbao, J., Fuel production by cracking of polyolefins pyrolysis waxes under fluid catalytic cracking (FCC) operating conditions. *Waste Manag.* 2019, *93*, 162–172.

[121] Vasilkovová, B., Hájeková, E., Hudec, P., Česáková, J., Horňáček, M., Kaliňák, M., Jorík, V., Two-stage thermal and catalytic cracking of polypropylene using natural clinoptilolite in a catalytic step to petrochemicals and fuels. *J. Anal. Appl. Pyrolysis* 2022, *167*, 105679.

[122] Renzini, M.S., Sedran, U., Pierella, L.B., H-ZSM-11 and Zn-ZSM-11 zeolites and their applications in the catalytic transformation of LDPE. *J. Anal. Appl. Pyrolysis* 2009, *86*, 215–220.

[123] Rodríguez, E., Palos, R., Gutiérrez, A., Trueba, D., Arandes, J.M., Bilbao, J., Towards waste refinery: Co-feeding HDPE pyrolysis waxes with VGO into the catalytic cracking unit. *Energy Convers. Manag.* 2020, *207*.

[124] Vela, F.J., Palos, R., Bilbao, J., Arandes, J.M., Gutiérrez, A., Effect of co-feeding HDPE on the product distribution in the hydrocracking of VGO. *Catal. Today* 2020, *353*, 197–203.

[125] Vela, F.J., Palos, R., Trueba, D., Bilbao, J., Arandes, J.M., Gutiérrez, A., Different approaches to convert waste polyolefins into automotive fuels via hydrocracking with a NiW/HY catalyst. *Fuel Process. Technol.* 2021, *220*, 106891.

[126] Marafi, M., Stanislaus, A., Furimsky, E., Chapter 3 - Hydroprocessing of Petroleum, in: Marafi, M., Stanislaus, A., Furimsky, E. (Eds.), *Handbook of Spent Hydroprocessing Catalysts*, Elsevier, Amsterdam 2010, pp. 17–49.

[127] Speight, J.G., Chapter 11 - Upgrading by Hydrocracking, in: Speight, J.G. (Ed.), *Heavy Oil Recovery and Upgrading*, Gulf Professional Publishing, 2019, pp. 467–528.

[128] Wang, H., He, S., Li, Y., Qin, H., Wu, Y., Monitoring the ambient oxidation of a NiMoSx/Al2O3 hydrotreating catalyst by a thermogravimetric method. *Thermochim. Acta* 2022, *718*, 179381.

[129] Speight, J.G., The desulfurization of heavy oils and residua, CRC Press, 1999.

[130] Stolyarova, E.A., Danilevich, V.V., Klimov, O.V., Gerasimov, E.Yu., Ushakov, V.A., Chetyrin, I.A., Lushchikova, A.E., Saiko, A.V., Kondrashev, D.O., Kleimenov, A.V., Noskov, A.S., Comparison of alumina supports and catalytic activity of CoMoP/γ-Al2O3 hydrotreating catalysts obtained using flash calcination of gibbsite and precipitation method. *Catal. Today* 2020, *353*, 88–98.

[131] Nie, H., Li, H., Yang, Q., Li, D., Effect of structure and stability of active phase on catalytic performance of hydrotreating catalysts. *Catal. Today* 2018, *316*, 13–20.

[132] Duarte, L., Garzón, L., Baldovino-Medrano, V.G., An analysis of the physicochemical properties of spent catalysts from an industrial hydrotreating unit. *Catal. Today* 2019, *338*, 100–107.

[133] Pimerzin, A., Roganov, A., Mozhaev, A., Maslakov, K., Nikulshin, P., Pimerzin, A., Active phase transformation in industrial CoMo/Al2O3 hydrotreating catalyst during its deactivation and rejuvenation with organic chemicals treatment. *Fuel Process. Technol.* 2018, *173*, 56–65.

[134] Kohli, K., Prajapati, R., Maity, S.K., Sau, M., Garg, M.O., Deactivation of hydrotreating catalyst by metals in resin and asphaltene parts of heavy oil and residues. *Fuel* 2016, *175*, 264–273.

[135] Komurcu, H., Yılmaz, K., Gurdal, S., Yasar, M., Hydrogenation reactions of kerosene on nickel-based catalysts. *Int. J. Hydrog. Energy* 2022.

[136] Chen, Z., Feng, S., Zhang, L., Shi, Q., Xu, Z., Zhao, S., Xu, C., Molecular-level kinetic modelling of fluid catalytic cracking slurry oil hydrotreating. *Chem. Eng. Sci.* 2019, *195*, 619–630.

[137] Stranges, A.N., A History of the Fischer-Tropsch Synthesis in Germany 1926–45, in: Davis, B.H., Occelli, M.L. (Eds.), *Studies in Surface Science and Catalysis*, Elsevier, 2007, pp. 1–27.

[138] Vogt, E.T.C., Whiting, G.T., Dutta Chowdhury, A., Weckhuysen, B.M., Chapter Two - Zeolites and Zeotypes for Oil and Gas Conversion, in: Jentoft, F.C. (Ed.), *Advances in Catalysis*, Academic Press, 2015, pp. 143–314.

[139] Speight, J.G., 2 - Introduction to refining processes, in: Speight, J.G. (Ed.), *The Refinery of the Future (Second Edition)*, Gulf Professional Publishing, 2020, pp. 43–84.

[140] Bricker, M., Thakkar, V., Petri, J., Hydrocracking in Petroleum Processing, in: Treese, S.A., Pujadó, P.R., Jones, D.S.J. (Eds.), *Handbook of Petroleum Processing*, Springer International Publishing, Cham 2015, pp. 317–359.

[141] Vance, B.C., Kots, P.A., Wang, C., Hinton, Z.R., Quinn, C.M., Epps, T.H., Korley, L.T.J., Vlachos, D.G., Single pot catalyst strategy to branched products via adhesive isomerization and hydrocracking of polyethylene over platinum tungstated zirconia. *Appl. Catal. B Environ.* 2021, *299*, 120483.

[142] Speight, J.G., Chapter 16 - The Future and the Environment, in: Speight, J.G. (Ed.), *Heavy Oil Recovery and Upgrading*, Gulf Professional Publishing, 2019, pp. 699–752.

[143] Saab, R., Polychronopoulou, K., Zheng, L., Kumar, S., Schiffer, A., Synthesis and performance evaluation of hydrocracking catalysts: A review. *J. Ind. Eng. Chem.* 2020, *89*, 83–103.

[144] Pinaeva, L.G., Klimov, O.V., Kazakov, M.O., Noskov, A.S., Development of Catalysts for Hydroprocesses in Oil Refining. *Catal. Ind.* 2021, *13*, 187–202.

[145] Galadima, A., Muraza, O., Hydrocracking catalysts based on hierarchical zeolites: A recent progress. *J. Ind. Eng. Chem.* 2018, *61*, 265–280.

[146] Robinson, P.R., Dolbear, G.E., Hydrotreating and Hydrocracking: Fundamentals, in: Hsu, C.S., Robinson, P.R. (Eds.), *Practical Advances in Petroleum Processing*, Springer, New York, NY 2006, pp. 177–218.

[147] Qin, X., Yu, W., Ye, L., Shen, H., Liu, J., Murad, A., Xie, J., Hou, L., Pu, X., Han, X., Li, J., Wang, R., Liu, N., Reaction laws of polycyclic aromatic hydrocarbons and heteroatomic compounds in hydrocracking process. *Fuel* 2023, *332*, 126242.

[148] Parkash, S., CHAPTER THREE - Hydrocracking Processes, in: Parkash, S. (Ed.), *Refining Processes Handbook*, Gulf Professional Publishing, Burlington 2003, pp. 62–108.

[149] Wang, Y., Yi, K., Sun, B., Sun, J., Xue, Y., An efficient operation optimization method for the series-parallel fractionation system of industrial hydrocracking. *Chem. Eng. Res. Des.* 2021, *171*, 111–124.

[150] Robinson, P.R., 10 - Hydroconversion processes and technology for clean fuel and chemical production, in: Khan, M.R. (Ed.), *Advances in Clean Hydrocarbon Fuel Processing*, Woodhead Publishing, 2011, pp. 287–325.

[151] Rana, M.S., Sámano, V., Ancheyta, J., Diaz, J.A.I., A review of recent advances on process technologies for upgrading of heavy oils and residua. *Fuel* 2007, *86*, 1216–1231.

[152] Peng, C., Fang, X., Zeng, R., Guo, R., Hao, W., Commercial analysis of catalytic hydroprocessing technologies in producing diesel and gasoline by light cycle oil. *Catal. Today* 2016, *276*, 11–18.

[153] Palos, R., Gutiérrez, A., Arandes, J.M., Bilbao, J., Catalyst used in fluid catalytic cracking (FCC) unit as a support of NiMoP catalyst for light cycle oil hydroprocessing. *Fuel* 2018, *216*, 142–152.

[154] Crespo, I., Palos, R., Trueba, D., Bilbao, J., Arandes, J.M., Gutiérrez, A., Intensifying gasoline production in the hydrocracking of pre-hydrotreated light cycle oil by means of Pt and Pd supported on a spent FCC catalyst. *Fuel* 2023, *334*, 126579.

[155] Palos, R., Gutiérrez, A., Arandes, J.M., Bilbao, J., Upgrading of high-density polyethylene and light cycle oil mixtures to fuels via hydroprocessing. *Catal. Today* 2018, *305*, 212–219.

[156] Hita, I., Arabiourrutia, M., Olazar, M., Bilbao, J., Arandes, J.M., Castaño, P., Opportunities and barriers for producing high quality fuels from the pyrolysis of scrap tires. *Renew. Sustain. Energy Rev.* 2016, *56*, 745–759.

[157] Grilc, M., Likozar, B., Levec, J., Hydrodeoxygenation and hydrocracking of solvolysed lignocellulosic biomass by oxide, reduced and sulphide form

of NiMo, Ni, Mo and Pd catalysts. *Appl. Catal. B Environ.* 2014, *150–151*, 275–287.

[158] Cruz, P.L., Iribarren, D., Dufour, J., Life Cycle Costing and Eco-Efficiency Assessment of Fuel Production by Coprocessing Biomass in Crude Oil Refineries. *Energies* 2019, *12*, 4664.

[159] Bouzouita, D., Lelevic, A., Lorentz, C., Venderbosch, R., Pedersen, T.H., Geantet, C., Schuurman, Y., Co-processing bio-liquids with vacuum gasoil through hydrocracking. *Appl. Catal. B Environ.* 2022, *304*, 120911.

[160] Narksri, P., Angnanon, S., Guntasub, J., Wijitrattanatri, K., Kingputtapong, S., Phumpradit, S., Hinchiranan, N., Production of alternative liquid fuels from catalytic hydrocracking of plastics over Ni/SBA-15 catalyst. *Mater. Today Proc.* 2022, *57*, 1040–1047.

[161] Choi, I.-H., Lee, H.-J., Rhim, G.-B., Chun, D.-H., Lee, K.-H., Hwang, K.-R., Catalytic hydrocracking of heavy wax from pyrolysis of plastic wastes using Pd/Hβ for naphtha-ranged hydrocarbon production. *J. Anal. Appl. Pyrolysis* 2022, *161*, 105424.

[162] Vela, F.J., Palos, R., Trueba, D., Cordero-Lanzac, T., Bilbao, J., Arandes, J.M., Gutiérrez, A., A six-lump kinetic model for HDPE/VGO blend hydrocracking. *Fuel* 2023, *333*, 126211.

[163] Han, W., Nie, H., Long, X., Li, D., A study on the role of Ni atoms in the HDN activity of NiMoS2/Al2O3 catalyst. *Appl. Catal. Gen.* 2020, *593*, 117458.

[164] Wan Mahari, W.A., Azwar, E., Foong, S.Y., Ahmed, A., Peng, W., Tabatabaei, M., Aghbashlo, M., Park, Y.-K., Sonne, C., Lam, S.S., Valorization of municipal wastes using co-pyrolysis for green energy production, energy security, and environmental sustainability: A review. *Chem. Eng. J.* 2021, *421*, 129749.

[165] Teles, C.A., de Souza, P.M., Rabelo-Neto, R.C., Teran, A., Jacobs, G., Vilela Weikert, C., Magriotis, Z.M., Gonçalves, V.O.O., Resasco, D.E., Noronha, F.B., Reaction pathways for the HDO of guaiacol over supported Pd catalysts: Effect of support type in the deoxygenation of hydroxyl and methoxy groups. *Mol. Catal.* 2022, *523*, 111491.

[166] Nguyen, T.-H., Nguyen, Q.-A., Cao, A.N.T., Ernest, T., Nguyen, T.B., Pham, P.T.H., Nguyen, T.M., Hydrodemetallization of heavy oil: Recent

progress, challenge, and future prospects. *J. Pet. Sci. Eng.* 2022, *216*, 110762.

[167] Baechler, S.M.A.R., Gonzalez-Cortes, S., Xiao, T., Al-Megren, H.A., Edwards, P.P., Perspective on the Deep Hydrotreating of Renewable and Non-Renewable Oils. *Adv. Solid Catal. Renew. Energy Prod.* 2018, 61–94.

[168] Rana, M.S., Ancheyta, J., Rayo, P., Maity, S.K., Heavy oil hydroprocessing over supported NiMo sulfided catalyst: An inhibition effect by added H2S. *Fuel* 2007, *86*, 1263–1269.

[169] Mohammadi, P., Chapter 5 - Ionic liquids for desulfurization, in: Jawaid, M., Ahmad, A., Reddy, A.V.B. (Eds.), *Ionic Liquid-Based Technologies for Environmental Sustainability*, Elsevier, 2022, pp. 61–74.

[170] Li, J., Yang, Z., Li, S., Jin, Q., Zhao, J., Review on oxidative desulfurization of fuel by supported heteropolyacid catalysts. *J. Ind. Eng. Chem.* 2020, *82*, 1–16.

[171] Gao, Q., Ofosu, T.N.K., Ma, S.-G., Komvokis, V.G., Williams, C.T., Segawa, K., Catalyst development for ultra-deep hydrodesulfurization (HDS) of dibenzothiophenes. I: Effects of Ni promotion in molybdenum-based catalysts. *Catal. Today* 2011, *164*, 538–543.

[172] AL-Hammadi, S.A., Al-Amer, A.M., Saleh, T.A., Alumina-carbon nanofiber composite as a support for MoCo catalysts in hydrodesulfurization reactions. *Chem. Eng. J.* 2018, *345*, 242–251.

[173] Jiang, B., Zhu, T., Song, H., Li, F., Hydrodeoxygenation and hydrodesulfurization over Fe promoted Ni2P/SBA-15 catalyst. *J. Alloys Compd.* 2019, *806*, 254–262.

[174] Ja'fari, M., Ebrahimi, S.L., Khosravi-Nikou, M.R., Ultrasound-assisted oxidative desulfurization and denitrogenation of liquid hydrocarbon fuels: A critical review. *Ultrason. Sonochem.* 2018, *40*, 955–968.

[175] Mikhaylova, P., de Oliveira, L.P., Merdrignac, I., Berlioz-Barbier, A., Nemri, M., Giusti, P., Pirngruber, G.D., Molecular analysis of nitrogen-containing compounds in vacuum gas oils hydrodenitrogenation by (ESI+/-)-FTICR-MS. *Fuel* 2022, *323*, 124302.

[176] Li, F., Srivatsa, S.C., Bhattacharya, S., A review on catalytic pyrolysis of microalgae to high-quality bio-oil with low oxygeneous and nitrogenous compounds. *Renew. Sustain. Energy Rev.* 2019, *108*, 481–497.

[177] Nguyen, M.T., Nguyen, D.L.T., Xia, C., Nguyen, T.B., Shokouhimehr, M., Sana, S.S., Grace, A.N., Aghbashlo, M., Tabatabaei, M., Sonne, C., Kim, S.Y., Lam, S.S., Le, Q.V., Recent advances in asphaltene transformation in heavy oil hydroprocessing: Progress, challenges, and future perspectives. *Fuel Process. Technol.* 2021, *213*, 106681.

[178] Meng, Q., Wang, A., Liu, C., Wang, E., Duan, A., Zhao, Z., Jiang, G., Preparation of Beta-KIT-5 composite material supported ternary metal catalyst and its hydrodenitrogenation performance of quinoline. *Fuel* 2022, *326*, 125084.

[179] Ambursa, M.M., Juan, J.C., Yahaya, Y., Taufiq-Yap, Y.H., Lin, Y.-C., Lee, H.V., A review on catalytic hydrodeoxygenation of lignin to transportation fuels by using nickel-based catalysts. *Renew. Sustain. Energy Rev.* 2021, *138*, 110667.

[180] Zhang, J., Fidalgo, B., Shen, D., Zhang, X., Gu, S., Mechanism of hydrodeoxygenation (HDO) in anisole decomposition over metal loaded Brønsted acid sites: Density Functional Theory (DFT) study. *Mol. Catal.* 2018, *454*, 30–37.

[181] Cordero-Lanzac, T., Palos, R., Hita, I., Arandes, J.M., Rodríguez-Mirasol, J., Cordero, T., Bilbao, J., Castaño, P., Revealing the pathways of catalyst deactivation by coke during the hydrodeoxygenation of raw bio-oil. *Appl. Catal. B Environ.* 2018, *239*, 513–524.

[182] Shi, Y., Ye, G., Yang, C., Tang, Y., Peng, C., Qian, G., Yuan, W., Duan, X., Zhou, X., Pore engineering of hierarchically structured hydrodemetallization catalyst pellets in a fixed bed reactor. *Chem. Eng. Sci.* 2019, *202*, 336–346.

[183] Kusenberg, M., Eschenbacher, A., Delva, L., De Meester, S., Delikonstantis, E., Stefanidis, G.D., Ragaert, K., Van Geem, K.M., Towards high-quality petrochemical feedstocks from mixed plastic packaging waste via advanced recycling: The past, present and future. *Fuel Process. Technol.* 2022, *238*, 107474.

[184] Thybaut, J.W., Marin, G.B., Chapter Two - Multiscale Aspects in Hydrocracking: From Reaction Mechanism Over Catalysts to Kinetics and Industrial Application, in: Song, C. (Ed.), *Advances in Catalysis*, Academic Press, 2016, pp. 109–238.

[185] Vedachalam, S., Boahene, P., Dalai, A.K., Production of jet fuel by hydrorefining of Fischer-Tropsch wax over Pt/Al-TUD-1 bifunctional catalyst. *Fuel* 2021, *300*, 121008.

[186] Zecevic, J., Vanbutsele, G., de Jong, K.P., Martens, J.A., Nanoscale intimacy in bifunctional catalysts for selective conversion of hydrocarbons. *Nature* 2015, *528*, 245–248.

[187] Naranov, E.R., Sadovnikov, A.A., Maximov, A.L., Karakhanov, E.A., Development of micro-mesoporous materials with lamellar structure as the support of NiW catalysts. *Microporous Mesoporous Mater.* 2018, *263*, 150–157.

[188] Looi, P.Y., Mohamed, A.R., Tye, C.T., Hydrocracking of residual oil using molybdenum supported over mesoporous alumina as a catalyst. *Chem. Eng. J.* 2012, *181–182*, 717–724.

[189] Busca, G., Silica-alumina catalytic materials: A critical review. *Catal. Today* 2020, *357*, 621–629.

[190] Saab, R., Polychronopoulou, K., Anjum, D.H., Charisiou, N.D., Goula, M.A., Hinder, S.J., Baker, M.A., Schiffer, A., Effect of SiO2/Al2O3 ratio in Ni/Zeolite-Y and Ni-W/Zeolite-Y catalysts on hydrocracking of heptane. *Mol. Catal.* 2022, *528*, 112484.

[191] Cui, G., Wang, J., Fan, H., Sun, X., Jiang, Y., Wang, S., Liu, D., Gui, J., Towards understanding the microstructures and hydrocracking performance of sulfided Ni–W catalysts: Effect of metal loading. *Fuel Process. Technol.* 2011, *92*, 2320–2327.

[192] Shin, S., Lee, J.H., Jo, Y.K., Nguyen, M.T., Park, B.K., Park, S., Lee, C.W., Kim, C.G., Chung, T.-M., Synthesis of noble molybdenum and tungsten complexes for hydrocracking catalyst of heavy oil. *J. Ind. Eng. Chem.* 2019, *72*, 408–413.

[193] Yang, J., Zhao, L., Liu, S., Wang, Y., Dai, L., High-quality bio-oil from one-pot catalytic hydrocracking of kraft lignin over supported noble metal catalysts in isopropanol system. *Bioresour. Technol.* 2016, *212*, 302–310.

[194] Martinez-Saavedra, J.M., Tavera-Mendez, C.L., Sandoval-Diaz, L.E., Pérez-Martínez, D. de J., Rodriguez-Niño, G., Trujillo, C.A., Fluorene hydrocracking over bifunctional platinum catalysts in a high-pressure simultaneous thermal analyzer. *Appl. Catal. Gen.* 2021, *616*, 118097.

[195] Peng, C., Liu, B., Feng, X., Du, Y., Fang, X., Engineering dual bed hydrocracking catalyst towards enhanced high-octane gasoline generation from light cycle oil. *Chem. Eng. J.* 2020, *389*, 123461.

[196] Cai, Z., Ma, Y., Zhang, J., Wu, W., Cao, Y., Jiang, L., Huang, K., Tunable ionic liquids as oil-soluble precursors of dispersed catalysts for suspended-bed hydrocracking of heavy residues. *Fuel* 2022, *313*, 122664.

[197] Rodríguez, E., Félix, G., Ancheyta, J., Trejo, F., Modeling of hydrotreating catalyst deactivation for heavy oil hydrocarbons. *Fuel* 2018, *225*, 118–133.

[198] Ancheyta, J., Rana, M.S., Furimsky, E., Hydroprocessing of heavy petroleum feeds: Tutorial. *Catal. Today* 2005, *109*, 3–15.

[199] Prajapati, R., Kohli, K., Maity, S.K., Slurry phase hydrocracking of heavy oil and residue to produce lighter fuels: An experimental review. *Fuel* 2021, *288*, 119686.

[200] Vivas-Báez, J.C., Servia, A., Pirngruber, G.D., Dubreuil, A.-C., Pérez-Martínez, D.J., Insights in the phenomena involved in deactivation of industrial hydrocracking catalysts through an accelerated deactivation protocol. *Fuel* 2021, *303*, 120681.

[201] Jiguang, L., Huandi, H., Haiping, S., A new insight into compatibility changing rules for inferior vacuum residue's thermal cracking and hydrocracking process. *J. Anal. Appl. Pyrolysis* 2022, *167*, 105632.

[202] Martinez-Grimaldo, H., Ortiz-Moreno, H., Sanchez-Minero, F., Ramírez, J., Cuevas-Garcia, R., Ancheyta-Juarez, J., Hydrocracking of Maya crude oil in a slurry-phase reactor. I. Effect of reaction temperature, in: *Catalysis Today*, Elsevier, 2014, pp. 295–300.

[203] Yang, T., Deng, W., Zhu, Y., Zhang, S., Liu, Y., Zhang, X., Yang, C., Li, W., Wang, Y., The influences of compositional and structural evolutions of asphaltenes on coking behavior during slurry-bed hydrocracking. *Fuel* 2022, *325*, 124839.

[204] Zhou, J., Zhao, J., Zhang, J., Zhang, T., Ye, M., Liu, Z., Regeneration of catalysts deactivated by coke deposition: A review. *Chin. J. Catal.* 2020, *41*, 1048–1061.

[205] Cerqueira, H.S., Caeiro, G., Costa, L., Ramôa Ribeiro, F., Deactivation of FCC catalysts. *J. Mol. Catal. Chem.* 2008, *292*, 1–13.

[206] Prajapati, R., Kohli, K., Maity, S.K.K., Garg, M.O.O., Coking propensity during hydroprocessing of vacuum residues, deasphalted oils, and asphaltenes. *Fuel* 2017, *203*, 514–521.

[207] Gould, K.A., Wiehe, I.A., Natural Hydrogen Donors in Petroleum Resids. *Energy Fuels* 2007, *21*, 1199–1204.

[208] Rana, M.S., Ancheyta, J., Rayo, P., Maity, S.K., Effect of alumina preparation on hydrodemetallization and hydrodesulfurization of Maya crude. *Catal. Today* 2004, *98*, 151–160.

[209] Liu, T., Ju, L., Zhou, Y., Wei, Q., Ding, S., Zhou, W., Luo, X., Jiang, S., Tao, X., Effect of pore size distribution (PSD) of Ni-Mo/Al2O3 catalysts on the Saudi Arabia vacuum residuum hydrodemetallization (HDM). *Catal. Today* 2016, *271*, 179–187.

[210] Arora, P., Abdolahi, H., Cheah, Y.W., Salam, M.A., Grennfelt, E.L., Rådberg, H., Creaser, D., Olsson, L., The role of catalyst poisons during hydrodeoxygenation of renewable oils. *Catal. Today* 2021, *367*, 28–42.

[211] Li, Z., Wang, X., Du, W., Yang, M., Li, Z., Liao, P., Data-driven adaptive predictive control of hydrocracking process using a covariance matrix adaption evolution strategy. *Control Eng. Pract.* 2022, *125*, 105222.

[212] Soto-Azuara, L.A., Ramírez-López, R., del Carmen Monterrubio-Badillo, Ma., Elizalde, I., Mathematical modeling of the hydrocracking kinetics of a heavy oil fraction using the discrete lumping approach: the effect of the variation of the lump number. *React. Kinet. Mech. Catal.* 2022, *135*, 655–667.

[213] Elizalde, I., Ancheyta, J., On the detailed solution and application of the continuous kinetic lumping modeling to hydrocracking of heavy oils. *Fuel* 2011, *90*, 3542–3550.

[214] Till, Z., Varga, T., Szabó, L., Chován, T., Identification and observability of lumped kinetic models for vacuum gas oil hydrocracking. *Energy Fuels* 2017, *31*, 12654–12664.

[215] Till, Z., Varga, T., Sója, J., Miskolczi, N., Chován, T., Reduction of lumped reaction networks based on global sensitivity analysis. *Chem. Eng. J.* 2019, *375*.

[216] Browning, B., Alvarez, P., Jansen, T., Lacroix, M., Geantet, C., Tayakout-Fayolle, M., A review of thermal cracking, hydrocracking, and slurry phase

hydroconversion kinetic parameters in lumped models for upgrading heavy oils. *Energy Fuels* 2021, *35*, 15360–15380.

[217] Félix, G., Ancheyta, J., Comparison of hydrocracking kinetic models based on SARA fractions obtained in slurry-phase reactor. *Fuel* 2019, *241*, 495–505.

[218] Bin Jumah, A., Malekshahian, M., Tedstone, A.A., Garforth, A.A., Kinetic modeling of hydrocracking of low-density polyethylene in a batch reactor. *ACS Sustain. Chem. Eng.* 2021, *9*, 16757–16769.

[219] Félix, G., Ancheyta, J., Using separate kinetic models to predict liquid, gas, and coke yields in heavy oil hydrocracking. *Ind. Eng. Chem. Res.* 2019, *58*, 7973–7979.

[220] Ancheyta, J., Sánchez, S., Rodríguez, M.A., Kinetic modeling of hydrocracking of heavy oil fractions: A review. *Catal. Today* 2005, *109*, 76–92.

[221] Schubert, T., Lechleitner, A., Lehner, M., Hofer, W., 4-Lump kinetic model of the co-pyrolysis of LDPE and a heavy petroleum fraction. *Fuel* 2020, *262*, 116597.

[222] Tirado, A., Félix, G., Varfolomeev, M.A., Yuan, C., Ancheyta, J., Comparison of parallel and in-series reaction schemes for kinetic modeling of VGO hydrocracking. *Chem. Eng. Sci.* 2023, *267*, 118314.

[223] Li, G., Cai, C., Estimation parameters of hydrocracking model with NSGA-ii (Non-dominated Sorting Genetic Algorithm) by using discrete kinetic lumping model. *Fuel* 2017, *200*, 333–344.

[224] Ancheyta-Juárez, J., Sotelo-Boyás, R., Estimation of Kinetic Constants of a Five-Lump Model for Fluid Catalytic Cracking Process Using Simpler Sub-models. *Energy Fuels* 2000, *14*, 1226–1231.

[225] Fuentes-Ordóñez, E.G., Salbidegoitia, J.A., González-Marcos, M.P., González-Velasco, J.R., Mechanism and kinetics in catalytic hydrocracking of polystyrene in solution. *Polym. Degrad. Stab.* 2016, *124*, 51–59.

[226] Becker, P.J., Celse, B., Guillaume, D., Costa, V., Bertier, L., Guillon, E., Pirngruber, G., A continuous lumping model for hydrocracking on a zeolite catalysts: model development and parameter identification. *Fuel* 2016, *164*, 73–82.

[227] Chehadeh, D., Ma, X., Al Bazzaz, H., Recent progress in hydrotreating kinetics and modeling of heavy oil and residue: A review. *Fuel* 2023, *334*, 126404.

[228] Albazzaz, H., Marafi, A.M., Ma, X., Ansari, T., Hydrodesulfurization Kinetics of Middle Distillates: A Four-Lumping Model with Consideration of Nitrogen and Aromatics Inhibitions. *Energy Fuels* 2017, *31*, 831–838.

[229] Ancheyta, J., Modeling and simulation of catalytic reactors for petroleum refining, John Wiley & Sons, 2011.

[230] Gutiérrez, A., Arandes, J.M., Castaño, P., Olazar, M., Barona, A., Bilbao, J., Effect of Temperature in Hydrocracking of Light Cycle Oil on a Noble Metal-Supported Catalyst for Fuel Production. *Chem. Eng. Technol.* 2012, *35*, 653–660.

[231] Keogh, R.A., Srinivasan, R., Davis, B.H., The effect of Pt concentration on the activity and selectivity of SO2-4-ZrO2 catalysts for the hydrocracking and hydroisomerization of n-hexadecane. *Appl. Catal. Gen.* 1996, *140*, 47–57.

[232] Gutiérrez, A., Arandes, J.M., Castaño, P., Olazar, M., Bilbao, J., Preliminary studies on fuel production through LCO hydrocracking on noble-metal supported catalysts. *Fuel* 2012, *94*, 504–515.

[233] De Lange, M.F., Vlugt, T.J.H.H., Gascon, J., Kapteijn, F., Adsorptive characterization of porous solids: Error analysis guides the way. *Microporous Mesoporous Mater.* 2014, *200*, 199–215.

[234] Al-Dughaither, A.S., de Lasa, H., Neat dimethyl ether conversion to olefins (DTO) over HZSM-5: Effect of SiO_2/Al_2O_3 on porosity, surface chemistry, and reactivity. *Fuel* 2014, *138*, 52–64.

[235] Marianou, A.A., Michailof, C.M., Pineda, A., Iliopoulou, E.F., Triantafyllidis, K.S., Lappas, A.A., Effect of Lewis and BrØnsted acidity on glucose conversion to 5-HMF and lactic acid in aqueous and organic media. *Appl. Catal. Gen.* 2018, *555*, 75–87.

[236] Krishna, S.H., Zhang, L., Hermans, I., Huber, G.W., Kuech, T.F., Dumesic, J.A., Rates of levoglucosanol hydrogenolysis over Brønsted and Lewis acid sites on platinum silica-alumina catalysts synthesized by atomic layer deposition. *J. Catal.* 2020, *389*, 111–120.

[237] Goodman, E.D., Dai, S., Yang, A.C., Wrasman, C.J., Gallo, A., Bare, S.R., Hoffman, A.S., Jaramillo, T.F., Graham, G.W., Pan, X., Cargnello, M., Uniform Pt/Pd Bimetallic Nanocrystals Demonstrate Platinum Effect on Palladium Methane Combustion Activity and Stability. *ACS Catal.* 2017, *7*, 4372–4380.

[238] Kubanek, P., Schmidt, H.W., Spliethoff, B., Schüth, F., Parallel IR spectroscopic characterization of CO chemisorption on Pt loaded zeolites. *Microporous Mesoporous Mater.* 2005, *77*, 89–96.

[239] Lapisardi, G., Urfels, L., Gélin, P., Primet, M., Kaddouri, A., Garbowski, E., Toppi, S., Tena, E., Superior catalytic behaviour of Pt-doped Pd catalysts in the complete oxidation of methane at low temperature. *Catal. Today* 2006, *117*, 564–568.

[240] Giuliano, M., Valsania, M.C., Ticali, P., Sartoretti, E., Morandi, S., Bensaid, S., Ricchiardi, G., Sgroi, M., Characterization of the evolution of noble metal particles in a commercial three-way catalyst: Correlation between real and simulated ageing. *Catalysts* 2021, *11*, 1–15.

[241] Poveda, J.C., Molina, D.R., Average molecular parameters of heavy crude oils and their fractions using NMR spectroscopy. *J. Pet. Sci. Eng.* 2012, *84–85*, 1–7.

[242] Anderson, P.C., Sharkey, J.M., Walsh, R.P., Calculation of the research octane number of motor gasolines from gas chromatographic data and a new approach to motor gasoline quality control. *J Inst Pet* 1972, *58*, 83–94.

[243] Wang, T., Chen, M., Liu, X., Zhang, Z.G., Xu, Y., Distinguishing external and internal coke depositions on micron-sized HZSM-5: Via catalyst-assisted temperature-programmed oxidation. *New J. Chem.* 2019, *43*, 13938–13946.

[244] Sing, K.S.W., Reporting physisorption data for gas/solid systems with special reference to the determination of surface area and porosity (Recommendations 1984). *Pure Appl. Chem.* 1985, *57*, 603–619.

[245] Liu, W., Long, Y., Zhang, J., Liu, S., Zhou, Y., Tong, X., Yin, Y., Li, X., Hu, K., Hu, J., Ag-Cu modified ZSM-5 zeolite to effectively eliminate NOx and slip ammonia from coal-fired flue gas: Catalytic performance and characterization. *J. Environ. Chem. Eng.* 2022, *10*, 108461.

[246] Bourane, A., Dulaurent, O., Salasc, S., Sarda, C., Bouly, C., Bianchi, D., Heats of Adsorption of Linear NO Species on a Pt/Al2O3 Catalyst Using in Situ Infrared Spectroscopy under Adsorption Equilibrium. *J. Catal.* 2001, *204*, 77–88.

[247] Dawody, J., Eurenius, L., Abdulhamid, H., Skoglundh, M., Olsson, E., Fridell, E., Platinum dispersion measurements for Pt/BaO/Al2O3, NOx storage catalysts. *Appl. Catal. Gen.* 2005, *296*, 157–168.

[248] Okumura, K., Takahashi, H., Takaba, H., Direct inclusion of triphenylmethane and triphenylsilane into the pores of zeolite Y. *Microporous Mesoporous Mater.* 2017, *248*, 122–128.

[249] Hossain, M.Z., Chowdhury, M.B.I., Alsharari, Q., Jhawar, A.K., Charpentier, P.A., Effect of mesoporosity of bimetallic Ni-Ru-Al2O3 catalysts for hydrogen production during supercritical water gasification of glucose. *Fuel Process. Technol.* 2017, *159*, 55–66.

[250] Boufaden, N., Akkari, R., Pawelec, B., Fierro, J.L.G., Said Zina, M., Ghorbel, A., Dehydrogenation of methylcyclohexane to toluene over partially reduced Mo–SiO_2 catalysts. *Appl. Catal. Gen.* 2015, *502*, 329–339.

[251] Firdous, N., Janjua, N.K., Wattoo, M.H.S., Promoting effect of ruthenium, platinum and palladium on alumina supported cobalt catalysts for ultimate generation of hydrogen from hydrazine. *Int. J. Hydrog. Energy* 2020, *45*, 21573–21587.

[252] Bin Jumah, A., Tedstone, A.A., Garforth, A.A., Hydrocracking of virgin and post-consumer polymers. *Microporous Mesoporous Mater.* 2021, *315*, 110912.

[253] Lazar, S.T., Howell, B.A., Daniel, Y.G., Li, K.J., Thermal decomposition of poly(styrene) in the presence of a hydrogen atom transfer agent. *J. Therm. Anal. Calorim.* 2017, *127*, 969–974.

[254] Mapiour, M., Sundaramurthy, V., Dalai, A.K., Adjaye, J., Effects of the operating variables on hydrotreating of heavy gas oil: Experimental, modeling, and kinetic studies. *Fuel* 2010, *89*, 2536–2543.

[255] Vela, F.J., Palos, R., Bilbao, J., Arandes, J.M., Gutiérrez, A., Hydrogen Pressure as a Key Parameter to Control the Quality of the Naphtha Produced in the Hydrocracking of an HDPE/VGO Blend. *Catalysts* 2022, *12*.

[256] An, X.-D., Xiao, J., Recent advances in hydride transfer-involved C(sp^3)–H activation reactions. *Org. Chem. Front.* 2021, *8*, 1364.

[257] Wang, L., Xiao, J., Hydrogen-atom transfer reactions. *Top. Curr. Chem.* 2016, *374*, 17.

[258] Palos, R., Gutiérrez, A., Fernández, M.L., Trueba, D., Bilbao, J., Arandes, J.M., Upgrading of heavy coker naphtha by means of catalytic cracking in refinery FCC unit. *Fuel Process. Technol.* 2020, *205*, 106454.

[259] Palos, R., Gutiérrez, A., Hita, I., Castaño, P., Thybaut, J.W., Arandes, J.M., Bilbao, J., Kinetic modeling of hydrotreating for enhanced upgrading of light cycle oil. *Ind. Eng. Chem. Res.* 2019, *58*, 13064–13075.

[260] Becker, P.J., Serrand, N., Celse, B., Guillaume, D., Dulot, H., A single events microkinetic model for hydrocracking of vacuum gas oil. *Comput. Chem. Eng.* 2017, *98*, 70–79.

[261] Cortés, J.C., Rodríguez, C., Molina, R., Moreno, S., Hydrocracking of 1-methylnaphtalene (1MN) over modified clays-supported NiMoS and NiWS catalyst. *Fuel* 2021, *295*, 120612.

[262] Vogelgsang, F., Shi, H., Lercher, J.A., Toward quantification of active sites and site-specific activity for polyaromatics hydrogenation on transition metal sulfides. *J. Catal.* 2021.

[263] Tan, Y., Hu, W., Du, Y., Li, J., Species and impacts of metal sites over bifunctional catalyst on long chain n-alkane hydroisomerization: A review. *Appl. Catal. Gen.* 2021, *611*, 117916.

[264] Yeletsky, P.M., Kukushkin, R.G., Yakovlev, V.A., Chen, B.H., Recent advances in one-stage conversion of lipid-based biomass-derived oils into fuel components – aromatics and isomerized alkanes. *Fuel* 2020, *278*, 118255.

[265] Kostyniuk, A., Bajec, D., Likozar, B., Catalytic hydrocracking reactions of tetralin biomass tar model compound to benzene, toluene and xylenes (BTX) over metal-modified ZSM-5 in ambient pressure reactor. *Renew. Energy* 2022, *188*, 240–255.

[266] Galadima, A., Muraza, O., Ring opening of hydrocarbons for diesel and aromatics production: Design of heterogeneous catalytic systems. *Fuel* 2016, *181*, 618–629.

[267] Tailleur, R.G., Hydrogenation and hydrodesulfurization in gas phase of light hydrocarbons from hydrocracking, desulfurization and delayed coking. I catalyst deactivation. *Chem. Eng. Sci.* 2019, *210*, 115195.

[268] Rana, M.S., AlHumaidan, F.S., Bouresli, R., Navvamani, R., Guard-bed catalyst: Impact of textural properties on catalyst stability and deactivation rate. *Mol. Catal.* 2021, *502*, 111375.

[269] Palos, R., Gutiérrez, A., Vela, F.J., Olazar, M., Arandes, J.M., Bilbao, J., Waste Refinery: the valorization of waste plastics and end-of-life tires in refinery units. A review. *Energy Fuels* 2021, *35*, 3529–3557.

[270] Guisnet, M., Magnoux, P., Organic chemistry of coke formation. *Appl. Catal. Gen.* 2001, *212*, 83–96.

[271] Cordero-Lanzac, T., Palos, R., Arandes, J.M., Castaño, P., Rodríguez-Mirasol, J., Cordero, T., Bilbao, J., Stability of an acid activated carbon based bifunctional catalyst for the raw bio-oil hydrodeoxygenation. *Appl. Catal. B Environ.* 2017, *203*, 389–399.

[272] Ma, Y., Wang, Y., Wu, W., Zhang, J., Cao, Y., Huang, K., Jiang, L., Slurry-phase hydrocracking of a decalin-phenanthrene mixture by MoS_2/SiO_2-ZrO_2 bifunctional catalysts. *Ind. Eng. Chem. Res.* 2021, *60*, 230–242.

[273] Alshareef, A.H., Asphaltenes: Definition, properties, and reactions of model compounds. *Energy Fuels* 2020, *34*, 16–30.

[274] Félix, G., Ancheyta, J., Regular solution model to predict the asphaltenes flocculation and sediments formation during hydrocracking of heavy oil. *Fuel* 2020, *260*, 116160.

[275] Pyhälahti, A., Kanervo, J., Kuitunen, S., Comprehensive residual oil hydrocracking reaction kinetic modeling combined with effective phase equilibrium calculation. *Ind. Eng. Chem. Res.* 2018, *57*, 11271–11279.

[276] Juybar, M., Khanmohammadi Khorrami, M., Bagheri Garmarudi, A., FTIR/PLS and SVM multivariate calibrations to determination of the coke amount into the deactivated catalysts and the product of the methanol to gasoline conversion. *Infrared Phys. Technol.* 2020, *105*, 103229.

[277] Corsetti, S., Zehentbauer, F.M., McGloin, D., Kiefer, J., Characterization of gasoline/ethanol blends by infrared and excess infrared spectroscopy. *Fuel* 2015, *141*, 136–142.

[278] Stanislaus, A., Hauser, A., Marafi, M., Investigation of the mechanism of sediment formation in residual oil hydrocracking process through characterization of sediment deposits. *Catal. Today* 2005, *109*, 167–177.

[279] Jin, X., Li, X., Kong, J., Xie, W., Wang, M., Wang, J., Bao, W., Chang, L., Insights into coke formation during thermal reaction of six different distillates from the same coal tar. *Fuel Process. Technol.* 2021, *211*, 106592.

[280] Wang, N., Zhi, Y., Wei, Y., Zhang, W., Liu, Z., Huang, J., Sun, T., Xu, S., Lin, S., He, Y., Zheng, A., Liu, Z., Molecular elucidating of an unusual growth mechanism for polycyclic aromatic hydrocarbons in confined space. *Nat. Commun.* 2020, *11*, 1–12.

[281] Torres-Mancera, P., Ancheyta, J., Martínez, J., Deactivation of a hydrotreating catalyst in a bench-scale continuous stirred tank reactor at different operating conditions. *Fuel* 2018, *234*, 326–334.

[282] Li, L., Zuo, S., An, P., Wu, H., Hou, F., Li, G., Liu, G., Hydrogen production via steam reforming of n-dodecane over NiPt alloy catalysts. *Fuel* 2020, *262*, 116469.

[283] Zhang, J., Hu, X., Yang, B., Su, N., Huang, H., Cheng, J., Yang, H., Saito, N., Novel synthesis of PtPd nanoparticles with good electrocatalytic activity and durability. *J. Alloys Compd.* 2017, *709*, 588–595.

[284] Park, J.-I., Al-Mutairi, A., Marafi, A.M.J., Mochida, I., Yoon, S.-H., Ma, X., Behaviors of metal compounds during hydrodemetallization of atmospheric residue. *J. Ind. Eng. Chem.* 2016, *40*, 34–39.

[285] Rana, M.S., AlHumaidan, F.S., Navvamani, R., Synthesis of large pore carbon-alumina supported catalysts for hydrodemetallization. *Catal. Today* 2020, *353*, 204–212.

[286] Kwak, W.C., Oh, Y.J., Kang, S.K., Lee, A.H., Jung, S.M., Lee, P.S., Regeneration of zeolite membranes deactivated by condensable molecules. *Int. J. Greenh. Gas Control* 2022, *119*, 103731.

[287] Yang, Q., Zhang, X., Xu, S., Wang, Z., Guo, W., Low-temperature co-current oxidizing pyrolysis of oil shale: Study on the physicochemical properties, reactivity and exothermic characters of semi-coke as heat generation donor. *J. Pet. Sci. Eng.* 2022, *216*, 110726.

[288] Hancsók, J., Nagy, G., Pölczmann, G., Beck, Á., Kalló, D., Hydrodearomatization of sulphur and nitrogen containing gas oils on bimetallic catalysts, in: Gédéon, A., Massiani, P., Babonneau, F. (Eds.), *Zeolites and Related Materials: Trends, Targets and Challenges*, Elsevier, 2008, pp. 1159–1162.

[289] Vela, F.J., Palos, R., García, J.R., Sedran, U., Bilbao, J., Arandes, J.M., Gutiérrez, A., Enhancing the performance of a PtPd/HY catalyst for HDPE/VGO hydrocracking through zeolite desilication. *Fuel* 2022, *329*, 125392.

[290] Žula, M., Grilc, M., Likozar, B., Hydrocracking, hydrogenation and hydrodeoxygenation of fatty acids, esters and glycerides: Mechanisms, kinetics and transport phenomena. *Chem. Eng. J.* 2022, *444*, 136564.

[291] Pham, D.V., Nguyen, N.T., Kang, K.H., Seo, P.W., Park, S., Study into the effects of the feedstock properties and stability on the catalytic hydrocracking of heavy oil. *Fuel* 2023, *339*, 127427.

[292] Cortazar, M., Gao, N., Quan, C., Suarez, M.A., Lopez, G., Orozco, S., Santamaria, L., Amutio, M., Olazar, M., Analysis of hydrogen production potential from waste plastics by pyrolysis and in line oxidative steam reforming. *Fuel Process. Technol.* 2022, *225*, 107044.

[293] Lopez, G., Artetxe, M., Amutio, M., Elordi, G., Aguado, R., Olazar, M., Bilbao, J., Recycling poly-(methyl methacrylate) by pyrolysis in a conical spouted bed reactor. *Chem. Eng. Process. Process Intensif.* 2010, *49*, 1089–1094.

[294] Miao, P., Zhu, X., Guo, Y., Miao, J., Yu, M., Li, C., Combined mild hydrocracking and fluid catalytic cracking process for efficient conversion of light cycle oil into high-quality gasoline. *Fuel* 2021, *292*, 120364.

[295] Zhang, N., Ma, J., Li, R., Jiao, H., Hydrocracking of Fused Aromatic Hydrocarbons Catalyzed by Al-Substituted HZSM-5—A Case Study of 9,10-Dihydroanthracene. *ACS Catal.* 2020, *10*, 9215–9226.

[296] Orozco, S., Alvarez, J., Lopez, G., Artetxe, M., Bilbao, J., Olazar, M., Pyrolysis of plastic wastes in a fountain confined conical spouted bed reactor: Determination of stable operating conditions. *Energy Convers. Manag.* 2021, *229*, 113768.

[297] Li, T., Tao, Z., Hu, C., Zhao, C., Yi, F., Zhao, G., Zhang, L., Yang, Y., Brønsted acidity of amorphous silica-aluminas for hydrocracking of

Fischer-Tropsch wax into diesel fractions. *Appl. Catal. Gen.* 2022, *630*, 118439.

[298] Liu, Z., Meng, X., Xu, C., Gao, J., Secondary Cracking of Gasoline and Diesel from Heavy Oil Catalytic Pyrolysis1 1Supported by the Major Research Plan of Ministry of Education of China (No.307008). *Chin. J. Chem. Eng.* 2007, *15*, 309–314.

[299] Wang, C., Yu, K., Sheludko, B., Xie, T., Kots, P.A., Vance, B.C., Kumar, P., Stach, E.A., Zheng, W., Vlachos, D.G., A general strategy and a consolidated mechanism for low-methane hydrogenolysis of polyethylene over ruthenium. *Appl. Catal. B Environ.* 2022, *319*, 121899.

[300] Mabaleha, S.S., Secondary cracking suppression through Pt/H-BEA: n-Hexadecane hydrocracking. *Microporous Mesoporous Mater.* 2022, *337*, 111902.

[301] Chen, F., Zhang, G., Weng, X., Zhang, Y., Zhao, L., Cao, L., Gao, J., Xu, C., Liu, X., Gao, X., High value utilization of inferior diesel for BTX production: Mechanisms, catalysts, conditions and challenges. *Appl. Catal. Gen.* 2021, *616*, 118095.

[302] Weitkamp, J., Catalytic Hydrocracking—Mechanisms and Versatility of the Process. *ChemCatChem* 2012, *4*, 292–306.

[303] Chub, O.V., Saadatkhah, N., Dubois, J.-L., Patience, G.S., Fluidized bed poly(methyl methacrylate) thermolysis to methyl methacrylate followed by catalytic hydrolysis to methacrylic acid. *Appl. Catal. Gen.* 2022, *638*, 118637.

[304] Halmenschlager, C.M., Brar, M., Apan, I.T., Klerk, A. de, Hydrocracking vacuum gas oil with wax. *Catal. Today* 2020, *353*, 187–196.

[305] Zhang, F., Wang, F., Wei, X., Yang, Y., Xu, S., Deng, D., Wang, Y.-Z., From trash to treasure: chemical recycling and upcycling of commodity plastic waste to fuels, high-valued chemicals and advanced materials. *J. Energy Chem.* 2022, *69*, 369–388.

[306] Calemma, V., Giardino, R., Ferrari, M., Upgrading of LCO by partial hydrogenation of aromatics and ring opening of naphthenes over bi-functional catalysts. *Fuel Process. Technol.* 2010, *91*, 770–776.

[307] Calemma, V., Gambaro, C., Parker, W.O., Carbone, R., Giardino, R., Scorletti, P., Middle distillates from hydrocracking of FT waxes:

Composition, characteristics and emission properties. *Catal. Today* 2010, *149*, 40–46.

[308] Calemma, V., Ferrari, M., Rabl, S., Weitkamp, J., Selective ring opening of naphthenes: From mechanistic studies with a model feed to the upgrading of a hydrotreated light cycle oil. *Fuel* 2013, *111*, 763–770.

[309] Gutiérrez, A., Arandes, J.M., Castaño, P., Olazar, M., Bilbao, J., Effect of Pressure on the Hydrocracking of Light Cycle Oil with a Pt–Pd/HY Catalyst. *Energy Fuels* 2012, *26*, 5897–5904.

[310] Kostyniuk, A., Bajec, D., Likozar, B., Hydrocracking, hydrogenation and isomerization of model biomass tar in a packed bed reactor over bimetallic NiMo zeolite catalysts: Tailoring structure/acidity. *Appl. Catal. Gen.* 2021, *612*, 118004.

[311] Karonis, D., Zahos-Siagos, I., Filimon, D., Vasileiou, F., A multivariate statistical analysis to evaluate and predict ignition quality of marine diesel fuel distillates from their physical properties. *Fuel Process. Technol.* 2017, *166*, 299–311.

[312] Tailleur, R.G., Deactivation of WNiPd/TiO2Al2O3 catalyst during the upgrading of LCO. *Fuel* 2008, *87*, 2551–2562.

[313] Castaño, P., Gutiérrez, A., Hita, I., Arandes, J.M., Aguayo, A.T., Bilbao, J., Deactivating species deposited on Pt-Pd catalysts in the hydrocracking of light-cycle oil. *Energy Fuels* 2012, *26*, 1509–1519.

[314] Vivas-Báez, J.C., Servia, A., Pirngruber, G.D., Dubreuil, A.C., Pérez-Martínez, D.J., Insights in the phenomena involved in deactivation of industrial hydrocracking catalysts through an accelerated deactivation protocol. *Fuel* 2021, *303*.

[315] Liu, X., Ardakani, S.J., Smith, K.J., The effect of Mg and K addition to a Mo2C/HY catalyst for the hydrogenation and ring opening of naphthalene. *Catal. Commun.* 2011, *12*, 454–458.

[316] Dufresne, P., Hydroprocessing catalysts regeneration and recycling. *Appl. Catal. Gen.* 2007, *322*, 67–75.

[317] Rigutto, M.S., Veen, R. van, Huve, L., Chapter 24 - Zeolites in Hydrocarbon Processing, in: Čejka, J., Bekkum, H. van, Corma, A., Schüth, F. (Eds.), *Introduction to Zeolite Science and Practice*, Elsevier, 2007, pp. 855–XXVI.

[318] Dusescu, C., Juganaru, T., Bombos, D., Mihai, O., Popovici, D., Multilayered catalysts for fatty acid ester hydrotreatment into fuel range hydrocarbons. *Comptes Rendus Chim.* 2018, *21*, 288–302.

[319] Priharto, N., Ronsse, F., Prins, W., Hita, I., Deuss, P.J., Heeres, H.J., Hydrotreatment of pyrolysis liquids derived from second-generation bioethanol production residues over NiMo and CoMo catalysts. *Biomass Bioenergy* 2019, *126*, 84–93.

[320] Palos, R., Kekäläinen, T., Duodu, F., Gutiérrez, A., Arandes, J.M., Jänis, J., Castaño, P., Detailed nature of tire pyrolysis oil blended with light cycle oil and its hydroprocessed products using a NiW/HY catalyst. *Waste Manag.* 2021, *128*, 36–44.

[321] Adamson, J.T., Hakansson, K., Chapter 14 - Electrospray Ionization Fourier Transform Ion Cyclotron Resonance Mass Spectrometry for Lectin Analysis, in: Nilsson, C.L. (Ed.), *Lectins*, Elsevier Science B.V., Amsterdam 2007, pp. 343–371.

[322] Palos, R., Kekäläinen, T., Duodu, F., Gutiérrez, A., Arandes, J.M., Jänis, J., Castaño, P., Screening hydrotreating catalysts for the valorization of a light cycle oil/scrap tires oil blend based on a detailed product analysis. *Appl. Catal. B Environ.* 2019, *256*, 117863.

[323] Islam, A., Cho, Y., Yim, U.H., Shim, W.J., Kim, Y.H., Kim, S., The comparison of naturally weathered oil and artificially photo-degraded oil at the molecular level by a combination of SARA fractionation and FT-ICR MS. *J. Hazard. Mater.* 2013, *263*, 404–411.

[324] Xia, Y., Wang, X., Ma, C., Wang, X., Zhao, C., Zhao, X., Zhang, Z., Yu, Y., Lin, X., Lu, X., Xu, G., A data processing pipeline for petroleomics based on liquid chromatography-high resolution mass spectrometry. *J. Chromatogr. A* 2022, *1673*, 463194.

[325] Bukhtiyarova, M.V., Toktarev, A.V., Kazakov, M.O., Kodenev, E.G., Pereyma, V.Y., Gabrienko, A.A., Bukhtiyarov, A.V., Echevsky, G.V., Effect of sulfosalicylic acid treatment on the properties of Beta zeolite and performance of NiW/Beta-based catalysts in hexadecane hydrocracking. *Appl. Catal. Gen.* 2020, *598*, 117573.

[326] Ferreira, C., Tayakout-Fayolle, M., Guibard, I., Lemos, F., Toulhoat, H., Ramôa Ribeiro, F., Hydrodesulfurization and hydrodemetallization of

different origin vacuum residues: Characterization and reactivity. *Fuel* 2012, *98*, 218–228.

[327] Xia, Y., Ma, C., Ju, R., Zhao, C., Zheng, F., Sun, X., Li, Z., Wang, C., Shi, D., Lin, X., Lu, X., Xu, G., Characterization of nitrogen-containing compounds in petroleum fractions by online reversed-phase liquid chromatography-electrospray ionization Orbitrap mass spectrometry. *Fuel* 2021, *284*, 119035.

[328] An, H., Li, H., Zhou, J., Zhang, J., Zhang, T., Ye, M., Liu, Z., Kinetics of steam regeneration of SAPO-34 zeolite catalyst in methanol-to-olefins (MTO) process. *Chin. J. Chem. Eng.* 2021, *35*, 231–238.

[329] Narksri, P., Angnanon, S., Guntasub, J., Wijitrattanatri, K., Kingputtapong, S., Phumpradit, S., Hinchiranan, N., Production of alternative liquid fuels from catalytic hydrocracking of plastics over Ni/SBA-15 catalyst. *Mater. Today Proc.* 2021.

[330] Otte, D.A.L., Borchmann, D.E., Lin, C., Weck, M., Woerpel, K.A., 13C NMR Spectroscopy for the Quantitative Determination of Compound Ratios and Polymer End Groups. *Org. Lett.* 2014, *16*, 1566–1569.

[331] Mao, J.D., Schmidt-Rohr, K., Accurate Quantification of Aromaticity and Nonprotonated Aromatic Carbon Fraction in Natural Organic Matter by 13C Solid-State Nuclear Magnetic Resonance. *Environ. Sci. Technol.* 2004, *38*, 2680–2684.

[332] Gabriëlse, W., Van Well, H.F.J.M., Veeman, W.S., Determination of the 13C magnetic shielding tensor in partially oriented polymer systems. *Solid State Nucl. Magn. Reson.* 1996, *6*, 231–240.

[333] Yue, H., Vieth-Hillebrand, A., Han, Y., Horsfield, B., Schleicher, A.M., Poetz, S., Unravelling the impact of lithofacies on the composition of NSO compounds in residual and expelled fluids of the Barnett, Niobrara and Posidonia formations. *Org. Geochem.* 2021, *155*, 104225.

[334] Guillemant, J., Albrieux, F., De Oliveira, L.P., Lacoue-Nègre, M., Duponchel, L., Joly, J.F., Insights from nitrogen compounds in gas oils highlighted by high-resolution Fourier transform mass spectrometry. *Anal. Chem.* 2019, *91*, 12644–12652.

[335] Nguyen, M.-T., Tayakout-Fayolle, M., Chainet, F., Pirngruber, G.D., Geantet, C., Use of kinetic modeling for investigating support acidity

effects of NiMo sulfide catalysts on quinoline hydrodenitrogenation. *Appl. Catal. Gen.* 2017, *530*, 132–144.

[336] Geantet, C., Laurenti, D., Guilhaume, N., Lorentz, C., Borghol, I., Bujoli, B., Chailleux, E., Checa, R., Schramm, S., Carré, V., Aubriet, F., Quefféléc, C., FT-ICR MS characterization of bio-binders for road pavement from HTL of microalgae residues. *J. Environ. Chem. Eng.* 2022, *10*, 107361.

[337] Qiu, Z., Wang, Y., Li, Z., Cao, Y., Li, Q., Hydrodenitrogenation of Quinoline with high selectivity to aromatics over α-MoC1-x. *Mol. Catal.* 2021, *516*, 112002.

[338] Lai, T., Mao, Y., Wang, W., Wang, X., Wang, N., Liu, Z., Characterization of basic nitrogen compounds isolated with FeCl3 in vacuum gas oil and its hydrotreated product. *Fuel* 2020, *262*, 116523.

[339] Zhang, P., Zhou, Y., Zhang, R., Fan, X., Wei, Q., Liu, X., Effect of sulfur compounds on the hydrodenitrogenation of 1,2,3,4-tetrahydroquinoline and its intermediates over NiMo/Al2O3 catalyst. *Fuel* 2020, *277*, 118186.

[340] Celse, B., Costa, V., Wahl, F., Verstraete, J.J., Dealing with uncertainties: Sensitivity analysis of vacuum gas oil hydrotreatment. *Chem. Eng. J.* 2015, *278*, 469–478.

[341] Pawelec, B., La Parola, V., Thomas, S., Fierro, J.L.G., Enhancement of naphthalene hydrogenation over PtPd/SiO2–Al2O3 catalyst modified by gold. *J. Mol. Catal. Chem.* 2006, *253*, 30–43.

[342] Hancsók, J., Szoboszlai, Z., Kasza, T., Holló, A., Thernesz, A., Kalló, D., Selective desulphurization and denitrogenation of hydrocarbon mixtures rich in olefins. *Catal. Today* 2011, *176*, 177–181.

[343] Ali, M.F., Al-Malki, A., Ahmed, S., Chemical desulfurization of petroleum fractions for ultra-low sulfur fuels. *Fuel Process. Technol.* 2009, *90*, 536–544.

[344] Guillemant, J., Berlioz-Barbier, A., Chainet, F., de Oliveira, L.P., Lacoue-Nègre, M., Joly, J.F., Duponchel, L., Sulfur compounds characterization using FT-ICR MS: Towards a better comprehension of vacuum gas oils hydrodesulfurization process. *Fuel Process. Technol.* 2020, *210*, 106529.

[345] Ding, L., Zheng, Y., Zhang, Z., Ring, Z., Chen, J., HDS, HDN, HDA, and hydrocracking of model compounds over Mo-Ni catalysts with various acidities. *Appl. Catal. Gen.* 2007, *319*, 25–37.

[346] Ahmaruzzaman, M., Sharma, D.K., Characterization of liquid products from the co-cracking of ternary and quaternary mixture of petroleum vacuum residue, polypropylene, Samla coal and Calotropis Procera. *Fuel* 2008, *87*, 1967–1973.

[347] Safa, M.A., Bouresli, R., Al-Majren, R., Al-Shamary, T., Ma, X., Oxidative desulfurization kinetics of refractory sulfur compounds in hydrotreated middle distillates. *Fuel* 2019, *239*, 24–31.

[348] Nadeina, K.A., Potapenko, O.V., Kazakov, M.O., Doronin, V.P., Saiko, A.V., Sorokina, T.P., Kleimenov, A.V., Klimov, O.V., Noskov, A.S., Influence of hydrotreatment depth on product composition of fluid catalytic cracking process for light olefins production. *Catal. Today* 2021, *378*, 2–9.

[349] Kim, S., Kwon, E.E., Kim, Y.T., Jung, S., Kim, H.J., Huber, G.W., Lee, J., Recent advances in hydrodeoxygenation of biomass-derived oxygenates over heterogeneous catalysts. *Green Chem.* 2019, *21*, 3715–3743.

[350] Tsai, T.-L., Lin, C.-C., Guo, G.-L., Chu, T.-C., Effects of microwave-assisted digestion on decomposition behavior of polymethyl methacrylate (PMMA). *Mater. Chem. Phys.* 2008, *108*, 382–390.

[351] Ban, Y., Jin, L., Li, Y., Yang, H., Hu, H., Pyrolysis behaviors of model compounds with representative oxygen-containing functional groups in carbonaceous feedstock over calcium. *Fuel* 2023, *335*, 127137.

[352] Dimonie, D., Socoteanu, R., Pop, S., Fierascu, I., Fierascu, R., Petrea, C., Zaharia, C., Petrache, M., Dimonie, D., Socoteanu, R., Pop, S., Fierascu, I., Fierascu, R., Petrea, C., Zaharia, C., Petrache, M., Overview on Mechanical Recycling by Chain Extension of POSTC-PET Bottles, IntechOpen, 2012.

[353] Li, S., Cañete Vela, I., Järvinen, M., Seemann, M., Polyethylene terephthalate (PET) recycling via steam gasification – The effect of operating conditions on gas and tar composition. *Waste Manag.* 2021, *130*, 117–126.

[354] Becker, P.J., Serrand, N., Celse, B., Guillaume, D., Dulot, H., Comparing hydrocracking models: continuous lumping vs. single events. *Fuel* 2016, *165*, 306–315.

[355] Martínez, J., Ancheyta, J., Kinetic model for hydrocracking of heavy oil in a CSTR involving short term catalyst deactivation. *Fuel* 2012, *100*, 193–199.

[356] Cordero-Lanzac, T., Aguayo, A.T., Gayubo, A.G., Castaño, P., Bilbao, J., Simultaneous modeling of the kinetics for n-pentane cracking and the deactivation of a HZSM-5 based catalyst. *Chem. Eng. J.* 2018, *331*, 818–830.

[357] Calderón, C.J., Ancheyta, J., Modeling of CSTR and SPR small-scale isothermal reactors for heavy oil hydrocracking and hydrotreating. *Fuel* 2018, *216*, 852–860.

[358] Sánchez, S., Ancheyta, J., Effect of pressure on the kinetics of moderate hydrocracking of Maya crude oil. *Energy Fuels* 2007, *21*, 653–661.

[359] Schwaab, M., Pinto, J.C., Optimum reference temperature for reparameterization of the Arrhenius equation. Part 1: problems involving one kinetic constant. *Chem. Eng. Sci.* 2007, *62*, 2750–2764.

[360] Gutiérrez, A., Arandes, J.M., Castaño, P., Aguayo, A.T., Bilbao, J., Role of acidity in the deactivation and steady hydroconversion of light cycle oil on noble metal supported catalysts. *Energy Fuels* 2011, *25*, 3389–3399.

[361] Elizalde, I., Ancheyta, J., Modeling catalyst deactivation during hydrocracking of atmospheric residue by using the continuous kinetic lumping model. *Fuel Process. Technol.* 2014, *123*, 114–121.

[362] Monzón, A., Romeo, E., Borgna, A., Relationship between the kinetic parameters of different catalyst deactivation models. *Chem. Eng. J.* 2003, *94*, 19–28.

[363] Corella, J., Monzón, A., Modeling of the deactivation kinetics of solid catalysts by two or more simultaneous and different causes. *Ind. Eng. Chem. Res.* 1988, *27*, 369–374.

[364] Gayubo, A.G., Aguayo, A.T., Olazar, M., Vivanco, R., Bilbao, J., Kinetics of the irreversible deactivation of the HZSM-5 catalyst in the MTO process. *Chem. Eng. Sci.* 2003, *58*, 5239–5249.

[365] Pérez-Uriarte, P., Ateka, A., Aguayo, A.T., Gayubo, A.G., Bilbao, J., Kinetic model for the reaction of DME to olefins over a HZSM-5 zeolite catalyst. *Chem. Eng. J.* 2016, *302*, 801–810.

[366] Chapra, S.C., Canale, R.P., Multidimensional uncontrained optimization, in: *Numerical Methods for Engineers*, McGraw-Hill, México D.F. 2010, pp. 352–353.

[367] Félix, G., Ancheyta, J., Trejo, F., Sensitivity analysis of kinetic parameters for heavy oil hydrocracking. *Fuel* 2019, *241*, 836–844.

[368] Pham, H.H., Kim, K.H., Go, K.S., Nho, N.S., Kim, W., Kwon, E.H., Jung, R.H., Lim, Y., Lim, S.H., Pham, D.A., Hydrocracking and hydrotreating reaction kinetics of heavy oil in CSTR using a dispersed catalyst. *J. Pet. Sci. Eng.* 2021, *197*, 107997.

[369] Amin, S.S., Abdollahi, H., Naseri, A., The influence of coupled kinetic-equilibrium in breaking the correlation between kinetic parameters. *Chemom. Intell. Lab. Syst.* 2021, *215*, 104349.

[370] De Almeida, R.M., Guirardello, R., Menegassi, R., Almeida, D., Guirardello, R., Hydroconversion kinetics of Marlim vacuum residue. *Catal. Today* 2005, *109*, 104–111.

[371] Pham, H.H., Thuy Nguyen, N., Go, K.S., Park, S., Sun Nho, N., Kim, G.T., Wee Lee, C., Felix, G., Kinetic study of thermal and catalytic hydrocracking of asphaltene. *Catal. Today* 2020, *353*, 112–118.

[372] Martínez, J., Ancheyta, J., Modeling the kinetics of parallel thermal and catalytic hydrotreating of heavy oil. *Fuel* 2014, *138*, 27–36.

[373] Munir, D., Irfan, M.F., Usman, M.R., Hydrocracking of virgin and waste plastics: A detailed review. *Renew. Sustain. Energy Rev.* 2018, *90*, 490–515.

[374] Schultz, G., Alexander, R., Lima, F.V., Giordano, R.C., Ribeiro, M.P.A., Kinetic modeling of the enzymatic synthesis of galacto-oligosaccharides: Describing galactobiose formation. *Food Bioprod. Process.* 2021, *127*, 1–13.

[375] Ketzer, F., de Castilhos, F., An assessment on kinetic modeling of esterification reaction from oleic acid and methyl acetate over USY zeolite. *Microporous Mesoporous Mater.* 2021, *314*, 110890.

[376] Cordero-Lanzac, T., Hita, I., García-Mateos, F.J., Castaño, P., Rodríguez-Mirasol, J., Cordero, T., Bilbao, J., Adaptable kinetic model for the transient and pseudo-steady states in the hydrodeoxygenation of raw bio-oil. *Chem. Eng. J.* 2020, *400*, 124679.

[377] El-Sawy, M.S., Hanafi, S.A., Ashour, F., Aboul-Fotouh, T.M., Co-hydroprocessing and hydrocracking of alternative feed mixture (vacuum gas oil/waste lubricating oil/waste cooking oil) with the aim of producing high quality fuels. *Fuel* 2020, *269*, 117437.

[378] Cao, Z., Zhang, X., Xu, C., Huang, X., Wu, Z., Peng, C., Duan, A., Selective hydrocracking of light cycle oil into high-octane gasoline over bi-functional catalysts. *J. Energy Chem.* 2021, *52*, 41–50.

[379] Weitkamp, J., Catalytic Hydrocracking—Mechanisms and Versatility of the Process. *ChemCatChem* 2012, *4*, 292–306.

LIST OF FIGURES

LIST OF TABLES